

2013

Los Alamos Space Weather Summer School Research Reports

Josef Koller, Robin D. Gurule (*Editors*)



2013

Los Alamos Space Weather Summer School
Research Reports

Josef Koller, Robin D. Gurule (*Editors*)

2013

Los Alamos Space Weather Summer School Research Reports

Preface

The third Los Alamos National Laboratory Space Weather Summer School has been even more successful than in previous year. With renewed support from the Institute of Geophysics, Planetary Physics, and Signatures (IGPPS) and additional funding from the Laboratory Directed Research and Development office, the National Science Foundation, the National Aeronautics and Space Administration, and Department of Energy – Office of Science, we were able to return for a third session, hosting a new class of thirteen students from various U.S. and now also two British research institutions from June 3rd – July 26th, 2013. The summer school format includes a series of structured didactic lectures as well as mentored research and practicum opportunities. Lecture topics include a range of general and specialized topics in the field of space weather given by a number of active researchers affiliated with LANL.

In addition to structured lectures and similar to previous years, students had the opportunity to engage in research projects at the lab through a mentored practicum experience. Each student is paired with a LANL-affiliated mentor to execute a collaborative research project, typically strongly linked with a larger on-going research effort at LANL. This model provides valuable experience and expertise to the student while developing the opportunity for future collaboration.

This report includes a summary of the research efforts fostered and facilitated by the Space Weather Summer School. These reports should be viewed as work-in-progress as the short session again typically only offers sufficient time for preliminary results. At the close of each summer school session, students present a summary of their research efforts, and a panel honors the best presenter with an all-expenses-paid trip to a major conference to present their work. This year we had two winners: Scott Hughes with "The Whistler Anisotropy Instability and the Inverse Cascade of Short-Wavelength Turbulence" and Federico Gasperini with "Solar rotation effects on CHAMP derived neutral and plasma densities." Congratulations!

This program continues to enjoy success through career development opportunities for students and opportunities for collaboration between students and mentors. Through continued support from a number of laboratory organizations, foremost IGPP, the

2013

Los Alamos Space Weather Summer School Research Reports

summer school will continue to be hosted at LANL, and plans are already underway for commencement of a 2014 session to be held next summer.

It has been a pleasure for me to organize the Los Alamos Space Weather Summer School, I am proud of its success, and foremost thankful for all the help that I have received. The time has come to hand the summer school over to a new director and I am grateful to announce Dr. Misa Cowee as the new Director. Misa has been involved in the Summer School from the beginning and has always expressed a keen interest in the success of the summer school. The summer school will be in good hands and I am confident of its continued success. Please join me in congratulating Misa on her new position.

Los Alamos, NM
December 2013

Dr. Josef Koller
Summer School Director

Students

| | |
|--------------------|--|
| Gabriel Dima | <i>University of Hawaii at Manoa</i> |
| Chuanfei Dong | <i>University of Michigan at Ann Arbor</i> |
| Sean Elvidge | <i>University of Birmingham</i> |
| Federico Gasperini | <i>University of Colorado at Boulder</i> |
| David Hartley | <i>Lancaster University</i> |
| R. Scott Hughes | <i>University of Southern California</i> |
| Roxanne Katus | <i>University of Michigan at Ann Arbor</i> |
| David Perez | <i>Rensselaer Polytechnic Institute</i> |
| Robert Robertson | <i>Virginia Tech</i> |
| Quintin Schiller | <i>University of Colorado at Boulder</i> |
| Vivek Vittaldev | <i>University of Texas at Austin</i> |
| Chao Yue | <i>University of California at Los Angeles</i> |
| Xiangyun Zhang | <i>University of Michigan at Ann Arbor</i> |

2013

Los Alamos Space Weather Summer School Research Reports

Pictures



Class of 2013:

(left to right John Steinberg, Xiangyn Zhang, Sean Elvidge, Ruth Skoug, Chao Yue, Federico Gasperini, David Hartley, Gabriel Dima, Michael Shoemaker, David Perez, Brent Wohlberg, Sorin Zaharia, Robert Robertson, R. Scott Hughes, Evgeny Titov, Roxanne Katus, Vivek Vittaldev, Richard Linares, Max Wagner, Misa Cowee, Steven Lockyer, David Palmer, Vania Jordanova, Josef Koller, Chuanfei Dong, Yue Chen, Robin Gurule and Humberto Godinez)

2013

Los Alamos Space Weather Summer School Research Reports

Lectures

- Python for Space Science 1*Jon Niehof*
- A Magnetospheric Overview*Geoff Reeves*
- Statistics for Space Science I: Exploratory Data Analysis*Steve Morley*
- Data Assimilation 1*Humberto Godinez*
- Data Assimilation 2*Humberto Godinez*
- Python for Space Science 2*Jon Niehof*
- Measurement Techniques in Space Plasma.....*Brian Larsen*
- Space Data and Pitfalls*Reiner Friedel*
- Adiabatic Particle Motion*Mike Henderson*
- Drag Coefficient Modeling*Andrew Walker*
- Detecting High Energy Particles*John Sullivan*
- Geomagnetic Storms.....*Vania Jordanova*
- Space Debris*Mike Shoemaker*
- Electromagnetic Wave Propagation*Max Light*
- Plasma Sheet*Sorin Zaharia*
- Substorms*Sorin Zaharia*
- Radial Diffusion*Weichao Tu*
- Pitch-Angle/Momentum Diffusion*Greg Cunningham*
- Plasma Waves*Peter Gary*
- Plasma Instabilities.....*Peter Gary*
- Magnetotail Dynamics*Joachim Birn*
- Solar Neutrons and Energetic Particles.....*William Feldman*



2013

Los Alamos Space Weather Summer School Research Reports

Sponsors

- Institute of Geophysics and Planetary Physics
- Laboratory Directed Research and Development
- National Science Foundation
- National Aeronautics and Space Administration
- NSF/DOE Partnership in Plasma Physics Research

Contact Information

Dr. Misa Cowee
Los Alamos Space Weather Summer School
P.O. Box 1663, MS D466
Los Alamos National Lab, NM 87545

<http://SpaceWeatherSchool.org>

Publication Release

LA-UR 13-29060

2013

Los Alamos Space Weather Summer School Research Reports

Project Reports

| | |
|--|----|
| <i>Modeling Ring Current Dynamics using the RAM-SCB Inner Magnetosphere Model</i> Mentor: Vania Jordanova Student: Gabriel Dima | 1 |
| <i>Plasma and Wave Properties Downstream of Martian Bow Shock: Hybrid Simulations</i> Mentor: Misa Cowee Student: Chuanfei Dong..... | 11 |
| <i>Improved Modelling of Upper Atmospheric Densities using Multi-modal Ensembles</i> Mentor: Humberto Godinez Student: Sean Elvidge..... | 19 |
| <i>Solar Rotation Effects on CHAMP Derived Neutral and Plasma Densities at Different Phases of the Solar Cycle</i> Mentor: Humberto Godinez Student: Federico Gasperini | 27 |
| <i>Testing the Cold Plasma Dispersion Relation for Whistler-mode Chorus using EMFISIS Wave Measurement from the Van Allen Probes</i> Mentor: Yue Chen Student: David Hartley | 37 |
| <i>The Whistler Anisotropy Instability and the Inverse Cascade of Short-Wavelength Turbulence</i> Mentor: Peter Gary Student: R. Scott Hughes..... | 47 |

2013

Los Alamos Space Weather Summer School Research Reports

| | |
|--|-----|
| <i>Nonlinear Electric Field Feedback During an Intense Geomagnetic Storm</i> Mentor: Ruth Skoug Student: Roxanne Katus | 53 |
| <i>Localized Density Prediction using a Neural Network-based model</i> Mentor: Michael Shoemaker, Brendt Wohlberg Student: David Perez | 59 |
| <i>Improved Understanding of the Flyby Anomaly using a High-fidelity Solar Radiation Pressure Model</i> Mentor: Michael Shoemaker Student: Robert Robertson | 71 |
| <i>Determining Source Rate Parameters of Energetic Electrons in the Outer Radiation Belt using a Kalman Filter</i> Mentor: Josef Koller Student: Quintin Schiller..... | 79 |
| <i>Improving Non-Gaussian Uncertainty Propagation for Satellite Conjunction Analysis</i> Mentor: Richard Linares Student: Vivek Vittaldev | 85 |
| <i>Isotropic Boundary due to Current Sheet Scattering based on 3-D Force Balanced Magnetic Field</i> Mentor: Vania Jordanova, Sorin Zaharia Student: Chao Yue..... | 95 |
| <i>Mysterious Southward Interplanetary Magnetic Field</i> Mentor: John Steinberg Student: Xiangyn Zhang | 105 |

Modeling Ring Current Dynamics Using the RAM-SCB Inner Magnetosphere Model

Gabriel Dima

Institute for Astronomy, University of Hawaii, Honolulu, HI 96822

Vania Jordanova, Yiqun Yu

Los Alamos National Laboratory, Los Alamos, NM 87545

Abstract

As part of an ongoing effort to improve the models available for understanding magnetospheric dynamics we performed two simulations of the ring current evolution during the October 31, 2012 geomagnetic storm. The simulations used a kinetic inner magnetosphere model (RAM-SCB) coupled to a global physics based MHD model (BATS-R-US) of the outer magnetosphere. Both simulations include all ions (H^+ , He^+ , O^+) that make a significant contribution to the ring current, but only one of the simulations includes electrons. The results from these simulations, in the form of particle fluxes and computed Dst index, are compared directly to recent measurements taken with the RBSP probes, as well as to similar results from an uncoupled RAM-SCB simulation of the same event. These early results indicate that the coupling timing and particle distribution function at the boundary needs to be improved. In its current form the model overestimates the particle fluxes with energies above 100 keV and underestimates the fluxes for lower energy particles. The simulation that did not include electrons returned a good fit to the observed decrease in Dst index at the peak of the storm but did not reproduce well the recovery phase of the storm, most likely due to the time scales used for the loss processes. The magnetic field for the inner magnetosphere is well reproduced for all simulation owing to the self-consistent treatment of plasma/magnetic field interaction in RAM-SCB.

Keywords: ring current, geomagnetic storm, magnetosphere.

1. Introduction

After their discovery by Explorer I in 1958 the radiation belts have been an important part of magnetospheric research. The ring current is formed from trapped plasma in the energy range 0.1 – 400 keV that form a ring around the Earth between ~ 2 -5 R_e . Although it does not carry the most energetic particles or the largest number densities of particles in the radiation belts, the ring current carries the bulk of the particle energy density [Lyons and Williams, 1980]. Hence, through its large fluctuations in response to disturbances in the solar wind, it has the largest effect on the geomagnetic field. Predicting the variation of the ring current is a key goal of magnetospheric research with direct applications to protecting space and ground assets that are sensitive to large variations in space and ground magnetic fields.

Due to the highly nonlinear nature of the interaction between energetic particles and fields computer models are needed in order to realistically model ring current response to solar wind variation. Furthermore, kinetic models need to be used since the energy-dependent gradient/curvature drifts that give rise to the ring current cannot be modeled using magneto-hydrodynamic (MHD) models alone. The geomagnetic field that interacts with the ring current has to be modeled self-consistently since the ring current variations induce changes in the geomagnetic field that in turn affect the ring current, forming a feedback loop.

The Ring current Atmosphere interactions Model (RAM) with Self Consistent (B) Magnetic field (SCB) is the newest form of a kinetic numerical code that has been developed over the past two decades to predict the dynamics of ring current plasma. One component of the model is RAM, a 2-Dimensional kinetic code that calculates the phase-space density changes in the ring current at the magnetic equator [Jordanova et al., 1994; 2006]. Pitch angle anisotropy is fully implemented and important ring current loss processes are included. The 2D-nature of the code in

configuration space is sufficient to study the ring current since changes take place on time scales larger than the gyration and bounce timescales of the particles. The other component of the model is 3D-EqB is a 3-Dimensional magnetic code that calculates the geomagnetic field topology in the inner magnetosphere that is in force-balance with the particle pressure [Zaharia et al., 2004; Zaharia, 2008]. Through the two-way linking between RAM and 3D-EqB self-consistent evolution is achieved for the ring current/geomagnetic field system.

For any realistic time-dependent simulations, boundary conditions in the form of time-dependent space observations need to be used to drive the model. Currently RAM-SCB requires three types of inputs: plasma fluxes, magnetic and electric fields. The origin of these inputs can be empirical models like the Volland-Stern model of the ionospheric potential [Volland, 1973; Stern, 1975] and the Tsyganenko 89 [Tsyganenko, 1989] model for the outer geomagnetic field. Recent developments in computational power allows large scale global models like the Ridley Ionospheric Model (RIM,[Ridley et al., 2004]) and the outer magnetosphere MHD code BATS-R-US ([Powell et al., 1999]) to become viable options for event specific inputs. Both of these physics based models are included in the Space Weather Modeling Framework (SWMF) working towards a unified self-consistent model of space weather prediction. Using fully self-consistent results from physics based simulation is an important goal in the evolution of RAM-SCB. Connection to the solar wind is through velocity, density, magnetic field and pressure measurements taken by satellites located on the dayside of the Earth. A schematic representation of the connections between inputs and the RAM-SCB model is shown in Figure 1.

Comparing the model results against observations is a crucial element in developing any type of predictive tools. The recent launch in August 2012 of the Radiation Storm Belt Probes (RBSP,[Mauk et al., 2012]) provides a great opportunity for validating ring current models. The RBSP mission includes two spacecraft that will examine the radiation belts in-depth by measuring magnetic and electric fields, as well as plasmas with energies ranging from eV to MeV, thus covering most of the energy range of the ring current. Furthermore, the probes will sample the full radial domain of the simulation between 2-6 R_e during a 9 hour orbit, allowing direct comparisons between model outputs and measurements.

Another important benchmark for ring current models is the prediction of the variation of the Disturbance storm time (Dst) index. This parameter is a measure of the fluctuations in the Earth's magnetic field as measured from ground stations distributed around the Earth. Since the storm time ring current produces a magnetic field that opposes the geomagnetic field, the Dst turns negative indicating a weakening of the field.

The goal of this project was to run several simulations for the ring current response during the small-to-moderate (Dst \sim -55 nT) geomagnetic storm that started at 16:00 on October 31st 2012. This is part of ongoing efforts with coupling RAM-SCB to physics based models. From the simulations we extract synthetic observations of particle fluxes and magnetic fields and compare them to observations taken by RBSP for the same period. We also generate a synthetic Dst index variation for this storm and compare it to the measured Dst variation. From the comparisons, we intend to explore limitations and capabilities of the model for our future improvement.

2. Methodology

This section describes two simulations of the ring current evolution during the geomagnetic storm triggered on October 31 2012. Both simulations covered a time-span of 61 hours starting 11:00 UT on October 31 and ending at 00:00 UT on November 3. This time frame includes five hours of quiet solar wind before the sudden storm commencement at 16:00 UT on October 31, as well the full initial, main and half of the recovery phase of the storm (Figure 2). The spatial domain covered by the simulation is split into two parts: an outer magnetosphere region spanning from 32 R_e on the dayside to 200 R_e on the night-side and 128 R_e in the other four directions; an inner magnetosphere region covering 2 – 6.5 R_e (see Figure 3 for a schematic of the simulation domain). At 2 R_e the boundary is open and the magnetic field is dipolar to a very good approximation. The outer magnetosphere region is modeled using the single fluid BATS-R-US MHD code, while the inner region is modeled by the RAM-SCB code. Although BATS-R-US computes density, temperature and magnetic fields self-consistently, currently only the density and temperature are passed to RAM-SCB during the simulations. The RAM-SCB outer boundary magnetic field is specified by the Tsyganenko 89 empirical model. The ionospheric convection electric field is computed using the RIM model and mapped to the RAM-SCB 2D equatorial domain using the magnetic field topology given by 3D-EqB.

At the dayside boundary solar wind data (Figure 2) obtained from the OMNI website¹ was used to drive BATS-R-US and RIM. The solar wind parameters include magnetic field values, velocity, density and temperature. The data is available at 5 minute cadence and missing data was interpolated between available measurements.

The main difference between the two simulations was the composition of the ring current plasma. While one simulation included only H⁺, He⁺ and O⁺ ions, the other also included electrons. Table 1 summarizes information about the coupled simulations as well as details for a third uncoupled simulation of the same geomagnetic storm. Simulation outputs include all plasma parameters inside the model domain. The synthetic Dst index is calculated using Biot-Savart integration of the currents in the whole domain for the BATS-R-US output. Based only on RAM-SCB output the Dst index is calculated solely from ring current energy through the Dessler-Parker-Sckopke (DPS) relation [Dessler and Parker, 1959; Sckopke, 1966]. Including the RBSP satellite orbit parameters and “flying” the satellite through the simulation domain allows synthetic observations of particle fluxes to be produced that can be compared directly to observations for the same date. The results of this comparison are presented in the following section.

Table 1: Summary of the three ring current simulations during the October 31 – November 2, 2012 geomagnetic storm.

| Simulation Name | Description | Boundary conditions for RAM-SCB |
|-----------------|--|--|
| Coupled-E | RAM-SCB is coupled to SWMF and electrons are included. | RIM for the electric field. BAST-R-US for the outer boundary density and temperature. Tsyganenko 89 for the outer magnetosphere magnetic field. |
| Coupled-NE | RAM-SCB is coupled to SWMF and electrons are not included. | RIM for the electric field. BAST-R-US for the outer boundary density and temperature. Tsyganenko 89 for the outer magnetosphere magnetic field. |
| NotCoupled-E | RAM-SCB is not coupled to SWMF and electrons are included. | Volland-Stern ionospheric potential. The Tsyganenko and Mukai [2003] empirical model for outer boundary density and temperature. Tsyganenko 89 for the outer magnetosphere magnetic field. |

3. Results

The pitch-angle averaged synthetic particle fluxes from the simulations Coupled-NE and Coupled-E (see Table 1) are shown in Figure 4 and Figure 5 respectively. For comparison purposes Figure 6 shows results from simulation NotCoupled-E for the same event. The gaps in the synthetic fluxes represent times where the satellite leaves the simulation domain. Some of the gaps are not present in the data from simulation NotCoupled-E since the simulation domain was extended out to 9 R_e. Comparing the ion fluxes between Coupled-E and Coupled-NE it is apparent that the inclusion of electrons leads to an overall decrease in maximum flux levels. This is due to increased pressure from the electrons on the self-consistent magnetic field computed with RAM-SCB. The flux levels show remarkably different time variation between the coupled and non-coupled simulations, indicating a strong dependence on boundary conditions.

Figure 7 shows a side-by-side comparison of the H⁺ fluxes from the Coupled-E, NotCoupled-E and RBSP measurements. Qualitatively it appears that NotCoupled-E agrees better with the evolution of the measurements but there is a large discrepancy for fluxes above 100 keV. The coupled simulation shows clear disagreement with the measurements for plasma fluxes below 100 keV. Figure 8 shows the extracted flux energy spectra for three significant times during the initial, peak and recovery phases of the storm from simulations Coupled-E, NotCoupled-E and RBSP measurements. This quantitative comparison shows that both Coupled-E and NotCoupled-E tend to underestimate the measured fluxes at low energies but behave differently for energies higher than 100 keV. In the high energy regime Coupled-E overestimates the fluxes, while NotCoupled-E underestimates the fluxes.

The synthetic Dst index computed using both Biot-Savart integration and the DPS relation for the simulation Coupled-NE is shown in Figure 9 alongside measured values for the Dst². We also plot the corrected Dst* index which is calculated by removing the contribution from the magnetopause currents using an empirical parameterized function of the dynamic pressure measured at the magnetopause (O’Brien and McPherron, 2000). The simulation

¹ <http://omniweb.gsfc.nasa.gov/>

² <http://swdcwww.kugi.kyoto-u.ac.jp/dstdir/index.html>

does a good job in predicting the decrease in Dst during the storm peak as well as the start of the decrease. It is also noticeable that the major contribution to the Dst index variation is from the ring current. The pre-storm discrepancy between the Dst measurements and predictions are due to the chosen initial conditions in the simulation domain. The recovery phase of the Dst does not agree with the measurements for this particular event since implementation of loss processes that operate universally is still in progress.

Figure 10 shows the computed inner magnetosphere magnetic field from Coupled-E along with RBSP measurements. The agreement is very good, especially at larger radii where most of the ring current plasma is trapped during a weak geomagnetic storm.

4. Conclusions

We compared results from three simulations of the ring current evolution during a moderate geomagnetic storm with measurements taken by the RBSP satellites for the same period.

The NotCoupled-E simulation results were qualitatively closer to observations than the Coupled-E and Coupled-NE simulations. However, all three simulations showed discrepancies between the synthetic and computed fluxes.

Compared to measurements both coupled simulations indicate an enhancement in flux for energies higher than 100 keV and a depletion in the fluxes below this value. The high degree of uniformity in the flux spectrum over the storm period and during the recovery period indicates a need to improve the way the distribution function at the boundary coupled to BATS-R-US.

Only the simulation Coupled-Ne modeled correctly the depression of the Dst index during the storm time but the recovery phase was not well modeled. This highlights the difficulty in estimating the time-scales for the relevant loss processes so this has to be addressed in the future.

The magnetic field for all three simulations compares very well with the measured magnetic field from RBSP indicating that the self-consistent approach of modeling the inner magnetospheric field together with the ring current evolution is highly robust.

This work highlights the sensitivity of large-scale simulation on boundary condition implementation as well as the complex interplay between the different physical processes included in the equations underlying the simulations. Future work will focus on improving the RAM-SCB coupling to BATS-R-US using an improved realistic distribution function for the particle fluxes on the boundary, as well as improving the time-scale on which loss processes operate. Furthermore, as more data products from RBSP data, such as pitch-angle distributions, become available, more refined results can be validated and the physics improved.

References

- Dessler, A. J., and E. N. Parker (1959), Hydromagnetic theory of magnetic storms, *J. Geophys. Res.*, 64, 2239.
- Tsyganenko, N. A., and T. Mukai (2003), Tail plasma sheet models derived from Geotail particle data, *J. Geophys. Res.*, 108, 1136.
- Lyons, L., and D. Williams (1980), A source for the geomagnetic storm main phase ring current, *J. Geophys. Res.*, 85(A2), 523–530.
- Jordanova, V. K., J. U. Kozyra, G. V. Khazanov, A. F. Nagy, C. E. Rasmussen, and M.-C. Fok (1994), A bounce-averaged kinetic model of the ring current ion population, *Geophys. Res. Lett.*, 21(25), 2785–2788.
- Jordanova, V. K., Y. S. Miyoshi, S. Zaharia, M. F. Thomsen, G. D. Reeves, D. S. Evans, C. G. Mouikis, and J. F. Fennell (2006), Kinetic simulations of ring current evolution during the Geospace Environment Modeling challenge events, *J. Geophys. Res.*, 111, A11S10.
- Mauk, B. H., N. J. Fox, S. G. Kanekal, R. L. Kessel, D. G. Sibeck, and A. Ukhorskiy (2012), Science objectives and rationale for the radiation belt storm probes mission, *Space Sci. Rev.*, 1–15.
- O'Brien, T. P., and R. L. McPherron (2000), An empirical phase space analysis of ring current dynamics: Solar wind control of injection and decay, *J. Geophys. Res.*, 105(A4), 7707.
- Powell, K. G., P. L. Roe, T. J. Linde, T. I. Gombosi, and D. L. DeZeeuw (1999), A solution-adaptive upwind scheme for ideal magnetohydrodynamics, *J. Comput. Phys.*, 154(2), 284.
- Ridley, A. J., T. I. Gombosi, and D. L. DeZeeuw (2004), Ionospheric control of the magnetosphere: Conductance, *Ann. Geophys.*, 22, 567.
- Sckopke, N. (1966), A general relation between the energy of trapped particles and the disturbance field near the Earth, *J. Geo. Res.*, 71, 3125.
- Stern, D. (1975), The motion of a proton in the equatorial magnetosphere, *J. Geophys. Res.*, 80(4), 595.
- Tsyganenko, N. A. (1989), A magnetospheric field model with a warped tail current sheet, *Planet. Space. Sci.*, 37, 5.
- Volland, H. (1973), A semieirical model of large-scale magnetospheric electric fields, *J. Geophys. Res.*, 78(1), 171.
- Zaharia, S., J. Birn, R. H. W. Friedel, G. D. Reeves, M. F. Thomsen, and C. Z. Cheng (2004), Substorm injection modeling with nondipolar, time-dependent background field, *J. Geophys. Res.*, 109, A10211.
- Zaharia, S. (2008), Improved Euler potential method for three-dimensional magnetospheric equilibrium, *J. Geophys. Res.*, 113, A08221.

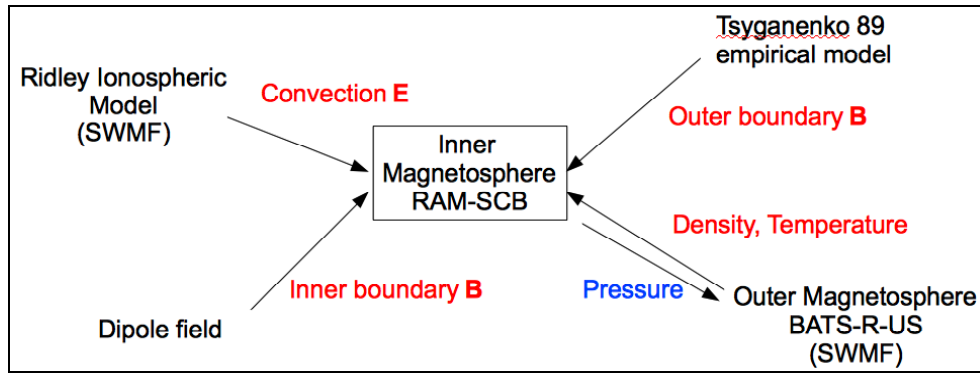


Figure 1: Schematic representation of the various inputs for the RAM-SCB inner magnetosphere model.

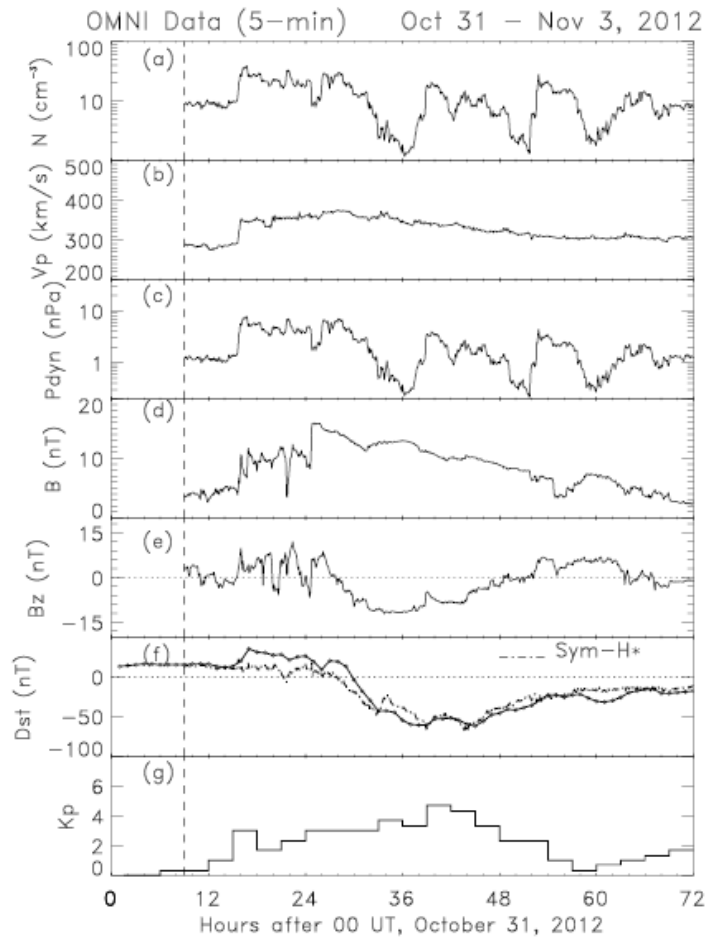


Figure 2. Measurements of solar wind plasma covering the time period of the simulations. Notice that our simulation time covers all relevant phases of the storm, including a 5 hour buffer of quiet solar wind before the sudden storm commencement around 16:00 on October 31, 2012. In order the measurements from top panel to bottom panel are: density, speed, dynamic pressure, magnetic field strength, B_z component of the magnetic field, Dst index and Kp index.

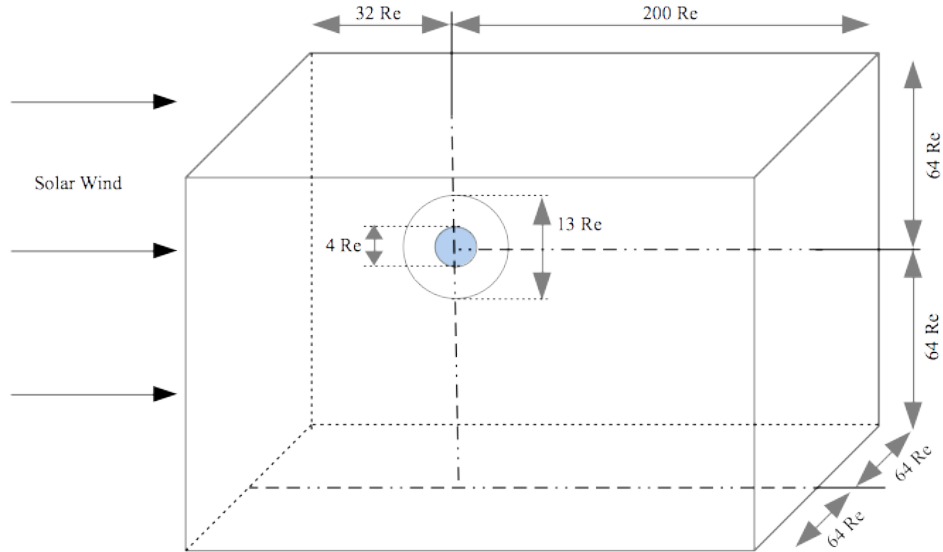


Figure 3: Schematic representation of the domain used for the coupled simulations. BATS-R-US simulates the outer magnetosphere evolution in response to solar wind driving while RAM-SCB simulates the ring current evolution between radii 2-6.5 R_e .

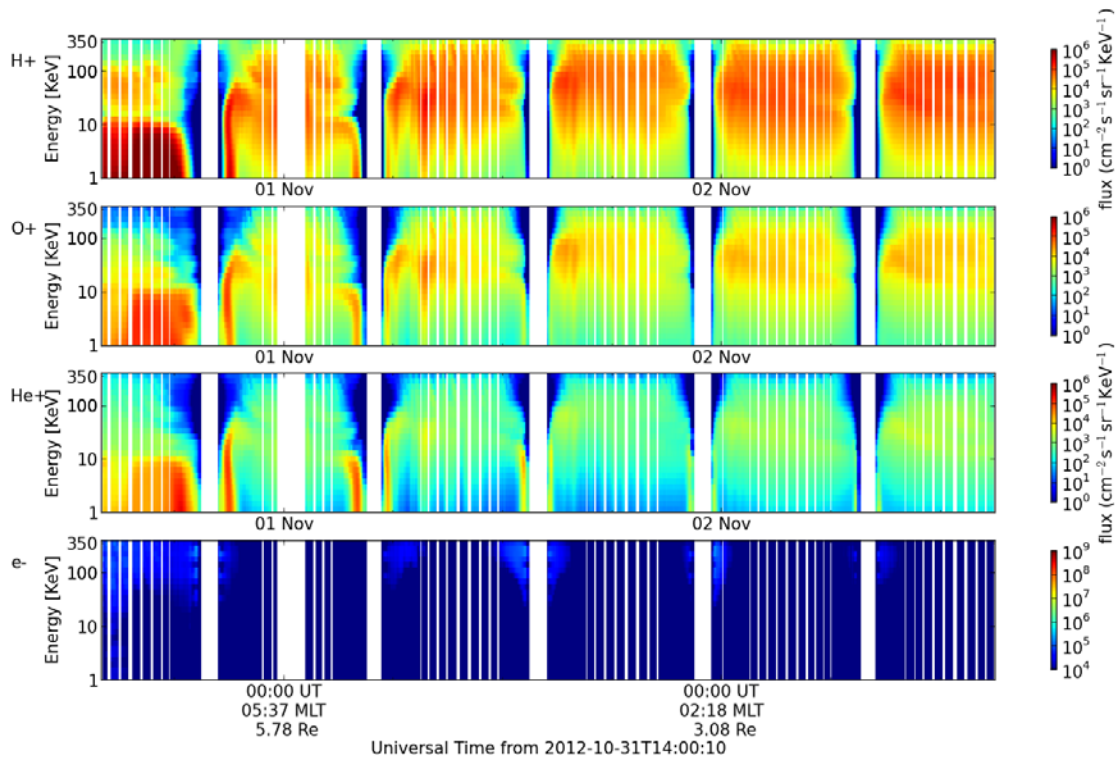


Figure 4. Synthetic RBSP observations of pitch-angle averaged ring current particle fluxes for Coupled-NE. The color coding reflects the intensity of the flux for each energy bin. The gaps in values represent times when the satellite leaves the simulation domain. The spurious values represent numerical residual values that remain in the declared arrays for the electrons, with negligible effects on the results for other ions.

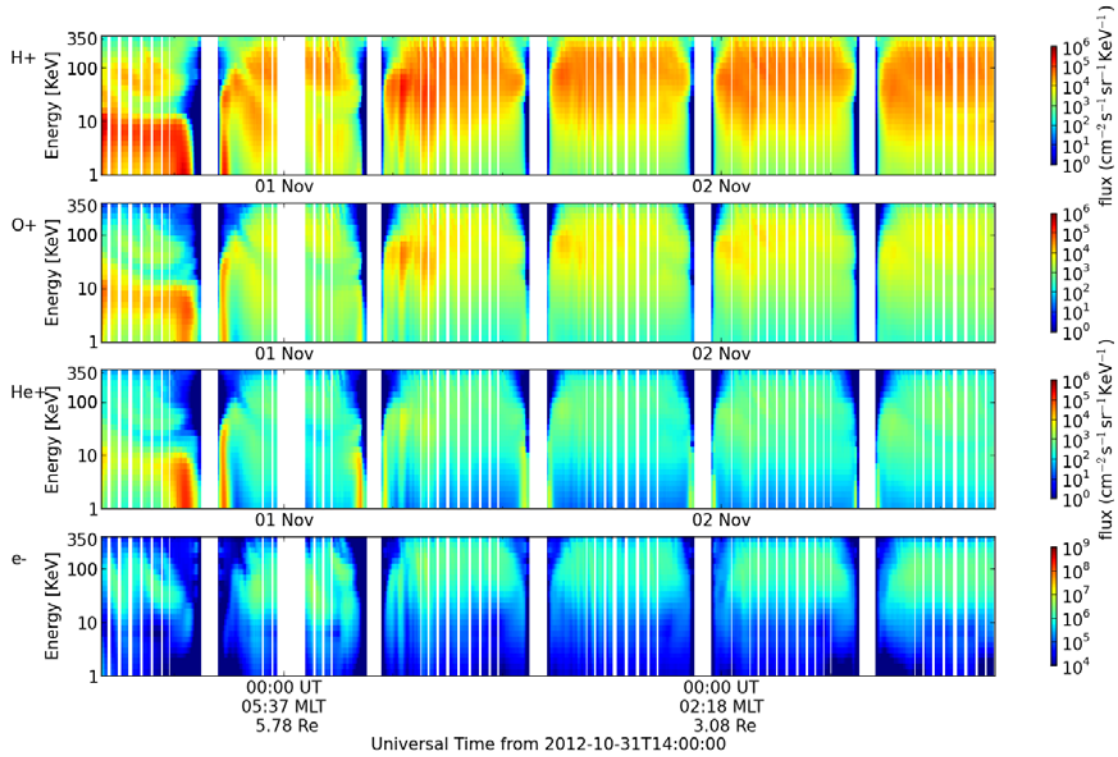


Figure 5. Same as Figure 4 but for results from Coupled-E. Notice that ions fluxes are different than Coupled-NE case due to the added pressure from the electrons in the force-balance calculation.

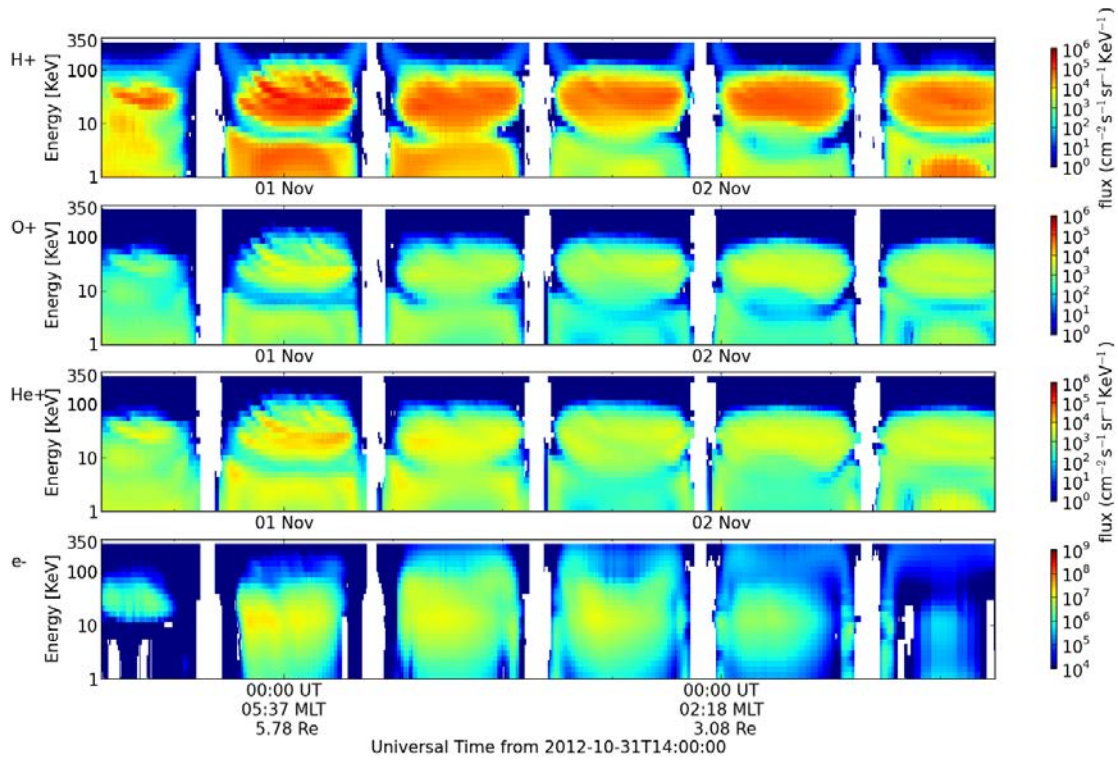


Figure 6. Same as Figures 4 and 5, this shows fluxes from the NotCoupled-E simulation. The boundary conditions for this simulation are substantially different and this results in very different fluxes than for the two coupled simulations.

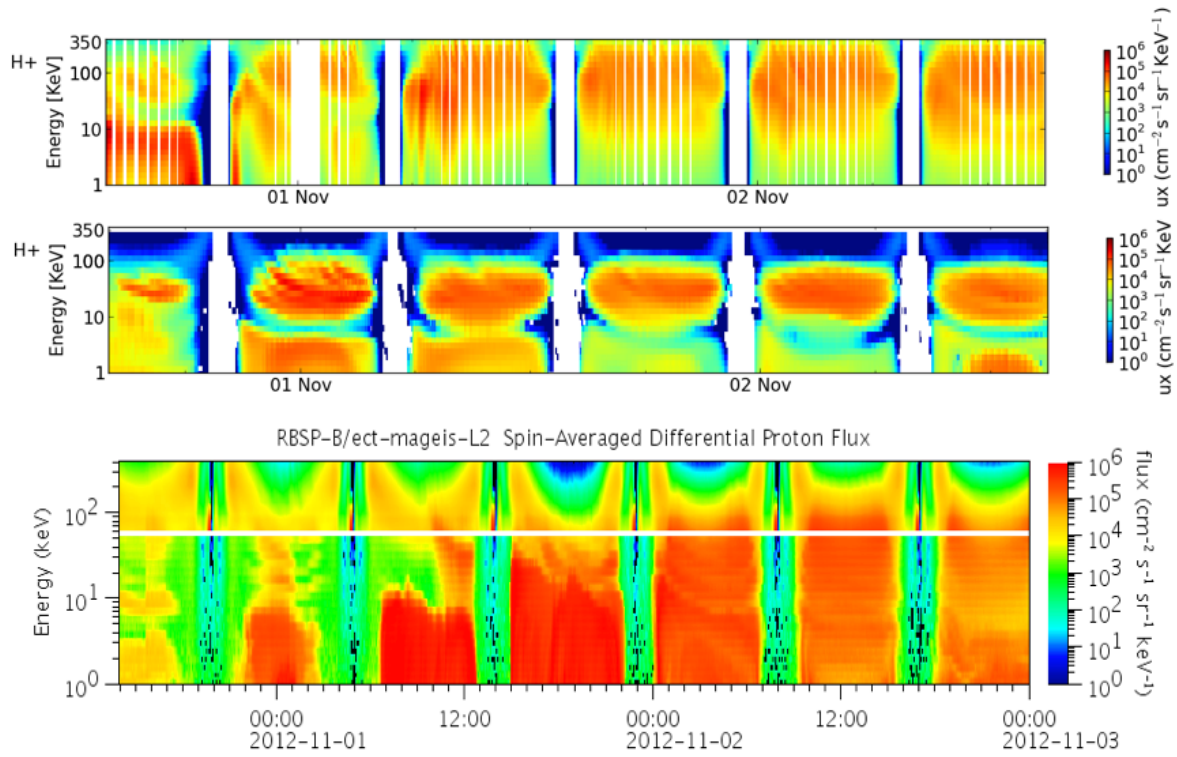


Figure 7. Shown is a side-by-side comparison of the H^+ fluxes from Coupled-E (top panel) and NotCoupled-E (middle panel), together with RBSP observations (bottom panel) for the same period and orbit. Notice that there are some qualitative similarities between the NotCoupled-E results and the observations, notably in reproducing the 10 keV gap in the fluxes. Compared to measurements the decoupled simulation underestimates the higher energy fluxes while the couple simulation overestimates them.

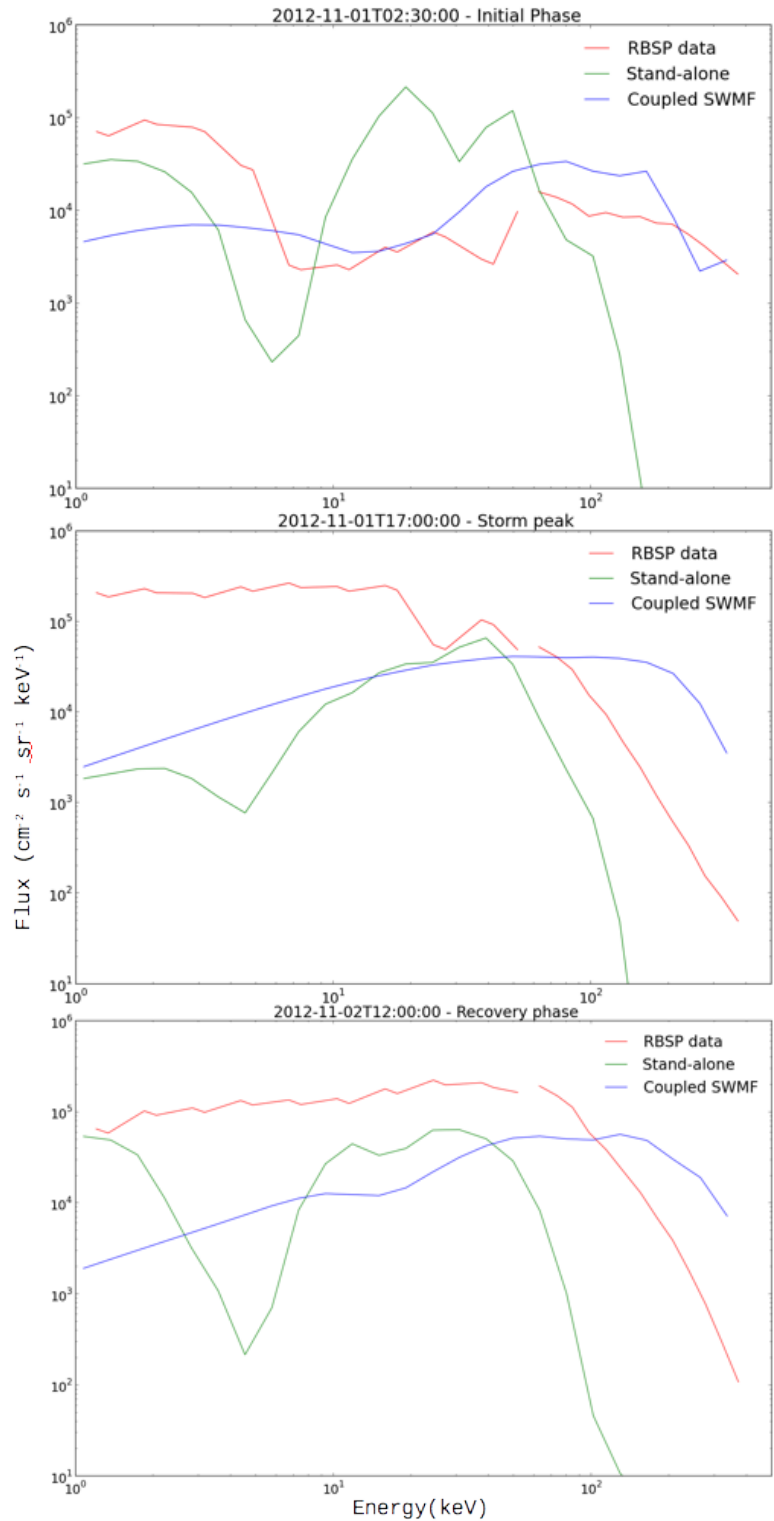


Figure 8. Pitch-angle averaged flux energy spectra from Coupled-E, NotCoupled-E and RBSP observations for three times selected from each phase of the storm: the initial, peak and recovery correspond to top, middle and bottom panels respectively. The gap in the RBSP data corresponds to a gap in the energy coverage between two of the instruments on board. Notice that both simulations tend to underestimate low energy particle fluxes below 100 keV while either over-estimating (Coupled-E) or under-estimating (NotCoupled-E) the higher energy fluxes.

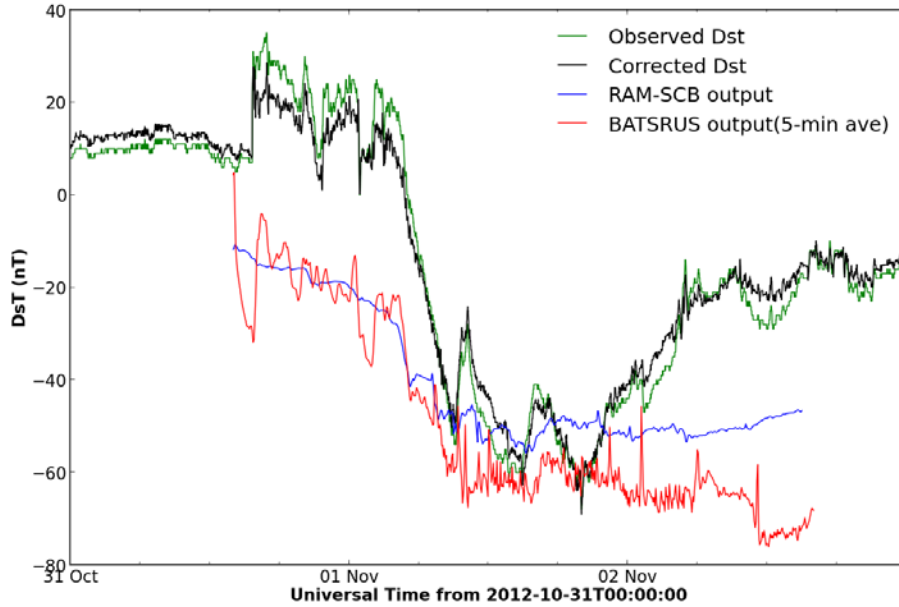


Figure 9. Comparison between measured and synthesized Dst. The synthesized Dst is from simulation Coupled-NE. This is the best fit to the observed Dst variation between all three simulations. The BATS-R-US output takes into account all current systems in the magnetosphere while RAM-SCB only calculates ring current influence.

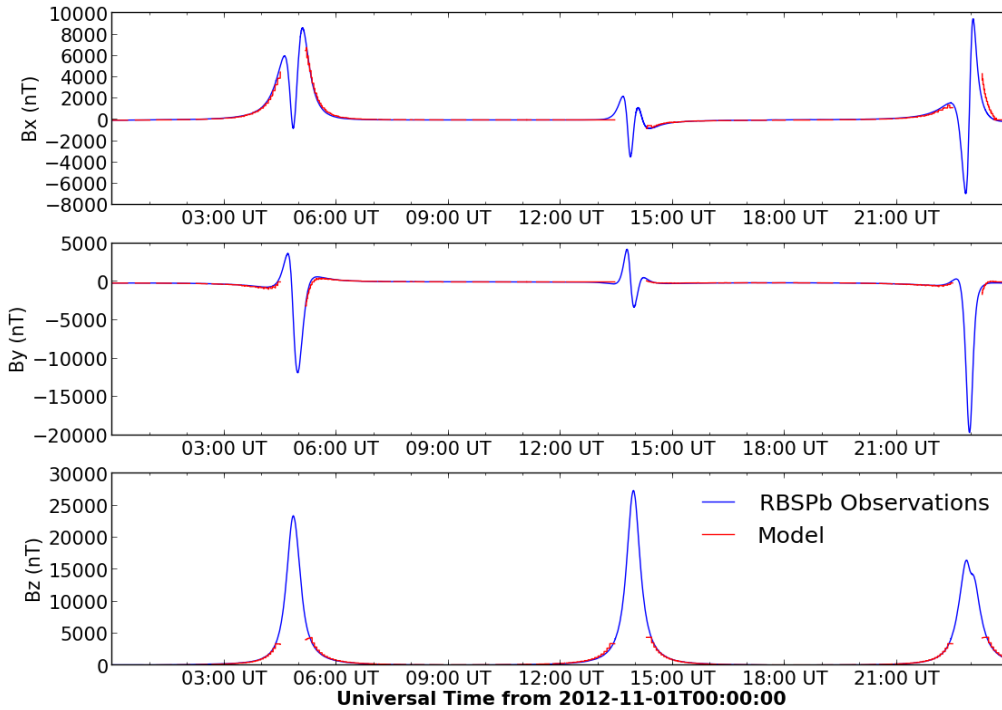


Figure 10. Comparison between simulation Coupled-E magnetic field and RBSP measurements. In regions where the radius of the orbit is less than $2 R_e$ the magnetic field was not calculated since these areas are outside the simulations domain. Away from these inner regions the agreement is very good.

Plasma and wave properties downstream of Martian bow shock: Hybrid simulations

Chuanfei Dong

Department of Atmospheric, Oceanic and Space Sciences, University of Michigan, Ann Arbor, Michigan, USA.

Los Alamos National Laboratory, Los Alamos, New Mexico, USA.

Misa M. Cowee

Los Alamos National Laboratory, Los Alamos, New Mexico, USA.

Dan Winske

Los Alamos National Laboratory, Los Alamos, New Mexico, USA.

Abstract

The two-dimensional Los Alamos hybrid simulation codes are employed to investigate the kinetic properties of plasmas and waves downstream of the Martian bow shock. The simulations are two-dimensional in space but three dimensional in field and velocity components. Simulations show that ion cyclotron waves are generated by temperature anisotropy resulting from the reflected protons around Martian bow shock. These proton cyclotron waves could propagate downward into the Martian ionosphere and are expected to heat the O^+ layer peaked at 250 to 300 km due to the resonant interaction. The proton cyclotron wave heating is anticipated to be a significant source of energy to the thermosphere which impacts escape rates. The simulation results, however, show that without considering the drift velocity resulted from the transport of ionospheric O^+ , the heating of O^+ via proton cyclotron wave resonant interaction is not likely, based on our simplified model. However, a more detailed 3-D model with nonlinear physics may reduce the frequency of the ion cyclotron waves by a factor of 3 and allow such cyclotron resonant heating to occur. It is also possible that some non-resonant heating mechanisms (e.g., stochastic heating) play an important role during the O^+ heating. The exact heating altitude depends on the Martian crustal field location and solar cycle condition since both the resonant condition and the stochastic threshold condition depend on the ambient magnetic field strength. The magnetic field strength profiles based on different crustal field locations and solar cycle conditions are adopted from the BATS-R-US multi-fluid MHD model.

Keywords: hybrid simulation, proton cyclotron wave, temperature anisotropy, Martian bow shock

1. Introduction

Mars has undergone dynamic atmospheric evolution over the last billion years. It is still unclear how Mars dramatically changed from a dense, wet, and warm atmosphere about 3.5 billion years ago (e.g., *Carr and Wänke* 1992) to the dry and cold present atmosphere. The loss of atmospheric particles to space, in particular, the loss of oxygen, has been identified as a major driver behind this change (*Lammer et al.*, 2004, and references therein). Although Mars does not have a strong intrinsic dipole magnetic field, unlike Venus and comets, Mars does have crustal magnetic fields, making it unique in the solar system. The crustal field is mainly concentrated in the southern hemisphere where it is highly localized. The strongest crustal sources exist at latitudes poleward of 30° S and at longitudes between 120° – 210° W (*Acuña et al.*, 1999). Without the shielding of a strong intrinsic magnetic field, the Martian upper

Email addresses: dcfy@umich.edu (Chuanfei Dong), mcowee@lanl.gov (Misa M. Cowee), winske@lanl.gov (Dan Winske)

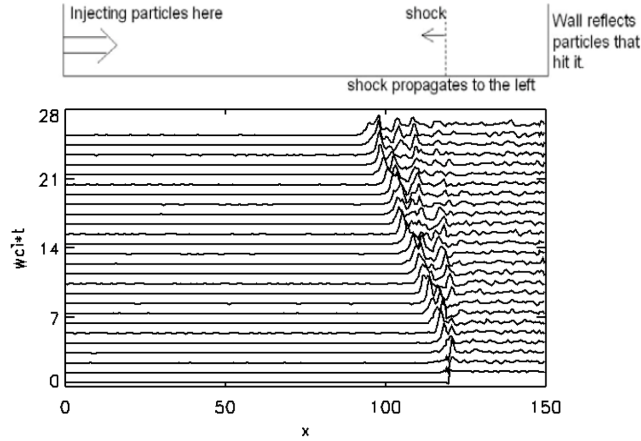


Figure 1: (top) A schematic diagram of a two-dimensional hybrid simulation setup. (bottom) Time evolution of the magnetic field B_y profile (at $y=32 c/\omega_{pi}$) along the x axis. Since the simulation is run in the downstream rest frame, the shock propagates to the left. In the bottom, x is normalized by c/w_{pi} where w_{pi} is the ion plasma frequency and time t is normalized by ω_{ci} where ω_{ci} is the ion gyrofrequency.

atmosphere directly interacts with the impacting solar wind plasma. In order to explore the Mars upper atmosphere and ionosphere, and to better understand their interaction with the solar wind environment, the Mars Atmosphere and Volatile EvolutionN (MAVEN) Mission launched with a window opening in November 2013. MAVEN will determine the role that loss of volatiles to space has played through time.

Among the large number of topics in this research area, the investigation of ion escape fluxes has become increasingly important due to its potential impact on the long-term evolution of Mars atmosphere (e.g., loss of water) over its history. Ion escape flux has been calculated by different plasma models, i.e., multi-species MHD model (*Ma et al., 2004; Ma and Nagy, 2007*), test particle model (*Fang et al., 2010; Curry et al., 2013*), multi-fluid MHD model (*Najib et al., 2011; Rioussset et al., 2013; Dong et al., 2013*), and hybrid model (*Modolo et al., 2006; Brecht and Ledvina, 2012*). Recent observations of plasma waves, electron and ion fluxes in the Martian ionosphere indicate that ion heating may have had a significant impact on Mars' atmospheric loss (*Ergun et al., 2006*). Note that none of the models above investigated the ion escape resulting from the heated ions due to plasma wave interactions in detail. *Ergun et al. (2006)* argued that it is an important source of ion escape, especially because the heating of the Martian ionospheric O^+ layer peaks ($\sim 5 \times 10^8 m^{-3}$) at 250 to 300 km in altitude where the ionosphere is relatively collisionless, indicating kinetic effects are anticipated to play an important role in this process. They adopted an analytic approach to estimate the source flux of O^+ and O^+ heating rates. By using the best available plasma observations in Mars' ionosphere at that time, they showed plasma wave heating in the upper ionosphere could bring $10^{25} atoms s^{-1} O^+$ to the ionopause on the day side and flanks of Mars. However, their assumptions of wave spectrum and power were only based on observations; they did not discuss in detail: 1) the exact generation mechanism of these waves; 2) how the O^+ ions are heated via wave-particle interaction.

In this paper, we aim to investigate the ion cyclotron wave generated around Martian bow shock by the kinetic hybrid code (*Winske et al., 1993, 2003*) and to study the corresponding plasma and wave properties downstream of the shock, which provides self-consistent simulation results to show the possibility of wave heating at Martian ionosphere. This is closely related to one of the eight major scientific objects of MAVEN mission: to investigate the ion heating in the Mars upper atmosphere in order to determine whether the wave heating has a significant effect on the ion escape flux.

2. Model Descriptions

The two-dimensional hybrid code has been adopted where the ions are treated as super-particles and the electrons are treated as massless, adiabatic fluid with $\gamma = 5/3$ (*Winske et al., 1993, 2003*). The hybrid code self-consistently computes the evolution of kinetic ions, fluid electrons, and the associated fluctuating electric and magnetic fields, thus capturing all the kinetic behavior of plasmas at ion inertial length and timescales. The computation domain is

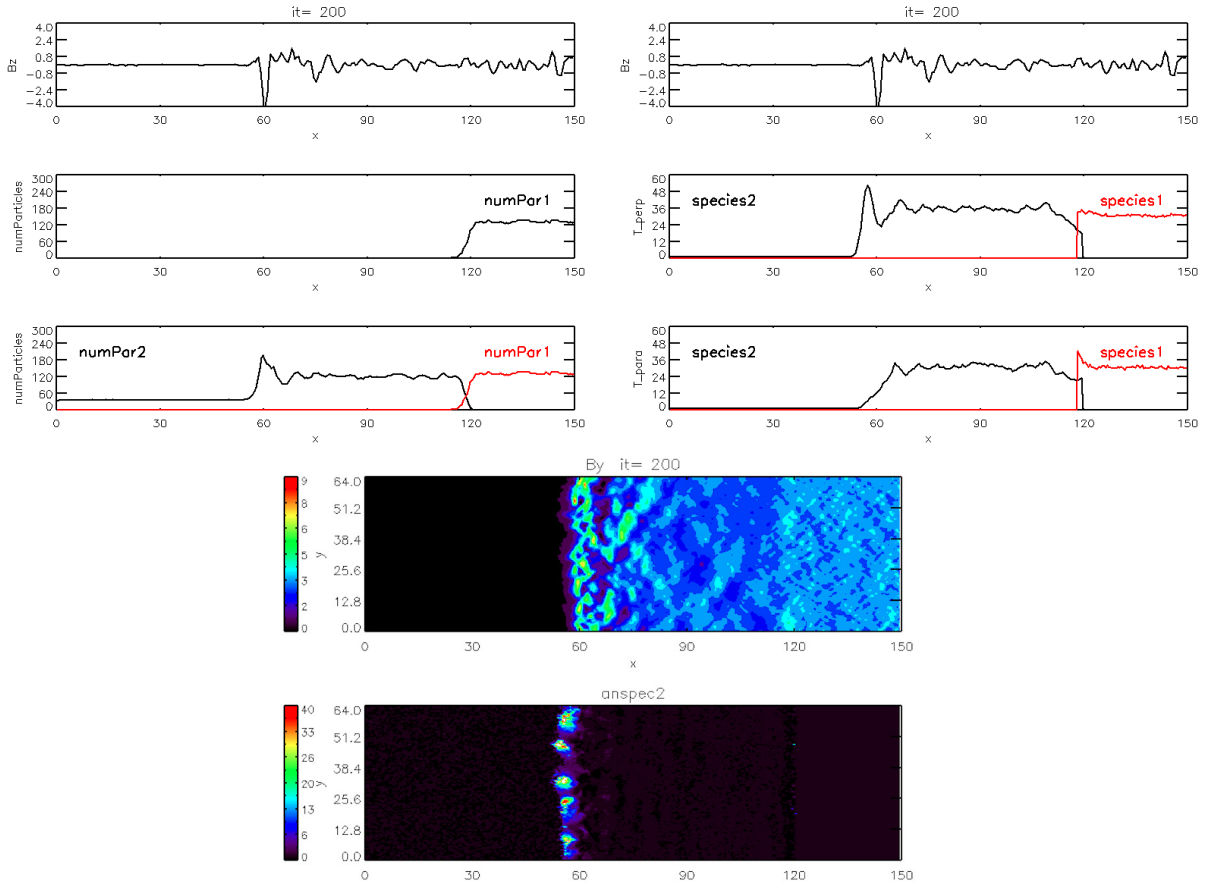


Figure 2: The curves illustrate B_z (at $y=32 c/\omega_{pi}$), number of particles and temperature (average over y axis) of both species one and two versus x which is normalized by c/ω_{pi} . The contour plots show the 2-D view of magnetic field perturbation B_y and temperature anisotropy which is defined as T_{\perp}/T_{\parallel} .

defined by $0 \leq X \leq 150 c/\omega_{pi}$ and $0 \leq Y \leq 64 c/\omega_{pi}$, where c/ω_{pi} is the ion inertial length based on Martian bow shock upstream solar wind condition which approximately equals to 100 km. The resolution in both x and y directions is $dx = dy = 0.5 c/\omega_{pi}$ (~ 50 km). The simulations are run in the downstream rest frame where the stationary shock propagates to the left (see Fig.1). Except where specified, the plots in this paper are all shown in the downstream rest frame. The solar wind plasma (species one) is continuously injected into the simulation domain at the left boundary with velocity $(u_u - u_d)$, where u_d is the downstream velocity in the shock frame calculated from the Rankine-Hugoniot relations. We initialized the simulation domain near right boundary ($120 c/\omega_{pi} \leq X \leq 150 c/\omega_{pi}$) with heated magnetosheath plasma (species two) that satisfies the Rankine-Hugoniot relations. This helps to initiate the shock correctly. Periodic boundary conditions are employed in the y direction and reflected boundary conditions are used in x direction. Although the simulations are two-dimensional in space, the ion velocities, fluid velocities and electromagnetic fields are fully three-dimensional. The total number of superparticles is 3.6×10^6 in the whole simulation. We assume all ions are protons, and the upstream B field is along y axis thus the shock is perpendicular to the shock normal $\theta_{bn} = 90^\circ$. We choose the upstream Alfvén Mach number $M_A=10$ in the simulation, which is well within the observational range. The solar wind thermal velocity distribution is assumed to be Maxwellian. All the variables in the code are normalized based on Martian bow shock upstream solar wind condition.

3. Simulation Results and Discussions

Firstly, in order to test the hybrid simulations, we compare the number of particles (average over y axis) and temperature (average over y axis) of species one and two, where the properties of species one are self-consistently calculated from the hybrid code while the properties of species two are initialized by the Rankine-Hugoniot relations. From Fig. 2, it is clear that the simulation results are consistent with the Rankine-Hugoniot relations. The upper panel of Fig. 2 shows the B_z component of the magnetic field perturbation (at $y=32 c/\omega_{pi}$), as will be explained later, which is associated with the ion cyclotron waves. It is also clear that species one and species two are not mixed due to pressure balance across the boundary at $x = 120 c/\omega_{pi}$. Inspection of Fig. 2 reveals that both B_z and perpendicular temperature of species two have maximum values around the shock front while for species two $T_{\parallel} < T_{\perp}$ near shock front; T_{\parallel} is even lower than the corresponding downstream parallel temperature, indicating that there exists large temperature anisotropy (defined as T_{\perp}/T_{\parallel}) around shock front. This is the reason why the amplitude of B_z peaks around the shock front since the large temperature anisotropy could lead to ion cyclotron instability which generates the ion cyclotron waves. As to the large temperature anisotropy, it results from the fact that some ions get reflected at shock front; which leads to the proton cyclotron motion with large gyroradii. This greatly increases the perpendicular temperature of species two. These particles eventually contribute to the heating of the downstream plasma, consistent with Rankine-Hugoniot relation. It is noteworthy that the peak of B_z falls a little behind the peak of T_{\perp} , thus also the peak of the temperature anisotropy. This is because the temperature anisotropy mainly results from the reflected ions at the shock front which makes the peak of T_{\perp} beyond the shock front. Also, it takes a while for the ion cyclotron waves to grow, so it always saturates behind the shock front. From the contour plot, the peak of B_y (as will be shown in Fig. 3, B_y and B_z peak at same position) indeed falls a little behind the temperature anisotropy peak of species two. At shock front, B_y and density will be greatly compressed, which basically forms a fast mode-like structure: the density peak and B_y peak are in phase. Therefore, the underlying physical mechanisms for large amplitude B_z and B_y at shock front are completely different.

Due to the importance of wave magnetic fluctuation energy density, $\delta B_w^2/B_0^2$, for ion heating, we investigated the evolution of all three components $\delta B_{w,x,y,z}^2/B_0^2$ along the x axis. Simulations show that they have similar amplitude. Here B_x and B_z are caused by the ion cyclotron wave while B_y results from the fast mode-like structure around the shock front. From the simulation, the normalized wave amplitudes are relatively large and approximately equal to 0.4 near the right boundary, which suggests the heating of ionospheric ions is possible. In order to verify that resonant wave-particle interaction is possible in the Martian ionosphere, we need to calculate the wave frequency generated from the ion cyclotron instability. We employed the FFT approach to analyze the temporal and spatial distributions of wave magnetic field (see Fig.4). The hybrid simulation shows that the ratio $B_{downstream}/B_{upstream} \approx 4$. The temporal FFT analysis (from t to ω_r) shows that $\omega_r/\omega_{ci}^{upstream} \approx 3.6$, which corresponds to $\omega_r \approx 0.9 \omega_{ci}^{downstream}$. The spatial FFT analysis (from y to k_y) illustrates the peak is located at $ck_y/\omega_{pi}^{upstream} \approx 1.7$, which corresponds to $ck_y/\omega_{pi}^{downstream} \approx 0.85$ and $\lambda \approx 7.39 c/\omega_{pi}^{downstream}$. Those results agree well with the linear theory predication for ion cyclotron wave properties (Davidson and Ogden, 1975; Gary, 1993). From ray-tracing models (Swanson, 2003; Benkevitch et al., 2010), the frequency of the wave is independent of background parameters during its propagation as long as one investigates a steady state problem.

According to the linear theory, ion cyclotron waves propagating along an ambient magnetic field can only interact with charged particles via cyclotron resonance $\omega_r \pm \omega_{ci}^q - kv_{\parallel} = 0$, where ω_r and k are the wave frequency and wave number, respectively; ω_{ci}^q denotes the gyrofrequency for species labeled q ; v_{\parallel} is the velocity component parallel to the ambient magnetic field; and \pm designates right- and left-hand polarization. Therefore, without considering the drift velocity v_{\parallel} , in order to make the proton cyclotron wave resonant with O^+ ion ($\omega_r \pm \omega_{ci}^{O^+} = 0$), the magnetic field strength would need to be $B_{O^+} \approx 0.9 \times 16 \times 3 \times 4 = 172.8 nT$ (the upstream solar wind magnetic field strength equals to $3 nT$). As shown by Fig.5, the magnetic field strength cannot reach this high value no matter the solar cycle conditions or where the crustal field is located. This indicates a change in the wave frequency by a factor of about 3 would be necessarily allow heating of the ionospheric oxygen ions. Even if we change the shock angle $\theta_{bn} < 90^\circ$, as indicted by Fig.3 in Davidson and Ogden (1975), the proton cyclotron wave resonance with O^+ cannot be satisfied. As such, the resonant interaction with proton cyclotron waves may be not important in heating of O^+ layer in the Martian ionosphere. However, we note that our simplified 2-D planar simulation model is just our first attempt to investigate the wave generation process. A 3-D simulation model with an appropriate Martian ionosphere and full 3-D nonlinear wave propagation may reduce the wave frequency by a factor of 3 and allow wave heating to occur.

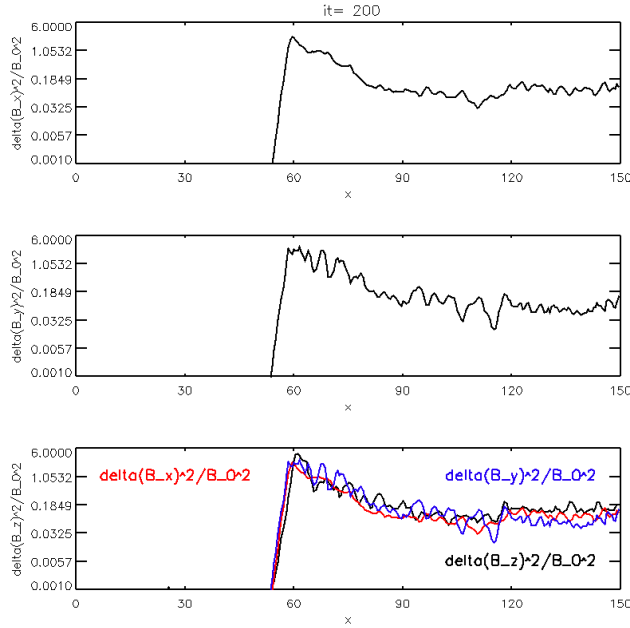


Figure 3: The wave magnetic fluctuation energy density $\delta B_{w,x,y,z}^2/B_0^2$ versus x which is normalized by c/w_{pi} .

Thus, we recommend more complete simulations and nonlinear theory be carried out to examine the cyclotron heating process in better detail. The resonant heating may also be possible if one considers the drift velocity v_{\parallel} resulted from O^+ ion transport from dayside to nightside in the Martian ionosphere (Bougher *et al.*, 2008). The magnitude of the drift velocity, however, is still an open question since there is no available observation with enough precision. The MAVEN mission may have an opportunity to provide us with the related observational data in the near future.

Besides having a hot hydrogen corona, Mars also has a hot oxygen corona, which has been studied in detail by the three-dimensional Direct Simulation Monte Carlo Exosphere Model (DSMC) (Valeille *et al.*, 2009). The ion cyclotron waves generated by picking up of the H^+ ions from the hot hydrogen corona has been well studied (Cowee *et al.*, 2012), however, the ion cyclotron waves generated by picking up of the O^+ ions from the hot oxygen corona has not been investigated yet due to the lack of current available observational data. Although the proton cyclotron wave may be not important in heating the Martian ionospheric O^+ , the ion cyclotron waves generated from the pickup of exospheric O^+ may be important in heating the cold ionospheric O^+ since the ion cyclotron waves generated from the pickup O^+ , in principle, have lower frequency than the proton cyclotron waves generated by the reflected protons around Martian bow shock. This will be investigated in detail in the future. It is also interesting to mention a recent popular stochastic heating mechanism which can occur even below the ion cyclotron frequency in low beta plasmas as long as the threshold condition is satisfied (Chandran *et al.*, 2010; Wang *et al.*, 2011; Dong *et al.*, 2011). Interestingly, the Martian ionosphere is also a low-beta region due to the magnetic field pileup near the Mars body (Najib *et al.*, 2011). It is possible that the the stochastic heating mechanism plays an important role in heating Martian ionospheric O^+ . We plan to investigate it in detail in our future work. It is important to note that whether the ionospheric O^+ heating eventually results from wave-particle resonant interaction or stochastic heating, the crustal field location and solar cycle condition always affect the exact heating altitude. The reason is that both the resonant condition and the stochastic threshold condition depend on the ambient magnetic field strength. For example, for solar cycle minimum condition, the heating altitude should become lower when the crustal field faces the dawn side than when it faces the sun. Finally, there also exist other possible energy sources to heat the ionospheric O^+ such as the plasma waves generated by electron beams and field-aligned currents as indicated in Ergun *et al.* (2006).

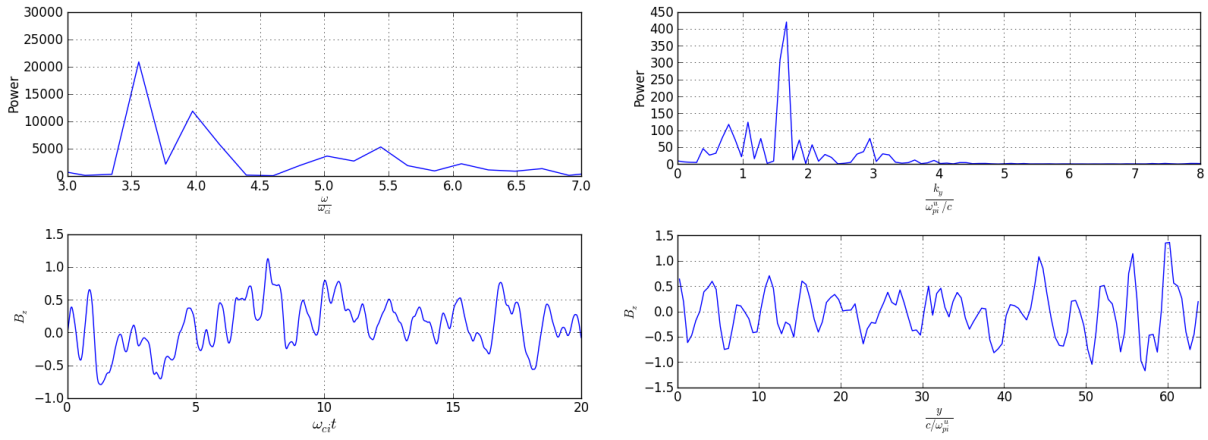


Figure 4: Temporal and spatial FFT analysis and the corresponding temporal and spatial distribution of B_z .

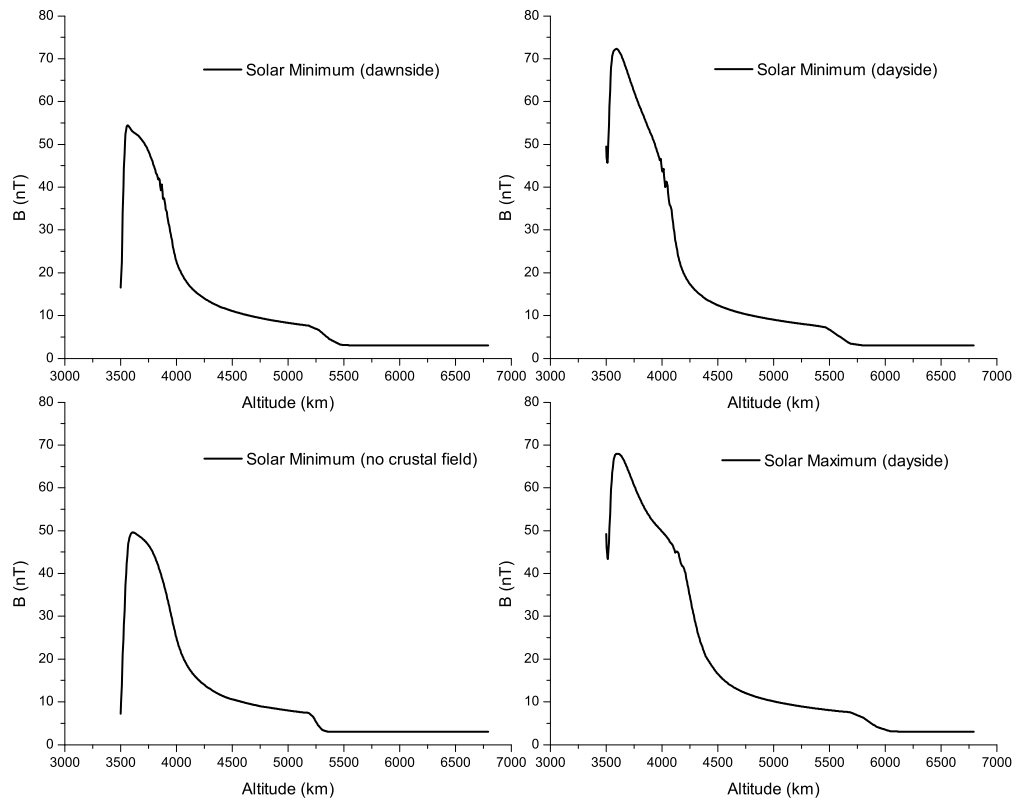


Figure 5: The magnetic field strength profiles along the subsolar line from the BATS-R-US multi-fluid MHD model (Dong *et al.*, 2013).

4. Conclusion

We investigated the plasma and wave properties downstream of the Martian bow shock by employing a two-dimensional hybrid code due to temperature anisotropy. The proton cyclotron waves generated around the Martian bow shock are caused by the reflected ions. By using the FFT analysis of our simplified simulation results, we find that without considering Doppler shift, the resonant heating of O^+ via proton cyclotron wave interaction is unlikely to be efficient in the Martian ionosphere. However, a change in the wave frequency by only a factor of about 3 would allow heating of the oxygen ions. This suggests that this wave heating process should be investigated in more detail using three-dimensional simulations and nonlinear, nonlocal theory. It is also possible that either the drift velocity, v_{\parallel} , resulted from O^+ transport satisfies the resonant condition or that some other heating mechanisms such as stochastic heating may be important in heating the ionospheric O^+ . The ion cyclotron waves generated from the pickup of hot corona O^+ may be important to heat the ionospheric O^+ as well. The crustal field locations and solar cycle conditions play an important role in determining the exact ionospheric O^+ heating altitude since both the resonant condition and the stochastic threshold condition depend on the ambient magnetic field strength. The upcoming MAVEN mission has a great chance to provide observational data to help us better understand the heating process in the Martian ionosphere in the near future.

References

- Acuña, M. H. et al. (1999), Global Distribution of Crustal Magnetization Discovered by the Mars Global Surveyor MAG/ER Experiment, *Science*, 284, 790–793.
- Benkevitch, L., I. Sokolov, D. Oberoi, T. Zurbuchen (2010), Algorithm for Tracing Radio Rays in Solar Corona and Chromosphere, arXiv:1006.5635.
- Bougher, S. W., P.-L. Blelly, M. R. Combi, J. L. Fox, I. Mueller-Wodarg, A. Ridley, and R. G. Roble (2008), Neutral Upper Atmosphere and Ionosphere Modeling, *Space Sci. Reviews*, 139, 107–141.
- Brain, D., et al. (2010), A comparison of global models for the solar wind interaction with Mars, *Icarus*, 206, 139–151.
- Brecht, S. H., and S. A. Ledvina (2012), Control of ion loss from Mars during solar minimum, *Earth, Planets and Space*, 64, 165–178.
- Carr, M. H., and H. Wänke (1992), Earth and Mars: water inventories as clues to accretional histories, *Icarus*, 98, 61–71.
- Chandran, B., B. Li, B. Rogers, E. Quataert, and K. Germaschewski (2010), Perpendicular Ion Heating by Low-Frequency Alfvén-Wave Turbulence in the Solar Wind, *Astrophys. J.*, 720, 503.
- Cowee, M. M., S. P. Gary, and H. Y. Wei (2012), Pickup ions and ion cyclotron wave amplitudes upstream of Mars: First results from the 1D hybrid simulation, *Geophysical Research Letters*, 39, L08104.
- Curry, S. M., M. W. Liemohn, X.-H. Fang, Y.-J. Ma, J. Espley (2013), The influence of production mechanisms on pick-up ion loss at Mars, *Journal of Geophysical Research*, 118, 554–569.
- Davidson, R. C., and J. M. Oden (1975), Electromagnetic ion cyclotron instability driven by ion energy anisotropy in high-beta plasmas, *Phys. Fluids*, 18, 1045.
- Dong, C. F., and C. S. Paty (2011), Heating of ions by low-frequency Alfvén waves in partially ionized plasmas, *Phys. Plasmas*, 18, 030702.
- Dong, C. F., S. W. Bougher, Y. J. Ma, G. Toth, A. F. Nagy, and D. Najib (2013), Solar wind interaction with Mars upper atmosphere: Results from the one-way coupling between the multi-fluid MHD model and the MTGCM model, in preparation.
- Ergun, R. E., L. Andersson, W. K. Peterson, D. Brain, G. T. Delory, D. L. Mitchell, R. P. Lin, and A. W. Yau (2006), Role of plasma waves in Mars' atmospheric loss, *Geophysical Research Letters*, 33, L14103.
- Fang, X., M. W. Liemohn, A. F. Nagy, J. G. Luhmann, and Y. J. Ma (2010), On the effect of the martian crustal magnetic field on atmospheric erosion, *Icarus*, 206, 130–138.
- Gary, S. P., (1993), Theory of Space Plasma Microinstabilities, 1st ed., Cambridge Univ. Press, New York.
- Lammer, H., J. F. Kasting, E. Chasseiére, R. E. Johnson, Y. N. Kulikov, F. Tian (2008), Atmospheric Escape and Evolution of Terrestrial Planets and Satellites, *Space Sci Rev*, 139, 399–436.
- Ma, Y. J., A. F. Nagy, I. V. Sokolov, and K. C. Hansen (2004), Three-dimensional, multispecies, high spatial resolution MHD studies of the solar wind interaction with Mars, *Journal of Geophysical Research*, 109, A07,211.
- Ma, Y. J., and A. F. Nagy (2007), Ion escape fluxes from Mars, *Geophysical Research Letters*, 34, L08,201.
- Modolo, R., G. M. Chantour, E. Dubinin, and A. P. Matthews (2006), Simulated solar wind plasma interaction with the Martian exosphere: influence of the solar EUV flux on the bow shock and the magnetic pile-up boundary, *Annales Geophysicae*, 24, 3403–3410.
- Najib, D., A. F. Nagy, G. Tóth, and Y. J. Ma (2011), Three-dimensional, multifluid, high spatial resolution MHD model studies of the solar wind interaction with Mars, *Journal of Geophysical Research*, 116, A05,204.
- RiOUSset, J. A., C. S. Paty, R. J. Lillis, M. O. Fillingim, S. L. England, P. G. Withers, and J. P. M. Hale (2013), Three-dimensional multifluid modeling of atmospheric electrodynamics in Mars' dynamo region, *Journal of Geophysical Research*, 118, 1–13.
- Swanson, D. G., (2003), Plasma Waves, 2nd ed., Institute of Physics Publishing, Bristol and Philadelphia.
- Valeille, A., V. Tenishev, S. W. Bougher, M. R. Combi, and A. F. Nagy (2009), Three-dimensional study of Mars upper thermosphere/ionosphere and hot oxygen corona: 1. General description and results at equinox for solar low conditions, *Journal of Geophysical Research*, 114, E11005.
- Wang, B., C. B. Wang, P. H. Yoon, and C. S. Wu (2011), Stochastic heating and acceleration of minor ions by Alfvén waves, *Geophysical Research Letters*, 38, L10103.

- Winske, D., and N. Omidi (1993), Hybrid codes: Methods and applications, in *Computer Space Plasma Physics: Simulation Techniques and Software*, edited by H. Matsumoto and Y. Omura, pp. 103-160, Terra Sci., Tokyo.
- Winske, D., L. Yin, N. Omidi, H. Karimabadi, and K. B. Quest (2003), Hybrid Simulation Codes: Past, present and Future – A Tutorial, in *Space Plasma Simulation*, edited by J. Buechner, C. T. Dum and M. Scholer, pp. 136-165, Springer Verlag, Germany.

Improved modelling of upper atmospheric densities using multi-model ensembles

Sean Elvidge

Poynting Institute, University of Birmingham, B15 2TT, UK

Humberto Godinez

Los Alamos National Laboratory, Los Alamos, NM 87545

Matthew Angling

Poynting Institute, University of Birmingham, B15 2TT, UK

QinetiQ, Malvern, UK

Josef Koller

Los Alamos National Laboratory, Los Alamos, NM 87545

Abstract

This paper presents the first stages of a data assimilation scheme that is being developed as part of the Integrated Modelling of Perturbations in Atmospheres for Conjunction Tracking (IMPACT) Project, which is led by the Los Alamos National Laboratory (LANL) in the USA. In particular, the paper focuses on a project undertaken as part of the 3rd LANL Space Weather Summer School programme. IMPACT aims to develop a new orbital dynamics and atmospheric drag model with accurate uncertainty quantification. To achieve this goal, novel ionospheric, plasmaspheric and thermospheric data assimilation techniques that combine model information and observational data, along with relevant error statistics are required. The approach described in this paper involves a weighted ensemble of models to produce a better forecast of the true state of the atmosphere using the Thermosphere-Ionosphere-Electrodynamics General Circulation Model (TIE-GCM). The main advantage of using multiple models is to reduce the effect of model errors and bias, since it is expected that the model errors will, at least partly, cancel. This is an advantage for forecasting since it has been previously shown that a reduction in the uncertainties in the initial conditions of a model generally increases model skill. It is shown that the corresponding model output is closer to the true state, providing a more accurate forecast of atmospheric densities, with a reduction in the RMS error of approximately 55%.

Keywords: Multi-model ensemble, data assimilation, modelling

1. Introduction

NASA predicts that, by 2030, orbital collisions could become frequent enough to cause a cascade, known as the Kessler Syndrome, with the potential to prevent the use of low Earth orbit (LEO). One way to mitigate the Kessler Syndrome is to more accurately predict orbital trajectories to better plan collision avoidance manoeuvres. A key component in orbital trajectory predictions is the accurate description of the upper atmospheric environment, in particular the ionosphere-thermosphere, since drag due to atmospheric density is one of the main forces that affect the orbit of satellites and space debris. The neutral air density from 200 to 1000 km altitude can change by 80% diurnally as well as by two to three orders of magnitude during geomagnetic storms; sometimes in just a few hours.

The forecast models currently in use are empirical. They are finely tuned but when applied to satellite orbit forecasts they result in large uncertainties in the orbital parameters (positional errors on the order of kilometres after a day [McLaughlin *et al.*, 2011; Vallado and Finkleman, 2008]).

There are a number of techniques to improve the predictability of the upper atmospheric environment. Data assimilation schemes have long been applied to the ionosphere-thermosphere system [Angling and Jackson-Booth, 2011; Codrescu *et al.*, 2012; McNamara *et al.*, 2013]. Unfortunately, model errors and/or bias can significantly degrade the performance of data assimilation results. In this work a multi-model ensemble (MME) technique has been implemented to enhance the prediction of the ionosphere-thermosphere. The main advantage of MME methods is that the use of a number of different models to simulate the same physical phenomena can reduce or eliminate model errors or bias caused by any one single model. The model variables or fields of interest are averaged with equal weights or with weights reflecting their individual errors and/or bias. The main objective is to minimize the effects of model errors and bias, and improve the prediction of the physical phenomena using the ensemble average.

Section 2 of this paper reviews the models used in this study. Section 3 describes the test scenario while Section 4 discusses the initial comparison of the models with a truth data set. Section 5 details the approach for constructing the MME, and Section 6 discusses the results of using the new state as the model input. Finally, Section 7 provides the conclusions of the study, and where further work should be undertaken.

2. Model & Observation Data

For this study three atmospheric density models have been used: the Navy Research Laboratory Mass Spectrometer and Incoherent Scatter Radar Exosphere model (NRLMSISE-00), the Thermosphere-Ionosphere-Electrodynamics General Circulation Model (TIE-GCM), and the Global Ionosphere-Thermosphere Model (GITM). NRLMSISE-00 is an empirical density model whereas GITM and TIE-GCM are physics based models. The models are driven using standard geophysical indices: i.e. F10.7, which is the solar flux at a wavelength of 10.7 cm at the Earth's orbit and is used as a proxy for solar output; Kp and Ap, which indicate the severity of the magnetic disturbances in near-Earth space.

The NRLMSISE-00 model, developed at the US Naval Research Laboratory, is a global, empirical model of the atmosphere, using F10.7 and Ap to model the density of various atmospheric parameters [Hedin, 1991; Picone *et al.*, 2002]. Empirical models are computationally cheap and provide a statistically accurate estimate on average (over time). However without accounting for any of the underlying physical processes they do not allow for extrapolation into areas where there is no data with any confidence.

The TIE-GCM model, developed in the National Center for Atmospheric Research (NCAR), is a non-linear three-dimensional model of the coupled thermosphere ionosphere system [Richmond, 1992]. At each time step the continuity, energy and momentum equations are solved for neutral and ion species using a fourth-order, centred finite difference scheme [Roble *et al.*, 1988]. Ion velocities are calculated from the drifts caused by electric and magnetic fields (i.e. ExB drifts). The model uses daily F10.7, a 81-day average F10.7 value, and Ap. The lower boundary condition atmospheric tides are provided by the Global Scale Wave Model (GSWM) [Hagan *et al.*, 2001].

GITM [Ridley *et al.*, 2006] is a physics-based three-dimensional global thermosphere and ionosphere model that solves the full Navier-Stokes equations for density, velocity, and temperature for a number of neutral and charged components. For inputs, GITM uses F10.7, the hemispheric power index (HPI) (which is derived from the 3-hour Kp), interplanetary magnetic field (IMF) data and solar wind velocity. GITM inherently allows for non-hydrostatic solutions to develop which allows for realistic dynamics in the auroral zones [Ridley *et al.*, 2006]; this is the main difference between GITM and TIE-GCM (hydrostatic solution). Furthermore, unlike TIE-GCM, the GITM model solves the ion momentum equations. Although both TIE-GCM and GITM can potentially provide a forecast of the upper atmospheric environment, they both suffer from significant model errors and bias. This is mainly due to missing physics in the models, as well as inaccurate initial conditions, boundary conditions, parameters, and inherent numerical errors. The dynamics are represented in different ways in the models; therefore it is possible that their combined fields can capture a more realistic evolution of the densities than any one single model.

The models are tested against neutral density data from the CHALLENGING Minisatellite Payload (CHAMP) satellite [Reigber *et al.*, 2002; 2003]. CHAMP was in operation from July 2000 to September 2010 and the neutral densities are derived from accelerometer data as described by Sutton [2009].

3. Test Scenario

The time period for this study was from August 28th 2009 to September 1st 2009. This is during solar minimum, where there is a large difference between the models. At solar minimum the impact of the solar input parameters on the models is relatively small, and thus other internal and external dynamics dominate the evolution of the ionosphere-thermosphere densities. The particular time period was chosen since it included a geomagnetic storm which took place on August 30th: the Ap reached a high of 67 between 15UT and 18UT, staying below 10 at other times. However, during this period the F10.7 showed little variability, fluctuating between 69.3 and 70.4. The performance of each model is compared against the derived density fields obtained from CHAMP. The models were run with a 30 minute time step and the observational data from the CHAMP satellite was restricted to the closest matching time for comparison.

4. Model Comparison

The models' outputs have been compared with density observations from CHAMP, in order to provide model performance and an initial indication of the models' skill.

Figure 1 shows the total neutral density from the CHAMP observations (in black) as well as the total density outputs from NRLMSISE-00 (orange), GITM (red) and TIE-GCM (blue). Table 1 shows the statistics of the time series of the models and Table 2 the corresponding error (model minus observation) statistics.

The NRLMSISE-00 empirical model results, as expected, show a good mean approximation to the observed state, however the model shows a larger variability in its output than the CHAMP observations. GITM shows a slight negative bias but has a standard deviation value close to the observations, i.e. the range of values that GITM produces have a similar range to the observations. Overall GITM performs the best of the three models in terms of the model mean, standard deviation and RMS values as seen in Table 1. It also performs better in terms of errors except for the standard deviation. GITM also seems to show some reaction to the storm, with a noticeable increase in neutral density just after the peak in observed neutral densities. TIE-GCM has a more pronounced discrepancy between model results and observations. The experiments show that TIE-GCM has a positive bias and a standard deviation much larger than that of the observations. However, the TIE-GCM does also show some reaction to the storm. Although there is no increase in the maximum reported values, there is an increase in the minimum values, (Figure 1).

The test results show that the models suffer from different errors and bias, and are unable to exactly match the observed density field from CHAMP. In particular, all models underestimate the peak. Therefore, in order to provide better forecasting abilities techniques must be used to combine the model output to minimize the impact of model errors and bias. The technique used in this work is the multi-model ensembles (MME) described in the next section.

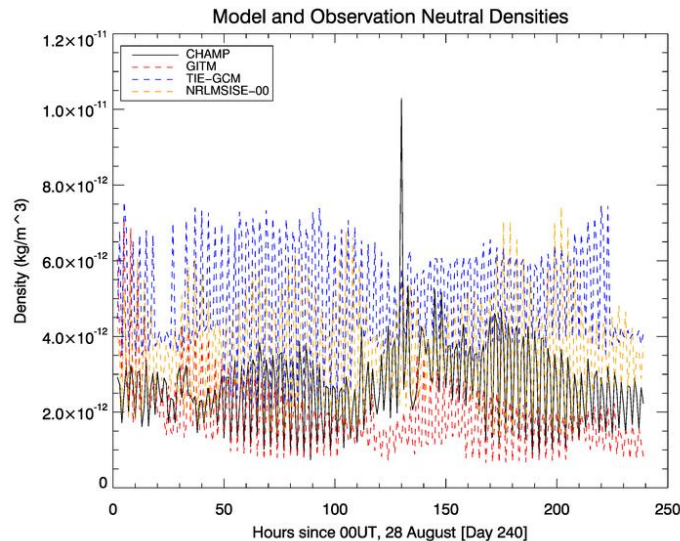


Figure 1: Plot showing the neutral density observation data from CHAMP with the three model outputs, NRLMSISE-00, GITM and TIE-GCM for the study period.

Table 1: Standard deviation and RMS of the observations and model output.

| | RMS (kgm^{-3}) | Std. Dev. (kgm^{-3}) |
|-------------|---------------------------|---------------------------------|
| CHAMP | 2.90×10^{-12} | 1.10×10^{-12} |
| NRLMSISE-00 | 3.84×10^{-12} | 1.40×10^{-12} |
| GITM | 2.08×10^{-12} | 9.92×10^{-13} |
| TIE-GCM | 5.22×10^{-12} | 1.48×10^{-12} |

Table 2: The error (model minus observation) statistics.

| | RMS (kgm^{-3}) | Std. Dev. (kgm^{-3}) |
|-------------|---------------------------|---------------------------------|
| NRLMSISE-00 | 1.62×10^{-12} | 1.36×10^{-12} |
| GITM | 1.55×10^{-12} | 1.30×10^{-12} |
| TIE-GCM | 2.60×10^{-12} | 1.19×10^{-12} |

5. Multi-Model Ensemble

Multi-model ensembles (MMEs) are widely used in atmospheric and climate modelling, where there have been multiple approaches proposed for constructing the ensemble [Kharin and Zwiers, 2002; Krishnamurti et al., 2000]. The uncertainties in any given model include missing physics, errors in initial condition, boundary condition, and parameter values. By using a MME it is possible to reduce the impact of these errors and hence increase the model forecast skill [Tebaldi and Knutti, 2007].

Tebaldi and Knutti [2007] argue that the expectation that combining results from multiple models will offer an improvement is based on the assumption that if the models are independent errors should cancel. This leads to the idea that the uncertainty in the model predictions should decrease as the number of models increases. However, it has been shown that different weighting schemes, each based on reasonable criteria, can give different results [Hagedorn et al., 2005]. Therefore, Chandler [2013] concluded that, without a formal reasoning for a particular weighting method, the choice becomes an added source of uncertainty. Therefore simply increasing the number of models in the MME should not continually decrease our uncertainty without formally characterising a method for combining the models [Tebaldi and Knutti, 2007].

Two approaches to constructing the MME are described here; first by ignoring model performance and creating an equally weighted average. Secondly a method for generating a weighted ensemble is discussed and implemented.

5.1. Equally Weighted Average MME

There are a number of difficulties in constructing a MME, including that different models do not all share common output variables. Another problem is that there is not observational data for each parameter, making a method for assessing model performance difficult. One of the ways to resolve the latter problem is to not take model performance into account and use an equally weighted average. Such methods have been shown to increase model skill [Weisheimer et al., 2009].

Figure 2 shows the neutral density plots of the models, but this time with the equally weighted average density also plotted. The combination of the models offers a significant improvement over each individual model, giving an RMS error value of $1.27 \times 10^{-12} \text{ kgm}^{-3}$. There is still a slight positive bias, especially in the times before the storm onset; however the post-storm densities are tracked accurately. The variability of the combination is close to the variability of the observations and the RMS error of the combination is smaller than any individual model.

5.2. Weighted MME

There are different methods to weight model results; they each depend on what measure of model skill is used. For example Tebaldi and Knutti [2007] state that the skill of a (climate) model should not be judged from its ability to predict the future, but instead from its ability to predict mean conditions, variability, and transient changes.

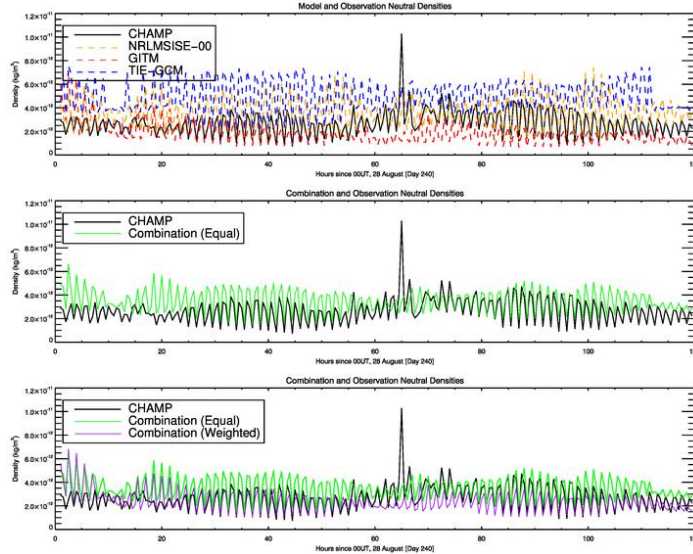


Figure 2: First shown are the model results with the CHAMP observations followed by the results from taking an equally weighted average of the three models. Finally the weighted combination is shown.

In line with Tebaldi and Knutti [2007] a weighting method for the MME was developed based on the models' mean conditions and variability. The models were restricted to low activity (< 3 Ap) times and the mean square error, which weights the square of the bias equally with the variance (of the model time series minus the observation time series) was used,

$$\text{Skill} = (\mu^2 + \sigma^2). \quad (1)$$

Where μ is the mean of the time series of errors and σ the standard deviation. This was implemented for each model at the quiet times to produce a single value representing model skill (3.03×10^{-24} for NRLMSISE-00, 1.06×10^{-24} for GITM and 8.15×10^{-23} for TIE-GCM). The inverse of the value was used to weight the models, so that the model with the lowest value was weighted most heavily. The resulting weighting was 23.7% NRLMSISE-00, 67.5% GITM and 8.80% TIE-GCM.

Figure 2 shows the neutral density plots of the observations, unweighted and weighted average, The RMS error for the weighted combination is $1.17 \times 10^{-12} \text{ kg m}^{-3}$. The weighted average provides variability very close to that of the CHAMP observations, and does not show any significant bias. However the storm period is not modelled as well as the equally weighted average. This is probably due to the fact that GITM tends to underestimate the true state during the storm, whilst being heavily favoured in the weighting scheme (67.5%), which is based on quiet times.

It has been shown that combining model simulations leads to increased skill at matching the CHAMP derived data. This reduced uncertainty in atmospheric densities can be used to provide the initial conditions of a forecast run of a model. This approach has been shown to increase model forecast skill [Tebaldi and Knutti, 2007].

6. Using the MME as the Initial Conditions for TIE-GCM

For this experiment, TIE-GCM is initialized using the MME average. The TIE-GCM is restarted every six hours, at which time the MME average field is used as the initial condition for the model. The main objective is to reduce the uncertainty in the initial conditions and increase the forecast skill of TIE-GCM.

Figure 3 shows the neutral density from the CHAMP observations, the original TIE-GCM run, the equally weighted combination MME and the results of rerunning TIE-GCM using the MME as the initial condition every six hours. Table 3 shows the errors of the reported densities from Figure 3.

Using the MME as the initial condition in TIE-GCM provides a clear improvement in RMS error compared to the standard run of TIE-GCM. Initially the model is well above the values, but this is due to the large initial values in the MME (caused by the GITM 'spin up' time, along with the already large TIE-GCM and NRLMSISE-00 values). However after approximately 20 hours the reported densities show very low bias, and have variability close to the observations. In particular, the post-storm period is modelled very accurately, and the RMS error of the new TIE-GCM run is smaller than the equally weighted MME density RMS error. Using the MME as the initial

conditions to TIE-GCM offers a 55% reduction of the RMS error compared to the initial TIE-GCM runs from Section 4.

Figure 4 shows the neutral density from the CHAMP observations, the original TIE-GCM run, the weighted combination MME and the results of rerunning TIE-GCM using the weighted MME as the initial condition every six hours. Table 3 shows the errors of the reported densities from Figure 4.

These figures show that using the weighted combination MME as the initial condition for TIE-GCM also provide significant improvement. Before the storm onset the new TIE-GCM run gives a non-biased result with variance close to that of the observations. However directly after the storm the output does not follow the density values so well; for the remaining 50 hours (from hour 70 to 120) the TIE-GCM result shows a smaller variability than that of the observations. Table 3 does however show that using the weighted MME as the initial condition still offers considerable improvement over not using it and the RMS error is reduced by 48%.

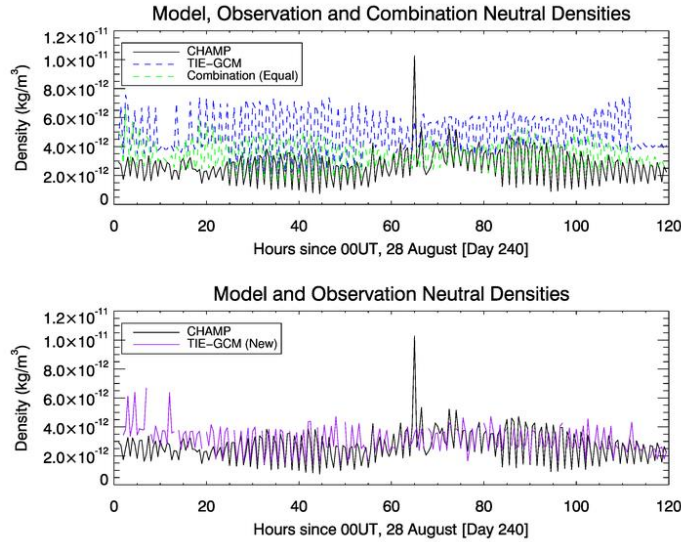


Figure 3: Top panel shows the neutral density from the CHAMP observations, from the original TIE-GCM run and the equal combination MME. The bottom panel shows the CHAMP observations and the new TIE-GCM output, using the MME as the initial condition every six hours.

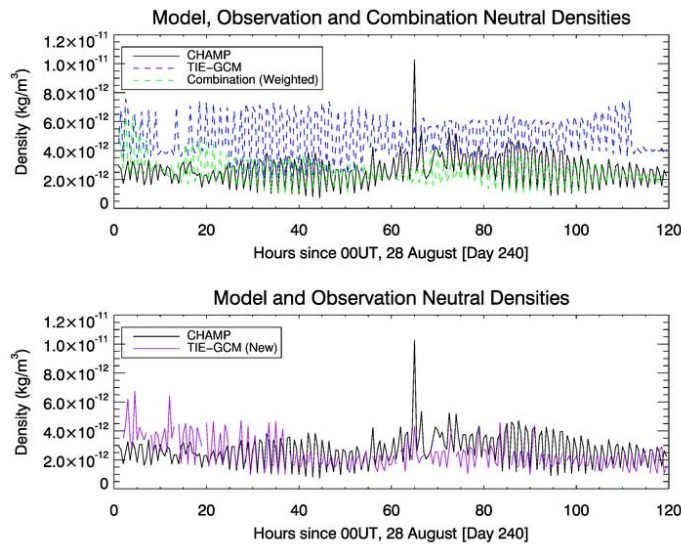


Figure 4: Top panel shows the neutral density from the CHAMP observations, from the original TIE-GCM run and the weighted MME. The bottom panel shows the CHAMP observations and the new TIE-GCM output, using the MME as the initial condition every six hours.

Table 3: Statistics of equal and weighted MME used as initial conditions for TIE-GCM.

| | | kgm ⁻³ | Errors (kgm ⁻³) |
|----------------------|--------------------|--------------------------|-----------------------------|
| Equal MME TIE-GCM | Mean | 3.12 x 10 ⁻¹² | 4.03 x 10 ⁻¹³ |
| | Standard Deviation | 9.54 x 10 ⁻¹³ | 1.10 x 10 ⁻¹² |
| | RMS | 3.26 x 10 ⁻¹² | 1.17 x 10 ⁻¹² |
| Weighted MME TIE-GCM | Mean | 2.31 x 10 ⁻¹² | -3.03 x 10 ⁻¹³ |
| | Standard Deviation | 1.08 x 10 ⁻¹² | 1.33 x 10 ⁻¹² |
| | RMS | 2.54 x 10 ⁻¹² | 1.36 x 10 ⁻¹² |

7. Conclusions

The current work shows the importance of multi-model ensembles for enhancing the forecast skill of ionosphere-thermosphere models. Three models were considered, an empirical model (NRLMSIS-00) and two physics-based models (TIE-GCM and GITM). The models' output density is compared against density fields from CHAMP, where all models are unable to match the observations. To improve the density estimation, a multi-model ensemble averaging technique is applied and tested. Two approaches for the MME are used, a simple model ensemble average where all models have the same weight, and a weighted model ensemble average where each model is weighted according to its skill (discrepancy between model and observation in an average sense). The results show a great improvement in both cases, where the weighted average provided a slightly more accurate upper atmospheric density. The multi-model ensemble is then used to initialize one of the physics-based models, TIE-GCM, to improve its forecast skill. As with the previous case, the first experiment uses an MME with a simple ensemble average to initialize TIE-GCM. This initialization shows a 55% reduction in RMS error over the previous experiments. The weighted MME performs worse than the simple ensemble average MME, offering an approximate 48% reduction in RMS error. There are a number of reasons for this worse performance. Firstly, the scheme uses the model quiet time to generate the model weights which is then applied across all time periods. A possible solution would be to use two different weighting schemes, one for quiet time and one for storm time. A further approach would be to change the weighting scheme altogether and adopt Reliability Ensemble Averaging (REA) [Giorgi and Mearns, 2002] that is often used to generate MMEs in climatology studies.

For future work, as well as using different weighting schemes, the MME should be applied to the GITM model to see if similar improvements are seen in the results. Also repeating the study during a solar maximum time, when the solar inputs of the model become the main factor in determining the model output, would show how much improvement using MMEs can offer.

8. Acknowledgements

This research was conducted as part of the Integrated Modelling of Perturbations in Atmospheres for Conjunction Tracking (IMPACT) project at Los Alamos National Laboratory. More information is available at www.impact.lanl.gov. The work was commenced under the 3rd Los Alamos National Laboratory Space Weather Summer School. LA-UR-13-26825.

References

- Angling, M. J., and N. Jackson-Booth (2011), A short note on the assimilation of collocated and concurrent GPS and ionosonde data into the Electron Density Assimilative Model, *Radio Sci.*, 46.
- Chandler, R. E. (2013), Exploiting strength, discounting weakness: combining information from multiple climate simulators, *Phil. Trans. R. Soc. A*.
- Codrescu, M., C. Negrea, M. Fedrizzi, T. Fuller-Rowell, A. Dobin, N. Jakowski, H. Khalsa, T. Matsuo, and N. Maruyama (2012), A Real-Time Run of the Coupled Thermosphere Ionosphere Plasmasphere Electrodynamic (CTIPE) Model, *Space Weather*, 10(2).
- Giorgi, F., and L. O. Mearns (2002), Calculation of Average, Uncertainty Range, and Reliability of Regional Climate Changes from AOGCM Simulations via the "Reliability Ensemble Averaging" (REA) Method, *J. Climate*, 15, 1141-1158.
- Hagan, M. E., R. G. Roble, and J. Hackney (2001), Migrating thermospheric tides, *J. Geophys. Res.*, 106, 12739-12752.
- Hagedorn, R., F. J. Doblas-Reyes, and T. N. Palmer (2005), The rationale behind the success of multi-model ensembles in seasonal forecasting - I. Basic Concept, *Tellus A*, 219-233.
- Hedin, A. E. (1991), Extension of the MSIS thermospheric model into the middle and lower atmosphere, *J. Geophysical Research*, 96, 1159-1172.
- Kharin, V. V., and F. W. Zwiers (2002), Climate Predictions with Multimodel Ensembles, *J. Climate*, 15, 793-799.

- Krishnamurti, T. N., C. M. Kishtawa, Z. Zhang, T. LaRow, D. Bachiochi, E. Williford, and S. Surendran (2000), Multimodel Ensemble Forecasts for Weather and Seasonal Climate, *J. Climate*, *13*, 4196-4216.
- McLaughlin, C. A., A. Hiatt, and T. Lechtenberg (2011), Precision orbit derived total density, *Journal of Spacecraft and Rockets*, *48*(1), 166-174.
- McNamara, L. F., M. J. Angling, S. Elvidge, S. V. Fridman, A. H. Hausman, L. J. Nickisch, and L.-A. McKinnell (2013), Assimilation Procedures for Updating Ionospheric Profiles below the F2 Peak, *Radio Sci*, *48*.
- Picone, J. M., A. E. Hedin, D. P. Drob, and A. C. Aikin (2002), NRLMSISE-00 empirical model of the atmosphere: Statistical comparisons and scientific issues, *J. Geo. Phys. Res.*, *107*, 1468.
- Reigber, C., H. Luhr, and P. Schwintzer (2002), CHAMP Mission Status, *Adv. Space. Res.*, *30*(2), 129-134.
- Reigber, C., H. Luhr, and P. Schwintzer (Eds.) (2003), *First CHAMP mission results for gravity, magnetic and atmospheric studies*, Springer.
- Richmond, A. D. (1992), Assimilative mapping of ionospheric electrodynamics, *Adv. Space. Res.*, *12*(6), 59-68.
- Ridley, A. J., Y. Deng, and G. Toth (2006), The Global Ionosphere-Thermosphere Model (GITM), *J. Atmos. Solar-Terr. Phys.*, *68*, 839-864.
- Roble, R. G., E. C. Ridley, A. D. Richmond, and R. E. Dickinson (1988), A coupled thermosphere/ionosphere general circulation model, *Geophys. Res. Lett.*, *15*(12), 1325-1328.
- Sutton, E. K. (2009), Normalized Force Coefficients for Satellites with Elongated Shapes, *Journal of Spacecraft and Rockets*, *46*(1), 112-116.
- Tebaldi, C., and R. Knutti (2007), The use of the multi-model ensemble in probabilistic climate projections, *Philosophical Transactions of the Royal Society A: Mathematical, Physical and Engineering Sciences*, 2053-2075.
- Vallado, D. A., and D. Finkleman (2008), A critical assessment of satellite drag and atmospheric density modeling, *Astrodynamics specialist conference and exhibit*, 18-21.
- Weisheimer, A. F., F. J. Doblas-Reyes, T. N. Palmer, A. Alessandri, A. Arribas, M. Déqué, and P. Roger (2009), Ensembles: A new multi-model ensemble for seasonal-to-annual predictions - Skill and progress beyond DEMETER in forecasting tropical Pacific SSTs, *Geophys. Res. Lett.*, *36*.

Solar rotation effects on CHAMP derived neutral and plasma densities at different phases of the solar cycle

Federico Gasperini

University of Colorado, Boulder, CO 80302

Humberto Godinez

Los Alamos National Laboratory, Los Alamos, NM 87545

Abstract

Thermospheric neutral and plasma densities derived from the Challenging Minisatellite Payload (CHAMP) accelerometer measurements are analyzed for 2003 and 2007. Statistical analysis in the time and frequency domain of neutral/plasma densities, and TIMED-SEE solar irradiances reveal a very different ionospheric response to solar radiation based on the phase of the solar cycle. We found that solar radiation dominates the dynamics of the ionospheric neutral density during solar maximum, whereas internal processes control its variability during solar minimum. We show that the radio flux (F10.7), commonly used as proxy for extreme ultraviolet (EUV) radiation, correlates well with neutral density only when the solar forcing is high, whereas when it is low the Ap index captures more variability. Additionally, we found that at solar maximum the 133.5 nm irradiance shows the best correlation with neutral density, indicating that far ultra-violet (FUV) radiation is more representative of the dynamics of the F-region ionosphere.

Keywords: solar radiation, ionosphere, neutral and electron density

¹ *Email addresses:* gasperini@colorado.edu (Federico Gasperini), hgodinez@lan.gov (Humberto Godinez)

1. Introduction

The region of the thermosphere above the turbopause is characterized by diffusive separation and the different species are distributed depending on their mass and temperature. In this region extreme ultraviolet (EUV) radiation is the primary energy input, while solar wind, particle precipitation, joule heating as well as geomagnetic activity, lower atmosphere processes and anthropogenic trace gases play a secondary role [Cole, 1962, 1971; Banks, 1977, Qian et al., 2007]. The EUV component ($10 < \lambda < 121$ nm) of the solar spectrum is highly dependent on solar activity [Hedin and Mayr, 1987], creating significant variability in neutral density, ranging from hours to decades. As a consequence, thermospheric neutral density is mainly modulated by the solar cycle variation of ~ 11 years, the semi-annual variation of ~ 6 months, and the solar rotation variation of ~ 27 day.

The atmosphere of the Sun rotates with a period close to 35 days near the poles and 25 days near the equator. This differential rotation creates twisting magnetic field lines, which lead to the formation of active regions on the surface of the sun releasing high energy radiation (i.e. EUV radiation) [Forbes et al., 2006]. The rotation of solar active regions produces a modulation of the EUV flux coming from the Sun, with a period close to 27 days as observed on Earth (or shorter periods, such as the 9-day variability in 2005 as discussed by Pedatella et al., 2011). Studying the 27-day signature in neutral and plasma densities allows us to discuss the relative influence of solar radiation in the thermosphere.

It is well known that the most difficult parameter to model in predicting orbits of low Earth orbit satellites is the atmospheric drag, due to the complexity of mass density variations caused by solar radiation, magnetospheric energy inputs and propagating waves coming from the lower atmosphere. Moreover, the knowledge of the ionospheric electron density is essential for a large number of applications, e.g., radio and telecommunications, satellite tracking, and Earth observation from space. Considerable efforts have been concentrated on modeling these ionospheric parameters, but a lot of work has yet to be done. Most of the neutral and electron density models are empirical and are highly dependent on solar indices, such as F10.7, extreme (EUV) and far (FUV) ultraviolet, and geomagnetic indices, such as Ap, Kp, and Dst. Investigating the link between densities and the solar and geomagnetic indices is key to understand the relative significance of solar forcing and geomagnetic disturbances to explain neutral and electron density variability, and ultimately improve modeling [Fuller-Rowell et al., 2009].

The objective of this study is to characterize the solar radiation influence on the ionospheric neutral and electron densities during two opposite phases of the solar cycle. Many studies have found good correlation between solar EUV radiation and neutral density at solar maximum, when solar radiation is the highest [Guo et al., 2007], and during geomagnetic storms [Liu et al., 2010], but uncertainty still persists on the ionospheric response at solar minimum. For this case we would expect internal processes (such as wave propagation, neutral wind response to geomagnetic activity, thermosphere-ionosphere coupling) to play a bigger role in explaining neutral density variability [Hedin and Mayr, 1987; Thayer et al., 2008].

The science questions that we aim to answer are:

1. To what degree is solar EUV radiation responsible for ionospheric neutral and plasma density variability?
 - Is the 27-day solar rotation evident in neutral and plasma densities?
 - How does neutral and plasma density correlate with F10.7 and the EUV irradiances?
 - Is this correlation strongly dependent on the phase of the solar cycle?
2. What is the best proxy to describe the absorption of solar EUV radiation in the ionosphere?
 - What solar wavelengths better describe neutral and plasma density variability?
 - Are there EUV irradiances showing better correlation than the F10.7?

Studying the variability of the neutral and plasma densities in the thermosphere is key to understand the Earth-Sun interaction, the connection upper atmosphere and ionosphere, and has practical space weather applications, such as improving orbital prediction models. With our study we seek to better understand how the thermospheric neutral and plasma densities are linked to solar radiation.

The following section provides a brief overview on the methodology used to answer the aforementioned science questions and describes the observational data implemented. Section 3 illustrates and describes solar rotation variability in the spectral and temporal domain, while section 4 summarizes our findings.

2. Data and Methodology

In order to answer the science questions listed in the introduction, we analyzed neutral (<http://thermosphere.tudelft.nl/acceldrag/data.php>) and plasma (<http://isdc.gfz-potsdam.de>) densities derived from CHAMP accelerometer measurements for 2003 and 2007 (at solar maximum and minimum respectively) [Doornbos *et al.*, 2010].

The Challenging Minisatellite Payload (CHAMP) satellite was launched in 2001 into a near-circular orbit with an inclination of 87.3° [Reigber *et al.*, 2002] and was put on a decaying orbit in late 2010. Launched at a nominal orbit of 456 Km it decayed to around 360 Km by 2007. It carried onboard several instruments (i.e. STAR triaxial accelerometer and Langmuir probe), whose measurements allowed us to estimate thermosphere and ionosphere parameters (i.e. total mass density and plasma density).

Total mass densities are derived from the accelerometer measurements following these three steps [Bruinsma *et al.*, 2004]: (1) a reduced-dynamic satellite orbit is simulated, (2) a dynamic satellite orbit is fitted to the pseudo-observations using calibrated STAR measurements, (3) this dataset is used to compute neutral densities at each orbit integration step. This methodology leads to an absolute uncertainty of 10-15%. In this study we can ignore this bias as we are focusing exclusively on temporal variability. Similar considerations hold for the retrieval of plasma densities. More details on the accelerometer and on its performance are provided by Grunwaldt and Meehan, [2003] and Perosanz *et al.*, [2003].

For the years 2003 and 2007 the TIMED-SEE solar EUV irradiances (at 27.34 nm, 30.4 nm, 33.5 nm, 36.8 nm, 121.5 nm, 133.5 nm and 145-165 nm) as provided by the Laboratory of Atmospheric and Space Physics (LASP) (<ftp://laspftp.colorado.edu>) are compared with the 10.7-cm radio flux (F10.7) (<ftp.ngdc.noaa.gov>) as proxy for solar variability. The Ap index of geomagnetic activity (<ftp.ngdc.noaa.gov>) is used as a proxy for geomagnetic variability. Neutral and plasma densities were normalized to constant height at each orbit using the DTM2000 empirical model [Bruinsma and Thuillier, 2003].

We analyzed the frequency domain of neutral and plasma densities, F10.7, TIMED-SEE irradiances, and Ap using a fast fourier transform (FFT). Neutral and plasma densities have a time resolution of 10 and 45 seconds respectively, F10.7 and Ap are daily averages, while the TIMED-SEE irradiances are provided once per orbit (~15 a day). The monthly mean sunspot number used in this study is retrieved from the National Geophysical Data Center at the National Oceanic and Atmospheric Administration (NOAA) (<http://www.ngdc.noaa.gov/stp/solar/ssndata.html>). We performed a wavelet analysis as provided by Torrence and Compo [1998] (<http://paos.colorado.edu/research/wavelets>) to study the temporal variability of periodicities in the 5/40-day range.

Additionally, we looked at the time series of each one of the parameters previously described. In order to isolate the ~27-day solar rotation effect, we processed the data as follows (similarly to Forbes *et al.*, 2006): we calculated residuals by subtracting 27-day means, shifted one day at the time, to the original data; we then applied a 5-day running mean to the residuals, to reduce noise due to day-to-day variability, i.e. caused by geomagnetic activity (we refer to these as 'mean residuals'). In order to minimize geomagnetic disturbances, we eliminated days with Ap greater than 30 and we performed a linear interpolation in the gaps (never on more than 10 days per year or for more than 3 consecutive days).

3. Results

Analyzing the two opposite phases of the solar cycle, we found that only during solar maximum (i.e. when solar radiation is at maximum) neutral density shares a large number of similarities with solar flux variability. For this case (i.e. 2003), we found an yearly-averaged Pearson correlation coefficient of 0.875. This value is particularly good considering that it is referred to unfiltered data. Conversely, for 2007 we found that neutral density and solar flux are completely uncorrelated. In the following we explain why this is in fact expected.

Mean density residuals for 2003 are shown in Figure 1a, together with mean F10.7 and Ap residuals. Figure 1b shows the correlation coefficient versus time for a moving 27-day fit of mean neutral density residuals with F10.7 and Ap. From Figure 1b we report correlation coefficients as high as 0.95, with a noticeable significant drop during the middle part of the year. This drop, as noted by *Forbes et al.* [2006], can be attributed to the decreased solar flux variability. Although not of primary interest in this study, we investigated the reason of this reduced variability and found (Figure 1c) that it is associated with an increased sunspot activity. We believe that the increased number of sunspots contributes to make the surface of the sun appear somewhat more uniform, hence preventing the 27-day modulation of the solar radiation to occur. From Figure 1b we also notice an increased correlation of neutral density with mean Ap residuals in the interval when the correlation with F10.7 drops (the reason is explained in the following paragraph).

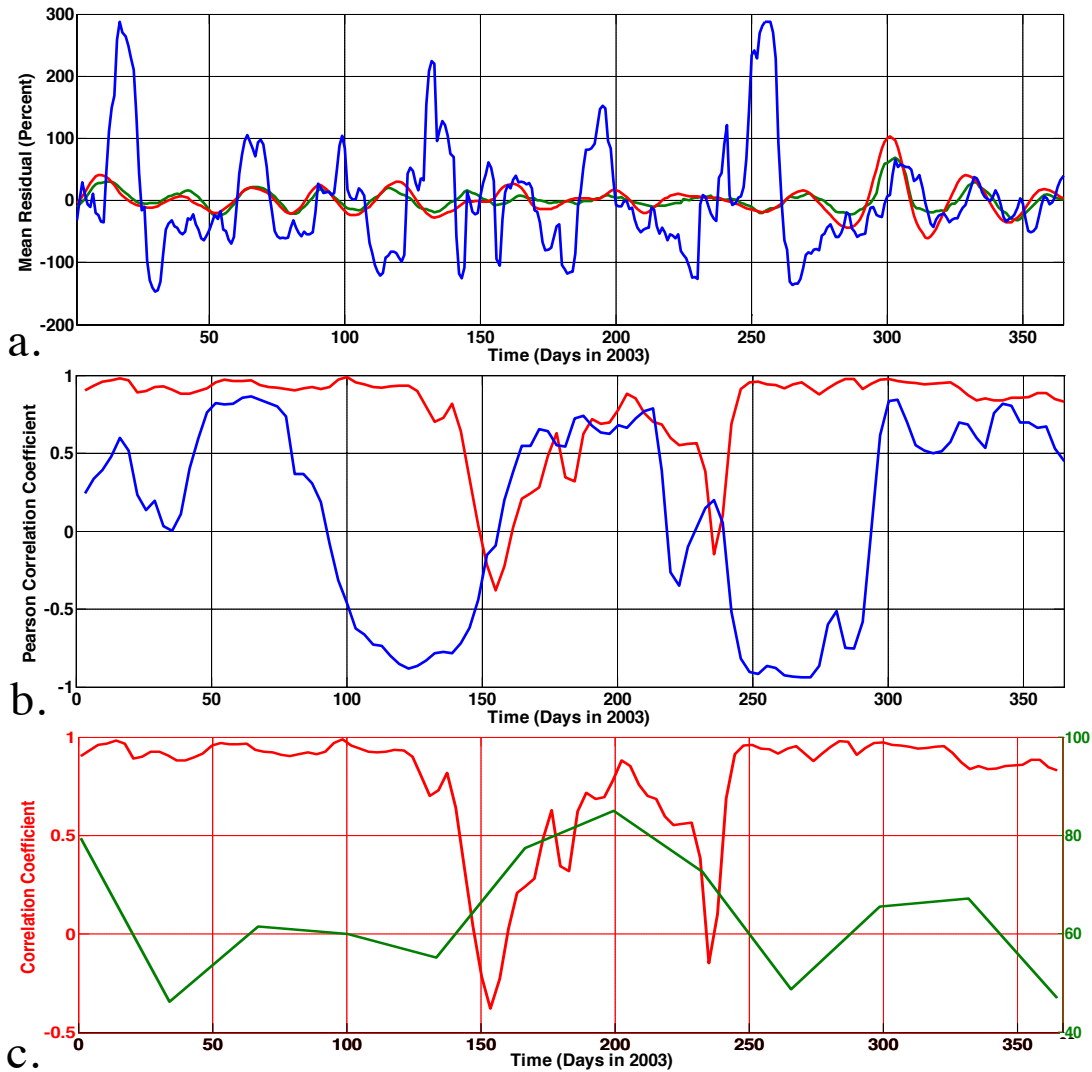


Figure 1: On the top panel (a): time series for 2003 of mean residuals (percent) of neutral density (green line), F10.7 (red line) and Ap (blue line). On the middle panel (b) moving Pearson correlation coefficient during 2003 of neutral density with F10.7 (red line) and Ap (blue line). On the bottom panel (c) moving correlation coefficient of neutral density with F10.7 (red line) and the monthly sunspot number (green line).

The same analysis for 2007 demonstrates that neutral density variability is for the most part uncorrelated with F10.7, with a yearly-averaged Pearson correlation coefficient equal to -0.462 . Instead, significant correlation between neutral density and A_p is found. Figure 2a shows the time series of residuals and Figure 2b the moving correlation coefficients. In these plots we notice very good correlation between neutral density and A_p during the second half of the year, with values often above 0.9 and constantly above 0.7 (except for the second week of december). This suggests that, as solar forcing diminishes, internal processes (captured by the geomagnetic index) tend to dominate the dynamics of the ionosphere-thermosphere system. We believe that the poor correlation at the beginning of 2007 can be explained by strong periodicities in the 9-15 day range present in the A_p but not in the neutral densities (see the wavelet analysis at the end of this section).

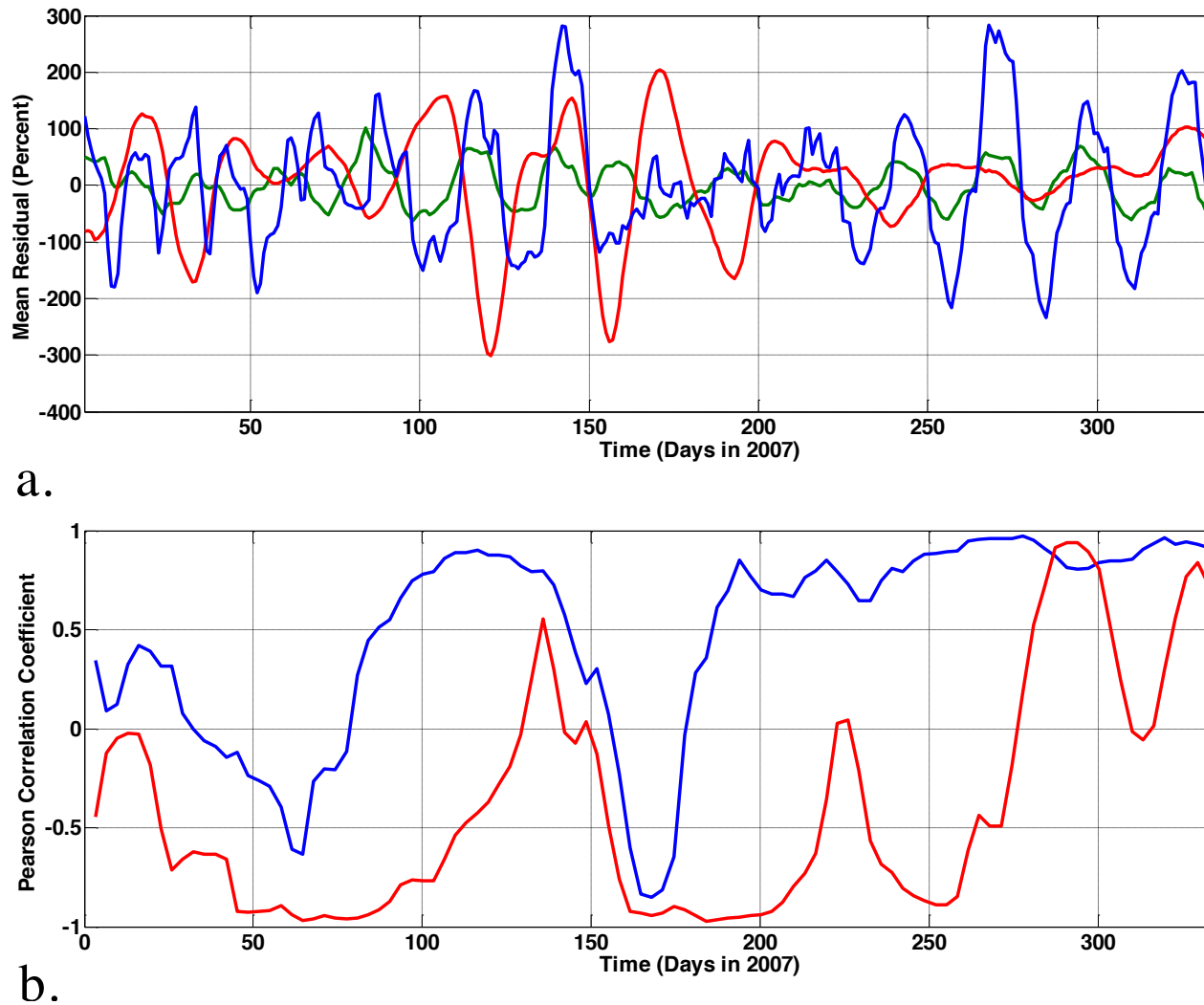


Figure 2: Same as in Figure 1, except for 2007 (no sunspot number plotted).

Tables 1a and 1b lists the Pearson correlation coefficients of neutral and electron densities with F10.7, the 0.1-7 nm, 27-34 nm, 30.4 nm, 33.5 nm, 36.8 nm, 121.5 nm, 133.5 nm, 145-165 nm TIMED-SEE irradiances and Ap for 2003 and 2007 respectively. For 2003, we notice that neutral density correlates remarkably well with the F10.7 and the EUV irradiances, but it is uncorrelated with Ap. In addition, we observe that the 133.5 nm wavelength has a slightly better correlation coefficient than the F10.7. We hypothesize that this is due to this irradiance being absorbed closer to the 300/350 Km altitude range where neutral densities were retrieved from in-situ CHAMP measurements. This suggests that this wavelength could serve as better proxy during solar maximum to describe neutral density variability. For the sake of brevity and given the very similar behavior to the F10.7, we are not showing the moving correlation coefficient for the EUV irradiances.

Table 1: Pearson correlation coefficients of neutral and plasma densities with F10.7, 0.1-7 nm, 27-34 nm, 30.4 nm, 33.5 nm, 36.8 nm, 121.5 nm, 133.5 nm, 145-165 nm irradiances, and Ap for 2003 (a) and 2007 (b). Highlighted in red the strong correlation of 0.875 of neutral density with F10.7 and 0.882 with the 133.5 nm wavelength for 2003 (a), and 0.581 with Ap for 2007 (b).

| <i>Correlation</i> | F107 | 0.1-7 | 27-34 | 30.4 | 33.5 | 36.8 | 121.5 | 133.5 | 145-165 | Ap |
|--------------------|--------------|--------------|--------------|-------------|-------------|-------------|--------------|--------------|----------------|-----------|
| N. Dens | 0.875 | 0.790 | 0.866 | 0.859 | 0.822 | 0.686 | 0.830 | 0.882 | 0.846 | 0.056 |
| E. Dens | 0.549 | 0.464 | 0.563 | 0.523 | 0.511 | 0.442 | 0.584 | 0.583 | 0.588 | 0.099 |

a.

| <i>Correlation</i> | F107 | 0.1-7 | 27-34 | 30.4 | 33.5 | 36.8 | 121.5 | 133.5 | 145-165 | Ap |
|--------------------|-------------|--------------|--------------|-------------|-------------|-------------|--------------|--------------|----------------|--------------|
| N. Dens | -0.462 | -0.499 | -0.419 | -0.346 | -0.419 | -0.224 | 0.500 | -0.419 | 0.280 | 0.581 |
| E. Dens | -0.490 | -0.417 | -0.241 | -0.305 | -0.152 | -0.133 | 0.522 | -0.508 | 0.254 | 0.099 |

b.

Electron density shows far less good correlation with any of the parameters analyzed, as expected by the many processes driving its variability. Nevertheless, its correlation with F10.7 during 2003 shows a value of 0.549, and up to 0.588 using the 145-165 nm wavelength. For the years analyzed, electron density appears to be completely uncorrelated to Ap. We are not showing the moving correlation coefficient for electron density, as it does not add valuable information.

We performed a fast fourier transform of all the quantities of interest. Figure 3a and Figure 3b show neutral and electron densities, F10.7, E1335 (irradiance at 133.5 nm) and Ap for 2003 and 2007 respectively. We have selected E1335 from the 8 irradiances provided by TIMED-SEE because it best correlates with neutral density. For both years we clearly see a 27-day peak in the neutral densities, as expected, but only for 2003 we see a correspondent 27-day peak in the F10.7 and EUV irradiances. In particular for 2003 we see how the spectrum for E1335 shows two secondary peaks at 26 and 33 days, present in the neutral density but not in the F10.7. As seen in the time series, this is an indication of how this wavelength is more representative than the F10.7 to describe neutral density variability (at least at solar maximum). Additionally, for both years we notice the quite complex structure of the electron density and a 9-day peak in the Ap (which reflects on the neutral density only in 2007).

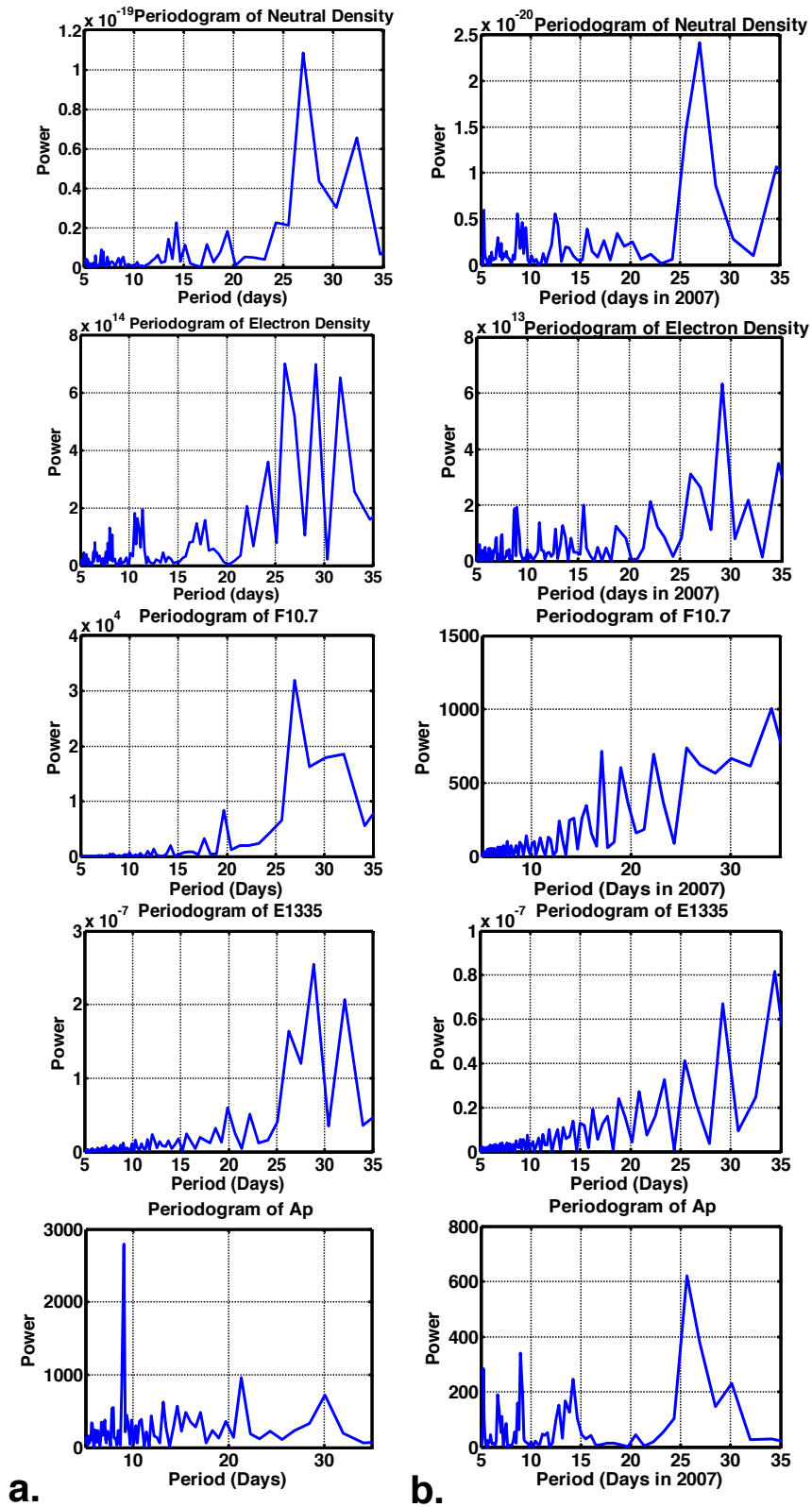


Figure 3: Periodograms of neutral density, electron density, F10.7, E1335 (irradiance at 133.5 nm), and Ap for 2003 (a) and 2007 (b). On the x-axis periods from 5 to 35 days and on the y-axis power.

Figures 4a and 4b show the wavelet of neutral and electron densities, F10.7, E1335 (irradiance at 133.5 nm) and Ap for 2003 and 2007 respectively. Morlet wavelet analysis allows to investigate the temporal variability of periodicities comprised between 5 and 40 days.

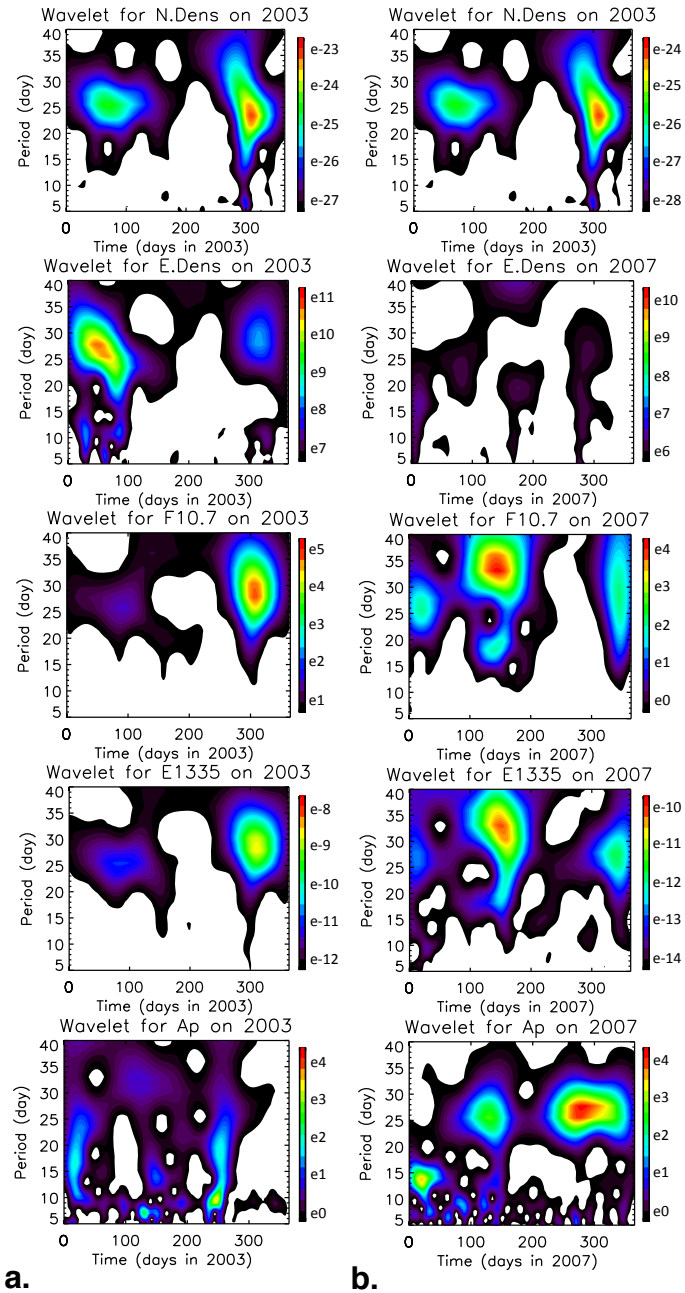


Figure 4: Wavelets of neutral density, electron density, F10.7, E1335 (irradiance at 133.5 nm), and Ap for 2003 (a) and 2007 (b). On the x-axis time (days in 2003 (a) and in 2007(b)) and on the y-axis period from 5 to 40 days (the scales were not fixed for each parameter to better highlight the wave patterns).

For 2003, we notice that neutral density, F10.7 and E1335 show two periods of strong 27-day variation at the beginning and at the end of the month (in accordance with what seen in the time series). Also electron density shows this basic trend, with a higher 27-day peak at the beginning of the year. Ap shows a lot of variability in the region 5/15-day but not around 27 days.

For 2007 we notice how neutral density differs significantly from both F10.7 and E1335, as discussed in the time domain. We also notice very weak periodicities in electron densities. The most significant result for 2007 is represented by Ap, which shows 27-day waves (at the beginning and the end of the month) very similar to the one seen in the neutral density. This result agrees with our findings previously discussed. One of the possible explanations for the poor correlation between Ap and neutral density at the beginning of the year is found in the presence of strong 5/15-day variability, as seen in the wavelet of Ap. For both years we notice how F10.7 compares very well with E1335, although such a comparison is poor looking at the peridiograms, shown in Figure 3. This can be attributed to the yearly average performed in peridiograms, and suggests that wavelet are a much better tool of analysis in this context.

Note that multi-day oscillations at the periods of 7 and 9 days observed in the thermospheric densities and in particular in the Ap are caused by the solar wind high-speed streams and the associated recurrent geomagnetic activity (not very strong in the years analyzed).

4. Conclusions

Understanding the sources of variability of the neutral and plasma densities in the thermosphere is fundamental to gain better knowledge of the Earth-Sun interaction and has several direct space weather applications, such as improving ionospheric models, satellite tracking, radio and telecommunications, and Earth observation from space.

With our study we aimed at better understanding how the thermospheric neutral and plasma densities are linked to solar radiation. We found that neutral density correlates well with solar forcing at solar maximum, whereas at solar minimum internal processes (such as wave propagation, geomagnetic activity, thermosphere-ionosphere coupling) dominate the dynamics of the ionospheric system. We determined that the phase of the solar cycle highly influence the best proxy for neutral density variability, with solar indices (F10.7 or EUV irradiances) best at solar max and geomagnetic indices (Ap) at solar minimum. We found clear evidence of the solar rotation peak in both neutral and plasma density, with solar forcing representing the major source of variability only during solar maximum. We found that electron densities do not correlate well with any of the solar indices (i.e. F10.7 and EUV irradiances) at any phase of the solar cycle, due to oscillations in the 7-9 day, 11-13 day and 17-19 day range (where 7 and 9 days oscillations are associated with solar wind high speed streams).

Additionally, we found that FUV radiation (133.5 nm and 145-165 nm) is more representative than EUV (<121 nm) of neutral and electron density variability in the ionospheric F-region at solar maximum. In particular, for this condition the 133.5 nm irradiance shows the best correlation with both neutral and plasma density.

Futures lines of work are: analyze other years (to have a complete estimate of the solar cycle dependences), and include an error budget associated with the correlation analysis.

References

- Banks, P. M. (1977), Observations of Joule and particle heating in the auroral zone, *J. Atmos. Terr. Phys.*, 39, 179-193, doi:10.1016/0021-9169(77)90112-X.
- Bruinsma, S., G. Thuillier, and F. Barlier (2003), The DTM-2000 empirical thermosphere model with new data assimilation and constraints at lower boundary: accuracy and properties, *J. Atmos. Terr. Phys.*, 65, 1053-1070, doi:10.1016/S1364-6826(03)00137-8.
- Bruinsma, S., D. Tamagnan, and R. Biancale (2004), Atmospheric densities derived from CHAMP/STAR accelerometer observations, *Planetary and Space Science*, 52, 4, 297- 312, doi:10.1016/j.pss.2003.11.004.
- Cole, K.D. (1962), Joule heating of the upper atmosphere, *Aust. J. Phys.*, 15, 223-235. Cole, K.D. (1971), Electrodynamical heating and movement of the thermosphere, *Planet. Space Sci.*, 19, 59-75, doi:10.1016/0032-0633(71)90067-5.
- Doornbos, E., J. van den IJssel, H. Luehr, M. Foerster, G. Koppenwallner, S. Bruinsma, E. Sutton, J.M. Forbes, F. Marcos, and F. Perosanz (2010), Neutral density and cross- wind determination from arbitrarily oriented multi-axis accelerometers on satellites, *J. Spacecraft and Rockets*, 47, 4, 580-589, doi:10.2514/1.48114.
- Forbes, J. M., S. Bruinsma, and F. G. Lemoine (2006), Solar rotation effects in the thermospheres of Mars and Earth, *Science*, 312, 1366-1368, doi:10.1126/science.1126389.
- Fuller-Rowell, T. J., Minter C., Codrescu M., Fedrizzi M. (2009), Estimating the Neutral Atmosphere Drivers using a Physical Model, DOD AF AFOSR, FA9550-06-1-0224.

- Grunwaldt, L., and T. Meehan (2003), CHAMP Orbit and Gravity Instrument Status, First CHAMP Mission Results for Gravity, Magnetic and Atmospheric Studies, Springer-Verlag, 3-10, doi: 10.1007/978-3-540-38366-6.
- Guo, J., W. Wan, J. M. Forbes, E. Sutton, R. S. Nerem, T. N. Woods, S. Bruinsma, and L. Liu (2007), Effects of solar variability on thermosphere density from CHAMP accelerometer data, *J. Geophys. Res.*, 112, A10308, doi:10.1029/2007JA012409.
- Hedin, A. E., and H. G. Mayr (1987), Characteristics of wavelike fluctuations in Dynamics Explorer neutral composition data, *J. Geophys. Res.*, 92, doi:10.1029/JGRE000092000A10011159000001.
- Liu, R., H. Luhr, H., E. Doornbos, and D. Y. Ma (2010), Thermospheric mass density variations during geomagnetic storms and a prediction model based on the merging electric field, *Annales Geophysicae*, 28, 9, 1633-1645, doi:10.5194/angeo-28-1633-2010.
- Pedatella, N. M., and J. M. Forbes (2011), Electrodynamic response of the ionosphere to high-speed solar wind streams, *J. Geophys. Res.*, 116, A12310, doi:10.1029/2011JA017050.
- Perosanz, F., R. Biancale, S. Loyer, J. M. Lemoine, A. Perret, P. Touboul, B. Foulon, G. Pradels, L. Grunwaldt, T. Fayard, N. Vales, and M. Sarrailh (2003), On Board Evaluation of the STAR Accelerometer, First CHAMP Mission Results for Gravity, Magnetic and Atmospheric Studies, Springer-Verlag, 11-18, doi:10.1007/978-3-540-38366-6.
- Qian, Y., W. Wang, L. R. Leung, and D. P. Kaiser (2007), Variability of Solar Radiation under Cloud-Free Skies in China: The Role of Aerosols, *Geophys. Res. Lett.*, 34, L12804, doi:10.1029/2006GL028800.
- Reigber, C., G. Balmino, P. Schwintzer, R. Biancale, A. Bode, J. Lemoine, R. König, S. Loyer, H. Neumayer, J. Marty, F. Barthelmes, F. Perosanz, and S. Y. Zhu (2002), A high-quality global gravity field model from CHAMP GPS tracking data and accelerometry (EIGEN-1S), *Geophys. Res. Lett.*, 29, doi: 10.1029/2002GL015064.
- Thayer, J. P., J. Lei, J. M. Forbes, E. K. Sutton, and R. S. Nerem (2008), Thermospheric density oscillations due to periodic solar wind high-speed streams, *J. Geophys. Res.*, 113, A06307, doi:10.1029/2008JA013190.
- Torrence, C., and G. P. Compo. (1998). A Practical Guide to Wavelet Analysis, *Bull. Amer. Meteor. Soc.*, 79, 61-78, doi:10.1175/1520-0477(1998)079<0061:APGTWA>2.0.CO;2.

Testing the cold plasma dispersion relation for whistler-mode chorus using EMFISIS wave measurements from the Van Allen Probes

David P. Hartley

Physics Department, Lancaster University, Lancaster, UK, LA1 4YB

Yue Chen

Los Alamos National Laboratory, Los Alamos, NM 87545

Abstract

In the Earth's outer electron radiation belt, the role of in-situ wave-particle resonance has recently been recognized as critical in controlling the belt dynamics, with whistler-mode chorus waves now considered the most likely candidate for energizing electrons up to MeV energies. In the past, due to the constraint of wave measurements (e.g. CRRES, PWE), previous studies often relied upon the cold plasma dispersion relation in order to calculate the wave magnetic field from the wave electric field. Given that the energy diffusion rates scale with the magnetic field intensity, and the assumptions used to obtain this parameter were untested, their conclusions can not be determinative. Recently, equipped with comprehensive wave and plasma instruments, the successfully launched Van Allen Probes mission provides an unprecedented opportunity to comprehensively explore this issue. Results from this study indicate that using the cold plasma dispersion relation can lead to large overestimates (up to three orders of magnitude) of the magnetic field wave intensity, with the largest overestimates occurring during periods of low geomagnetic activity. More importantly, during high geomagnetic activity, underestimates of the wave intensity are increasingly likely to occur. Additionally, the cold plasma dispersion relation appears to yield more accurate results when applied to lower band chorus than when applied to upper band chorus.

Keywords:

1. Introduction

Relativistic electron fluxes in the outer radiation belt ($3 < L < 7$) are highly dynamic during periods with enhanced geomagnetic activity (e.g. *Onsager et al.*, (2002); *Green et al.*, (2004); *Borovsky and Denton* (2009)). This variability is driven by an imbalance between source, loss and transport mechanisms, each of which may become enhanced during geomagnetic storms (e.g. *Reeves et al.*, (2003); *Liemohn and Chan* (2007); *Morley et al.*, (2010)). Understanding these competing processes is of paramount importance due to the serious hazards that relativistic electrons can pose to hardware in space.

Previous studies have indicated that enhancements of energetic electrons in the outer radiation belt are driven by acceleration processes within the magnetosphere (e.g. *Li et al.*, (1997)). It is well established that radial diffusion, which violates the third adiabatic invariant of particle motion, can transport electrons inwards and therefore increase their energy (e.g. *Schulz and Lanzerotti* (1974); *Friedel et al.*, (2002)). This type of acceleration would need positive gradients in the phase space density vs. L -shell profile inwards of the source region, however, studies have shown local maxima in the phase space density profiles between $4 < L < 5$ (e.g. *Green and Kivelson* (2004); *Chen et al.* (2007); *Reeves et al.*, (2003)). This demonstrates the dominance of local acceleration mechanisms, which violate either the first or second adiabatic invariants of particle motion, such as wave-particle interactions.

Email addresses: d.hartley1@lancaster.ac.uk (David P. Hartley), chen@lanl.gov (Yue Chen)

Resonance with whistler-mode chorus waves are widely considered to be the most likely process for local acceleration of electrons up to MeV energies (Thorne, 2010). Chorus waves typically occur in two bands, lower and upper, separated by half of the electron gyrofrequency. Electron interactions with this type of wave have been the topic of several studies (e.g. Horne and Thorne (2003); Meredith et al., (2003a); Li et al., (2009a,b)), however, due to the limited availability of in-situ wave data, untested assumptions were often employed and thus their conclusions are not determinative, until the recent successful launch of Van Allen Probes.

2. Background

Due to the Combined Release and Radiation Effects Satellite's (CRRES) equatorial orbit across the radiation belts and its wave instrumentation, previous studies often used this data to investigate the importance of the role that chorus waves in play radiation belt dynamics, more specifically, the acceleration of electrons to MeV energies (e.g. Meredith et al., (2003a,b, 2012)). The plasma wave instrumentation from CRRES measured electric fields in the frequency range 5.6 Hz to 400 kHz, however no magnetic field wave measurements were available (Anderson et al., 1992). Given that the primary purpose of these investigations was to investigate the energization of radiation belt electrons, and the energy diffusion rates scale with the magnetic field intensity (Summers and Ma, 2000), it was required to convert the electric field spectral intensities (as measured by CRRES) to magnetic field spectral intensities. This was done using the expression

$$S_B = \frac{1}{c^2} \left(1 - \frac{f_{pe}^2}{f(f - f_{ce})} \right) S_E \quad (1)$$

derived from Maxwells third equation, and assuming a cold plasma dispersion relation for parallel propagating whistler mode waves (Meredith et al., 2004). S_B and S_E are the magnetic and electric field spectral intensities respectively, c is the speed of light, f is the wave frequency, f_{pe} is the electron plasma frequency and f_{ce} is the electron gyrofrequency. The validity of these assumptions was untested when employed in previous studies, but with the comprehensive wave instrumentation aboard the Van Allen Probes mission, it is now possible to test how successful these assumptions are when used in calculating the magnetic field spectral intensity and wave intensity.

3. Methodology

The EMFISIS instrument suite onboard the Van Allen Probes (Kletzing et al., 2013) measures both electric and magnetic field spectral intensities across the chorus wave frequency range. Comparing the measured magnetic field spectral intensity with the magnetic field spectral intensity calculated using the measured electric field spectral intensity and Equation 1, should definitively determine the accuracy of the assumptions used in previous studies. Equation 1 requires the electron gyrofrequency as an input parameter, which is easily calculated using the expression

$$f_{ce} = \frac{eB}{2\pi m_e} \quad (2)$$

where e is the elementary charge, B is the magnetic field magnitude measured by the Van Allen Probes and m_e is the electron mass. Therefore, the only unknown parameter in Equation 1 is the plasma frequency, f_{pe} . Ideally, it would be possible to use the measured electron plasma density from the HOPE instrument on the Van Allen Probes to calculate the plasma frequency using the relation shown in Equation 3 (with the plasma frequency, f_{pe} , in Hz and the plasma density, n_e , in m^{-3}), however this data is currently unavailable and therefore a different approach is employed.

$$f_{pe} = 8.97 \sqrt{n_e} \quad (3)$$

It is possible to solve Equation 1 in the frequency range 0.1 to 0.9 f_{ce} (as well as 0.1 to 0.5 f_{ce} and 0.5 to 0.9 f_{ce} for lower and upper band chorus respectively) for the plasma frequency, yielding a set of results at each time increment as a function of the measured wave frequencies, $f_{pe}(f)$. Taking the median of $f_{pe}(f)$ (less sensitive than the mean to extreme outliers) for each time step provides the plasma frequency that can be used in Equation 1 when calculating the wave magnetic spectral intensity from the electric field wave intensity. The magnetic field wave intensity can then be

calculated by integrating the spectral intensity between 0.1 and 0.9 f_{ce} for the entire band, and between 0.1 and 0.5 f_{ce} and 0.5 and 0.9 f_{ce} for the lower and upper band respectively. Some of the measured frequency bands are removed due to increased noise levels (visible in Figure 1 centered around 2kHz and 4kHz). Several time periods were selected, as listed in Table 1, in order to perform a statistical study to investigate the accuracy of using the cold plasma dispersion relation to calculate the magnetic field spectral intensity and wave intensity across a range of conditions.

| Date | Start Time (UT) | End Time (UT) | Activity Levels |
|-------------------|-----------------|---------------|-----------------|
| October 7, 2012 | 6:00 | 11:00 | Low |
| October 9, 2012 | 3:00 | 8:00 | High |
| December 6, 2012 | 3:00 | 8:00 | Low |
| December 10, 2012 | 6:00 | 10:00 | Moderate |
| December 16, 2012 | 6:00 | 10:00 | High |
| December 17, 2012 | 8:00 | 14:00 | High |
| December 17, 2012 | 17:00 | 22:00 | Low |
| December 20, 2012 | 8:00 | 12:00 | High |
| December 23, 2012 | 8:00 | 13:00 | Moderate |

Table 1: List of time periods used in statistical study. High activity means that chorus waves are readily apparent during the listed time period, moderate activity means that there is some level of activity although it is not obviously chorus waves, and low activity means that there was very little wave activity during the listed time period.

Several parameter studies were conducted. In addition to studying the accuracy of the cold plasma dispersion relation for the lower and upper bands of chorus waves, we also investigate the dayside/nightside variation. Since returning from Los Alamos, using all of the Van Allen Probe A data to date, we also study the variation with geomagnetic activity (Dst Index) and local time for lower band chorus waves only (since relativistic electrons interact most readily with lower band chorus (*Horne and Thorne, 1998*)). This is done by sorting the measurements in to 1-hour magnetic local time (MLT) bins, as well as sorting in three Dst Index bins; minor activity being greater than -20 nT, moderate activity being between -20 nT and -50 nT and high activity being less than -50 nT. We then take the mean of the values in each bin.

4. Results

Figure 1 shows the magnetic field spectral intensity for chorus waves as measured by Van Allen Probe A, the magnetic field spectral intensity as calculated using the methodology described above, as well as the logarithm of the ratio between the two (observed/calculated) for a four-hour period on December 17, 2012 where chorus activity is easily observable. The solid black line indicates half of the electron gyrofrequency, and the lower (upper) envelope is for 0.1 (0.9) f_{ce} . The highest intensity of chorus waves occurs between 9 and 10 UT, which is when the logarithm of the ratio across the entire frequency band is closest to zero (calculated spectral intensity is closest to observed spectral intensity). After this time, between 10 and 12:30 UT, near to half of the electron gyrofrequency, the calculated spectral intensity is around two orders of magnitude greater than the measured value from Van Allen Probe A. During the same time period, at frequencies closer to 0.1 and 0.9 f_{ce} , the ratio is closer to zero, or greater than zero, indicating that the calculated spectral intensity is similar or greater than the observed value. From 12:30 UT, until the end of the period of interest at 14 UT, there is relatively low wave activity and the observed and calculated spectral intensities appear to match quite well (except for an increase in activity centered around 13 UT in the calculated magnetic field spectral intensity).

Figure 2 displays the power spectral density, both observed and calculated, for two specific instances of time (indicated by the vertical pink and red lines on Figure 1). The first instance of time, 09:03:05 on December 17, 2012

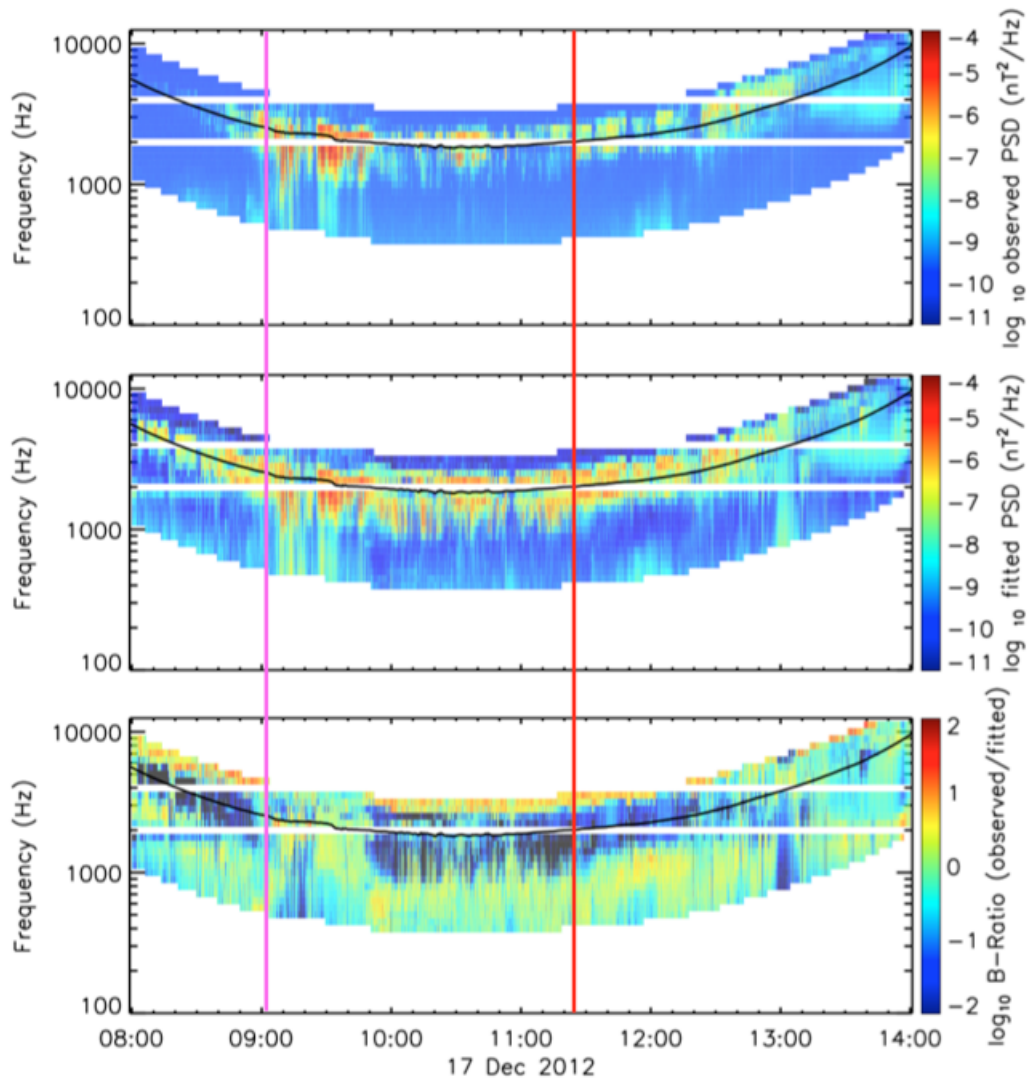


Figure 1: (Top to Bottom) The magnetic field spectral intensity as measured by Van Allen Probe A, the magnetic field spectral intensity as calculated using the methodology described above, the logarithm of the ratio between the two (observed/calculated) for a six-hour period on December 17, 2012 where chorus activity is easily observable. The solid black line indicates half of the electron gyrofrequency. The pink and red lines indicate the times of Figure 2, panel (a) and (b) respectively.

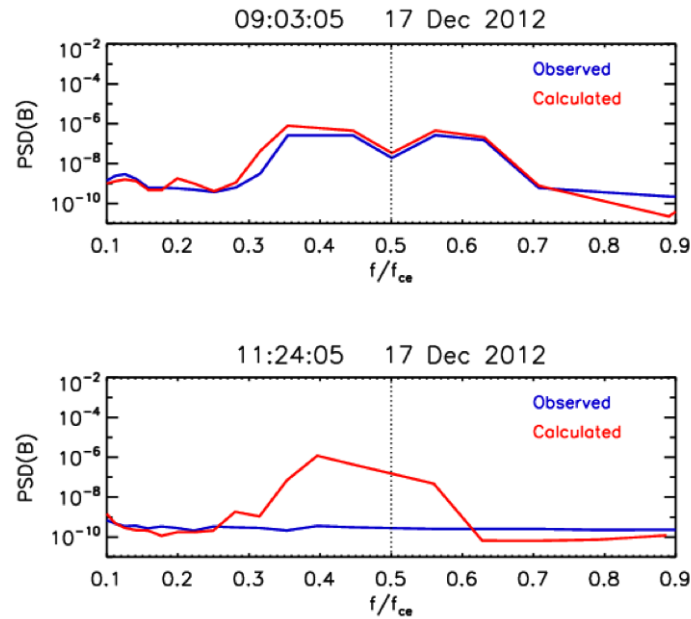


Figure 2: (Top) The observed and calculated magnetic field power spectral density as a function of frequency at 09:03:05 on December 17, 2012 (shown by the pink vertical line in Figure 1). (Bottom) The observed and magnetic field power spectral density as a function of frequency at 11:24:05 on December 17, 2012 (shown by the red vertical line in Figure 1).

(pink line), displays a time where using the cold plasma dispersion relation quite accurately calculates the magnetic field power spectral density between 0.1 and 0.9 f_{ce} . Both upper and lower band chorus waves are apparent during this period with a gap between the two at approximately half of the electron gyrofrequency. The second instance of time, 11:24:05 on December 17, 2012 (red line), displays a time where there is very little activity in the observed magnetic field power spectral density, with no signature of chorus waves. However, the calculated quantity exhibits a peak centered around half of the electron gyrofrequency. This discrepancy will certainly affect the calculated magnetic field wave intensity, leading to a large overestimate of this quantity at this time.

The top panel of Figure 3 shows both the observed and calculated magnetic field wave intensity (integral of the power spectral density between 0.1 and 0.9 f_{ce}), for the periods of time listed in Table 1, with the color indicating the logarithm of the number of occurrences in each bin. In this way, distributions of calculated magnetic wave intensities for a given observed magnetic wave intensity can be clearly seen. It is apparent that for the vast majority of the time periods studied, the calculated magnetic field wave intensity is greater than that observed by Van Allen Probe A. These overestimates appear largest during periods where the observed magnetic field wave intensity is low. The vertical feature at very low observed wave intensities may be due to the magnetic field instrument's background noise level. At times where the observed magnetic field wave intensity is elevated ($>10^{-3}$ nT²) the higher density of points appears below the line of equality; the observed magnetic field wave intensity is greater than that calculated using the cold plasma dispersion relation. The data are then sorted between day/night side and between upper/lower band chorus frequencies in order to study as to whether using the cold plasma dispersion relation to calculate magnetic field power spectral densities, and thus wave intensities, is more accurate at given local times or frequency bands. The bottom four panels of Figure 3 displays the same quantities as the top panel of Figure 3, after this sorting in MLT and frequency has taken place. Initially, just comparing between upper and lower band chorus, it is apparent that a much higher density of points lie near the line of equality for lower band chorus than for upper band chorus. For both upper and lower band, the majority of the calculated wave intensities are greater than those observed by Van Allen Probe A, with the largest overestimates occurring for upper band chorus. When comparing between the dayside and the nightside, it is apparent that there are a much higher number of observations on the nightside than the dayside. This is due to the orbit of Van Allen Probe A, which moves into the pre-dawn sector in December 2012. While there

is certainly less spread from the line of equality for the dayside when compared to the nightside, there are much fewer data points. It is therefore unclear as to whether this result is significant without examining more data.

Figure 4 displays the magnetic field wave intensity, both observed and calculated, in addition to the logarithm of the ratio between the two (observed/calculated) for lower band chorus waves for all available Van Allen Probe A data from the mission so far (September 8, 2012 to August 10, 2013). Data is sorted by magnetic local time (MLT) and L-shell in 1-hour local time bins and in 0.1 L-shell bins. Data is also sorted by geomagnetic activity levels (as indicated by the Dst index) in three bins; minor activity ($Dst > -20$ nT), moderate activity ($-20 \text{ nT} > Dst > -50$ nT) and high activity ($Dst < -50$ nT). The mean is taken of the data in each bin in order to obtain the average lower-band chorus intensities as a function of geomagnetic activity, L-shell and MLT. This process is performed for both the observed magnetic field wave intensity from Van Allen Probe A and the magnetic field wave intensity calculated using the cold plasma dispersion relation. As in Meredith et al., [2003] who used the AE-Index to investigate the substorm dependence of lower band chorus magnetic field wave intensities as a function of L-shell and MLT, during low geomagnetic activity we see the strongest wave intensities in the dawn sector. The wave intensities increase in magnitude and cover a broader range of MLT as geomagnetic activity increases (AE or Dst), with the maximum wave intensities occurring during high geomagnetic activity. Comparing between observed and calculated wave intensities it is apparent that, as with the selected events in Table 1, the majority of calculated wave intensities are greater than those observed, with the largest overestimates occurring during low geomagnetic activity. When geomagnetic activity is elevated, the number of large overestimates decreases. During high geomagnetic activity there are periods where the calculated magnetic field wave intensity is less than that observed by Van Allen Probe A, this does not appear to occur during periods of low geomagnetic activity. Also, outside $L \sim 4$, the calculated wave intensities appear to most closely match those observed, with the logarithm of the ratio between the two being closest to zero. Chorus waves are not typically observed inside the 18-21 MLT sector, it is therefore thought that the higher ratios in this region may arise from background noise. A more thorough analysis of the MLT dependence will be possible in the future, once the Van Allen Probe data set is more comprehensive.

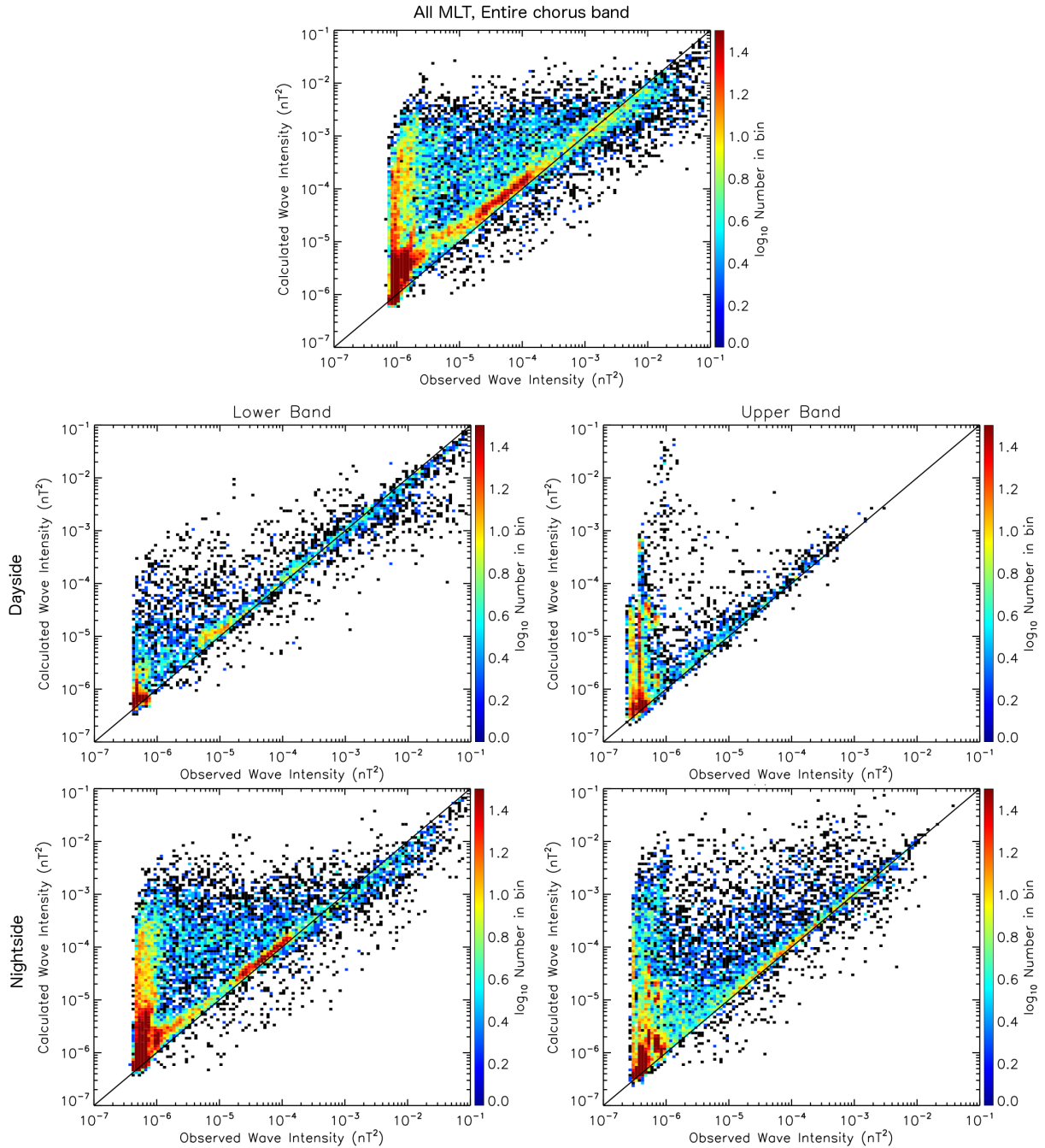


Figure 3: (Top) A plot showing how the observed wave intensity from Van Allen Probe A compares with that calculated using the cold plasma dispersion relation. The color indicates the number of occurrences in each bin. (Bottom 4 panels) The same quantities as shown above but split into Lower Band and Upper Band Chorus, and day and night-side. The color still indicates the number of occurrences in each bin.

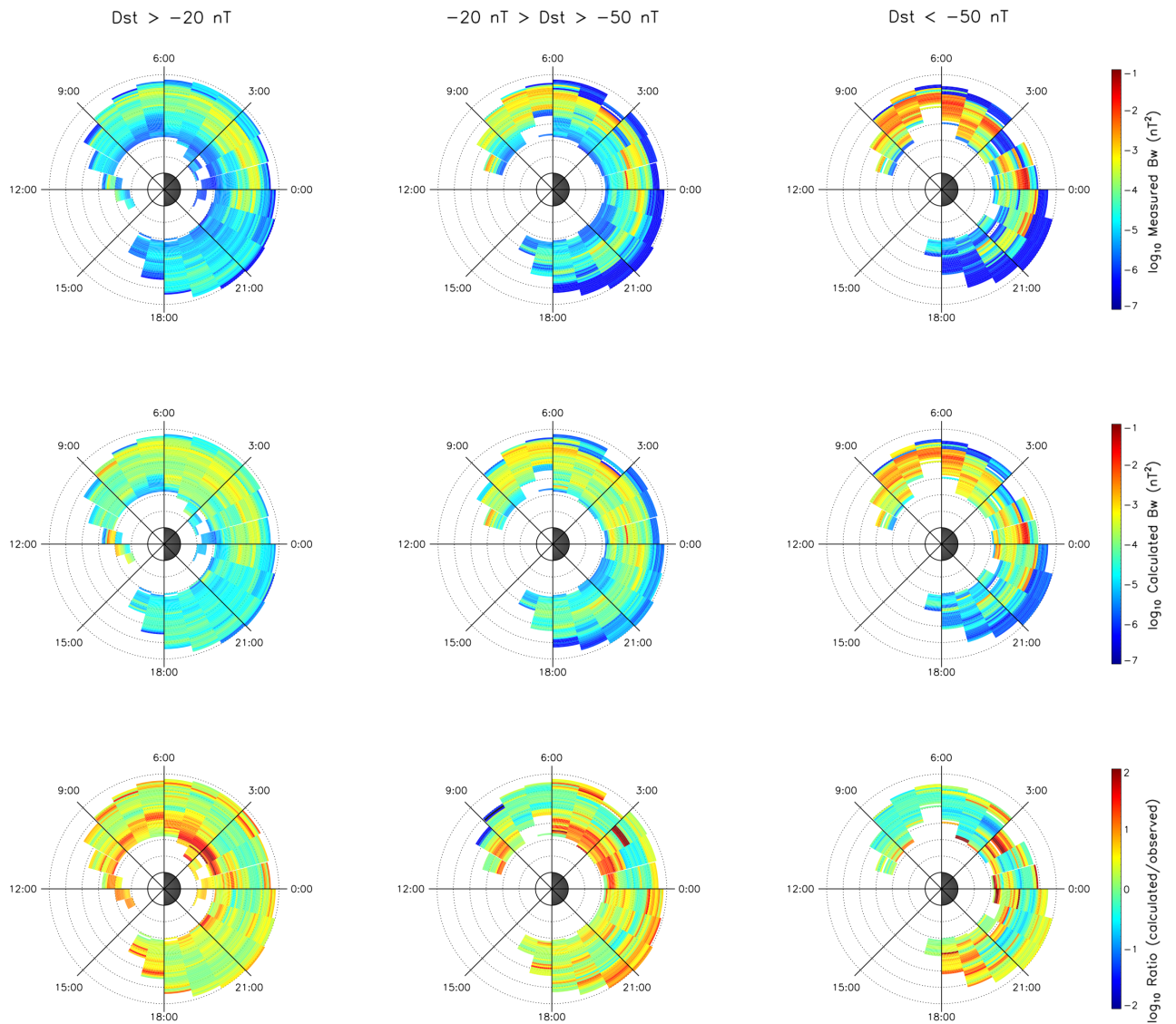


Figure 4: The local time and geomagnetic activity dependence of the observed and calculated magnetic field wave intensity. Top three panels show the magnetic field wave intensity as measured by Van Allen Probes A. Middle three panels show the magnetic field wave intensity as calculated using the cold plasma dispersion relation. Bottom three panels show the logarithm of the ratio between the calculated and observed magnetic field wave intensity. The columns show how the calculated and observed magnetic field wave intensity vary with geomagnetic activity; (left) $Dst > -20$ nT, (center) $-20 \text{ nT} > Dst > -50$ nT, (right) $Dst < -50$ nT.

5. Summary and Conclusions

This study aims to test the validity of using the cold plasma dispersion relation to convert electric field spectral intensities to magnetic field spectral intensities and thus wave intensities (i.e. Meredith et al., [2003a; 2003b; 2004]). The results indicate that some of the time, this technique yields results that closely match observations. However, a significant amount of observations of magnetic field wave intensities were much lower than those calculated using the cold plasma dispersion relation. The largest overestimates of the magnetic field wave intensity occur when the observed wave intensity is low. In order to establish what conditions cause low wave intensity, and therefore large overestimates of the calculated wave intensity using the cold plasma dispersion relation, we investigate the effect of MLT and geomagnetic activity variations. The results indicate that the largest overestimates of the magnetic field wave intensity occur at low L shell ($L < 4$) in the early morning sector (0-6 LT) during low to moderate geomagnetic activity ($Dst > -50$ nT). The magnetic field wave intensities calculated using the cold plasma dispersion relation appear most accurate outside $L \sim 4$. With increasing geomagnetic activity (decreasing Dst Index), the number of large overestimates appears to decrease with more calculated magnetic field wave intensities closer matching those observed by Van Allen Probe A. Additionally, with elevated geomagnetic activity, there are times where the calculated magnetic field wave intensity is actually less than that observed by Van Allen Probe A, which does not appear to occur during periods of low geomagnetic activity.

In conclusion:

1. The cold plasma dispersion relation appears more accurate when applied to Lower Band Chorus than Upper Band Chorus.
2. Using the cold plasma dispersion relation to calculate the magnetic field wave intensity from the electric field wave intensity can lead to large overestimates, particularly during low geomagnetic activity (low wave intensity). However, from the radiation belt dynamic perspective, this is not a critical issue given that we are more interested in periods with intensive chorus waves.
3. Using the cold plasma dispersion relation typically leads to overestimates of the Lower Band wave intensity below observed wave intensities of $\sim 10^{-3}$ nT² and typically underestimates wave intensities above observed wave intensities of $\sim 10^{-3}$ nT². This means that empirical wave models based upon CRRES data may tend to underestimate chorus waves during high geomagnetic activity category, and thus lead to underestimate of their effects on MeV electrons in diffusive models.
4. Using the cold plasma dispersion relation seems to almost always lead to overestimates of Upper Band Chorus wave intensity.
5. Not comprehensive enough MLT coverage for thorough local time comparison; will be possible as more Van Allen Probes data becomes available.

References

- Anderson, R.R. and D.A. Gurnett (1992), The development of static and dynamic models of the Earth's radiation belt environment through the study of plasma waves, wave-particle interactions and plasma number densities from in situ observations in the Earth's magnetosphere with the CRRES spacerad instruments, PL-TR-92-2035, Philips Lab., Hanscom AFB, MA
- Borovsky, J. E., and M. H. Denton (2009), Relativistic-electron dropouts and recovery: A superposed epoch study of the magnetosphere and the solar wind, *J. Geophys. Res.*, 114, A02201, doi:10.1029/2008JA013128.
- Chen, Y., G. D. Reeves and R. H. Friedel (2007), The energization of relativistic electrons in the outer Van Allen radiation belt, *Nature Physics.*, 3, 614, doi:10.1038/nphys655.
- Denton, M. H. et al., (2006), Geomagnetic storms driven by ICME- and CIR-dominated solar wind, *J. Geophys. Res.*, 111, A07S07, doi:10.1029/2005JA011436.
- Friedel, R. H., W., G. D. Reeves, and T. Obara, (2002), Relativistic electron dynamics in the inner magnetosphere: a review, *J. Atmos. Sol. Terr. Phys.*, 64, 265, 2002.
- Green, J. C. et al., (2004), Testing loss mechanisms capable of rapidly depleting relativistic electron flux in the Earth's outer radiation belt, *J. Geophys. Res.*, 109(A12), A12211, doi:10.1029/2004JA010579.
- Horne, R. B., and R. M. Thorne, Potential waves for relativistic electron scattering and stochastic acceleration during magnetic storms, *Geophys. Res. Lett.*, 25(15), 3011, 1998.
- Horne, R. B., and R. M. Thorne, Relativistic electron acceleration and precipitation during resonant interactions with whistler-mode chorus, *Geophys. Res. Lett.*, 30(10), 1527, doi:10.1029/2003GL016973, 2003.
- Green, J. C., and M. G. Kivelson (2004), Relativistic electrons in the outer radiation belt: Differentiating between acceleration mechanisms, *J. Geophys. Res.*, 109, A03213, doi:10.1029/2003JA010153.

- Kletzing, C.A., W.S. Kurth, M. Acuna, R.J. MacDowall, R.B. Torbert, T. Averkamp, D. Bodet, S.R. Bounds, M. Chutter, J. Connerney, D. Crawford, J.S. Dolan, R. Dvorsky, G.B. Hospodarsky, J. Howard, V. Jordanova, R.A. Johnson, D.L. Kirchner, B. Mokrzycki, G. Needell, J. Odom, D. Mark, R. Pfaff Jr., J.R. Phillips, C.W. Piker, S.L. Remington, D. Rowland, O. Santolik, R. Schnurr, D. Sheppard, C.W. Smith, R.M. Thorne, and J. Tyler, The Electric and Magnetic Field Instrument Suite and Integrated Science (EMFISIS) on RBSP, *Space Science Reviews*, doi:10.1007/s11214-013-9993-6, in press, May 9, 2013; published online June 1, 2013.
- Li, X., D. N. Baker, M. Temerin, D. Larson, R. P. Lin, G. D. Reeves, M. Looper, S. G. Kanekal, and R. A. Mewaldt, (1997), Are energetic electrons in the solar wind the source of the outer radiation belt?, *Geophys. Res. Lett.*, 24(8), 923, 1997.
- Li, W., R. M. Thorne, V. Angelopoulos, J. Bortnik, C. M. Cully, B. Ni, O. LeContel, A. Roux, U. Auster, and W. Magnes (2009a), Global distribution of whistlermode chorus waves observed on the THEMIS spacecraft, *Geophys. Res. Lett.*, 36, L09104, doi:10.1029/2009GL037595.
- Li, W., R. M. Thorne, V. Angelopoulos, J. W. Bonnell, J. P. McFadden, C. W. Carlson, O. LeContel, A. Roux, K. H. Glassmeier, and H. U. Auster (2009b), Evaluation of whistlermode chorus intensification on the nightside during an injection event observed on the THEMIS spacecraft, *J. Geophys. Res.*, 114, A00C14, doi:10.1029/2008JA013554.
- Liemohn, M. W., and A. A. Chan (2007), Unravelling the causes of radiation belt enhancements, *Eos Trans. AGU*, 88(42), doi:10.1029/2007EO420001.
- Meredith, N. P., R. B. Horne, R. M. Thorne, and R. R. Anderson (2003a), Favored regions for chorus-driven electron acceleration to relativistic energies in the Earth's outer radiation belt, *Geophys. Res. Lett.*, 30(16), 1871, doi:10.1029/2003GL017698.
- Meredith, N. P., M. Cain, R. B. Horne, R. M. Thorne, D. Summers, and R. R. Anderson, (2003b), Evidence for chorus-driven electron acceleration to relativistic energies from a survey of geomagnetically disturbed periods, *J. Geophys. Res.*, 108(A6), 1248, doi:10.1029/2002JA009764, 2003.
- Meredith, N. P., R. B. Horne, R. M. Thorne, D. Summers, and R. R. Anderson (2004), Substorm dependence of plasmaspheric hiss, *J. Geophys. Res.*, 109, A06209, doi:10.1029/2004JA010387.
- Meredith, N.P., R.B. Thorne, A. Sicard-Piet, D. Boscher, K.H. Yearby, W. Li, and R.M. Thorne (2012), Global model of lower band and upper band chorus from multiple satellite observations, *J. Geophys. Res.*, 117, A10225, 10.1029/2012JA017978
- Morley, S. K., R. H. W. Friedel, E. L. Spanswick, G. D. Reeves, J. T. Steinberg, J. Koller, T. Cayton and E. Noveroske (2010), Dropouts of the outer electron radiation belt in response to solar wind stream interfaces: global positioning system observations, *Proc. R. Soc.*, A 2010 466, doi: 10.1098/rspa.2010.0078 first published online 6 May 2010.
- Onsager, T. G. et al., (2002), Radiation belt electron flux dropouts: Local time, radial, and particle-energy dependence, *J. Geophys. Res.*, 107(A11), 1382, doi:10.1029/2001JA000187.
- Reeves, G. D., K. L. McAdams, R. H. W. Friedel, and T. P. O'Brien (2003), Acceleration and loss of relativistic electrons during geomagnetic storms, *Geophys. Res. Lett.*, 30(10), 1529, doi:10.1029/2002GL016513.
- Reeves, G.D., et al. (2013), Electron acceleration in the heart of the Van Allen radiation belts, *Science*, 341, 991-994, 10.1126/science.1237743
- Schulz, M., and L. J. Lanzerotti, Particle Diffusion in the Radiation Belts, Springer-Verlag, New York, 1974.
- Summers, D., and C. Ma, A model for generating relativistic electrons in the Earth's inner magnetosphere based on gyroresonant wave-particle interactions, *J. Geophys. Res.*, 105(A2), 2625, 2000.
- Thorne, R.M. (2010), Radiation belt dynamics: The importance of wave-particle interactions, *GRL*, 37, L22107, 10.1029/2010GL044990

The Whistler Anisotropy Instability and the Inverse Cascade of Short-Wavelength Turbulence

R. Scott Hughes

Department of Astronautical Engineering, University of Southern California, Los Angeles, California, USA

S. Peter Gary

Space Science Institute, Boulder, Colorado, USA

Abstract

A three-dimensional (3D) particle-in-cell (PIC) simulation of whistler turbulence is carried out for a collisionless, homogeneous, magnetized plasma. The simulation is initialized with an anisotropic electron velocity distribution such that $T_{e\perp}/T_{e\parallel} > 1$. Such a condition is conducive to the generation of the so called whistler anisotropy instability. Here \perp and \parallel denote directions relative to the background magnetic field \mathbf{B}_0 . The wavevector range of the initial magnetic fluctuations generated by the instability are in good agreement with those predicted by linear theory, with a narrowband spectra and a peak in fluctuation energy near $kc/\omega_e \simeq 1$ and $\mathbf{k} \times \mathbf{B}_0 = 0$. These initial fluctuations have a preferential tendency to propagate along the magnetic field lines. As the simulation progresses and the instability saturates the initial fluctuation energy splits into three wavevector zones. The bulk of the fluctuation energy remains near the initial instability region. A second zone is formed by a transfer of energy from the initial region to larger wavevectors, indicative of a forward cascade. A third zone is formed by a transfer of energy to much smaller wavevectors. This is a region of particular interest as this indicates the occurrence of an inverse cascade of energy. The fluctuations in the inverse cascade region have a preferential tendency to propagate across magnetic field lines.

Keywords: Whistler Turbulence, Solar Wind, Plasma

1. Introduction

The energy contained in the solar wind is pervasive. The exact configuration of that energy has significant implications regarding how the solar wind interacts with the near-earth space environment and, by extension, the impact the solar wind has on our space-based, and even ground-based, assets. This energy is primarily stored in two forms. The first is in the form of electromagnetic fields, which can be categorized as static fields and fluctuating fields. The second form is in the kinetic energies of the individual charged particles which make up the solar wind. Energy can be transferred between these two forms.

An important mode of interaction between fields and particles is through waves. A variety of waves at various frequencies can propagate through a tenuous plasma such as the solar wind. A large collection of overlapping waves which propagate with differing frequencies and in varying directions is referred to as turbulence. Solar wind turbulence is extremely complex as its generation and evolution depends on interactions, not only between individual particles and waves, but also between the waves themselves. Studying the behavior of solar wind turbulence is worthwhile, however, as it provides insight into how the energy in the solar wind is distributed, and how that distribution changes over time.

2. Background

Many previous studies of solar wind turbulence suggest that as the waves are subjected to interactions, the average wavelength in the spectrum continues to decrease until a point is reached where nonlinear processes cause the electromagnetic energy to dissipate resulting in heating of the medium (Zhou *et al.*, 2004). This process is known as a forward cascade. Some numerical studies utilizing electron magnetohydrodynamic (EMHD) models (Wareing and Hollerbach, 2010) have suggested that the opposite process is also possible. That is, waves of initially short wavelength interact in such a way as to form new waves with increased wavelengths. This process is known as an inverse cascade. The discovery that such processes do exist in nature would alter our understanding of how energy in the solar wind is distributed and how it reconfigures over time.

One type of wave which is suspected to play an important role in solar wind dynamics is the whistler wave. Whistler waves possess frequencies on the order of 1 KHz, and wavelengths on the order of the electron inertial length, c/ω_e , where ω_e is the electron plasma frequency. Whistler wave dynamics occur on time scales comparable with the electron cyclotron frequency, Ω_e . For this reason these waves primarily interact with the lightweight electron population of the plasma, while the relatively large inertia of the ions prevents noticeable perturbations in the ion population over the time period of interest.

Previous work has been conducted on simulating the behavior of whistler turbulence by using the Particle-in-Cell (PIC) method (Chang *et al.*, 2011) (Chang *et al.*, 2013). These studies have taken the approach of beginning with a pre-loaded set of relatively long wavelength whistler waves with wavevector components isotropically distributed perpendicular and parallel to a steady state background magnetic field. The simulation then proceeds and the evolution of the whistler turbulence is inferred by observing the changes in the wavevector power spectrum. Such simulations have consistently resulted in a forward cascade of fluctuation energy, preferentially in directions perpendicular to the background magnetic field.

The goal of this current work is, as in previous studies, to use the PIC method to investigate how whistler turbulence evolves in a tenuous magnetized plasma. In this case, however, the whistler turbulence is introduced into the system in a more natural way. Rather than artificially loading whistler waves into the system at pre-selected wavelengths, a temperature anisotropy in the electron population $T_{e\perp}/T_{e\parallel} > 1$ is imposed. This temperature anisotropy results in the so called whistler anisotropy instability which, as the name suggests, produces a turbulent spectrum of whistler waves. Therefore, in the case of this study the whistler waves are self-generated by the simulation with properties naturally determined by the generation process. The simulation then proceeds and the evolution of the initial whistler turbulence spectrum is observed.

3. Methodology

In this study a full particle relativistic electromagnetic PIC code is employed on a three dimensional domain with periodic boundary conditions to simulate a collisionless, homogeneous plasma. As described in (Wang *et al.*, 1995), plasma particles are pushed using a standard relativistic particle algorithm, currents are deposited using a rigorous charge conservation scheme, and the self-consistent electromagnetic field is solved using a local finite difference time domain solution to the full Maxwell's equations. The domain contains 1024 cells in each dimension with a grid spacing of $0.10c/\omega_e$. Both ions (protons) and electrons are simulated as macro-particles with a realistic mass ratio $m_i/m_e = 1836$. The number of electrons per cell is 48 while the number of ions per cell is 16. The ions are weighted with a larger charge such that the system remains quasi-neutral. This is done in order to increase the electron resolution without additional computational expense.

The electrons are initialized with a thermal velocity $v_{te} = 0.1c$, and the ions with a thermal velocity such that $T_i/T_{e\parallel} = 1.0$. The electron temperature anisotropy is set to $T_{e\perp}/T_{e\parallel} = 3.0$. This value was selected as it surpasses the threshold value, predicted by linear theory, required for instability onset to occur while remaining small enough to be representative of a value that could be reached in the solar wind. A background magnetic field is imposed along the z direction such that $\omega_e/\Omega_e = \sqrt{5}$ and $\beta_{e\parallel} = 0.1$. As the field is directed along the z direction, a subscript \parallel is synonymous with z . The simulation time step is $\Delta t = 0.05\omega_e$.

The output of the simulation provides the fluctuation magnetic energy components in the x, y and z directions at regular time intervals. From this information the wavevector power spectrum $|\delta\mathbf{B}(\mathbf{k})|^2$ is calculated. The two dimensional power spectrum is defined as the spectrum obtained by summing the fluctuation power over one dimension.

That is, for example

$$|\delta\mathbf{B}(k_{\parallel}, k_{\perp})|^2 \equiv \sum_{\mathbf{k}_{\perp}} |\delta\mathbf{B}(\mathbf{k})|^2 \quad (1)$$

The wavevector anisotropy angle θ_B is a measure of the amount of energy contained in wavevector components perpendicular to the magnetic field relative to the amount contained in wavevector components parallel to the magnetic field. This provides a means of quantifying the preferential direction of magnetic fluctuations relative to the background magnetic field. The wavevector anisotropy factor is defined as

$$\tan^2 \theta_B \equiv \frac{\sum_{\mathbf{k}} k_{\perp}^2 |\delta\mathbf{B}(\mathbf{k})|^2}{\sum_{\mathbf{k}} k_{\parallel}^2 |\delta\mathbf{B}(\mathbf{k})|^2} \quad (2)$$

4. Results

Figure 1 shows the time histories of key properties of the system. In panel (a) the magnetic fluctuation energy density as a function of time is displayed. Panel (b) shows the evolution of the electron parallel and perpendicular temperatures as well as the electron temperature anisotropy. The initial state of the system possesses nearly zero fluctuation energy. As the instability takes hold electromagnetic waves are generated and system energy is transferred into the form of magnetic field fluctuations. The increase in fluctuation energy at early times is exponential and the fluctuations reach a maximum amplitude at $t \approx 475\omega_e$. During this time the temperature anisotropy sees a significant drop as electrons are heated parallel to the background magnetic field. As the temperature anisotropy drops, the instability can no longer sustain itself and the magnetic fluctuation magnitude saturates. Late times show a steady decrease in the temperature ratio as the electrons continue to gain thermal energy in the parallel direction and lose energy in perpendicular directions. The fluctuation energy also decreases during this period as the waves are subjected to Landau damping.

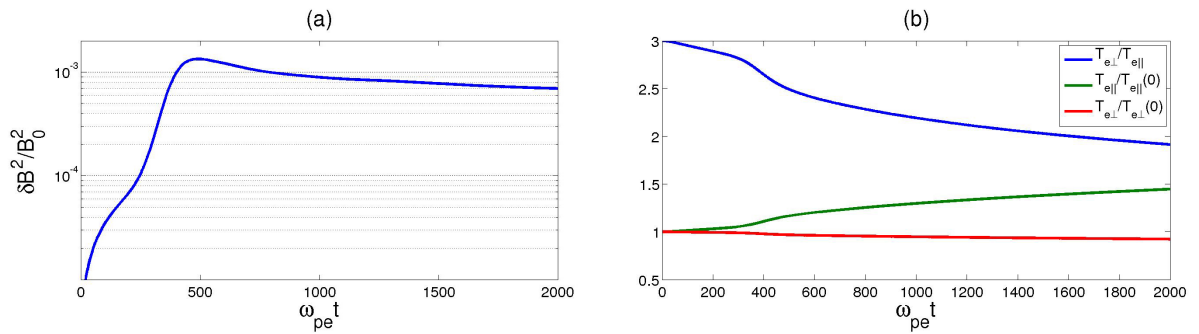


Figure 1: (a) The normalized fluctuating magnetic field energy density (b) the electron temperature anisotropy and the normalized parallel and perpendicular electron temperature as functions of time.

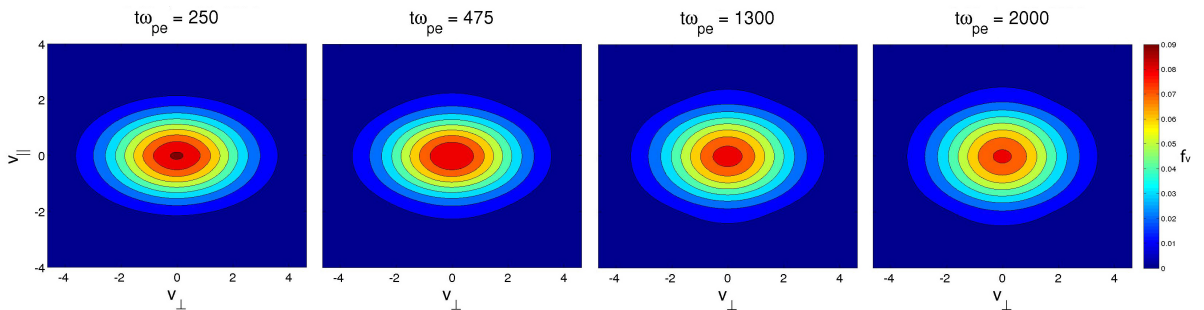


Figure 2: The normalized electron velocity distribution contours reduced to $v_{e\perp}$ vs $v_{e\parallel}$ at four times.

The change in the distribution of electron thermal velocity can be seen in figure 2. In this figure the contours represent the fraction of electrons with given parallel and perpendicular velocity components. The initial state is clearly bi-Maxwellian, and takes the form of an ellipse in velocity space. The temperature anisotropy is seen by the larger spread in velocities in the perpendicular direction. As the simulation proceeds electrons are scattered primarily from the region near $|v_{\perp}| = 0$. As the peak in this region is reduced the electron population becomes thermalized. The distribution of velocities attempts to become circular in order to move the system towards equilibrium. In this effort, however, electrons with near zero perpendicular velocities are more rapidly scattered to high parallel velocities and the distribution assumes a distorted circular shape. This is explained by panel (b) of figure 1. As the perpendicular temperatures decrease and the parallel temperatures increase, the electrons with minimal perpendicular temperature stand to gain the most energy.

The distribution of energy among the magnetic waves that compose the turbulence is presented in figure 3. Here the spectrum of magnetic fluctuation power at wavevector components perpendicular and parallel to the background magnetic field is shown. Panel (a) shows the power spectrum reduced along one of the principal perpendicular directions, and panel (b) shows the power spectrum reduced along the parallel direction. From panel (b) it can be seen that there is no tendency for waves to propagate in any particular perpendicular direction. The fluctuations are gyrotropic with a mean fluctuation energy at a perpendicular wavenumber of zero. This primarily provides a sanity check on the simulation. As the system is initialized with a gyrotropic velocity distribution, there is no reason for the fluctuations to deviate from this gyrotropic state.

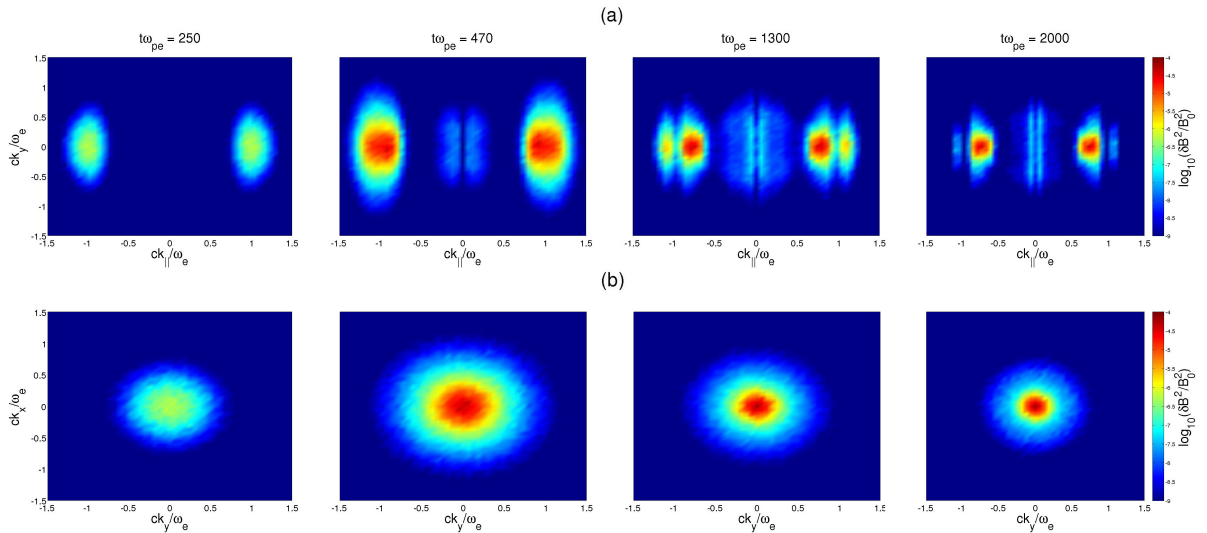


Figure 3: Reduced wavevector magnetic fluctuation energy spectra $|\delta\mathbf{B}|^2$ at four times. (a) $k_{\parallel}c/\omega_e$ vs $k_y c/\omega_e$ (b) $k_y c/\omega_e$ vs $k_x c/\omega_e$

Panel (a) shows how the energy is distributed amongst parallel directed waves. The onset of the instability concentrates fluctuation growth near $|k_{\parallel}c/\omega_e| \approx 1$ with a mean perpendicular wavevector component of zero. This is in agreement with linear theory of whistler waves which predicts wave growth in this range of wavevectors for the given temperature anisotropy magnitude. The second frame is taken at the time of maximum fluctuation energy. The power in the initial region has continued to increase. However a new region has begun to form at $|k_{\parallel}c/\omega_e| < 0.5$. As instability growth has subsided by this point in time, the newly formed region is interpreted as the outcome of a transfer of energy from the primary region, an inverse cascade of energy. While, in this region, the maximum wavenumber in the parallel direction had drastically decreased, there is only a slight decrease in the maximum magnitude of the perpendicular wavenumber, which indicates an enhanced preference to propagate across the background magnetic field lines. At later times, the turbulence has begun to dampen, however the inverse cascade region has grown larger, with a stronger concentration of energy at the smallest parallel wavenumbers that the simulation can resolve. Also, a third region has begun to form at parallel wavenumbers larger than those of the primary region, indicating the presence of a forward cascade. At the latest times, the fluctuations have been significantly dampened. In particular, the energy in

the forward cascade region has reduced to nearly zero. The inverse cascade region is still present, and the energy in this region has all shifted to the smallest resolvable parallel wavenumbers.

To gain a greater understanding of the behavior of the three spectral regions, the fluctuation energy contained in each region has been plotted against time in panel (a) of figure 4. The primary region, as would be expected, exhibits an early and rapid increase in fluctuation energy, and maintains the overwhelming majority of the energy at all later times. Both the forward and inverse cascade regions do not show any signs of significant growth until the primary region has nearly saturated. This again illustrates that these two regions are in fact the direct result of an energy transfer from the primary region. The cascaded regions both reach their energy peaks shortly after the primary region, at which point the forward cascade region exhibits rapid damping and dissipates to below the background noise level at a time of approximately $1200\omega_e$. The inverse cascade region experiences minimal damping rates, comparable to those of the primary region.

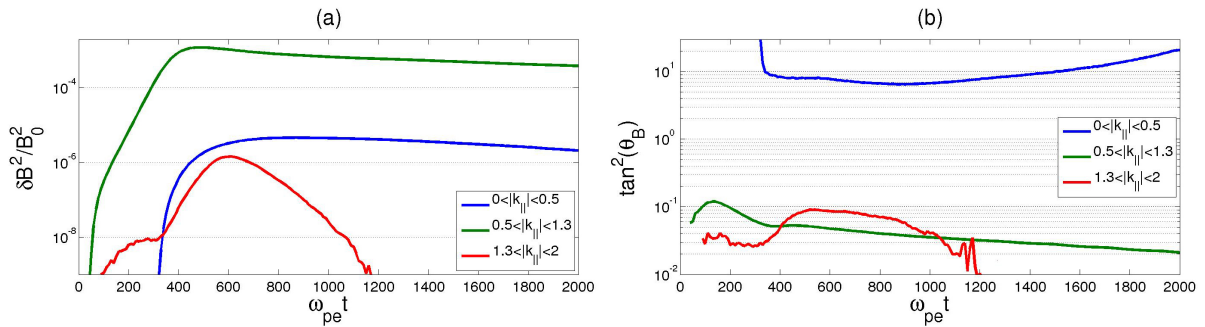


Figure 4: Simulation results as functions of time summed over $0 < |k_{\parallel}c/\omega_e| < 0.5$ (blue lines), summed over $0.5 \leq |k_{\parallel}c/\omega_e| < 1.30$ (green lines), and summed over $1.30 \leq |k_{\parallel}c/\omega_e| \leq 2.0$ (red lines). (a) Magnetic fluctuation energy (b) Magnetic fluctuation wavevector anisotropy factor $\tan^2(\theta_B)$.

Panel (b) of figure 4 follows the fluctuation anisotropy factor over time. At intermediate wavelengths ($0.5 \leq k_{\parallel}c/\omega_e < 1.3$), the primary spectral contribution is due to growth of the whistler instability with maximum growth at $\mathbf{k} \times \mathbf{B}_0 = 0$, so $k_{\perp} \ll k_{\parallel}$. At long wavelengths ($k_{\parallel}c/\omega_e < 0.5$), the primary spectral contribution is due to the inverse cascade which, as is clear from Figure 3, corresponds to substantial decreases in k_{\parallel} without significant change in k_{\perp} leading to $k_{\perp} \gg k_{\parallel}$. At late times, the anisotropy factor in this region continues to grow. As the damping is mild, this implies that the energy continues to cascade to smaller and smaller k_{\parallel} , where it accumulates near the smallest k_{\parallel} the system can resolve. At short wavelengths ($1.3 \leq k_{\parallel}c/\omega_e \leq 2$), the primary spectral contribution is due to the forward cascade which, again, yields no important changes in k_{\perp} but, in contrast, increases k_{\parallel} , reinforcing the $k_{\perp} \ll k_{\parallel}$ condition of the intermediate wavelength regime.

5. Conclusion

The generation and evolution of a narrow band spectrum of whistler turbulence has been simulated and analyzed. The means of turbulence generation was via the whistler temperature anisotropy instability, with an electron temperature ratio $T_{e\perp}/T_{e\parallel} = 3$. At early simulation times the magnetic energy fluctuation spectrum was in good agreement with what would be expected from linear theory. As time progressed, non-linear interactions between waves and particles took hold resulting in a cascade of fluctuation energy from the primary instability region (in wavenumber space). Fluctuation energy began to decrease by effect of Landau damping, which resulted in the heating of the electron population in directions parallel to the background magnetic field.

Many numerical kinetic studies, employing alternative techniques of turbulence generation, have come to similar conclusions. The interesting result here is that, not only did this spectrum of whistler turbulence exhibit a forward cascade to shorter wavelengths, but it also exhibited an inverse cascade of fluctuation energy towards the smallest parallel wavenumbers that could be resolved. An important difference between the configuration here and those of past studies, (Chang *et al.*, 2011) in particular, is that of the range of initial wavevector magnitudes. In those studies, the selected initial whistler modes were the few smallest values that the system could resolve. This means that only a forward cascade could be observed. In the case of this work, the initial fluctuations were at a wavenumber

$kc/\omega_e \approx 1$ and displayed a strong parallel fluctuation anisotropy. This provided room in wavenumber space for an inverse cascade to be observed. The energy distribution in the inverse cascade region was that of having a strong perpendicular fluctuation anisotropy, which agrees with the results of (Chang *et al.*, 2011), where the entire spectrum was centered at very small wavenumbers. This begs the question, if an inverse cascade can occur in nature, how likely is it to occur. Furthermore, between the forward and inverse cascade, which mechanism dominates the dynamics of solar wind turbulence and ultimately dictates the configuration of energy in the solar wind.

References

- Chang, O., S. P. Gary, and J. Wang (2011), Whistler turbulence forward cascade: Three-dimensional particle-in-cell simulations, *Geophys. Res. Lett.*, *38*, L22102
- Chang, O., S. P. Gary, and J. Wang (2013), Whistler turbulence at variable electron beta: Three-dimensional particle-in-cell simulations, *J. Geophys. Res.*, *118*, 2824, doi:10.1002/jgra.50365
- Wang, J., P. Liewer, and V. Decyk (1995), 3D electromagnetic plasma particle simulations on a MIMD parallel computer, *Comput. Phys. Commun.*, *87*, 35
- Wareing, C.J., and R. Hollerbach (2010), Cascades in decaying three-dimensional electron magnetohydrodynamic turbulence, *J. Plasma Phys.*, *76*, 117
- Zhou, Y., W.H. Matthaeus, and P. Dmitruk (2004), Magnetohydrodynamic turbulence and time scales in astrophysical and space plasmas, *Revs. Mod. Phys.*, *76*, 1015

Nonlinear Electric Field Feedback During an Intense Geomagnetic Storm

Roxanne M. Katus

University of Michigan, Ann Arbor, MI 48105

Ruth M. Skoug

Los Alamos National Laboratory, Los Alamos, NM 87545

Abstract

The role of nonlinear feedback associated with the spatial configuration of the hot ions in the inner magnetosphere was examined during an intense geomagnetic storm that occurred on June, 1, 2013. This examination was conducted using the Van Allen Storm Probe data. HOPE proton fluxes in the 1-40 keV range were used to identify the peak in plasma pressure. Both Van Allen Storm Probe EMFISIS data and IGRF magnetic field model data were used to investigate the magnetic field perturbation in terms of the pressure peak. The EFW instrument was used to investigate the electric field perturbations linked to the peak in plasma pressure. Approaching Apogee, the Van Allen Probes takes up to an hour to pass through a pressure peak. Therefore, to remove the high-frequency oscillations the electric field was averaged over several minutes, revealing the longer perturbations related to the pressure peak. While the fluxes indicate that the satellite is passing through a peak in pressure, the magnetic field perturbation shows the location pressure extrema relative to the location of the spacecraft. The results are used to test the theory that an azimuthally localized pressure peak should create a systematic and predictable small-scale reconfiguration of the electric field. The reconfiguration of the electric field is caused by the field –aligned currents near each end of the high-pressure region closing through ionospheric Pedersen currents. The magnitude of this reconfigurations, relative to the expected dawn-dusk electric field within the magnetosphere, indicates the intensity of the nonlinear feedback.

Keywords: Inner magnetosphere, Electric fields, Ring current

1. Introduction

Space weather is a term used to describe both the state of the near-Earth space environment and its effect on humanity. Space weather forecasting is important because the effects of geomagnetic disturbances on life and technology can be significant. The reliability of space weather forecasting depends on a combination of data and models to explain the physical phenomena and safeguard global economic investments. Predicting the response to space weather events will protect satellites, power grids, and the health of individuals.

One extreme example of the potential of space weather to affect human life is the Hydro Quebec blackout. The event resulted from a large geomagnetic storm that occurred in March of 1989. Hydro Quebec's electric transmission system collapsed in less than two minutes. This caused the transformers to draw a tremendous surge in reactive power from the grid, which in turn led to the long high voltage lines to carry far less than load and left six million people without power [Czeck *et al.*, 1992].

All geomagnetic storms start with activity on the Sun such as solar flares. The solar activity then causes propagation of magnetized plasma structures in the solar wind. The solar wind flow then interacts with the Earth's magnetosphere and produces a disturbance in near-Earth space [Gonzalez *et al.*, 1994]. During a disturbance, particles are convected earthward from the tail of the magnetosphere. This convection causes a region of high particle pressure centered at local midnight. The region of high particle pressure then extends towards dusk by

gradient curvature drifting particles. Near the furthest extending magnetic local time (MLT) ends of this high-pressure region, field aligned currents (FAC) extend into and out of the ionosphere. These FAC change the electric potential causing a peak and well. These potential peaks and wells then cause localized electric fields. The localized electric fields and the Earth's internal magnetic field then cause the particles to ExB drift around the FAC regions. This process was described in Liemohn et al., [2008] using the cartoon shown in Figure 1. In this figure the high particle pressure region is described in light blue, the FAC regions are shown in dark blue, the electric fields are designated by green arrows, the ExB drift is presented as dashed arrows, and the internal magnetic field is assumed to point out of the page.

To better understand this theoretical model of inner magnetosphere dynamics, assume that the high particle pressure region in Figure 1 is rotated so that it is centered at local midnight. Flying a satellite through the middle of this idealized model would produce the idealized results shown in Figure 2. This figure shows the idealized pressure, electric field, and magnetic perturbation from a satellite cutting through the center of the pressure peak. The normalized y-component of the electric field from the cross tail potential drop is reversed locally (in the high pressure region). The red and blue curves in Figure 2 show what the decrease is expected to look like for weak and strong non-linear feedback. The decrease may be just a small perturbation on the cross tail field or the perturbation might be a complete reversal of the cross tail field.

A satellite flying through the edge of the high-pressure region of the theoretical model would be expected to see the reversed E_y perturbation to that shown in Figure 2. The cross-tail E_y would be enhanced depending on the spacecraft's location relative to the potential extrema and the level of nonlinear feedback. The result might be a weak or significant increase in the dawn-dusk field.

A satellite flying through the FAC regions would be expected to undergo a systematic twist in E_y as the E_y is deflected in the x-direction. The deflection would begin in one direction and then switch to the other.

If the high-pressure region is not centered at midnight all of these relationships are rotated. The feedback electric field no longer aligns with the cross-tail electric field. But we can still draw a simple picture similar to Figure 2. The magnetic perturbation in the z-direction should be related to the pressure (and current). The idealized normalization is shown in Figure 2 (internal field removed). The shape and magnitude of this perturbation should be largest at the pressure peak. This perturbation should ultimately tell us something about the types of currents flowing nearby.

The hazard posed by geomagnetic disturbances has led scientists to develop several important models used to study and predict space weather effects. In this study, we compare the theoretical model of inner magnetospheric behavior to measurements from the Van Allen Storm Probes. The comparison is then used to assess the role of nonlinear feedback associated with the spatial configuration of the hot ions in the inner magnetosphere during an intense geomagnetic storm.

2. Data

The study of space weather requires several regional data sets and indices to characterize the state of the magnetosphere. A geomagnetic storm can be defined using the decrease in the north-south component (H) of the terrestrial magnetosphere at low to middle latitudes [Iyemori, 1990]. These events are attributed to solar wind driven particle injection into the inner magnetosphere that causes intensification of near Earth space currents. The hour average of four low-to-middle latitude magnetometers, approximately equally spaced in local time, is used to calculate the disturbance storm time index (Dst). This index is well correlated to solar wind parameters [e.g., Burton et al., 1975; O'Brien and McPherron, 2000] and the total energy content of the ring current [Dessler and Parker, 1959; Sckopke, 1966; Greenspan and Hamilton, 2000; Turner et al., 2001; Liemohn and Kozyra, 2003; Jorgensen et al., 2004]. Thus, Dst is used to describe the magnetospheric response to changes in the solar wind [Gonzalez et al., 1994]. Its evolution characterizes the progression of solar wind and geomagnetic activity. This relationship can be seen by considering the storm sudden commencement, which is identified by a rapid rise in Dst associated with a sharp increase in solar wind dynamic pressure. Furthermore, a large southward interplanetary magnetic field (IMF) is a critical element in driving the main phase of a disturbance, which is also reflected in Dst.

The Van Allen Storm Probes provide measurements required to describe and quantify the plasma processes in the inner magnetosphere. The two Van Allen Probe spacecraft have nearly identical orbits with perigee near 700 km and apogee near 5.8 R_E . The probes in-situ measurements provide data about the particle flux for a large range of energies, the magnetic field, electric field, and more. In this study, we examine the particle flux using the Helium, Oxygen, Proton, and Electron (HOPE) mass spectrometer, which provides measurements over 1 eV to 50 keV energies. The magnetic field is examined using the Electric and Magnetic Field Instrument Suite and Integrated Science (EMFISIS) but the electric field data will be used from the Electric Field and Waves Suite (EFW). The

electric field data is smoothed using a moving average to remove high-resolution affects due to inner magnetospheric waves.

3. Results

In this study we want to compare the theoretical satellite data associated with the theoretical model of the inner magnetospheric dynamics with the actual measurements from the Van Allen Storm Probes during a moderate to intense geomagnetic event. The first step in this project was to find all of the storms that have occurred to date that overlap with the mission. This was done by searching for peaks in the Dst index less than -50 nT. The list of events was then filtered to find the storm in which the spacecraft was traveling through the region in which we would expect to see the pressure peak during the main phase of the storm. In particular, the best path for the spacecraft would have apogee near 18 MLT.

The June 1, 2013 event was chosen for this project based on the spacecraft position, storm phase, and data availability. The Dst along with several observations from and the location of the Van Allen Storm Probe A are shown in Figure 3. The top two plots in Figure 3 show that from midnight to 0600 UT on June 1, 2013 the spacecraft was moving from the dusk side of the earth towards midnight local time and away from the planet. The bottom plot shows the Dst dropping to less than -100 nT during this time. The third plot shows the proton energy-flux spectrogram, which shows all energies along the spacecraft trajectory for this time. The fourth plot from the top shows the flux for three of the higher energy channels. The fifth, sixth, and seventh plots from the top of Figure 3 show the measured and modeled magnetic field in the x, y, and z-directions. For the modeled magnetic field, we simply used the magnetic field data from the day before ($-5 \text{ nT} \leq \text{Dst} \leq 23 \text{ nT}$) at time with close mlt location. While this method is not perfect, it makes the quiet time range of the magnetic field for the spacecraft position obvious. The eighth plot from the top shows the two minute smoothed y-direction of the measured electric field.

Throughout the main phase of the storm, the z and y-components of the terrestrial magnetic field are below the quiet time value while the y-component is enhanced. Examination of the proton energy flux spectrogram and the three energy channels show several enhancements. The first enhancement is the most obvious. The enhancement begins at low energy (around 01:20 UT) then abruptly increased in all energies (around 01:48 UT). Additional large enhancements in high energies occur around 02:20 UT, 03:10 UT, 05:15 UT, and 05:50 UT. During each of these times, the electric field is increased and then quickly drops significantly. This is consistent with what would be expected from a satellite flying through the FAC regions. That is, we see systematic twists in the y-component of the electric field as the field is deflected in the x-direction.

4. Conclusions

In this study we examined the spatial structure of hot ions in the inner magnetosphere during the intense geomagnetic storm that occurred on June 1, 2013 using Van Allen Storm Probe data. The date is particularly significant when considering this meant the data was about a month old at the time and not all of the instruments were providing data (or data in a reasonable coordinate system) that quickly. Throughout the study, I learned a lot about the satellite as well as the data quality, processing, and availability. While the work was often very frustrating, it was also very rewarding and I am very grateful for the opportunity.

Using the June 1 storm we examined the localized electric field disturbance from the EFW instrument in relationship to the plasma pressure peak as identified by the HOPE fluxes as well as the magnetic field perturbations from EMFISIS. Near apogee, the Van Allen Probes take 30 to 60 minutes to traverse a ion flux peak. Therefore, the electric field was averaged over several minutes to remove the higher-frequency wave oscillations, revealing the loner baseline perturbations associated with the pressure peak. The y-component of the electric field was found to have a systematic sinusoidal perturbation. While the fluxes indicate that the satellite is passing through a pressure peak, the magnetic field perturbation reveals the spatial location of the pressure extrema relative to the spacecraft location.

The electric field pattern relative to the location of the plasma pressure peak is in agreement with the hypothesis based on theory that an azimuthally localized pressure peak should create a systematic and predictable small-scale reconfiguration of the electric field. The modification in the electric field is caused by the field-aligned currents near each end of the pressure crescent and close via Pedersen currents, perturbing the electric field in this region, as regulated by the ionospheric conductance. The level of this reconfiguration, relative to the expected dawn-dusk electric field within the magnetosphere, indicates the intensity of the nonlinear feedback.

References

- Czech, P., S. Chano, H. Huynh, and A. Dutil (1992). The Hydro-Québec system blackout of 13 March 1989: system response to geomagnetic disturbance, *EPRI Report*. 100450.
- Liemohn, M. W., J.-C. Zhang, M. F. Thomsen, J. E. Borovsky, J. U. Kozyra, and R. Ilie, (2008) Superstorms at geosynchronous orbit: how different are they?, *Geophys. Res. Lett.*, **35**, L06S06, doi: 10.1029/2007GL031717.
- Burton, R. K., R. L. McPherron, and C. T. Russell (1975), An empirical relationship between interplanetary conditions and Dst, *J. Geophys. Res.*, **80**(31), 4204–4214, doi:[10.1029/JA080i031p04204](https://doi.org/10.1029/JA080i031p04204).
- O'Brien, T. P., and R. L. McPherron (2000), An empirical phase space analysis of ring current dynamics: Solar wind control of injection and decay, *J. Geophys. Res.*, **105**(A4), 7707–7719, doi:[10.1029/1998JA000437](https://doi.org/10.1029/1998JA000437).
- Dessler, A. J., and E. N. Parker (1959), Hydromagnetic Theory of Geomagnetic Storms, *J. Geophys. Res.*, **64**(12), 2239–2252, doi:[10.1029/JZ064i012p02239](https://doi.org/10.1029/JZ064i012p02239).
- Scopke, N. (1966), A general relation between the energy of trapped particles and the disturbance field near the earth, *J. Geophys. Res.*, **71**(13), 3125–3130, doi:[10.1029/JZ071i013p03125](https://doi.org/10.1029/JZ071i013p03125).
- Greenspan, M. E., and D. C. Hamilton (2000), A test of the Dessler-Parker-Scopke relation during magnetic storms, *J. Geophys. Res.*, **105**(A3), 5419–5430, doi:[10.1029/1999JA000284](https://doi.org/10.1029/1999JA000284).
- Iyemori, T. (1990) Storm-time magnetospheric currents inferred from mid-latitude geomagnetic field variations, *J. Geomag. Geoelectr.*, **42**, 1249-1265.
- Turner, N. E., D. N. Baker, T. I. Pulkkinen, J. L. Roeder, J. F. Fennell, and V. K. Jordanova (2001), Energy content in the storm time ring current, *J. Geophys. Res.*, **106**, 19,149–19,156, doi:[10.1029/2000JA003025](https://doi.org/10.1029/2000JA003025).
- Liemohn, M. W., and J. U. Kozyra (2003), Lognormal form of the ring current energy content, *J. Atmos. Solar-Terr. Phys.*, **65**, 871.
- Jorgensen, A. M., H. E. Spence, W. J. Hughes, and H. J. Singer (2004), A statistical study of the global structure of the ring current, *J. Geophys. Res.*, **97**, A12204, doi:[10.1029/2003JA010090](https://doi.org/10.1029/2003JA010090).
- Gonzalez, W. D., J. A. Joselyn, Y. Kamide, H. W. Kroehl, G. Rostoker, B. T. Tsurutani, and V. M. Vasyliunas (1994), What is a Geomagnetic Storm?, *J. Geophys. Res.*, **99**(A4), 5771–5792, doi:[10.1029/93JA02867](https://doi.org/10.1029/93JA02867).

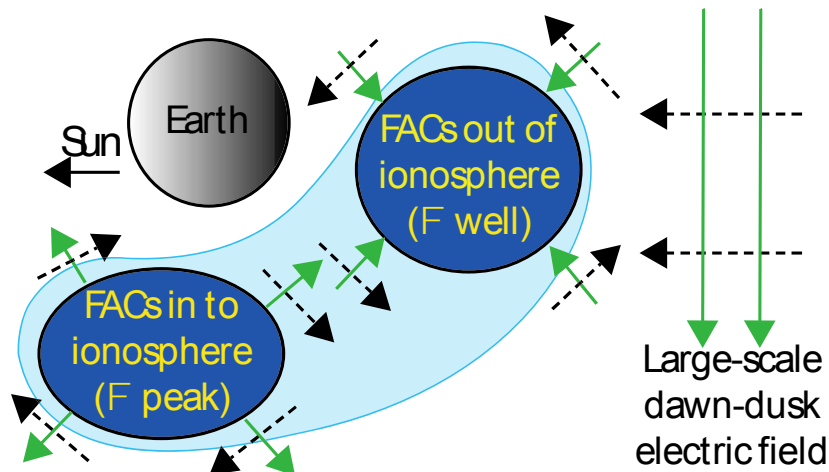


Figure 1: Cartoon model of the equatorial inner magnetospheric dynamics from Liemohn et al., 2008

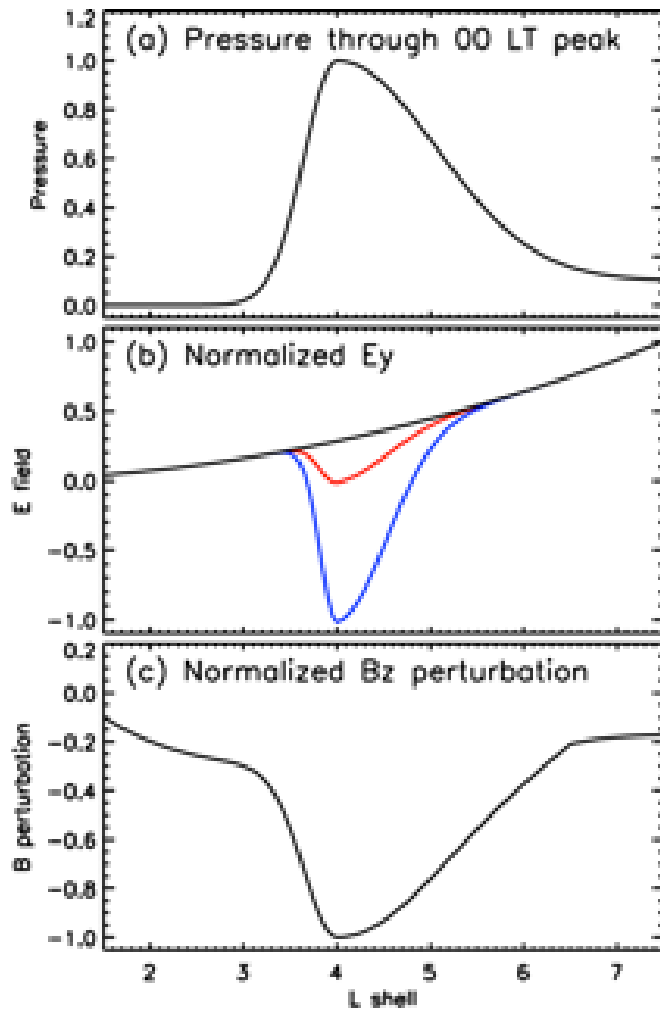


Figure 2: Idealized satellite data measured cutting through the center of the inner magnetosphere's hot ion pressure peak.

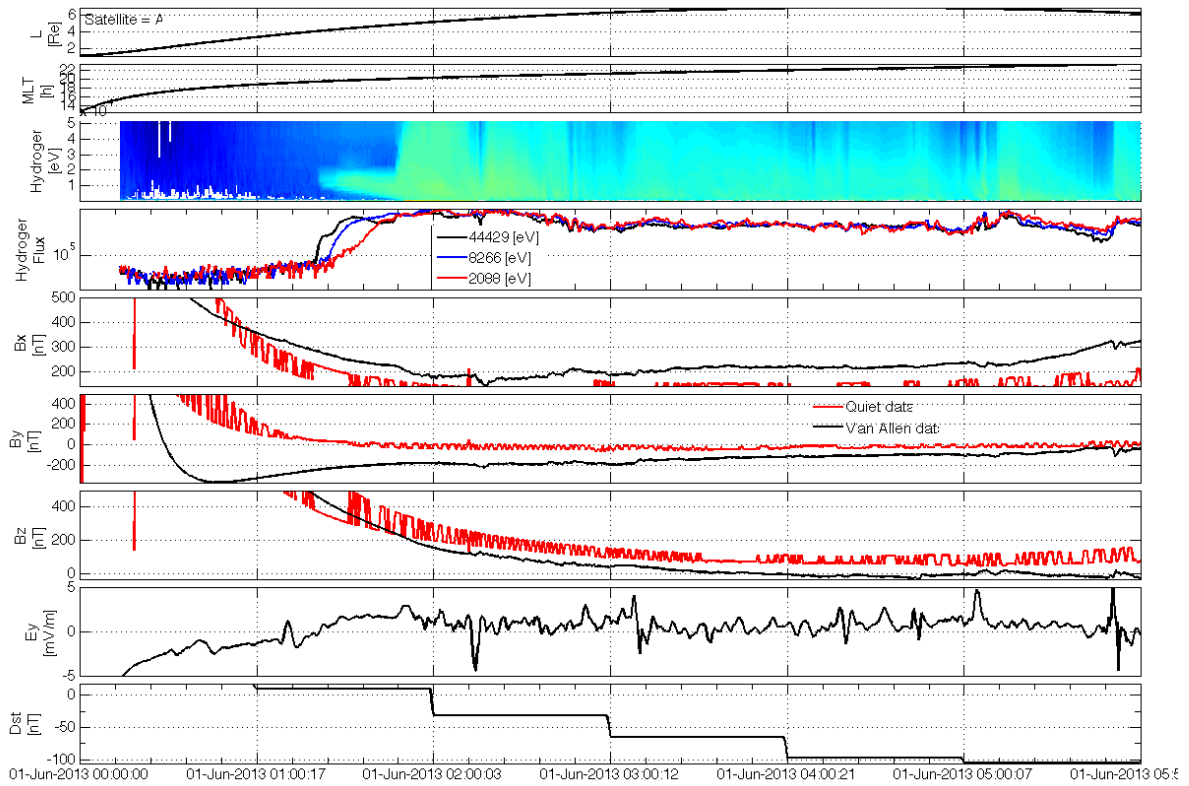


Figure 3: Dst and several measurements from the Van Allen Storm Probes instruments throughout the June 1, 2013 geomagnetic storm. The top two plots show the spacecraft position in Lshell and MLT. The third and fourth plots show the proton flux at range of HOPE energies throughout the event. The fifth, sixth, and seventh plots show the measured and expected range of magnetic field in the x, y, and z-direction, respectively. The eighth plot shows the y-component of the electric field measured by the EFW instrument.

Localized Density Prediction using a Neural Network based model

David Pérez

Rensselaer Polytechnic Institute, Troy, NY 12180

Brendt Wohlberg

Los Alamos National Laboratory, Los Alamos, NM 87545

Michael Shoemaker

Los Alamos National Laboratory, Los Alamos, NM 87545

Thomas Alan Lovell

Air Force Research Laboratory, Albuquerque, NM 87116

Abstract

At low Earth orbits, drag force is the greatest source of error for propagating the motion of spacecraft. The main factor driving the changes on the drag force is the neutral density. Global atmospheric models provide estimates for the density; although, such results are significantly affected by bias due to misrepresentations of the underlying physics and limitations on the statistical models. In this work a localized predictor based on a neural network is presented. Such predictor uses density measurements or estimations and a set of proxies for solar and geomagnetic activities to predict the value of the density along the future orbit of the spacecraft. The performance of the localized predictor is studied for different neural network structures, testing periods of high and low solar and geomagnetic activities and different prediction windows.

Keywords: Thermospheric Density, Modeling, Neural Networks

1. Introduction

At low Earth orbits (LEO), after gravity, atmospheric drag is the most significant force acting on spacecraft, and given that it is not easy to estimate, it constitutes the largest source of error on force models. The drag force itself is a function of several time varying factors, such as atmospheric winds, drag coefficient and density. However, the largest variations in the drag force are caused by changes in the atmospheric density, as the spacecraft flies through different regions of the thermosphere with different densities, and as the density itself fluctuates with the solar and geomagnetic activities. Consequently, precise models for the density are necessary for accurately estimating the drag force which in turn is necessary for precise onboard determination. Reliable onboard orbit determination will be a key factor in the development of better methods for maneuver planning and coverage calculations. Furthermore in the last 30 years starting with the work of Leonard et al. [1989] there has been an increasing body of work focusing on using the drag force for maneuvering spacecraft in LEO [Maclay and Tuttle, 2005; Kumar and Ng, 2008; Perez and Bevilacqua, 2012, 2013]. Accurate onboard estimation of the density can be used to improve some of the methods proposed for maneuvering with the drag force, since it will provide the controllers with an accurate estimate of the control force. In this work a localized predictor for the density along the future orbit of the spacecraft is developed and tested using density values estimated from accelerometers.

Email addresses: perezd3@rpi.edu (David Perez), brendt@lanl.gov (Brendt Wohlberg), shoemaker@lanl.gov (Michael Shoemaker), thomas.lovell@kirtland.af.mil (Thomas Alan Lovell).

Over the last 50 years several different global atmospheric models have been developed for calculating the main characteristics of the thermosphere including density. Global models can be classified into empirical and physics based models. The seminal work for empirical global atmospheric models is Jacchia 1960 model [Jacchia, 1960] which uses measurements from satellites and statistical methods to generate estimations of the density. Further improvements of this approach include Jacchia models 1971, 1977 [Jacchia, 1971, 1977] up to Jacchia-Bowman 2006 and 2008 (JB2006, JB2008, see Bowman et al, 2008, 2008a). The High Accuracy Satellite Drag Model (HASDM) uses calibration data from up to 75 inactive satellites and the Dynamic Calibration Atmosphere method to correct older models such as the Jacchia models [Storz et al., 2002]. Another highly used empirical global model is MSIS-86, which was part of the COSPAR International Reference Atmosphere (CIRA) 1986 [CIRA, 1988]. MSIS-86 uses data from satellites and also from and data from incoherent scatter radars to estimate density among other things. Several improvements to the original MSIS from 1986, have been made including MSISE-90 [Hedin, 1991] and the NRLMSISE-00 developed by the US Naval Research Laboratory [Picone et al., 2002]. Global circulation models (physics based models) are an alternative for obtaining density estimations to the global empirical models. Among these physics based models there the Global Ionosphere Thermosphere Model (GITM, Ridley et al., 2006), developed at the University of Michigan. GITM consists of a three dimensional spherical code that solves the energy, momentum and continuity equations among other things.

Global atmospheric models are designed to estimate much more than just the density. Furthermore, the physics can be misrepresented in the case of the physical models and the data used for generating the empirical ones is still limited. These three factors results in errors in the estimation of the density and make forecasting the density even more difficult. Furthermore, the physics based models are computationally expensive and require several real-time inputs which hamper onboard calculations. For this reasons it is desirable to use a different approach for designing a density predictor capable of running onboard.

An alternative originally proposed by Stastny et al. [2009] is a localized density model. Such approach consists on limiting the model to estimate only the density along the orbit of a single spacecraft. By introducing these restrictions the ability of the model for accurately estimating the density is greatly enhanced. Provided that measurements or estimations of the density of the medium around the spacecraft are available on-board, time series forecasting techniques can be used to predict what the density is going to be along the future orbit of the spacecraft. In his work Stastny et al. [2009] used a linear model as the predictor and showed that such model provided accurate results and with less bias than two of the latest empirical models HASDM and JB2006 for predicting one orbit into the future.

In this work a similar approach to that of Stastny et al. [2009] is used. However, instead of using a linear model as the predictor, a neural network is used. The neural network is capable of forecasting nonlinear behavior since it contains nonlinearities in its neurons, and therefore it is expected to give better results at modeling the nonlinear behavior of the density along the orbit of the spacecraft. To train, validate and test the neural network, density data from the CHALLENGING Minisatellite Payload [Reigber et al., 2002] mission was used.

The results of this work plus some additional results have been submitted by the authors for publication at Acta Astronautica.

2. Methodology

2.1. Neural Networks

A time-delay feed-forward neural network structure was chosen for the development of the density predictor. This neural network architecture contains a set of delays at the input layer that allow for retention of the evolution of the inputs in time, and enhances the ability of the network for forecasting applications. Furthermore, the neural network predictor contains two layers (hidden or input layer, and output layer). The output layer contains one single linear neuron. The number of neurons and delays in the hidden layer were determined by testing different configurations. Figure 1 shows a Simulink block diagram for a time-delay feed-forward neural network with two delays and three neurons in the hidden layer.

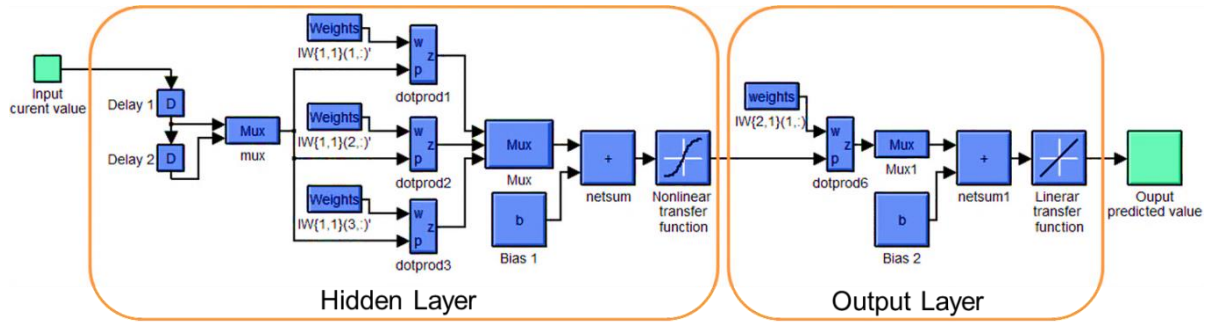


Figure 1: Simulink model for a time-delay feed-forward neural network with two layers, two delays, three nonlinear neurons in the hidden layer and one linear neuron in the output layer

In the context of density prediction, the input to the neural network is the present value of the density and the output is the predicted value over a predefined prediction window. Additional inputs such as the current values of the solar and geomagnetic indices (Dst and F10.7) can also be included. For purposes of inputting past density values, the inputs are delayed a defined number of times inside the neural network in order to capture some of their evolution in time. Such formulation is shown in the following expression:

$$(1) \quad \hat{y}(t + W_p) = g \left(\begin{array}{c} x(t - t_s), \dots, x(t - Dt_s), \\ DST(t - t_s), \dots, DST(t - Dt_s), \\ F_{10.7}(t - t_s), \dots, F_{10.7}(t - Dt_s) \end{array} \right), x = \ln(\rho), \hat{y} = \ln(\hat{\rho})$$

where g is the overall nonlinear function of the neural network, ρ is the measured density, $\hat{\rho}$ is the predicted density value (neural network output), W_p is the prediction window, t_s is the sampling period of the data, t is the time, and D is the number of delays in the hidden layer.

The Levenberg-Marquardt algorithm [Levenberg, 1944 and Marquardt, 1963] was used to train the neural networks. This algorithm, which is included in MATLAB's Neural Network Toolbox [The MathWorks, 2013] was chosen since it often has higher rates of convergence than the other algorithms provided in the Toolbox. This method solves the least squares problem (in this case it finds the weights that minimize the performance function) using regularization, by interpolating between Newton's and gradient descent methods, thus providing some of the robustness of gradient descent and some of the speed of convergence of Newton's method. The mean squared error (MSE), as explained in Eq(2), was selected as the performance function.

$$(2) \quad MSE = \frac{1}{n} \sum_{i=1}^n (\hat{y}_i - x_i)^2$$

2.2. Data used

The use of neural networks requires data sets for training, validation, and testing the model's performance. The training and validation sets must contain data covering the different behaviors to be modeled by the neural network. The CHAMP satellite was equipped with high precision accelerometers. CHAMP was launched in 2000 into a circular, almost polar orbit with an initial altitude of 460km. Sutton presented a method for estimating density and winds [Sutton et al., 2007] from accelerometers such as the ones included in CHAMP. The estimated density from CHAMP, which was used for this work, is available online. The density data used were obtained from Forbes et al. [2013].

For each neural network the training density data was divided into two segments: one segment of past values, assumed to be available for the training and validation of the neural network; and one segment of future values, which are values of density that would not be available during training and validation, but instead are used exclusively for testing the neural networks. The past values were sampled randomly and 70% were used for training, and the remaining 30% for validation. Furthermore, the available density data were not evenly distributed in time, therefore, for implementing the neural network, a linear interpolation was applied to make sure that there was a constant difference in time between consecutive samples in the data. The values of the density are in the order of magnitude of 10^{-12} kg/m³ for day 140 of 2002 (see Figure 2). This results in numerical problems during the training of the neural networks. To address this issue, the natural logarithm of the density values was used for the neural networks instead of the density values themselves. Another advantage of using the natural logarithm shown by

Lütkepohl and Xu [2012] is that it often stabilizes the variance of the series, which allows for better modeling of the time series.

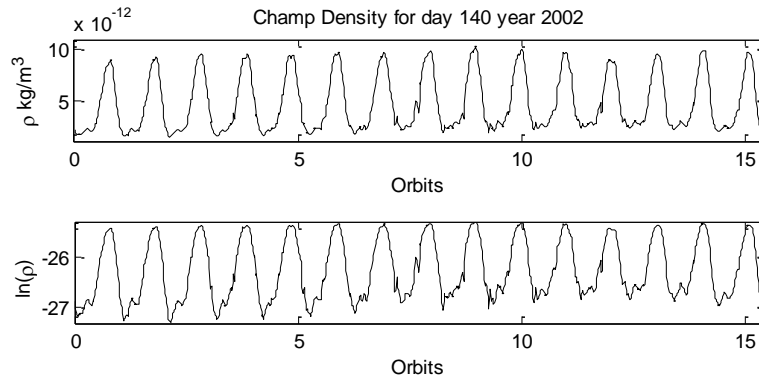


Figure 2: Density (top) and natural log of density (bottom) from CHAMP day 140 of 2002

Several different periods of interest for training, validation, and testing the neural networks were identified. Stastny et al. [2009] chose two representative days for low and high geomagnetic activities for testing his linear model and for comparing it to JB2006 and HASDM. The first of these days was day 141 of 2002; during this day there was very low geomagnetic activity ($Dst=-16$, $ap=10$ and $F10.7=190.4$). The second day used by Stastny et al. [2009] was day 276 of 2001; during this day a moderate geomagnetic storm occurred, so there was a higher geomagnetic activity ($Dst=-107$, $ap=69$ and $F10.7=191.8$). For obtaining the linear model, Stastny et al. [2009] used the data from day 140 ($Dst=-12$, $ap=10$ and $F10.7=175.4$). This same data set was used to train, validate and test the neural networks. These data sets included $n=1080$ data points for each day with a sampling rate of 80 sec.

To study the longterm performance of the neural networks, it was decided to test them over one-year intervals. Out of the years that CHAMP was collecting data, years 2003 and 2007 were certainly very interesting from the point of view of space weather and therefore were selected for testing. During 2003 ($Dst=-22$, $ap=128$ and $F10.7=21.8$) the geomagnetic activity was the highest of that solar cycle [Belov et al., 2004]. In contrast, during 2007 ($Dst=-8$, $ap=73$ and $F10.7=7.5$) the solar cycle went through a period of very low activity (solar minimum, see Belov et al [2009]) and therefore the solar and geomagnetic activities were very low. Data from 2002 was used to train and validate the neural networks tested on 2003, and data from 2006 was used to train and validate the neural network tested on 2007. For these longterm experiments, the density data sets included $n=3152812$ data points for each year with a sampling rate of 120 sec. When only using the density values, the input vector includes the density at each sample time, while, when using the external inputs, it is made of the density vector, the Dst vector, and the $F10.7$ vector.

By including additional inputs other than the known present values (in this case the density values), the performance of a neural network as a predictor improves, provided that the output of the neural network is a function of these inputs. Because the density is driven by the solar and geomagnetic activities, the Dst and $F10.7$ indices were selected as additional inputs. The indices were averaged hourly and were included in the corresponding training, validation, and testing sets (of 1080 and 3152812 data points for the one day and one year data sets respectively). For the one orbit prediction case at a sampling rate of 80 seconds, 68 samples per window are used; for the eight orbits case at a sampling rate of 120 seconds, 360 samples per window are used; and for the 32 orbits case at a sampling rate of 120 seconds, 1440 samples per window are used. As with the density values, during operation the neural networks only have access to present values of the indices. The values for the Dst and $F10.7$ indices used in this work were obtained from Papitashvili [2013].

3. Results

The training, validation, and testing of the neural networks was done in MATLAB using the Neural Network Toolbox [The MathWorks, 2013]. As a benchmark for all the tests, a model using the persistence method was used. The persistence method is a very simple technique for forecasting in which the prediction is equal to the input.

To assess the performance of the different models, different metrics were used: the MSE (shown in Eq. (2)), the mean of the ratio between the target and the outputs, its standard deviation (shown in Eqs.(3) and (4)) and the Pearson correlation coefficient of the targets to the model outputs (shown in Eq.(5)). The former two were the metrics used by Stastny et al. [2009], and therefore allow comparing the results of this work to his.

$$(3) \quad \bar{r} = \frac{1}{n} \sum_{i=1}^n r_i, \quad r_i = \frac{x}{\hat{y}_i}$$

$$(4) \quad s_r = \left(\frac{1}{n-1} \sum_{i=1}^n (r_i - \bar{r})^2 \right)^{1/2}$$

$$(5) \quad R = \frac{\frac{1}{n-1} \sum_{i=1}^n (x_i - \bar{y})(\hat{x}_i - \bar{y})}{s_{\hat{p}} s_{\rho}}$$

Where $s_{\hat{p}}$ and s_{ρ} are the standard deviations of the neural network outputs and targets, respectively.

Given the selected structure of the neural network predictors, the appropriate number of neurons and delays in the hidden layer, for the localized density forecasting problem were found. This was accomplished empirically by trying different combinations. All the tests performed for this purpose were run on days 141 of 2002 and 276 of 2001, with the training and validation sets being day 140 of 2002. Again, these days cover high and low geomagnetic activity and were used also by Stastny et al. [2009] to test his linear model.

To find the appropriate number of neurons in the hidden layer several tests were performed in which all the other parameters were fixed and the number of neurons was varied. The prediction window was set to one orbit into the future; 17 delays (1/4 of the prediction windows) and a sampling rate of 80 sec were used. The results for these tests are summarized in the following table.

Table 1: Neural network performance for different number of neurons in the hidden layer (bold for best results, italics for worst)

| Testing Data Set | Model Configuration | MSE | R | Mean target/output \bar{r} | Stdev target/output s_r |
|--------------------|---------------------|--------------|--------------|------------------------------|---------------------------|
| Day 141 2002 CHAMP | Persistence Model | 0.023 | 0.969 | 1.0003 | 0.0058 |
| | 1 Neuron | 0.016 | 0.977 | 1.0008 | 0.0046 |
| | 5 Neurons | 0.016 | 0.98 | <i>1.0011</i> | 0.0046 |
| | 10 Neurons | 0.016 | 0.979 | 1.0007 | 0.0047 |
| | 50 Neurons | 0.016 | 0.979 | 1.0006 | 0.0047 |
| | 150 Neurons | <i>0.026</i> | <i>0.965</i> | 1.0001 | <i>0.0059</i> |
| Day 276 2001 CHAMP | Persistence Model | 0.033 | 0.872 | 1.0001 | 0.0070 |
| | 1 Neuron | 0.023 | 0.911 | 0.9995 | 0.0058 |
| | 5 Neurons | 0.025 | 0.907 | 0.9999 | 0.0058 |
| | 10 Neurons | 0.037 | 0.891 | 0.9967 | 0.0066 |
| | 50 Neurons | 0.045 | 0.879 | 0.9963 | 0.0072 |
| | 150 Neurons | <i>0.267</i> | <i>0.743</i> | <i>0.9885</i> | <i>0.0154</i> |

As shown in Table 1 as the number of neurons is increased, the performance of the neural networks worsens. This occurs because increasing the number of neurons causes the neural network to become overtrained. For the problem of predicting density, the results included in Table 1 indicate that for the given neural network structure, having one neuron in the hidden layer gives the best results.

To find the appropriate number of delays in the hidden layer all the other parameters were fixed and the number of delays was varied. The prediction window was set to one orbit into the future, the neural networks had one neuron in the hidden layer (the best result from the previous test) and again a sampling rate of 80 sec was used. The results for these tests are summarized in the next table.

Table 2: Neural network performance for different number of delays in the hidden layer (bold for best results, italics for worst)

| Testing Data Set | Model Configuration | MSE | R | Mean target/output \bar{r} | Stdev target/output s_r |
|--------------------|----------------------|--------------|--------------|------------------------------|---------------------------|
| Day 141 2002 CHAMP | Persistence Model | <i>0.023</i> | <i>0.969</i> | 1.0003 | <i>0.0058</i> |
| | 1 delay | 0.016 | 0.978 | 1.0005 | 0.0048 |
| | 17 delays(1/4 orbit) | 0.016 | 0.977 | 1.0008 | 0.0046 |
| | 34 delays(1/2 orbit) | 0.014 | 0.982 | 1.0009 | 0.0044 |
| | 68 delays(1 orbit) | 0.015 | 0.981 | 1.0011 | 0.0045 |
| | 204 delays(3 orbits) | 0.018 | 0.978 | <i>1.0013</i> | 0.0048 |
| Day 276 2001 CHAMP | Persistence Model | 0.033 | 0.872 | 1.0001 | <i>0.007</i> |
| | 1 delay | 0.028 | 0.891 | 1.0001 | 0.0064 |
| | 17 delays(1/4 orbit) | 0.023 | 0.911 | 0.9995 | 0.0058 |
| | 34 delays(1/2 orbit) | 0.027 | 0.913 | 0.9973 | 0.0056 |

| | | | | |
|----------------------|-------|-------|--------|--------|
| 68 delays(1 orbit) | 0.028 | 0.907 | 0.9972 | 0.0058 |
| 204 delays(3 orbits) | 0.037 | 0.877 | 0.9965 | 0.0065 |

As can be observed from Table 2, the number of delays in the hidden layer significantly determines the neural network performance. Having too few delays results in underfitting, while having too many results in overfitting. The best results are obtained when the number of delays is between 17 and 68 (between ¼ and one full prediction window). It is important to note that there is not a significant difference in the performance of the neural networks when the number of delays is in this range.

One interesting result, that can be observed from Table 1 and Table 2, is that the ratio of the targets to the outputs (\bar{r}) does not seem to change significantly for all the parameters tested (number of delays and neurons, and sampling rate) even for the neural networks with the worst performance (both underfitted and overfitted). This is explained by the fact that this metric measures the bias in the model. The bias in models that use actual values as inputs, such as the neural networks, will be very small provided that the mean of the time series does not vary significantly.

3.1. Predicting one orbit into the future on days 241 of 2002 and 276 of 2001

Once the appropriate structure of the neural network was found (one neuron and enough delays to store from ¼ to one prediction window) several different neural networks were tested again on days 141 of 2002 and 276 of 2001. This was done to evaluate the improvements in performance by increasing the size of the training and validation sets from one day to a year and by using the solar and geomagnetic indices (Dst and F10.7) as additional inputs. The one year training and validation data set used for testing the networks on day 141 of 2002 contained the data from the 365 preceding days (day 140 2001 to day 14 2002). The one year training and validation data set used for testing the networks on day 276 of 2001 contained the data from year 2002 (day 1 2002 to day 365 2002), since the CHAMP data did not went back a year before day 276 2001. Even though this means that the neural network used was trained on data corresponding to the future of day 276 2001, the training data and validation data set is still different to the testing set which makes the test valid (of course for practical implementation of the neural networks the training and validation set would always be past and therefore available values). A sampling rate of 80 sec was used since it is the same used by Stastny et al. [2009]. The results of the tests for days 141 of 2002 and 276 of 2001 are summarized in the following table.

Table 3: Results for predicting one orbit into the future (bold for best results, italics for worst)

| Testing Data Set | Model Configuration | MSE | R | Mean target/output \bar{r} | Stdev target/output s_r |
|--------------------------|---|---------------|---------------|------------------------------|---------------------------|
| Day 141 2002 CHAMP | NN, preceding 365 days for Training | 0.0108 | 0.9843 | 0.9998 | 0.0039 |
| | NN, preceding 365 days for Training, Dst and $F_{10.7}$ | 0.0108 | 0.9842 | 0.9998 | 0.0039 |
| | NN, day 140 of data for Training | 0.0156 | 0.9774 | 1.0008 | 0.0046 |
| | Persistence Model | <i>0.0234</i> | <i>0.9685</i> | 1.0003 | 0.0058 |
| | Linear model* | N/A | N/A | 1.0058 | 0.0822 |
| | HASDM* | N/A | N/A | 0.8662 | <i>0.1204</i> |
| | JB2006* | N/A | N/A | <i>0.8564</i> | 0.095 |
| Day 276 2001 CHAMP | NN, year 2002 of data for Training | 0.0229 | 0.9086 | 0.9999 | 0.0058 |
| | NN, Year 2002 of data for Training, Dst and $F_{10.7}$ | 0.0225 | 0.9099 | 0.9999 | 0.0058 |
| | NN, day 140 Year 2002 of data for Training | 0.0229 | 0.9106 | 0.9995 | 0.0058 |
| | Persistence Model | <i>0.0328</i> | <i>0.8718</i> | 1.0001 | 0.007 |
| | Linear model* | N/A | N/A | 1.0094 | 0.0822 |
| | HASDM* | N/A | N/A | 0.8415 | 0.1344 |
| | JB2006* | N/A | N/A | <i>0.6471</i> | <i>0.1355</i> |

*Obtained from Stastny et al. [2009]

For the 2001 scenario, training data from 2002 is used, as Stastny et al. [2009] also did in their work. Training with future values and "predicting" past values is valid from the point of view of neural network, since the training/validation and testing data sets are still different. From the point of view of spacecraft onboard implementation this of course would be invalid, but here the purpose is just showing the neural network's performances and comparing with existing literature. The results in Table 3 indicate that the global models

(HASDM and JB 2006 results obtained from Stastny et al. [2009]) suffer from large biases in their results. This causes their performance to be much worse than the performance of all the other models including the persistence model. The neural network predictors give significantly better results than the linear model from Stastny et al. [2009], the global models, and the persistence model. For day 141 of 2002, by increasing the size of the training and validation sets, the performance of the neural networks increases; however, for day 276 of 2001 there is not a significant improvement by increasing the size of the training and validation sets nor by including the solar and geomagnetic indices. The addition of the indices does not benefit the neural networks because the number of delays (17 which corresponds to $\frac{1}{4}$ of the prediction window) cannot capture more than one value in time of the indices since the indices are averaged hourly. This might be solved by increasing the number of delays; however, they cannot be increased beyond 68 (one prediction window) since as shown in Table 2, this results in overfitting the neural network. An alternative solution would be retaining the same number of delays, but space them non-uniformly in time.

For day 141 of 2002, utilizing one years' worth of data to train and validate the neural network provided the best results. The actual output of this neural network and the targets are shown in Figure 3 along with the prediction error. For day 276 of 2001, the neural network that uses the additional inputs (Dst and $F_{10.7}$) and that was trained and validated using the data from one year yielded the best results. The actual output of this neural network, the targets, and the prediction error are shown in Figure 4.

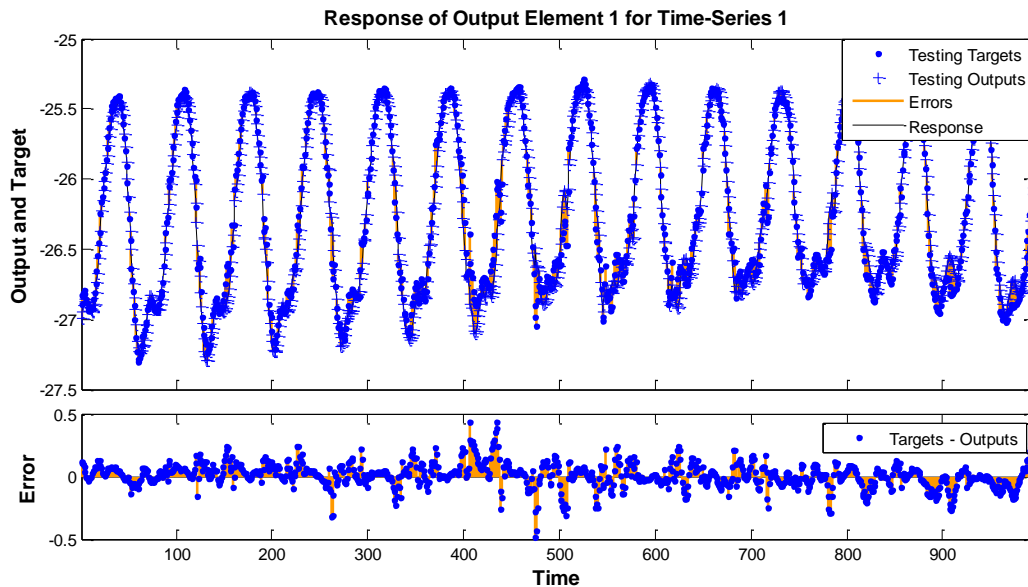


Figure 3: Neural network response for best case with a prediction window of one orbit over day 141 of 2002

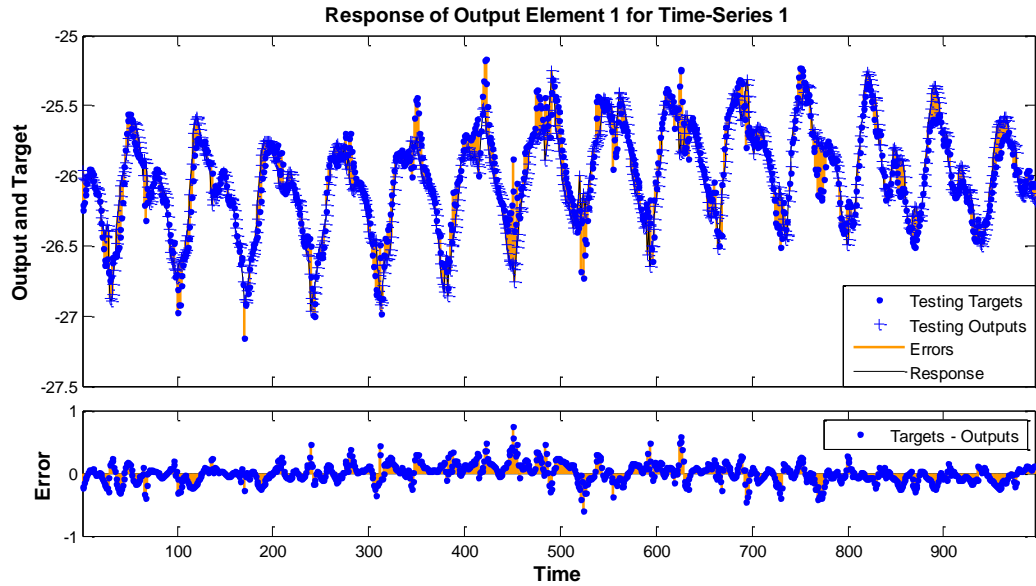


Figure 4: Neural network response for best case with a prediction window of one orbit over day 276 of 2001

3.2. Predicting eight and 32 orbits into the future

For most applications of the neural network density predictors, longer prediction windows are desired. For this reason additional neural network predictors were trained, validated, and tested for predicting eight and 32 orbits into the future (roughly half a day and two days respectively). For these results, the neural networks were tested over year 2003 for the 32 orbits prediction window and over years 2003 and 2007 for the eight orbits prediction window. This was done to evaluate their performance over much wider data sets including periods of low and high solar and geomagnetic activities. Again, the use of additional inputs (Dst and F10.7) was studied along with the use of different numbers of delays. A sampling rate of 120 sec was used in order to reduce time for training and validation the neural networks. The results are summarized in Table 4 and Table 5 for the prediction windows of eight and 32 orbits respectively.

Table 4: Results for predicting eight orbits into the future (bold for best results, italics for worst)

| Testing Data Set | Model Configuration | MSE | R | Mean target/output \bar{r} | Stdev target/output s_r |
|------------------|---|---------------|---------------|------------------------------|---------------------------|
| CHAMP 2003 | ANN, 90 delays (2 orbits), 1 year 2002 of data for Training | 0.0433 | 0.8971 | <i>1.0007</i> | 0.0078 |
| | ANN, 90 delays (2 orbits), 1 year 2002 of data and Dst and $F_{10.7}$ for Training | 0.0429 | 0.8976 | 1.0000 | 0.0078 |
| | ANN, 360 delays (8 orbits), 1 year 2002 of data and Dst and $F_{10.7}$ for Training | 0.0401 | 0.9044 | 0.9999 | 0.0075 |
| | Persistence Model | <i>0.2614</i> | <i>0.4037</i> | 1.0002 | <i>0.0192</i> |
| CHAMP 2007 | ANN, 90 delays (2 orbits), 1 year 2006 of data for Training | 0.0417 | 0.9093 | <i>1.0002</i> | 0.0075 |
| | ANN, 90 delays (2 orbits), 1 year 2006 of data and Dst and $F_{10.7}$ for Training | 0.0407 | 0.9114 | 1.0000 | 0.0074 |
| | ANN, 360 delays (8 orbits), 1 year 2006 of data and Dst and $F_{10.7}$ for Training | 0.0403 | 0.9122 | 1.0000 | 0.0074 |
| | Persistence Model | <i>0.1902</i> | <i>0.6031</i> | 1.0001 | <i>0.0160</i> |

The best case included in Table 4 for both years 2003 and 2007 were those obtained with the neural network that included the additional inputs and that had 360 delays (one prediction window). Figure 5 and Figure 6 show the MSE over the entire years 2003 and 2007 for the best cases along with the Dst and F10.7 averaged daily.

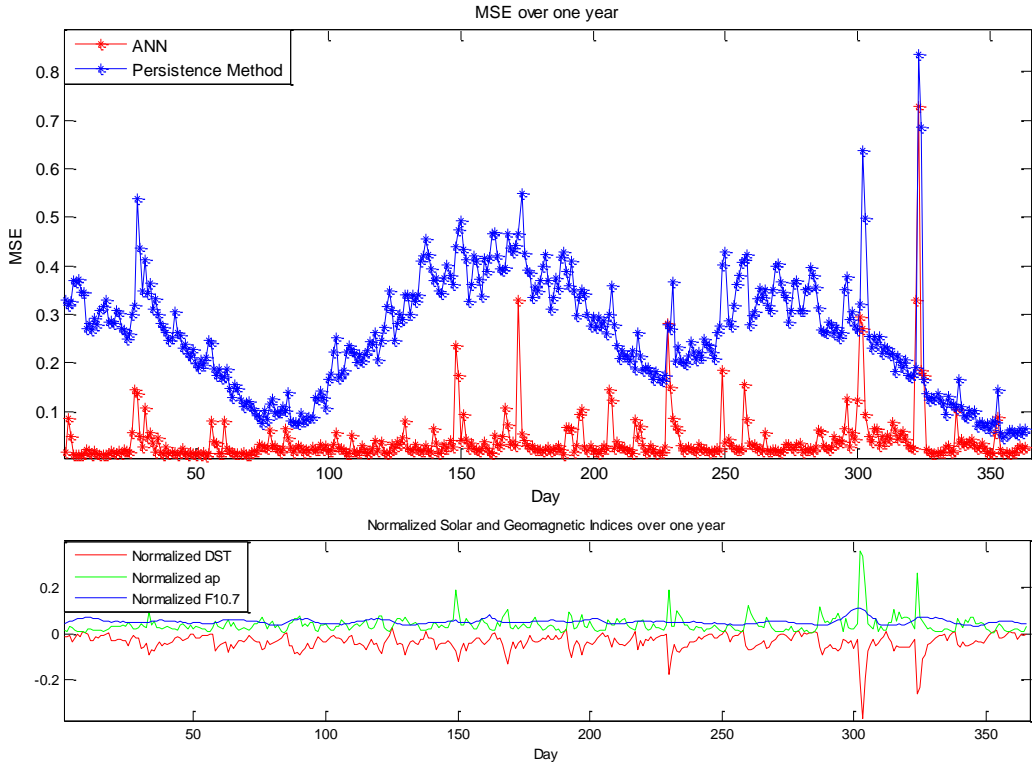


Figure 5: MSE for best case with a prediction window of eight orbits and normalized indices over year 2003

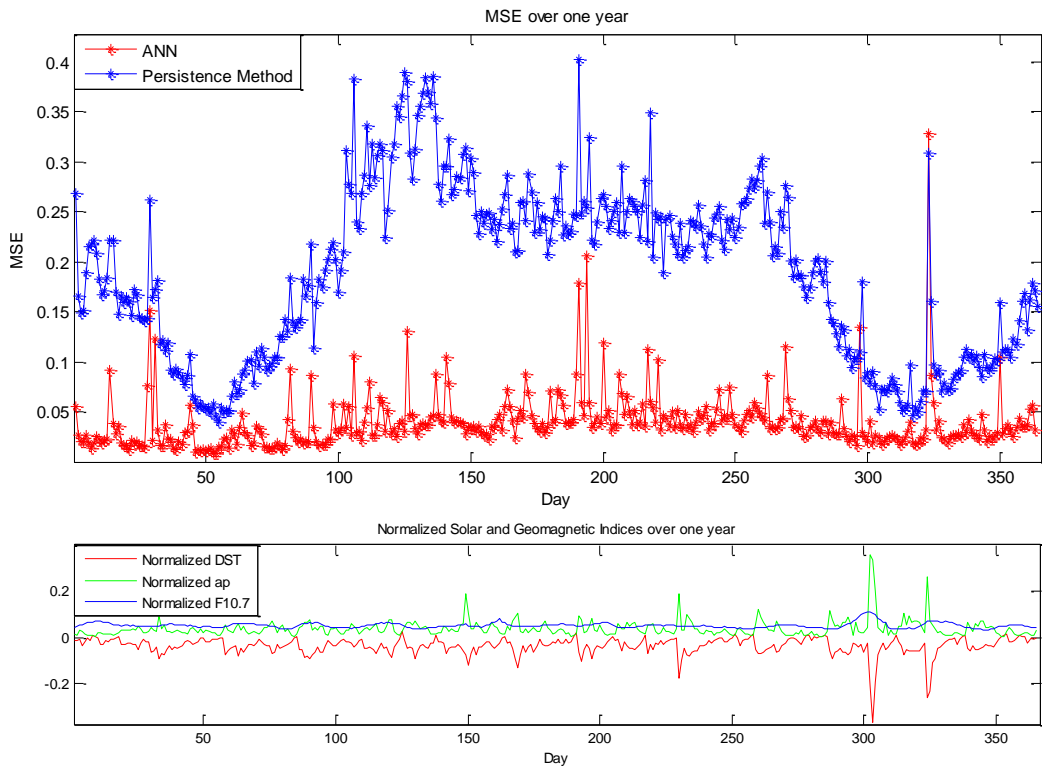


Figure 6: MSE for best case with a prediction window of eight orbits and normalized indices over year 2007

Table 5: Results for predicting 32 orbits into the future (bold for best results, italics for worst)

| Testing Data Set | Model Configuration | MSE | R | Mean target/output \bar{r} | Stdev target/output s_r |
|------------------|---|---------------|---------------|------------------------------|---------------------------|
| CHAMP 2003 | ANN, 360 delays (8 orbits), 1 year 2002 of data for Training | 0.0917 | 0.7702 | <i>1.0013</i> | 0.0113 |
| | ANN, 360 delays (8 orbits), 1 year 2002 of data and Dst and $F_{10.7}$ for Training | 0.0895 | 0.7740 | 1.0000 | 0.0112 |
| | Persistence Model | <i>0.1813</i> | <i>0.5874</i> | 1.0001 | <i>0.0160</i> |

The best case shown in Table 5 for year 2003 was obtained with the neural network that used the Dst and $F_{10.7}$ indices. The MSE over the entire year 2003 for the best case, along with the Dst and $F_{10.7}$ averaged daily are shown in Figure 7.

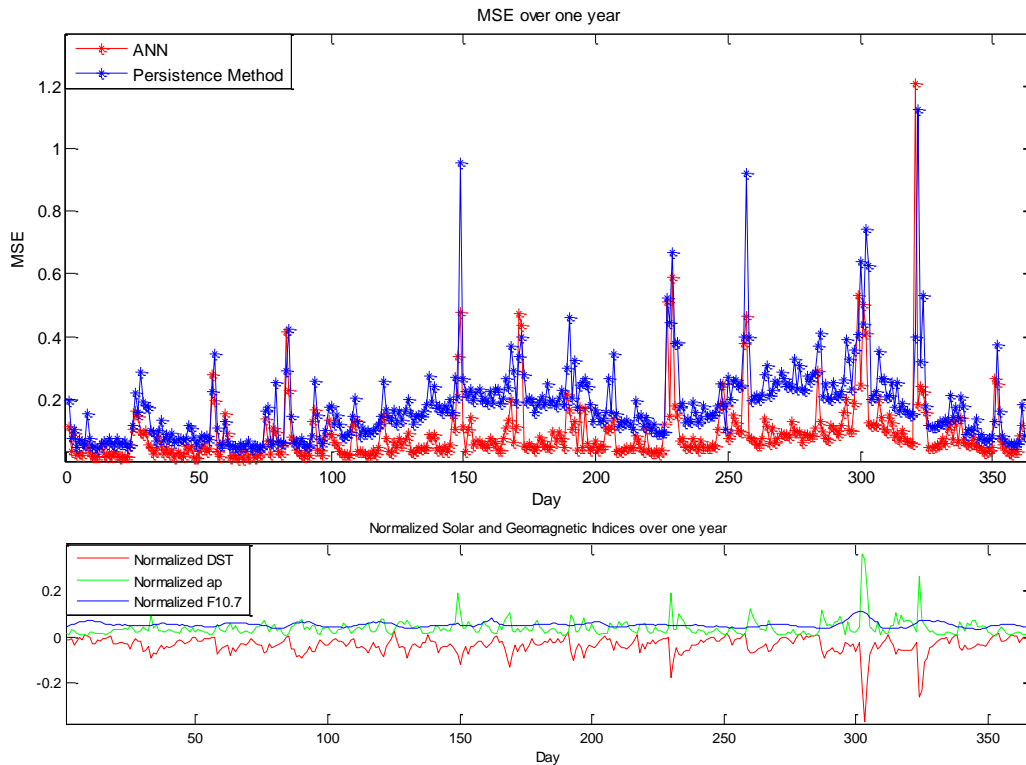


Figure 7: MSE for best case with a prediction window of 32 orbits and normalized indices over year 2003

4. Conclusions

This work introduced a localized model for atmospheric density prediction along a spacecraft’s future orbit, provided that the current density value is known. The model consists of a time-delay feed-forward neural network, with two layers: a hidden layer and an output layer. The hidden layer contains nonlinear neurons and delays that store the values of the inputs, while the output layer contains one linear neuron. The appropriate number of neurons and delays in the hidden layer and the sampling rate for the data were found empirically by testing the neural networks on two separate days of high and low geomagnetic activities. The neural networks were trained, validated, and tested using density data from the CHAMP mission.

The neural network predictors provided significantly better results than a linear model, and the global models HASDM and JB2006 for predicting the value of the density one orbit into the future for periods of high and low geomagnetic activity. The neural network predictors were also tested for predicting eight and 32 orbits into the future (about half a day and two days). For these tests the performance of the neural network predictors was evaluated over the years 2003 and 2007, which cover the periods with the highest and lowest solar and geomagnetic

activities available from the CHAMP mission. The performance of the neural network predictors decreases as the prediction window increases, but even for the 32 orbit case the results were satisfactory.

The neural network predictors can also use the current value of the Dst (geomagnetic activity) and F10.7 (solar activity) indices averaged hourly as additional inputs which resulted in an improvement of the performance of the neural networks, provided that enough delays were included in the hidden layer to store some of the behavior in time of the indices. However, the number of delays cannot be increased beyond those required to store one prediction window or the neural networks will suffer from overfitting in terms of the density values. For this reason, it is expected that the performance of the neural network predictors can be improved further by having different number of delays for the density values and the solar and geomagnetic indices. An alternative solution would be retaining the same number of delays, but space them non-uniformly in time. This will allow for storing more information of the indices in the neural network predictors, which may improve the performance during periods of high geomagnetic activity.

The neural network predictors are computationally simple and can be implemented onboard spacecraft and therefore allow for precise onboard orbit propagation at low computational cost.

References

- Leonard, C. L., Hollister, W., M., and Bergmann, E. V. "Orbital Formationkeeping with Differential Drag". *AIAA Journal of Guidance, Control and Dynamics*, Vol. 12 (1) (1989),
- Maclay, and C. Tuttle, "Satellite Station-Keeping of the ORBCOMM Constellation Via Active Control of Atmospheric Drag: Operations, Constraints, and Performance," *Advances in the Astronautical Sciences*, Vol. 120, Part I, 2005, pp.763-773. AAS 05-152.
- Kumar, B. S., and Ng, A., "A Bang-Bang Control Approach to Maneuver Spacecraft in a Formation with Differential Drag", *Proceedings of the AIAA Guidance, Navigation and Control Conference and Exhibit*, Honolulu, Hawaii, August 2008.
- Perez, D., Bevilacqua, R., "Differential Drag Spacecraft Rendezvous using an Adaptive Lyapunov Control Strategy", *Acta Astronautica* 83 (2013) 196–207 <http://dx.doi.org/10.1016/j.actaastro.2012.09.005>.
- Perez, D., Bevilacqua, R., "Spacecraft Maneuvering via Atmospheric Differential Drag using an Adaptive Lyapunov Controller", paper AAS 13-440 at the 23rd AAS/AIAA Spaceflight Mechanics Meeting, Kauai, Hawaii, February 2013.
- Jacchia, L. G., "A variable atmospheric-density model from satellite accelerations". *J Geophys. Research*, 65, 2775-2782, 1960.
- L. G. Jacchia, "Revised Static Models of the Thermosphere and Exosphere with Empirical Temperature Profiles", *Smithson. Astrophys. Obs. Spec. Rept. No. 332*, 1971.
- L. G. Jacchia, "Thermospheric Temperature, Density, and Composition: New Models", *Smithson. Astrophys. Obs. Spec. Rept. No. 375*, 1977.
- Bowman, B.R et al, "The JB2006 Empirical Thermospheric Density Model", *Journal of Atmospheric and Solar Terrestrial Physics*, Vol. 70, 774-793, 2008 .
- Bowman, B.R., W.K. Tobiska, F.A. Marcos, C.Y. Huang, C.S. Lin, W.J. Burke, "A new Empirical Thermospheric Density Model JB2008 Using New Solar and Geomagnetic Indices", *AIAA/AAS Astrodynamics Specialist Conference*, AIAA2008-6438,2008a.
- Storz, M.F, Bowman, B.R., Branson, J.I., "High Accuracy Satellite Drag Model (HASDM)", *AIAA/AAS Astrodynamics Specialist Conference*, Monterey, CA, Aug. 2002.
- CIRA 1986, "Part I: Thermosphere Model", D. Rees (ed.), *Adv. Space Res.* 8, #5-#6, 1988.
- A. E. Hedin, "Extension of the MSIS Thermospheric Model into the Middle and Lower Atmosphere", *J. Geophys. Res.* 96, 1159, 1991.
- J.M. Picone, A.E. Hedin, D.P. Drob, and A.C. Aikin, "NRLMSISE-00 empirical model of the atmosphere: Statistical comparisons and scientific issues", *J. Geophys. Res.*, 107(A12), 1468, doi:10.1029/2002JA009430, 2002.
- Ridley, A. J., Y. Deng, and G. Toth., 2006, "The Global Ionosphere-Thermosphere Model (GITM)", *J. Atmos. Solar-Terrest. Phys.* 68, 839-864.
- Stastny, N. B., Chavez, F. R., Lin, C., Lovell, A. T., & Bettinger, R. A. (2009). "Localized Density/Drag Prediction for Improved Onboard Orbit Propagation", *Proceedings of the Advanced Maui Optical and Space Surveillance Technologies Conference* (p. p.E5). Wailea: The Maui Economic Development Board.
- Reigber, C., Lühr, H., and Schwintzer, P., "CHAMP Mission Status", *Advances in Space Research*, Vol. 30, No. 2, 2002, pp. 129–134.
- Levenberg, K. "A Method for the Solution of Certain Problems in Least Squares", *Quart. Appl. Math.* 2, 164-168, 1944.
- Marquardt, D. "An Algorithm for Least-Squares Estimation of Nonlinear Parameters", *SIAM J. Appl. Math.* 11, 431-441, 1963.
- The MathWorks (August 30, 2013). *Neural Network Toolbox*. Available: <http://www.mathworks.com/help/nnet/index.html> Last accessed September 3, 2013.
- Sutton, E.K., Nerem, R.S., and Forbes, J.M., "Density and Winds in the Thermosphere Deduced from Accelerometer Data", *Journal of Spacecraft and Rockets*, 44(6):1210-1219,2007. doi: 10.2514/1.28641E.K. Sutton, R.S. Nerem, and J.M. Forbes."Density and Winds in the Thermosphere Deduced from Accelerometer Data", *Journal of Spacecraft and Rockets*, 44(6):1210-1219,2007. doi: 10.2514/1.28641
- Forbes, J. M., Nerem, R. S, Sutton, E. K, Zhang, X. Bruinsma, S. (July 2, 2013). *Thermosphere Studies Using Accelerometer Measurements from the CHAMP and GRACE Satellites*. Available: <http://sisko.colorado.edu/sutton/>. Last accessed August 19, 2013.
- Lütkepohl, H., Xu, F., "The role of the log transformation in forecasting economic variables," *Empirical Economics*, Springer, vol. 42(3), 619-638 (2012)
- A. V. Belov, S. P. Gaidash, K. G. Ivanov, and Kh. D. Kanonidi, "Unusually High Geomagnetic Activity in 2003", *Cosmic Research*. Vol 42 (6), 1–10 (2004). doi: 10.1007/s10604-005-0001-0
- A. V. Belov, S. P. Gaidash, K. G. "Anomalously low solar and geomagnetic activities in 2007," *Geomagnetism and Aeronomy*. Vol 49 (5), 566–573 (2009). doi: 10.1134/S001679320905003X
- Papitashvili, N. (June 11, 2013). *OMNIWeb*. Available: <http://omniweb.gsfc.nasa.gov/ow.html>. Last accessed August 19, 2013.

Improved Understanding of the Flyby Anomaly Using a High Fidelity Solar Radiation Pressure Model

Robbie Robertson

Center for Space Science and Engineering Research, Virginia Tech, Blacksburg, VA 24061.

Michael Shoemaker

Space Science Applications Group, Los Alamos National Lab, Los Alamos, NM 87545.

Abstract

Numerous deep-space missions have used Earth flybys to gain or lose heliocentric orbital energy en-route to their destinations. During a number of these gravity assist maneuvers, beginning with the first Galileo Earth flyby in December of 1990, mission operators have observed motion which cannot be explained by their detailed force models. Numerous explanations have been unsuccessfully proposed and investigated as the source of the Earth flyby anomaly. In this paper, we investigate solar radiation pressure modeling during penumbra transitions as a contributor to or explanation for the anomaly. We compare propagated Earth flyby trajectories generated using a detailed, highly physical penumbra SRP model to propagated trajectories generated using a simpler geometric method representative of what is typically used in orbit determination programs. Initial results suggest that penumbra SRP modeling is not responsible for or significantly contributing to the anomaly, however further work must be done to conclusively determine its significance.

Keywords: Flyby Anomaly, Solar Radiation Pressure, Orbit Determination

1. Introduction

During Earth flybys, spacecraft follow hyperbolic trajectories which take them close to Earth. During these maneuvers, ground based Doppler radars are used to precisely track the spacecraft. Doppler radar observations are assimilated by orbit determination programs which include detailed models of the significant known forces acting on the spacecraft. Unfortunately, limitations on the ability of radars to track spacecraft motion near perigee lead to Doppler blackout periods around perigee on the order of hours. On numerous occasions, the preencounter and postencounter flyby trajectory estimates do not match one another. This disagreement points to either measurement errors or a change in orbital energy during these perigee passes that is not captured in orbit determination programs. (Anderson et al., 2008)

The unexplained change in orbital energy of the Earth flyby anomaly is described by the anomalous change in hyperbolic excess velocity, Δv_∞ . Scalar hyperbolic excess velocity is defined as:

$$v_\infty^2 = \vec{v} \bullet \vec{v} - \frac{2\mu}{r} \quad (1)$$

where v is the spacecraft velocity, μ is Earth's gravitational parameter, and r is the magnitude of the spacecraft position vector. Δv_∞ is the difference in v_∞ between the postencounter and preencounter estimated trajectories. Table 1 shows Δv_∞ values, estimated realistic errors in the Δv_∞ values, σ_{v_∞} , and other relevant parameters for the past anomalous Earth flybys. In addition to the past flybys, information is provided for the October 2013 Juno Earth flyby, which

Email addresses: voorhies@vt.edu (Robbie Robertson), shoemaker@lanl.gov (Michael Shoemaker)

Table 1: Data from past Earth flyby anomalies up to MESSENGER courtesy of Anderson et al. (2008). Note that the majority of observed anomalous Δv_∞ values are at least an order of magnitude greater than the estimated errors in hyperbolic excess velocities. Note that Juno mass used here is the initial value from NASA (2011) and should be updated in the future based on reduced fuel mass at the Earth flyby.

| Spacecraft | Galileo | Galileo | NEAR | Cassini | Rosetta | MESSENGER | Juno |
|----------------------------|-----------|-----------|-----------|-----------|----------|-----------|-----------|
| Flyby Date | 12/8/1990 | 12/8/1992 | 1/23/1998 | 8/18/1999 | 3/4/2005 | 8/2/2005 | 10/9/2013 |
| S/C Mass (kg) | 2497 | 2497 | 730 | 4612 | 2895 | 1086 | 3625 |
| Perigee Alt. (km) | 960 | 303 | 539 | 1175 | 1956 | 2347 | 562 |
| v_∞ (km/s) | 8.949 | 8.877 | 6.851 | 16.010 | 3.863 | 4.056 | - |
| Δv_∞ (mm/s) | 3.92 | -4.6 | 13.46 | -2 | 1.8 | .02 | - |
| σ_{v_∞} (mm/s) | 0.3 | 1.0 | 0.01 | 1 | 0.03 | 0.01 | - |

had not yet occurred at the outset of this work. Estimated Δv_∞ errors in Table 1 illustrate the high atmospheric drag in the 1992 Galileo flyby and thruster activity in the Cassini flyby which caused difficulty in identifying the anomaly. (Anderson et al., 2008) The MESSENGER flyby data did not significantly exhibit the effects of the anomaly.

Since the Earth flyby anomaly was first identified following the 1990 Galileo flyby, researchers have proposed a broad range of explanations for the anomaly. Lammerzahn et al. (2008) presents a summary of these explanations which include hardware and Doppler ranging related issues, errors in modeling well known environmental forces, and more exotic explanations which concern new physics such as non-Newtonian gravity and modifications of relativity.

SRP is one of the dominant non-gravitational forces acting on spacecraft. SRP is influenced by a variety of complex factors. The computational load and complexities of SRP modeling are generally dominated by modeling how incident photons will interact with spacecraft surfaces and transfer momentum to the spacecraft. These calculations are related to the orientation, exterior geometry, and optical properties of the spacecraft. This focus on the SRP force modeling is practical because a spacecraft spends the majority of its time in full sunlight or in umbra. However, during penumbra transitions between full sunlight and umbra, assigning a physically representative solar radiation field becomes similarly complex and computationally intensive. During these transition periods, solar radiation passes through Earth's lower atmosphere. The optics of the atmosphere lead to significant atmospheric refraction and Rayleigh scattering. Refraction bends light around Earth, extending the penumbra transition in the umbra direction and augmenting the direction of light rays incident on the spacecraft. Rayleigh scattering attenuates the total solar flux in the incident radiation field and changes its spectral composition. Additionally, the irregular, oblate shape of the solid Earth changes the timing of transitions. Current orbit determination programs do not explicitly consider these atmospheric effects.

The SOLARS (SRP with Oblateness and Lower Atmospheric Refraction and Scattering) model has been developed to physically model penumbra SRP. In some respects, penumbra SRP modeling appears to be a promising candidate for explaining the flyby anomaly. Anderson et al. (2008) was able to precisely fit an expression providing the Δv_∞ values from past anomalies based on the orbital inclinations of the flyby trajectories. The SOLARS model includes a global, latitude dependent atmosphere model which leads to a correlation between orbital inclination and penumbra SRP. This connection between SRP force and inclination is not captured by the traditional non-physical methods included in orbit determination programs. However, this study shows definitively that penumbra SRP modeling is not responsible for the flyby anomaly. First, only Galileo during the 1990 flyby and Cassini during its flyby passed into Earth's shadow and therefore experienced penumbra transitions. Finally, Lammerzahn et al. (2008) indicates that the anomalous acceleration is on the order of 10^{-4} m/s², which is far greater than the nm/s² scale SRP accelerations of these spacecraft. Regardless of these findings, the influence of penumbra SRP modeling could be greater than the estimated errors in hyperbolic excess velocities. Therefore we followed through with this investigation to evaluate whether penumbra SRP modeling has a significant influence on the anomaly and whether it could be used to better understand or predict the cause. In this paper, we focus on the flybys which did experience penumbra transitions: Galileo's 1990 flyby and the Cassini flyby. Additionally, we investigate the 2013 Juno flyby which had not occurred at the outset of this work. The predicted trajectory for the 2013 Juno flyby indicated that Juno would pass into umbra and therefore experience penumbra transitions.

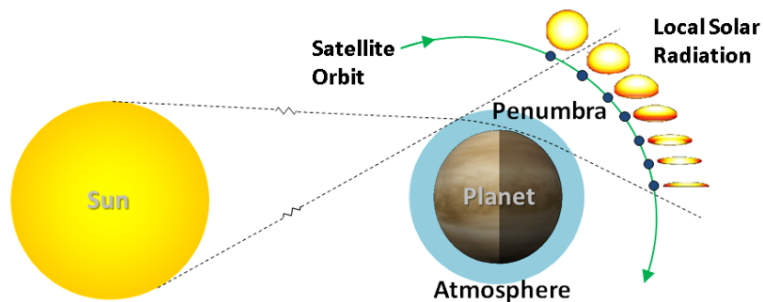


Figure 1: Illustration of the penumbra geometry and solar radiation fields for a satellite when atmospheric effects are included.

2. Method

We quantify the influence of penumbra SRP modeling on the flyby anomaly by comparing flyby trajectories propagated using the geometric model with those propagated using the SOLARS model. Hyperbolic excess velocity is computed at each time step in these propagated trajectories. The contribution of SRP modeling to the anomalous change in Δv_∞ is quantified by computing the difference between these hyperbolic excess velocities at each time step.

2.1. Orbit Propagation

The orbit propagator includes physical, detailed models of other orbit perturbations (in addition to SRP). Residual air drag forces are modeled using the Jaccia70 atmosphere model. Third body gravity forces are included for the Sun and Moon. The irregularities in Earth's gravity field are modeled according to Vallado (2001) using a 10th degree and order implementation of the EGM96 gravity field model.

2.2. Highly Physical SOLARS Penumbra SRP Model

SOLARS uses a finite element approach which models the solar radiation field at a given spacecraft location using a finite number of light rays. This finite element approach is based on the method presented by Vokrouhlický et al. (1993). The spectral composition, angle of incidence, and solar flux associated with each light ray is computed based on physical modeling of atmospheric refraction and wavelength dependent Rayleigh scattering. Variations in lower atmosphere conditions and Earth radius are accounted for using the NRLMSISE-00 atmosphere model and an oblate spheroid model of Earth. (Picone, 2002) Figure 1 illustrates the influence of atmospheric effects on local solar radiation fields and on the overall shape of the penumbra region. The coloring of the solar radiation fields in Figure 1 represents solar flux, and these solar radiation fields were produced by applying SOLARS to the GRACE satellite orbit. The SOLARS model has been tested by modeling SRP accelerations of the GRACE satellites and comparing with their highly precise, nm/s²-scale accelerometer data. (Robertson et al., 2012)

While the SOLARS SRP model is based primarily on the one introduced by Vokrouhlický et al. (1993), various improvements have been made. These improvements take advantage of developments in refraction and atmosphere modeling, enable more complex force modeling, and leverage greater computing power. Each light ray in a SOLARS finite element solar radiation field is assigned an intensity based on its direction of incidence on the satellite. This intensity is dependent on its path through the atmosphere and location of emission from the Sun. Following the method from Vokrouhlický et al. (1993), the location of emission determines the initial solar flux assigned to the light ray according to Eddington's approximation for solar limb darkening. Refraction in the atmosphere determines the path, which then determines how much of the intensity is scattered by the atmosphere. SOLARS accounts for changes in the spectral composition of light as it passes through the atmosphere, as Rayleigh scattering is highly wavelength dependent. Earth is modeled as an oblate spheroid to account for polar flattening.

2.3. Geometric Penumbra SRP Model

The simpler penumbra model chosen to represent a more typical approach uses geometric parameters to model SRP in transitions. This model is based on Ziebart et al. (2004), and applies an attenuation factor resulting in linearly

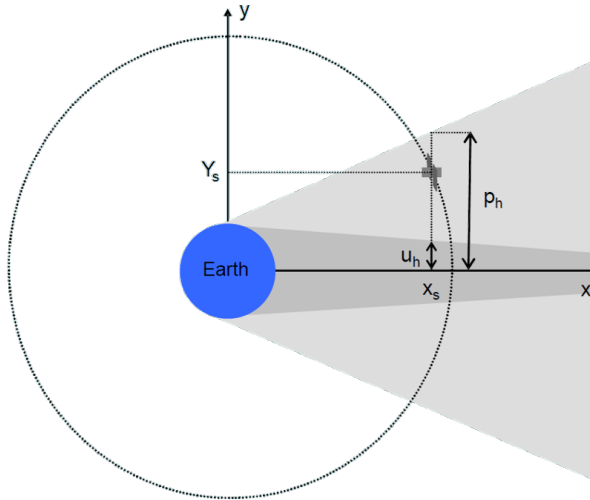


Figure 2: Illustration courtesy of Ziebart et al. (2004) showing parameters involved in geometric penumbra SRP model.

decreasing solar flux with respect to vertical distance into the penumbra region. The vertical height of the penumbra region, p_h , and the umbra height, u_h , are computed based on a spherical Earth with no atmosphere. The illustration in Figure 2 shows these heights and the geometry of the penumbra region when the atmosphere is not considered. The penumbra SRP attenuation factor, F , is defined according to Ziebart et al. (2004) as:

$$F = 1 - \frac{y_s - u_h}{p_h - u_h} \quad (2)$$

where y_s is vertical position of the satellite as shown in Figure 2.

2.4. SRP Force Modeling

The SOLARS and geometric penumbra SRP models are implemented such that modeled solar radiation fields outside the penumbra periods are identical. Towards the same aim, both modes of operation for the orbit propagator use the same method for modeling the SRP force imposed on a spacecraft by a given solar radiation field. Since the focus of this work is the modeling of solar radiation fields, simple force modeling techniques are used. Cassini and Galileo have irregular, compact geometries as a result of their radioisotope thermoelectric power sources. These irregular geometries are approximated as spheres. Conversely, Juno is solar powered, and therefore has a higher area-to-mass ratio and a more uniform, flat geometry. The Juno geometry is approximated as a flat plate pointing to the Sun. Optical properties are applied based on the dominant outer material on the three spacecraft. For the Cassini and Galileo spacecraft, this material is reflective aluminized kapton. (Doody, 2009) For Juno, the dominant (Sun pointing) surfaces are solar panels. Computed full sunlight SRP forces for Galileo are within 10% of results from Longuski et al. (1992).

3. Results

Each of the three flybys modeled here exhibit unique trajectories relative to the Earth and Sun. This Sun-Earth-spacecraft geometry drives the length and behavior of SRP during penumbra transitions. The first, preencounter penumbra transition of the Galileo 1990 flyby occurred furthest from perigee. Figure 3 shows the results of our modeling of this Galileo flyby. The left subplots present results from this first transition, with SRP accelerations from both penumbra SRP methods in the upper subplot and the modeled SRP contributions to the anomalous Δv_∞ in the lower subplot. SRP results from the geometric model show the expected linear attenuation of SRP in the penumbra region. The SOLARS SPR accelerations show a significantly longer transition of over 600s. The lower speeds and relatively consistent direction of the trajectory at this distance from perigee extend the transition. The

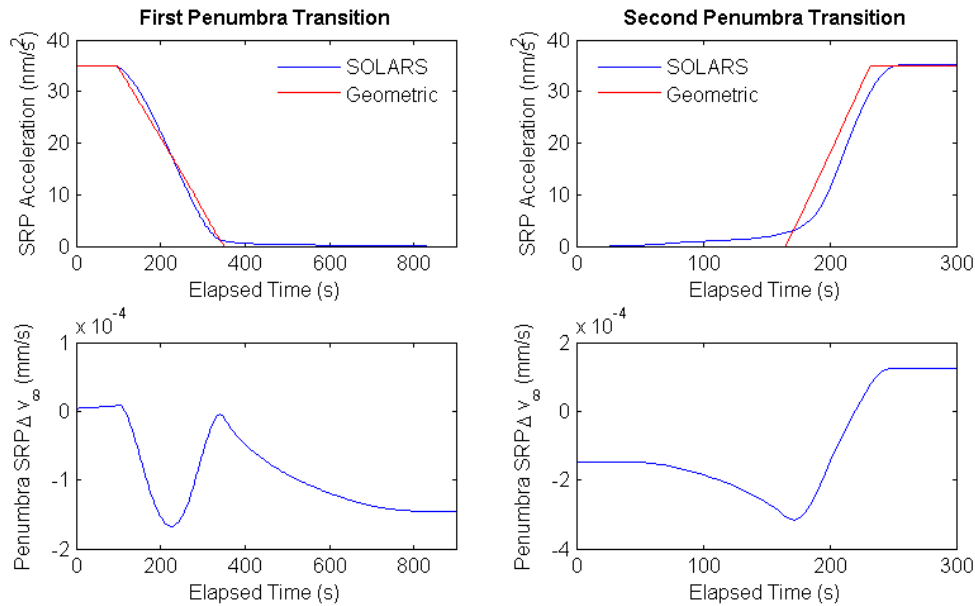


Figure 3: SRP and flyby anomaly modeling results for the 1990 Galileo Earth flyby.

long tail on SOLARS SRP accelerations from 350s to 850s in the upper left subplot is caused by refraction of light around Earth by the lower atmosphere. These SRP accelerations in the tail are relatively small due to Rayleigh scattering attenuation of solar flux which increases as the light takes successively longer paths through the atmosphere at successively lower altitudes. As shown in the right subplot of Figure 3, the second, postencounter Galileo transition is significantly shorter because it occurs closer to perigee. Penumbra SRP Δv_∞ results in the lower subplots of Figure 3 show increases in Δv_∞ which correspond to periods of disagreement between the geometric and SOLARS penumbra SRP models. However, the final postencounter penumbra SRP Δv_∞ is only 124 nm/s, which is significantly smaller than the observed anomalous Δv_∞ of 3.92 mm/s from Table 1. This indicates that for the Galileo 1990 flyby, penumbra SRP modeling did not contribute significantly to the anomaly.

Modeling results are shown for the Cassini flyby in Figure 4 and for the Juno flyby in Figure 5. The results for these cases illustrate behavior very similar to those shown for Galileo in Figure 3. The SRP acceleration results for the first Juno transition show a significant timing disagreement between the SOLARS and geometric models. This disagreement is driven by Earth oblateness, which is considered by the SOLARS model but not by the geometric model. The effect of oblateness on transition timing is more clear in this first Juno transition as it occurred relatively close to perigee and was shorter. While this timing mismatch led to a greater increase in penumbra SRP contribution to Δv_∞ , the contribution was still insignificant. The final postencounter penumbra SRP Δv_∞ is -64.1 nm/s for the Cassini flyby and -273 nm/s for the Juno flyby. Therefore, for all three flyby trajectories addressed, our modeling indicates that penumbra SRP modeling is not a significant contributor to the anomaly. These results indicate that the magnitude of SRP accelerations would need to be orders of magnitude larger to lead to considerable penumbra SRP contributions to the anomaly.

4. Conclusions

In this investigation, we quantified the contribution of penumbra SRP to the Earth flyby anomaly and evaluated its potential for influencing anomalous Δv_∞ results. We quantified this penumbra SRP modeling contribution by applying two models: a geometric model from Ziebart et al. (2004) and the highly physical SOLARS model. Of the six past Earth flybys which exhibited the anomaly, only the first Galileo flyby in 1990 and the Cassini flyby included penumbra transitions. Therefore, penumbra SRP cannot be the source of the flyby anomaly. However, it is

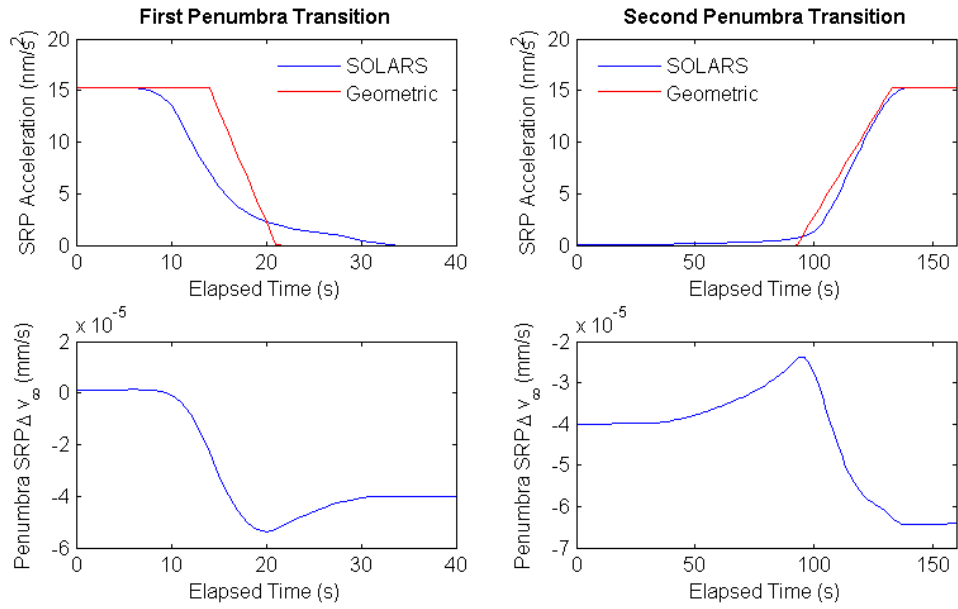


Figure 4: SRP and flyby anomaly modeling results for the 1999 Cassini Earth flyby.

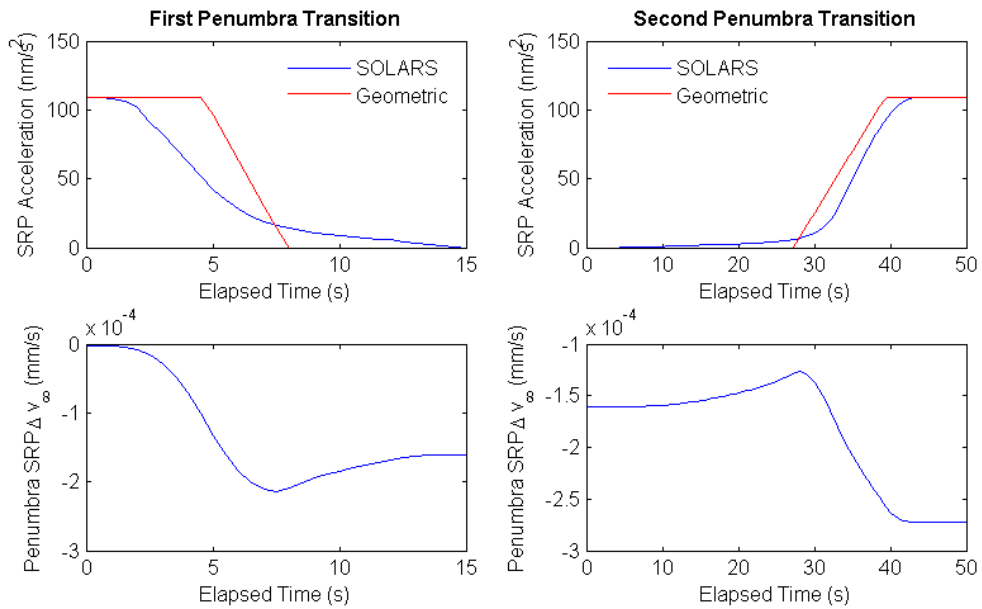


Figure 5: SRP and flyby anomaly modeling results for the 2013 Juno Earth flyby.

useful to investigate whether the reported anomalous changes in energy for those flybys having penumbra transitions should be modified to account for penumbra SRP effects. In this paper, we addressed the very recent Juno flyby in addition to the the past anomalous flybys, Cassini and Galileo 1990. Our results indicate that penumbra SRP is not a significant contributor to the flyby anomaly as the modeled contributions are orders of magnitude smaller than both the observed anomalous Δv_∞ values and the estimated errors in those observed values. SRP results illustrate a significant disagreement between the traditional geometric type of model and the highly physical SOLARS model, however spacecraft area-to-mass ratios and resulting SRP accelerations would need to be significantly larger to lead to a considerable influence of penumbra SRP modeling on the Earth flyby anomaly.

5. Further Work

Our method for quantifying the contribution of SRP modeling to the anomalous Δv_∞ needs to be improved to confirm the initial results presented here. The anomalous Δv_∞ values presented by Anderson et al. (2008) are computed by estimating two unique orbits based on the preencounter and postencounter trajectories and comparing v_∞ results from each estimate. We will implement a batch weighted-least-squares orbit determination program with our orbit propagator to produce results analogous to those presented by Anderson et al. (2008). These anomalous Δv_∞ results will be computed using the geometric SRP model and the SOLARS model. Comparing these two sets of results will more conclusively indicate the significance of penumbra SRP modeling on the Earth flyby anomaly.

References

- Anderson, J., Campbell, J., Ekelund, J., Ellis, J., Jordan, J., 2008. Anomalous orbital-energy changes observed during spacecraft flybys of earth. *Physical Review Letters* 100.
- Doody, D., 2009. *Deep Space Craft: An Overview of Interplanetary Flight*. Springer-Verlag.
- Lammerzahl, C., Preuss, O., Dissus, H., 2008. Is the physics within the solar system really understood?, in: *Lasers, Clocks, and Drag-Free Control*. Springer-Verlag, Berlin, pp. 75–98.
- Longuski, J.M., Todd, R.E., König, W.W., 1992. Survey of nongravitational forces and space environmental torques: Applied to galileo. *Journal of Guidance, Control, and Dynamics* 15, 545–553.
- NASA, 2011. Juno launch press kit. Online.
- Picone, J.M., 2002. Nrlmsise-00 empirical model of the atmosphere: Statistical comparisons and scientific issues. *Journal of Geophysical Research* 107.
- Robertson, R.V., Flury, J., Schilling, M., Bandikova, T., 2012. Precise solar radiation pressure modeling for grace with atmospheric refraction and absorption, in: *Poster Presented at AGU Fall Meeting, San Francisco, CA*.
- Vallado, D.A., 2001. *Fundamentals of Astrodynamics and Applications, Second Edition*. Microcosm Press, El Segundo, California.
- Vokrouhlický, D., Farinella, P., Mignard, F., 1993. Solar radiation pressure perturbations for Earth satellites, i. A complete theory including penumbra transitions. *Astronomy and Astrophysics* 280, 295–312.
- Ziebart, M., Adhya, S., Sibthorpe, A., Edwards, S., Cross, P., 2004. A high precision analytical surface force model for gps block iir satellites, in: *Poster Presented at IGS Workshop and Symposium 2004 in Bern, Switzerland, International GPS Service*.

Determining Source Rate Parameters of Energetic Electrons in the Outer Radiation Belt using a Kalman Filter

Quintin Schiller

Laboratory for Atmospheric and Space Physics, University of Colorado, 1234 Innovation Dr., Boulder, CO 80303

Humberto Godinez

Los Alamos National Laboratory, Los Alamos, NM 87544

1. Introduction

Based on the work from last summer(2), it was apparent that the offline method employed was a superior method for estimating all source rate parameters. In Schiller and Godinez, source rate width and location were estimated offline, but source rate amplitude was estimated as a direct output of the Kalman filter. The downside of this method is that the Kalman filter can take up to 36 hours to spin up to correctly estimate the amplitude parameter. If the source rate intensity changes on timescales less than 36 hours, which is likely to occur, the Kalman filter may not be able to respond quickly enough. Thus, a new method is required to estimate the amplitude parameter offline, increasing the number of dimensions in the parameter space to three - amplitude, location, and width. However, finding the minimum in two dimensional parameter space without an optimization technique can take hundreds, sometimes thousands of experiments. Increasing the dimension would exponentially increase the number of experiments required to find a solution. Performing so many experiments for each time step is unreasonable, so an optimization technique is required.

2. Goal

We chose a reasonable goal to aim for at the end of my three weeks at LANL in the summer of 2013. This goal was to choose an optimization method that would work for our problem; specifically, the technique must not require finding a derivative and can be used for three dimensions. We would then implement the technique in the existing two dimensional space to verify its functionality. Finally, by the end of the three weeks we would implement the scheme in the three dimensional space.

3. Optimizing LANL Dataset in Two Dimensions

Almost immediately we saw problems with using the Nelder-Mead method on the parameter space from the LANL dataset we were assimilating. The topology of the parameter space had multiple minimums and wide, shallow valleys. The Nelder-Mean method cannot distinguish local minima from global minima, and can mistake the wide, shallow valleys for minima. Reeves et al.(1) suggest that a source term is needed to account for the gap in observations between GPS and GEO satellites in that dataset. The filter could be confusing a source term accounting for absent data with a physical source term. We performed identical twin experiments to see if the topology between the assimilated LANL dataset and a synthesized dataset with two source terms (Figure 4) were similar. They were, as can be seen in Figure 3, where there are multiple minima and shallow valleys. This motivated a change from the LANL dataset to a Radiation Belt Storm Probes dataset.

Email addresses: quintin.schiller@colorado.edu (Quintin Schiller), hgodinez@lanl.gov (Humberto Godinez)

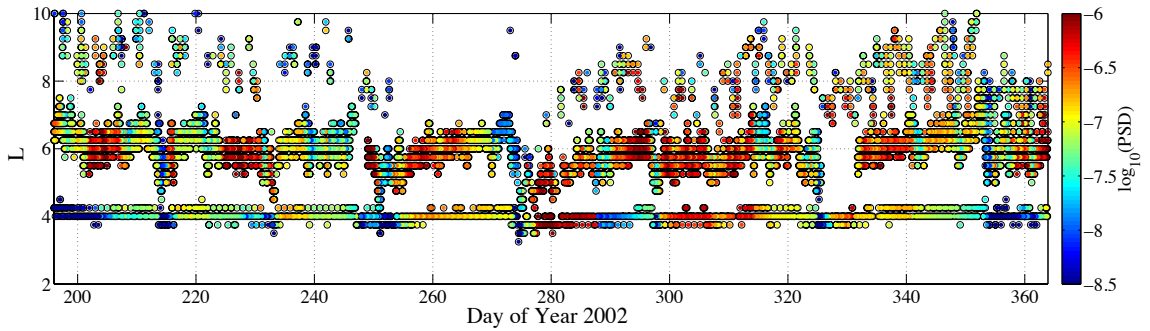


Figure 1: The LANL dataset which, for one timestep, is assimilated in Figure 2

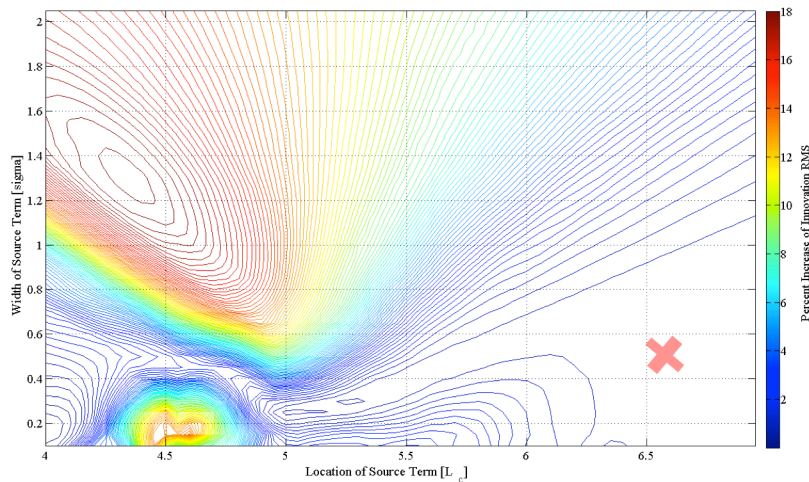


Figure 2: 2400 experiments run on the LANL dataset in the $4 < L_c < 6.5$ and $0.1 < \text{Width} < 2.1$ parameter space. The Nelder-Mead method often converges to the red 'x' at $L_c=6.6$ and $\text{width}=0.5$, when the true global minima exists at $L_c=5.3$ and $\text{width}=0.3$.

4. Optimizing RBSP Dataset in Two Dimensions

RBSP takes measurements from $1 < L < 6$ twice every 9-hour orbit. This dataset is ideal since a wide L range is sampled with relatively high frequency. The RBSP Flux data was converted to PSD by binning the MagEIS M75 and HIGH flux measurements into $975 < \mu < 1025$ MeV/G and $I < 3 [R_E]$. The period of interest is Jan 10 to Jan 20 2013, due to, among other reasons, a clear flux enhancement occurring near $L=5$, increasing the flux by 100x in ~ 24 hours. The RBSP PSD data can be seen in Figure 5. The data was assimilated using both the 'old' brute-force technique, performing thousands of experiments to map the entire parameter space (Figures 8 and 6), and the 'new' technique using the Nelder-Mead method (Figures 7 and 6). The results are comparable, but the Nelder-Mead method finds solutions outside of the old method's specified parameter space. The parameter space can be extended, but at the cost of adding hundreds of experiments per timestep.

5. Future Work

Three weeks wasn't enough time to get the 3-D optimization method in place using the RBSP PSD data. It should take ~ 2 weeks to implement a reliable Nelder-Mead 3-D optimization scheme with the RBSP data. It also

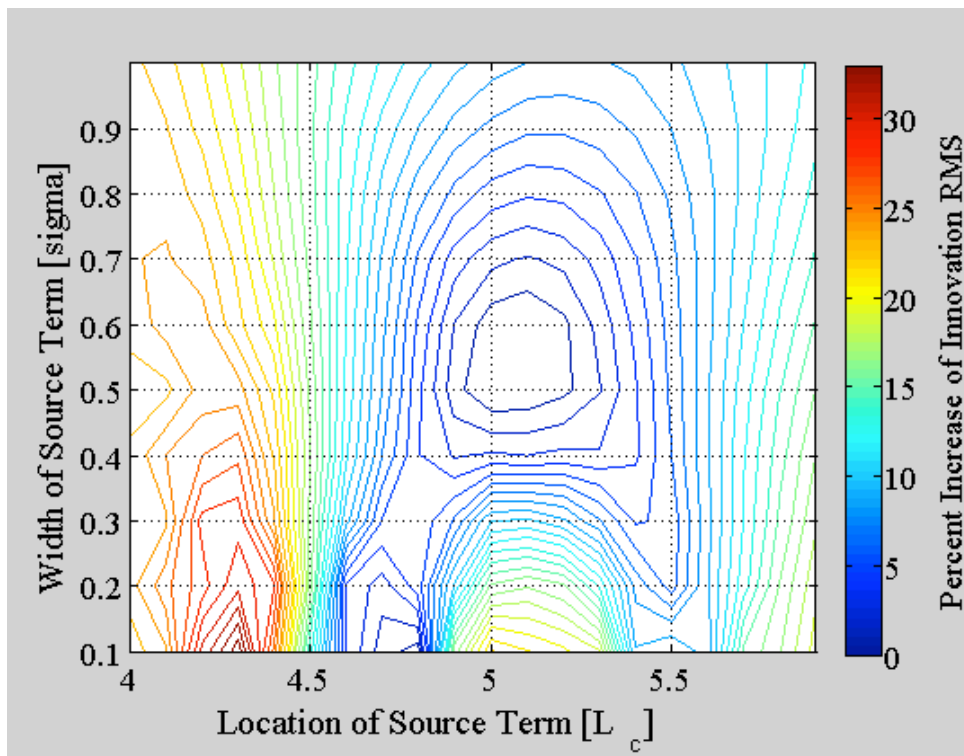


Figure 3: A common topology given the two source terms.

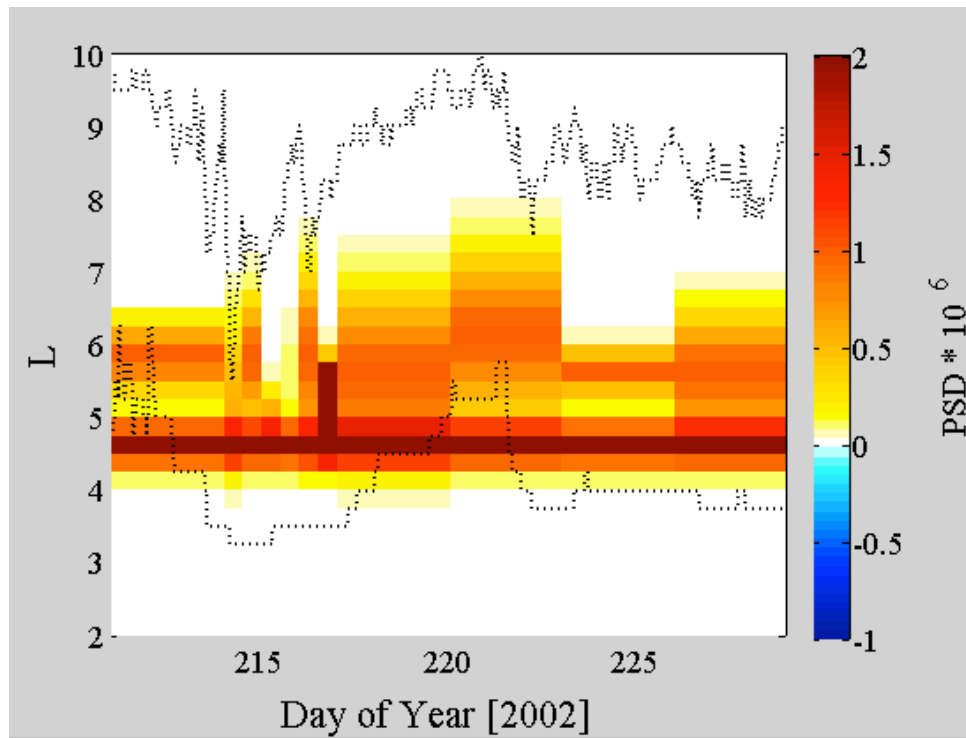


Figure 4: There are two source terms in this experiment: one unvarying at $L=4.5$ with width 0.2, and a second at higher L with varying location, width, and amplitude.

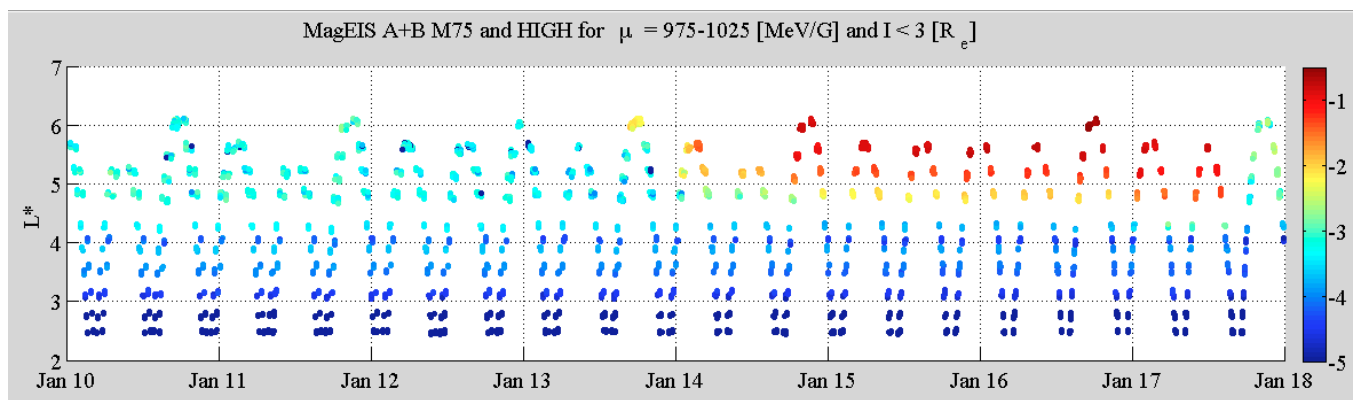


Figure 5: Phase space density measurements from the RBSP MagEIS M75 and HIGH instruments.

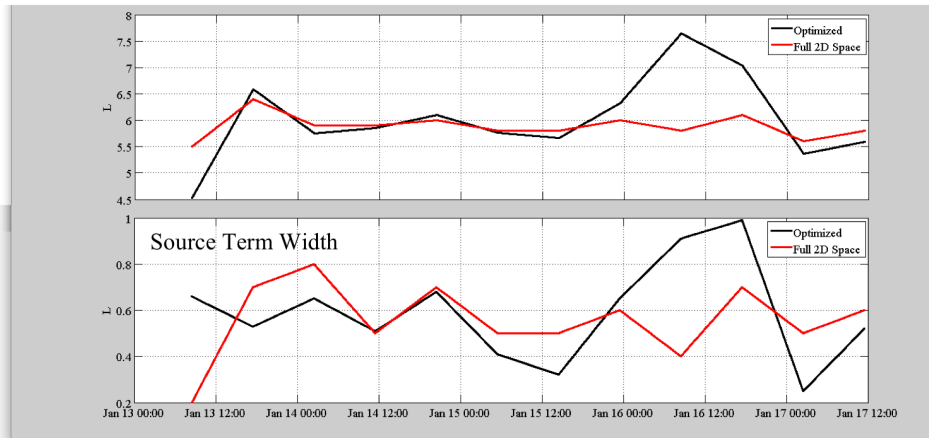


Figure 6: The results of running the 'old' method, where experiments are run for every grid point in $4 \leq L \leq 6.5$ and $0.1 \leq \text{Width} \leq 2.1$ parameter space in red, and the optimization method in black. The optimization method can find minima outside the bounds of the old method, as well as performing dozens of experiments to converge on a solution, as opposed to the thousands using the old method.

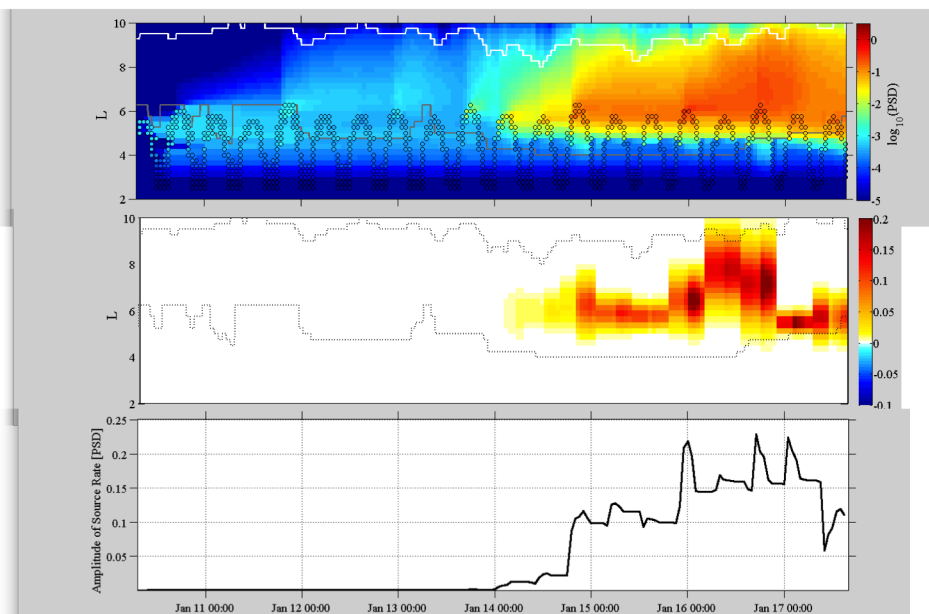


Figure 7: Results from the optimization method.

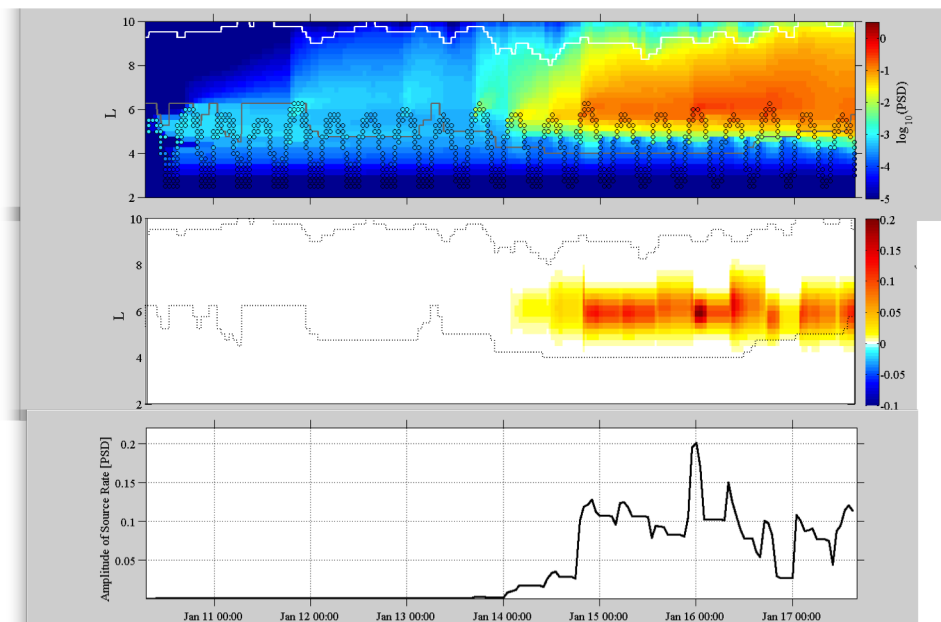


Figure 8: Results from the full method in a rigid parameter space.

wasn't enough time to do more than a high-level conversion to PSD. The delay in the release of RBSP Level 4 PSD data forces a home-grown method to get PSD from flux values. It would take a considerable amount of time to create a reliable home-grown method. However, improvements can be made on the technique already used which would improve reliability. It should take ~ 2 weeks to understand and apply the appropriate improvements to the PSD conversion. A reasonable goal would be to have the 3D optimization technique implemented to a more reliable RBSP dataset within one month after GEM, with the target near the July 22nd timeframe.

References

- [1] Reeves, G. D., Y. Chen, G. S. Cunningham, R. W. H. Friedel, M. G. Henderson, V. K. Jordanova, J. Koller, S. K. Morley, M. F. Thomsen, and S. Zaharia (2012), Dynamic Radiation Environment Assimilation Model: DREAM, *Space Weather*, 10, S03006, doi:10.1029/2011SW000729.
- [2] Q. Schiller and H. Godinez (2012), Determining source rate parameters of energetic electrons in the outer radiation belt using a Kalman filter, Los Alamos National Lab Space Weather Summer School.
- [3] Nelder, J. A. and R. Mead (1965), A simplex method for function minimization, *Computer J.*, Vol. 7, pp. 308

Improving Non-Gaussian Uncertainty Propagation for Satellite Conjunction Analysis

Vivek Vittaldev

Department of Aerospace Engineering and Engineering Mechanics, The University of Texas at Austin, Austin, TX

Richard Linares

Los Alamos National Laboratory, Los Alamos, NM

Abstract

The increasing number of Resident Space Objects (RSOs) has resulted in an overcrowding of space. To prevent the Kessler syndrome and to protect assets in space, it is imperative to predict the probability of collisions between RSOs. Since orbital motion is highly non-linear, it is important to capture the non-Gaussianity of the uncertainty distribution. We have combined 2 different methods of describing non-Gaussian distributions, Polynomial Chaos (PC) and Gaussian Mixture Models (GMMs) in order to propagate non-Gaussian distributions in a more computationally efficient manner. Using PC with GMMs can also be used for other applications such as state estimation where uncertainty has to be propagated.

Keywords: Polynomial Chaos, Conjunction Analysis, Gaussian Mixture Model

1. Introduction

Conjunction Analysis (CA) for RSOs is a very relevant area of research to protect important assets in space and to prevent the Kessler syndrome (Kessler, 1991). Computing the collision probability accurately helps to mitigate collisions and to avoid unnecessary evasion maneuvers. The probability of collision involves finding the intersection of two non-Gaussian distributions. There exist many theories that efficiently compute the collision probability by assuming that the distributions are Gaussian (Alfano, 2007, 2005; Chan, 2008). However, the most accurate method is to use Monte Carlo (MC) simulations (Alfano, 2009).

Both PC and GMMs are methods of capturing non-Gaussian distributions using fewer points than a full-blown MC run. PC uses orthogonal polynomials to capture the evolution of a probability distribution function (pdf). Using the polynomials requires orders of magnitude fewer simulations than MC. GMMs approximate a non-Gaussian distribution as a weighted sum of Gaussian distributions. All the Gaussian propagation methods can now be used on the individual Gaussian distributions, which results in huge computational savings. CA has been carried out using PC (Jones and Doostan, in press, 2013; Jones et al., accepted, 2012) and with GMMs (Vittaldev and Russell, 2013; DeMars and Jah). A combination of both techniques vastly increases the accuracy of the uncertainty propagation while having a lower computational cost than a MC simulation.

The GMM and PC theory is first presented in Section 2 followed by the motivation behind the combination. In Section 3, a small orbit propagation simulation is carried out to qualitatively show the performance of the PC GMM combination. Finally the conclusions are presented in Section 4.

2. Theory

In this section GMMs, PC, and the combination of GMM and PC will be presented.

Email addresses: v.vittaldev@utexas.edu (Vivek Vittaldev), linares@lanl.gov (Richard Linares)

2.1. Gaussian Mixture Models

A GMM uses a sum of Gaussin probability distribution function to approximate any probability distribution (Horwood et al., 2011; Alspach and Sorenson, 1972; DeMars et al., 2011).

$$p(\mathbf{x}) = \sum_{i=1}^N \alpha_i p_g(\mathbf{x}; \boldsymbol{\mu}_i, \mathbf{P}_i) \quad (1)$$

where N is the total number of elements in the GMM and α_i is a weight, which satisfies the following constraint:

$$\sum_{i=1}^N \alpha_i = 1 \quad (2)$$

The weights can be computed by minimizing the L_2 distance between p and a Gaussian distribution p_g .

$$\begin{aligned} L_2(p_1, p_2) &= \sum_{i=1}^{k_1} \sum_{j=1}^{k_1} \alpha_{1,i} \alpha_{1,j} K(\boldsymbol{\mu}_{1,i}, \boldsymbol{\mu}_{1,j}, \mathbf{P}_{1,i}, \mathbf{P}_{1,j}) \\ &+ \sum_{i=1}^{k_2} \sum_{j=1}^{k_2} \alpha_{2,i} \alpha_{2,j} K(\boldsymbol{\mu}_{2,i}, \boldsymbol{\mu}_{2,j}, \mathbf{P}_{2,i}, \mathbf{P}_{2,j}) \\ &- 2 \sum_{i=1}^{k_1} \sum_{j=1}^{k_2} \alpha_{1,i} \alpha_{2,j} K(\boldsymbol{\mu}_{1,i}, \boldsymbol{\mu}_{2,j}, \mathbf{P}_{1,i}, \mathbf{P}_{2,j}) \end{aligned} \quad (3)$$

where K is

$$\begin{aligned} K(\boldsymbol{\mu}_1, \boldsymbol{\mu}_2, \mathbf{P}_1, \mathbf{P}_2) &= |2\pi(\mathbf{P}_1 + \mathbf{P}_2)|^{-1/2} \\ &\times \exp\left(-\frac{1}{2}(\boldsymbol{\mu}_1 - \boldsymbol{\mu}_2)^T (\mathbf{P}_1 + \mathbf{P}_2)^{-1} (\boldsymbol{\mu}_1 - \boldsymbol{\mu}_2)\right) \end{aligned} \quad (4)$$

For a given order, the σ are usually kept constant for all the elements. Therefore, only the means and the weights vary between the elements. In this work, an available library (Vittaldev and Russell, 2013) with up to 25 elements was used.

Most applications where GMMs can be used deal with multivariate states and therefore, multivariate pdfs. Thus, the univariate libraries have to applied to split a multivariate Gaussian distribution. This extension can be done by applying the univariate splitting library to a specified direction of the multivariate covariance matrix. The direction be chosen from the square root or the spectral decomposition of the covariance matrix. We have chosen to use an eigenvector since there is a physical meaning behind it.

2.2. Polynomial Chaos

The idea of PC originates from a paper from Norbert Wiener (Weiner, 1938), where the term *chaos* is used to refer to uncertainty. This theory has been used frequently for Uncertainty Quantification (UQ) and is now also being used in the Aerospace field (Madankan et al., 2013; Jones et al., accepted, 2012; Jones and Doostan, in press, 2013; Hosder et al., 2006; Hosder and Walter, 2010). In the PC, the uncertainty in variables through a transformation is represented by a series of orthogonal polynomials.

$$u(\xi, t) = \sum_{i=0}^{\infty} c_i(t) \Psi_i(\xi) \quad (5)$$

In Eq. (5) ξ is a random variable. The orthogonal polynomials Ψ_i are defined by the following inner product in a Hilbert space:

$$\int_{-\infty}^{\infty} \Psi_m(\xi) \Psi_n(\xi) w(\xi) = 0 \quad (6)$$

| Distribution Type | Density | Polynomial | Weight | Range |
|-------------------|---|----------------------|---------------------------|---------------------|
| Normal | $\frac{1}{\sqrt{2\pi}}e^{-\frac{x^2}{2}}$ | Hermite | $e^{-\frac{x^2}{2}}$ | $[-\infty, \infty]$ |
| Uniform | $\frac{1}{2}$ | Legendre | 1 | $[-1, 1]$ |
| Beta | $\frac{(1-x)^\alpha(1+x)^\beta}{2^{\alpha+\beta+1}\Gamma(\alpha+1)\Gamma(\beta+1)}$ | Jacobi | $(1-x)^\alpha(1+x)^\beta$ | $[-1, 1]$ |
| Exponential | e^{-x} | Laguerre | e^{-x} | $[0, \infty]$ |
| Gamma | $\frac{x^\alpha e^{-x}}{\Gamma(\alpha+1)}$ | Generalized Laguerre | $x^\alpha e^{-x}$ | $[0, \infty]$ |

Table 1: The Wiener-Askey scheme

| Order | Multi-index | Multivariate Polynomial |
|-------|---------------------|---|
| 0 | $\alpha_0 = [0, 0]$ | $\Psi_{\alpha_0}(\xi) = 1$ |
| 1 | $\alpha_1 = [1, 0]$ | $\Psi_{\alpha_1}(\xi) = \Psi_1(\xi_1)$ |
| 1 | $\alpha_2 = [0, 1]$ | $\Psi_{\alpha_2}(\xi) = \Psi_1(\xi_2)$ |
| 2 | $\alpha_3 = [2, 0]$ | $\Psi_{\alpha_3}(\xi) = \Psi_2(\xi_1)$ |
| 2 | $\alpha_4 = [0, 2]$ | $\Psi_{\alpha_4}(\xi) = \Psi_2(\xi_2)$ |
| 2 | $\alpha_5 = [1, 1]$ | $\Psi_{\alpha_5}(\xi) = \Psi_1(\xi_1)\Psi_2(\xi_1)$ |

Table 2: Two-dimensional multivariate polynomials up to order 2

Based on the distribution of the random variable, the orthogonal polynomial type and weighing function, $w(\xi)$ from Eq. (6), are chosen from the Wiener-Askey (Xiu and Karniadakis, 2002) scheme found in Table 1.

Since most applications assume the initial distribution to be Gaussian, Hermite polynomials are chosen according to the Wiener-Askey scheme. We, however, use normalized probabilists Hermite polynomials where the weight function is changed to:

$$w(x) = \frac{1}{\sqrt{2\pi}}e^{-\frac{x^2}{2}} \quad (7)$$

The new weight function assumes that the distribution has a mean of 0 and a standard distribution of 1, which effectively normalizes and improves the numerical properties. The normalized Hermite polynomials can be found by using the following recursive relation:

$$(n+1)! \times \Psi_{n+1}(\xi) = \xi \Psi_n(\xi) - n \Psi_{n-1}(\xi) \quad (8)$$

where

$$\Psi_0 = 1 \quad \Psi_1 = \xi \quad (9)$$

In reality, the infinite series from Eq. (5) is truncated at some order. The orthogonal univariate Hermite polynomials up to order 5 can be seen in Figure 1. The conjunction problem is a multivariate problem and therefore, requires orthogonal multivariate polynomials. Multivariate polynomials can be created using the multi-index notation. Two-dimensional multivariate polynomials up to order 2 can be seen in Table 2. The multivariate polynomial can then be written as:

$$u(\xi, t) = \sum_{i=0}^L c_i(t) \Psi_{\alpha_i}(\xi) \quad (10)$$

In Eq. (10), L can be found from

$$L = \frac{(n+l)!}{n!l!} \quad (11)$$

where n is the dimension of ξ and l is the maximum order of the truncated univariate polynomial. A given order \bar{L} of the multivariate polynomial equals the sum of the elements of the multi-index vector. If the output is also a vector function of dimension n , $\mathbf{u}(\xi, t)$, $n \times L$ coefficients $c_i(t)$ have to be computed.

The final challenge is to find the coefficients $c_i(t)$. The two major methods of finding these coefficients are:

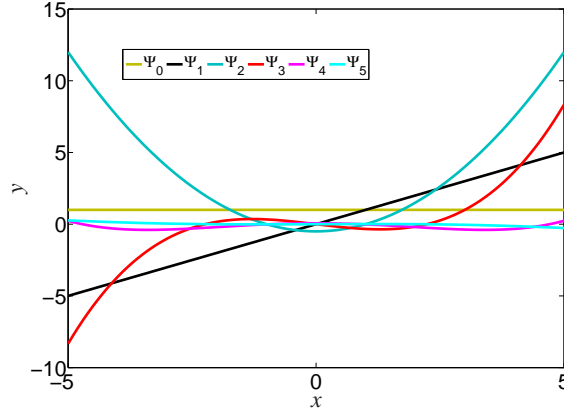


Figure 1: Normalized probabilists Hermite polynomials

- Intrusive method
- Non-intrusive method

The intrusive method requires knowledge of the propagation function that determines the evolution of the random vector of inputs. This then results in a system of equations that need to be solved for $c_i(t)$. The intrusive cannot be used with black-box dynamics, and therefore is not considered in this work. The non-intrusive method does not require any knowledge of the propagation function. Given that we can solve the system for a sample initial condition, we use the projection property (Galerkin Projection) for approximating Eq. (10):

$$c_i(t) = \int u(\xi, t) \Psi_i(\xi) p(\xi) d\xi \quad (12)$$

where $p(\xi)$ is the pdf of ξ .

The coefficients in the non-intrusive method can be solved using either Least Squares (LS), or a quadrature. When LS is implemented, the initial states are randomly sampled. If the quadrature method is used, the initial states are chosen based on the node locations of the quadrature rule. The number of initial states to be used can be vastly reduced by using Compressive Sampling (CS) when using LS, and by using Sparse Grids (SG) when using the quadrature method. In this work, the quadrature method is used with a Smolyak (Smolyak, 1963) SG (SSG). The SSG uses fewer grid points than a full tensor product quadrature as can be seen in Figure 2. In the quadrature method, a grid is generated with N_q node points, which each have a location ξ_n and weight q_n associated with them. The coefficients $c_i(t)$ are then found using the following summation:

$$c_i(t) = \sum_{n=1}^{N_q} q_n u(\xi_n, t) \Psi_{ai}(\xi_n) \quad (13)$$

It should be noted that the node points are generated from a $\mathbf{0}$ mean and identity covariance matrix multivariate distribution for numerical accuracy. The initial points are simply scaled to the actual mean and covariance inside the transformation function u .

2.3. Polynomial Chaos with Gaussian Mixture Models

Both PC and GMMs help in representing non-Gaussian distributions with fewer points computations than a full blown MC simulation. However, they both have their limitations. The biggest problem with PC is the curse of dimensionality. The number of coefficients required with increasing order and increasing dimension for multivariate polynomials can be computed from Eq. (11) and seen in Figure 3a. The number of nodes where computation has to be carried out also increases rapidly with increasing order and dimension as seen in Figure 3b. Another problem is that

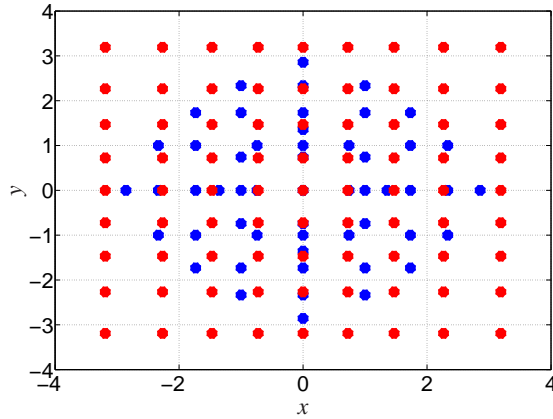


Figure 2: Difference between a full (red) and sparse (blue) two-dimensional quadrature grid

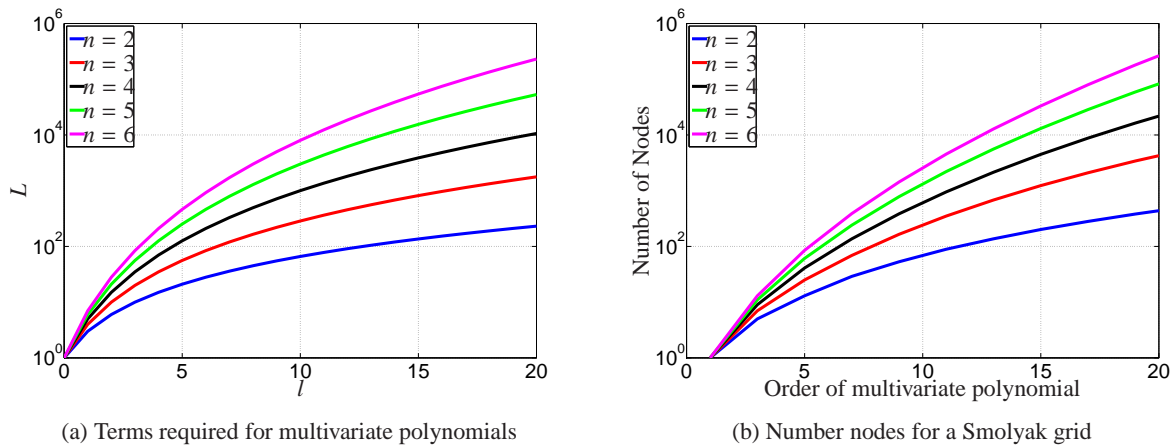


Figure 3: Curse of dimensionality with Polynomial Chaos

increasing the order of the polynomial results in diminishing returns. Increasing the order of the PC only marginally increases the accuracy, while the computational cost increases greatly. When GMMs are used for multivariate applications, the univariate library is applied along one specified direction. Thus, the spectral direction along which the splitting is carried out can play a very important role in the quality of the resulting non-Gaussian distribution after a non-linear transformation (Vittaldev and Russell, 2013). Since each of the elements of the GMM remains Gaussian after the transformation, the complete non-Gaussianness cannot be captured.

A combination of GMMs with PC results in a theory that can outperform each of the separate theories due to them complementing each other. In this method, each of the mixture elements is represented by a PC expansion. What this effectively does is to reduce the size of the distribution that each PC expansion has to account for. This is analogous to reducing the range for Taylor series expansion (TSE), or the Finite Element Method (FEM). Therefore, we use more simple elements (lower order PC expansions) over smaller subdomains (a GMM) to approximate the final non-Gaussian distribution over a larger domain. The steps involved in creating a GMM PC are:

1. Choose a splitting direction and number of elements (n)
2. Convert the initial multivariate Gaussian distribution into a GMM
3. Solve the coefficients for the multivariate polynomials (n sets)

The main difference between the PC method and the PC GMM method during the computation is that the PC solution method has to be carried out n times, where n is the number of elements in the GMM. Each of the n initial

| Variable | Value | Standard Deviaton |
|----------|--------|-------------------|
| r | 100 km | 2 km |
| θ | 90° | 20° |

Table 3: The initial conditions in Polar coordinates

| Variable | Value | Standard Deviation |
|-----------|----------------------------|-------------------------|
| x | 6,780.30 km | 1×10^{-2} km |
| y | 0.00 km | 1×10^{-2} km |
| \dot{x} | 0.00 km/s | 1×10^{-3} km/s |
| \dot{y} | 7.69×10^{-3} km/s | 1×10^{-3} km/s |

Table 4: Initial conditions for a 2-dimensional orbit

conditions has a different mean, but the same covariance. The multivariate GMM set has n elements that each have a different weight and mean, but the same covariance.

The weight only comes in to effect during the sampling process at the end. The weight is analogous to the probability that a sampled point is generated by that particular GMM element. During sampling, a number should be generated between 0 and 1 based on a uniform distribution. This number allows us to chose the element from which to create the sample point.

The benefit can be seen in a very simple test case where an initial Gaussian distribution of a state in polar coordinates Table 3 is converted to Cartesian coordinates. Since this transformation is non-linear, the resulting distribution becomes non-Gaussian. The true (MC) and approximated distributions can be seen in Figure 4. The PC approximation is much better than the strictly Gaussian approximation as can be seen in Figures 4a and 4b. Combining PC and GMM, however, results in a much lower discrepancy between the MC and approximated distributions.

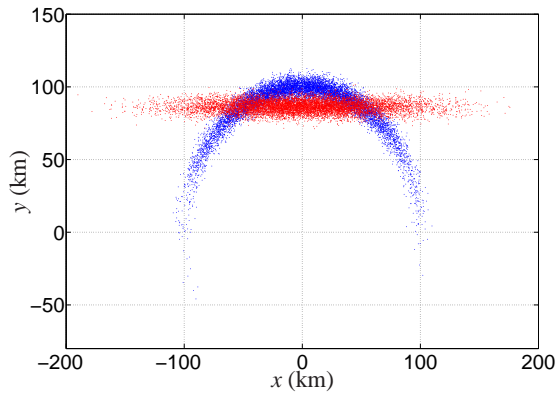
3. Results

In this section, a test simulation is carried out to investigate the validity of the PC GMM combination for an orbital application. The non-linearity of the orbital equations combined with the presence of perturbation such as the atmosphere, make the distribution non-Gaussian with increasing flight time. Thus, the test case propagates a satellite in an almost circular Low Earth Orbit (LEO) at an altitude of approximately 450 km, under the influence of atmospheric drag simulated using the Jacchia-Bowman 2008 (JB2008) Emperical Thermospheric Density Model (Bowman et al., 2008).

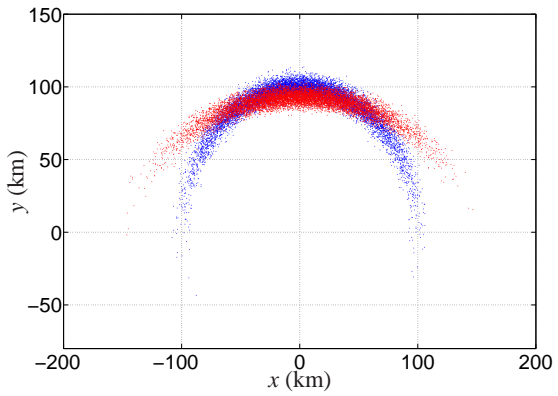
A Gaussian distribution was generated about an initial condition of the orbit (Table 4). A MC and a PC GMM simulation was then carried out for 1 day (Figure 6a) and for 5 days (Figure 6b). The simulation was only carried out as a planar 2-dimensional trajectory due to time constraints, but can easily be extended to a full 3-dimensional simulation in the future. As can be seen in the results found in Figure 6, the final distribution is highly non-Gaussian. However, the PC GMM simulation with orders of magnitude fewer runs is able to represent the final distribution well.

4. Conclusion

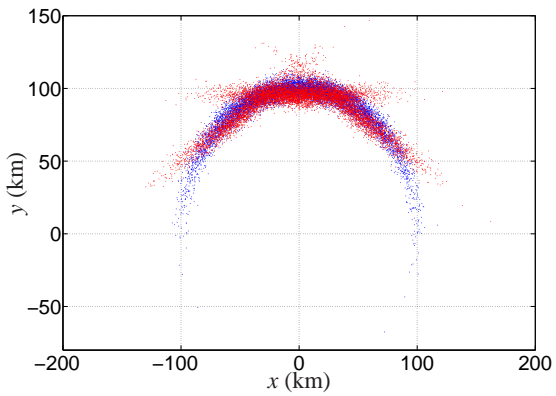
Mixing PC with GMMs results in a framework than can efficiently capture the evolution of an initially Gaussian distribution into a highly non-Gaussian distribution through a non-linear transformation. This combination combines the strengths of the individual components while allowing them to fill the deficiency of each other. PC allows the initially Gaussian elements of GMM to become non-Gaussian. Using an initial GMM reduces the domain covered by the PC and thus, lower order polynomials can be used to get accurate results. Increasing the order of the polynomials increases the computational load in an exponential manner, while increasing the number of elements results in a linear increase. Increasing the polynomial order only marginally increases the accuracy after a certain order.



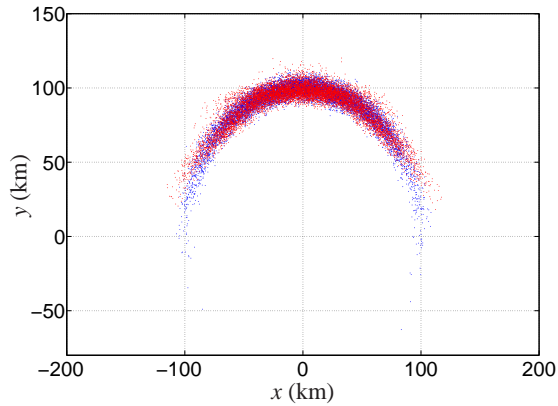
(a) Gaussian approximation using the Unscented Transform



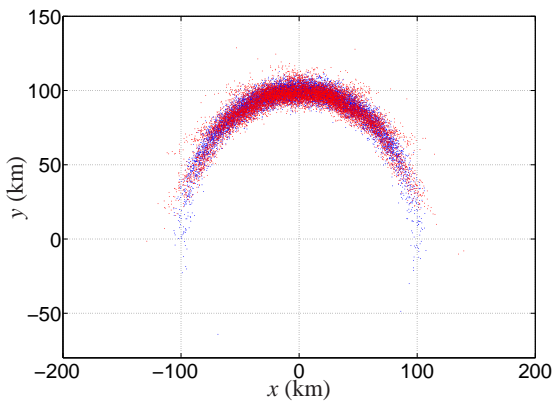
(b) Polynomial Chaos approximation



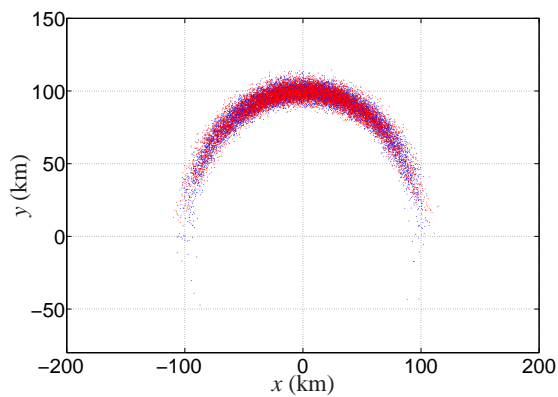
(c) GMM approximation with 3 elements



(d) PC GMM approximation with 3 elements

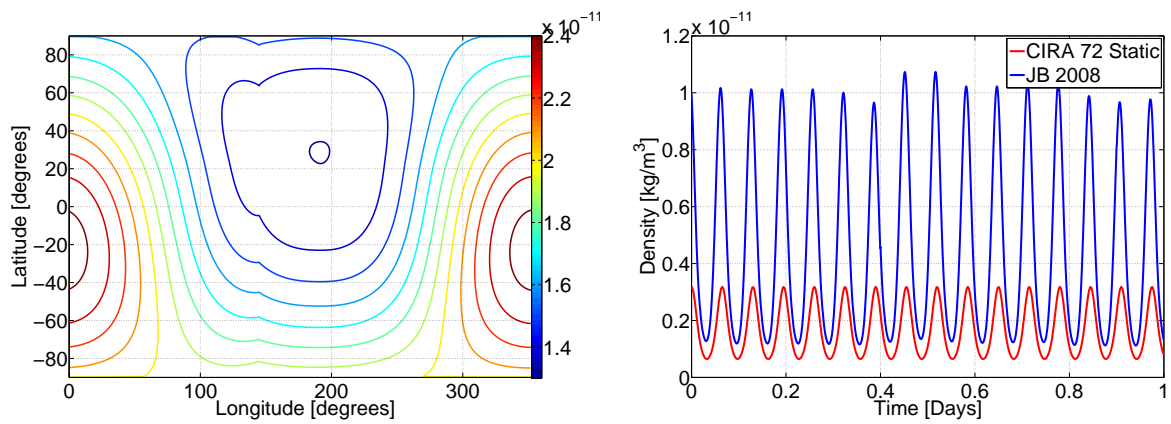


(e) GMM approximation with 5 elements



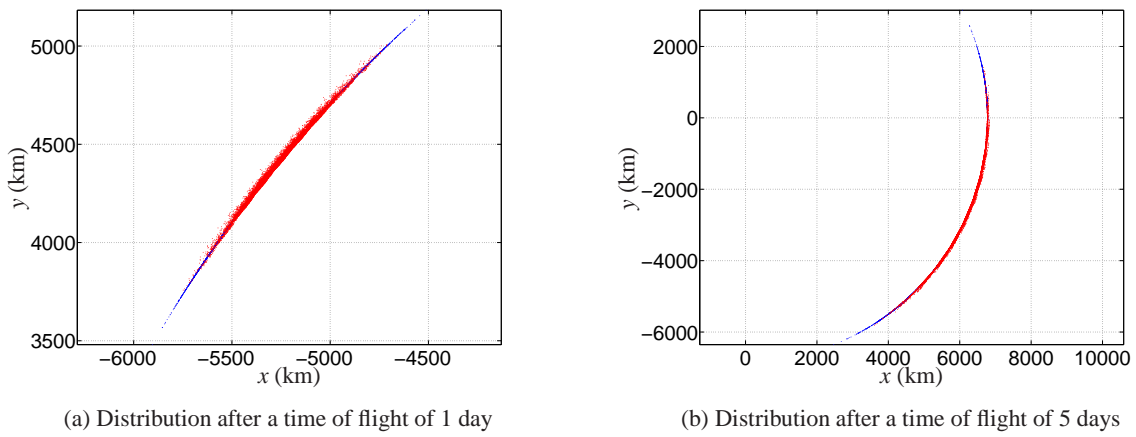
(f) PC GMM approximation with 5 elements

Figure 4: True distribution (blue) and approximated distribution (red) after conversion from Polar coordinates to Cartesian coordinates



(a) Density variation across the Earth at an altitude of 450 km (b) Density comparison: JB2008 and an exponential atmosphere

Figure 5: Density results using the JB2008 atmosphere model



(a) Distribution after a time of flight of 1 day

(b) Distribution after a time of flight of 5 days

Figure 6: MC results (blue) and PC GMM results (red) for the test orbit

References

- Alfano, S., 2005. A numerical implementation of spherical object collision probability. *Journal of the Astronautical Sciences* 53, 103–109.
- Alfano, S., 2007. Review of conjunction probability methods for short-term encounters, in: *AAS/AIAA Space Flight Mechanics Meeting*, Sedona, Arizona, AAS 07-148.
- Alfano, S., 2009. Satellite conjunction monte carlo analysis, in: *AIAA Space Flight Mechanics Meeting*, AAS 09-233.
- Alspach, D.L., Sorenson, H.W., 1972. Nonlinear bayesian estimation using gaussian sum approximations. *IEEE Transactions on Automatic Control* AC-17, 439–448.
- Bowman, B.R., Tobiska, W.K., Marcos, F.A., Huang, C.Y., Lin, C.S., Burke, W.J., 2008. A new empirical thermospheric density model jb2008 using new solar and geomagnetic indices, aiaa 2008 - 6483, in: *AIAA/AAS Astrodynamics Specialist Conference*, Honolulu, Hawaii.
- Chan, F.K., 2008. *Spacecraft Collision Probability*. The Aerospace Press, American Institute of Aeronautics and Astronautics, Inc.
- DeMars, K., Bishop, R., Jah, M., 2011. A splitting gaussian mixture method for the propagation of uncertainty in orbital mechanics, in: *New Orleans, Louisiana, 21st AAS/AIAA Space Flight Mechanics Meeting*.
- DeMars, K.J., Jah, M.K., . A probabilistic approach to initial orbit determination via gaussian mixture models. *Journal of Guidance, Control, and Dynamics* (submitted) .
- Horwood, J.T., Aragon, N.D., Poore, A.B., 2011. Gaussian sum filters for space surveillance: Theory and simulations. *Journal of Guidance, Control, and Dynamics* 34, 1839–1851.
- Hosder, S., Walter, R.W., 2010. Non-intrusive polynomial chaos methods for uncertainty quantification in fluid dynamics, in: *48th AIAA Aerospace Sciences Meeting Including the New Horizons Forum and Aerospace Exposition*, Orlando, Florida.
- Hosder, S., Walter, R.W., Perez, R., 2006. A non-intrusive polynomial chaos method for uncertainty propagation in cfd simulations, in: *44th AIAA Aerospace Sciences Meeting and Exhibit*, Reno, Nevada.
- Jones, B.A., Doostan, A., in press, 2013. Satellite collision probability estimation using polynomial chaos. *Advances in Space Research* .
- Jones, B.A., Doostan, A., Born, G.H., accepted, 2012. Nonlinear propagation of orbit uncertainty using non-intrusive polynomial chaos. *Journal of Guidance, Control, and Dynamics* .
- Kessler, D.J., 1991. Collisional cascading: The limits of population growth in low earth orbit. *Advances in Space Research* 11, 63 – 66.
- Madankan, R., Singla, P., Singh, T., Scott, P.D., 2013. Polynomial-chaos-based bayesian approach for state and parameter estimations. *Journal of Guidance, Control, and Dynamics* 36, 1058–1074.
- Smolyak, S.A., 1963. Quadrature and interpolation formulas for ternsor products of certain classes of function. *Soviet Mat. Dokl.* 4, 240–243.
- Vittaldev, V., Russell, R.P., 2013. Collision probability for resident space objects using gaussian mixture models, paper aas 13-351, in: *23rd AAS/AIAA Spaceflight Mechanics Meeting*, Kauai, Hawaii.
- Weiner, N., 1938. The homogeneous chaos. *American Journal of Mathematics* 60, 897–936.
- Xiu, D., Karniadakis, G.M., 2002. The wiener-asky polynomial chaos for stochastic differential equations. *SIAM J. Sci. Comput.* 24, 619–644.

Isotropic boundary due to current sheet scattering based on 3D force balanced magnetic field

Chao Yue

Department of Atmospheric and Oceanic Sciences, University of California, Los Angeles, CA, 90095

Chih-Ping Wang

Department of Atmospheric and Oceanic Sciences, University of California, Los Angeles, CA, 90095

Sorin Zaharia

Space Science and Applications, Los Alamos National Laboratory, Los Alamos, NM, 87545

Michael Henderson

Space Science and Applications, Los Alamos National Laboratory, Los Alamos, NM, 87545

Larry Lyons

Department of Atmospheric and Oceanic Sciences, University of California, Los Angeles, CA, 90095

Ying Zou

Department of Atmospheric and Oceanic Sciences, University of California, Los Angeles, CA, 90095

Yukitoshi Nishimura

Department of Atmospheric and Oceanic Sciences, University of California, Los Angeles, CA, 90095

Vassilis Angelopoulos

Department of Earth and Space Science, University of California, Los Angeles, CA, 90095

Abstract

In order to evaluate our 3D magnetic field model accuracy and Determine if current sheet scattering alone is sufficient to account for the observed IB, we have calculated the ion isotropic boundary (IB) for different energies based on our 3D force balanced magnetic field model and compared with observations. We have found that IB moves to (1) higher latitudes from midnight towards dawn/dusk; (2) lower latitudes as energy increases as well as Kp and solar wind dynamic pressure (Psw) increases. In addition, the calculated IB matches well at midnight and post-midnight with the observed inner boundary of isotropic distribution obtained from THEMIS spacecraft while it shows discrepancy at pre-midnight. Meanwhile, the modeled IB is consistent with low altitude FAST observations under low Kp (< 3), but shows 1-2° difference as Kp increase, especially at pre-midnight. According to the Geotail and THEMIS ion differential energy flux data, we calculated the maximum ion precipitating flux and found that the precipitation flux increase and its peak move to lower latitudes as Kp and Psw increases. Comparing with ground NORSTAR MSP aurora observation, the computed precipitating flux matches well with equatorward boundary of proton aurora under low Kp (< 2). The discrepancy between our model result and the observation may be caused by the wave activity since EMIC wave intensity increases as Kp increases.

Keywords: Isotropic boundary, 3D force balanced magnetic field model, ion precipitation flux

1. Introduction

A typical observation of a low-altitude polar satellite crossing the auroral oval is the anisotropic (loss cone is nearly empty) energetic proton fluxes at subauroral latitudes, which change sharply at the isotropic flux distribution (in the loss cone) in the poleward part of the oval as a satellite moves poleward. This feature of particle fluxes is observed at all magnetic local times (MLT) and for all magnetospheric conditions.

As introduced by Sergeev and Malkov [1988], sharp boundary (isotropy boundary, IB) of energetic particles measured at low altitudes marks the boundary between regions of adiabatic and stochastic particle motion in the plasma sheet or in the outer dayside cusp [Sergeev et al., 1997]. The IB is based on the physical mechanism, when the ratio between magnetic field curvature radius R_c and the proton gyroradius ρ decreases below the threshold $R_c/\rho \sim 8$ [Sergeev et al. 1988]. Particularly in the current sheet:

$$R_c/\rho = Bn^2/(G\partial Bt/\partial n) \quad (1)$$

Here n and t denote the normal and tangential directions with respect to the current sheet, and $G=mv/q$, where G , m , v and q are the rigidity, mass, velocity and charge of the measured particles, accordingly. This threshold condition allows one to find the isotropic boundaries in any magnetospheric model. For the protons with energies of ~ 80 keV the transition between adiabatic and nonadiabatic behavior on the nightside occurs at the distance 5–9 RE at the equator based on Tsyganenko-2001 model [Lvova et al., 2005].

Equatorward of the IB, the field line ends in regions of the equatorial magnetosphere where the motion is bounce trapped, with conserved adiabatic invariants and anisotropy. Poleward of IB, there is strong pitch-angle scattering, leading to filling of the loss cone and precipitation. And the IB is also the equatorward boundary of strong ion precipitation, which leads to the proton aurora [e.g., Shelley et al., 1972].

The isotropy boundary has been used and verified to be a very good predictor of the magnetotail field stretching [e.g., Sergeev and Gvozdevsky, 1992; Sergeev et al., 1993]. For example, Sergeev et al. [1993] showed that the IB for the 100 keV protons at various local times has a very high correlation (~ 0.9) with the inclination of the B-field as measured on the night side at geosynchronous orbit, indicating that the IB latitude is effectively controlled by the tail magnetic field.

In order to evaluate our force-balanced magnetic field model [Wang et al., 2013; Yue et al., 2013] accuracy and determine if the current sheet scattering itself can explain the observed IB at night side in the low altitude, we will use our computed magnetic field to calculate the IB by using equation (1) and compared with equatorial THEMIS observation and low altitude FAST satellite observation of particle fluxes as well as ground-based NORSTAR MSP proton aurora observation.

2. Force-balanced magnetic field model

The magnetic field model used in this study is based on Zaharia [2008] by solving the single-fluid force balance equation $\nabla P = \mathbf{J} \times \mathbf{B}$ in terms of Euler potentials as $\mathbf{B} = \nabla\alpha \times \nabla\beta$, where P is plasma pressure. In this model P can be either isotropic or anisotropic. Here, we assume P is isotropic. The 3D force balance equation can be decoupled into 2 coupled “quasi-2D” equations in the directions parallel to $(\mathbf{B} \times \nabla\alpha)$ and $(\mathbf{B} \times \nabla\beta)$, respectively as follows:

$$\mathbf{J} \cdot \nabla\alpha = \nabla \cdot [(\nabla\alpha)^2 \nabla\beta - (\nabla\alpha \cdot \nabla\beta) \nabla\alpha] = -\frac{\partial P}{\partial \beta} \quad (2)$$

$$\mathbf{J} \cdot \nabla\beta = \nabla \cdot [(\nabla\beta \cdot \nabla\alpha) \nabla\beta - (\nabla\beta)^2 \nabla\alpha] = -\frac{\partial P}{\partial \alpha} \quad (3)$$

The constant α and β surfaces are found from solving the equations (2) and (3) numerically, through an alternating iterative process. Both boundary conditions and the inhomogeneous terms on the right hand sides ($\frac{\partial P}{\partial \alpha}$

and $\frac{\partial P}{\partial \beta}$) need to be prescribed.

Here, the pair of Euler potentials (α, β) are chosen as below:

$$\alpha' = \alpha + F(\beta)$$

$$\beta' = \beta$$

with $F(\beta)$ to be determined. Here α is defined to be proportional to the poloidal magnetic flux into the Earth, the other potential β is chosen to be equivalent to the azimuthal angle. Since β is equivalent to the azimuthal angle, $F(\beta)$ must be periodic, i.e., $F(\beta + 2\pi) = F(\beta)$. The outer boundary condition for α' is obtained by tracing

empirical magnetic field (e.g., Tsyganenko models) from a prescribed ellipse shape on the equatorial plane. By obtaining $F(\beta)$ through prescribing an outer contour of α , the freedom of choosing the inner contour disappears; a more complete description of this model has been given by Zaharia [2008]. The third coordinate, χ , determines the position along the field line and completes the nonorthogonal flux coordinate system (α, β, χ) .

The two pressure gradients, $\frac{\partial P}{\partial \alpha}$ and $\frac{\partial P}{\partial \beta}$ in (2) and (3) are prescribed by a given pressure spatial profile from our 2D equatorial pressure model. The prescribed pressure is kept spatially fixed on the equatorial plane and changes at each iteration as α and β change. The iteration process is repeated until the $\alpha = cont.$ and $\beta = const.$ surfaces converge to some tolerance, i.e., when the cumulative difference between α or β between two consecutive iterations decreases to a specified amount (here set to be 0.5%), indicating force balance is achieved.

Here, we get the magnetic field model input pressure from an empirical pressure model. In our approach, we first sort the observational plasma pressure data from THEMIS and Geotail according to different levels of solar wind driving ($P_{SW}=1.5$ or 3 nT) or geomagnetic activity (Kp from 0 to 5). The pressure is normalized to corresponding to a fixed P_{SW} values using the linear fit. We then fit the distribution of the normalized pressure (Pn) to a model pressure (Pm) described by an analytic form as following,

$$P_{fit} = e^{b_6 r} \left[b_2 + b_3 \sin(\varphi) + b_4 \sin^2(\varphi) + b_5 \cos^2(\varphi) \right] + R^{b_6} \left[b_7 + b_8 \sin(\varphi) + b_9 \sin^2(\varphi) + b_{10} \cos^2(\varphi) \right] + b_{11} \quad (4)$$

where r is the radial distance in R_E and φ is the azimuthal angle (0° at noon, 90° at dusk, 180° at midnight, and 270° at dawn). b_1 to b_5 mainly control the pressure in the inner magnetosphere while b_6 to b_{10} determine the plasma sheet pressure, b_{11} is the pressure residual. The parameters for the best fit were obtained by minimizing the difference between Pn and Pm. More details are in Wang et al., [2013].

3. Dataset and Methodology

In this study we have used Geotail and THEMIS data to obtain the equatorial pressure distribution for different Kp and Psw situation. Geotail data is from January 1, 1995 to December 31, 2005, and it covers regions from $r \sim 8$ to $30 R_E$. Plasma data from two instruments onboard Geotail are used: the ion and electron data from the Low Energy Particle (LEP) instrument [Mukai et al., 1994] that covers the ion energy range from 21 eV/q to 44 keV/q and the electron energy range from 43 eV to 41 keV, and the proton data from the Energetic Particles and Ion Composition (EPIC) instrument [Williams et al., 1994] that covers the ion energy range from 46 keV to 3005 keV (EPIC only measures > 32 keV and > 110 keV integral electrons so electron moments is not available). The ion moments are from a summation of the LEP and EPIC data and the electron moments are from the LEP data.

For THEMIS, the ions and electrons are measured by an electrostatic analyzer (ESA, 0.006 – 20 keV/q for ions and 0.007 – 26 keV for electrons) [McFadden et al., 2008] and a solid state telescope (SST, 35 keV – 6 MeV for ions and 30 keV – 6 MeV for electrons). Full distributions are used with time resolution of a few minutes. The total plasma moments are a summation of the ESA and SST moments.

After we get the observed pressure distribution, we modeled the equatorial observed pressure to get the smoothed pressure profile as the input to the numerical code of 3D force-balanced magnetic field model. Then we obtain the 3D magnetic field for different Kp and Psw. According to our computed 3D forced balanced B-field, we are able to obtain the field curvature and the proton gyro-radius on the surface of minimum B as following:

$$\text{Curvature radius: } Rc = Bz / (dB_{xy}/dz)$$

$$\text{Gyro radius: } \rho = mV / eBz$$

This allows us to calculate the tail current sheet scattering parameter $S = Rc/\rho$. We have used $0.1 < S < 8$ as our criterion for current sheet scattering [Lyons and Williams, 1984, Sergeev et al., 1983]. Then we computed the IB ($S=8$) for different energies and compared our model IB with THEMIS and FAST observations.

Finally, we have used Geotail and THEMIS ion differential energy flux of 42 channels (energy from ~ 5 eV to > 650 keV) to calculate the maximum ion precipitation. Precipitating energy fluxes integrated over energies from Emin ($S = 8$) to Emax ($S = 0.1$), and compared with ground aurora observations.

4. Results

Figure 1 illustrate ratio of curvature radius to gyro-radius for 27 keV proton on the equatorial plane for different Kp and solar wind dynamic pressure cases. The ratio has minimum value around midnight and extended toward

dawn and dusk, the low value penetrates towards the Earth as K_p and P_{sw} increases. And the IB (black line with $S=8$) is inside $10 R_E$ at midnight, it moves from about $9.5 R_E$ to $6.5 R_E$ when K_p increase from 0 to 5. Figure 2 illustrates the IBs of different energy ions mapping on ionosphere for 12 different K_p and P_{sw} cases. It's shown that IB moves to higher latitudes from midnight towards dawn/dusk and it moves to lower latitudes as energy increases (about 0.3° lower for 71 keV proton than that for 27 keV proton). In addition, the IB moves to lower latitudes as K_p and P_{sw} increases. This is due to increasing K_p or P_{sw} causes the cross-tail current increases, leading to the stretch of magnetic field lines [Yue et al., 2013]. Figure 3 demonstrates the comparison between 27.67 keV proton equatorial isotropic distribution based on THEMIS observations and the computed 27 keV IB (black line) for different K_p (from 0 to 4, $K_p=5$ cases didn't show due to the large data gap) and P_{sw} cases. From Figure 3, we know that the calculated IB of 27 keV matches well with the observed inner boundary of isotropic distribution around midnight and post-midnight while there is some discrepancy at pre-midnight, especially for higher K_p cases, this may due to our pressure model inaccuracy or due to the increasing wave activities as K_p increases. We have done IB comparison of 14 different energy proton channels with observed inner boundary of isotropic distribution of corresponding energy protons. Due to the paper limit, we won't show here. Furthermore, we compared our modeled IB of 10 keV proton with low altitude FAST satellite observation for different K_p cases as shown in Figure 4. The computed IBs matches well with FAST observations under low K_p (<3), but it shows $1-2^\circ$ difference as K_p increase, maximum at pre-midnight, the observed IB mapped to lower latitude. As mentioned earlier, the difference may be due to wave-particle interaction causing the particle precipitating in the low latitude at pre-midnight or the inaccuracy of our pressure model.

Based on the Geotail and THEMIS ion differential energy flux data, we calculated the precipitating flux mapping on the ionosphere for different K_p and P_{sw} cases, and compared with ground-based NORSTAR MSP proton aurora equatorward boundary (red line) for three different K_p categories ($K_p \leq 1$, $2 \leq K_p < 4$, $4 \leq K_p \leq 5$ due to the limited database) as shown in Figure 5. The precipitating flux increase as K_p and P_{sw} increases, while P_{sw} effect is dominant. Meanwhile, its peak moves to lower latitude as K_p and P_{sw} increases. Comparing with the observed proton auroral equatorward boundary, the predicted precipitation location matches well with aurora observation under low K_p (<3), and the precipitation location is consistent with proton auroral equatorward boundary at post-midnight even under high K_p . However, there are about 2° difference around mid-night and pre-midnight for high K_p . Again, this may be due to the pressure gradient in our model is not large enough to map the precipitation flux to the lower latitude or because of the intensified wave activity during high K_p situation.

5. Conclusions

In this study, we have computed ion IB of different energy protons based on our 3D self-consistent magnetic field model. And by using THEMIS and Geotail differential energy flux, we have calculated the maximum ion precipitations. Then we compared our model results with high/low altitude satellites and ground-based observations. We have found that IB moves to (1) higher latitudes from midnight towards dawn/dusk; (2) lower latitudes as energy increases as well as K_p and P_{sw} increases. In addition, the calculated IB matches well at midnight and post-midnight with the observed ion inner boundary of isotropic distribution obtained from THEMIS spacecraft while it shows discrepancy at pre-midnight. Meanwhile, the modeled IB is consistent with low altitude FAST observations under low K_p (<3), but shows $1-2^\circ$ difference as K_p increase, especially at pre-midnight. According to the Geotail and THEMIS ion differential energy flux data, we have calculated the maximum ion precipitating flux and found that the precipitation flux increase and its peak move to lower latitudes as K_p and P_{sw} increases. Comparing with ground NORSTAR MSP aurora observation, the computed precipitating flux matches well with equatorward boundary of proton aurora under low K_p (<2).

The result of comparison between our model prediction and observations is that in the quiet conditions ($K_p < 2$) they agree well, whereas large differences are found during geomagnetic active times ($K_p > 3$). Such differences can be explained in several ways. First of all, we have to take into account the possible deficiencies of our magnetospheric model (how well it describes the distribution of 3D magnetic field), arising due to inaccurate empirical plasma pressure model compared with observations [Wang et al., 2013], or due to insufficient statistical observation. Our results then indicate that the magnetic field depression in the inner magnetosphere is deeper than that predicted by our self-consistent magnetic field model. A second reason can be the enhanced wave activity, which provides the additional pitch-angle scattering in the inner region. Typically, this scattering is weak and produces very anisotropic fluxes in the loss cone (called the low-latitude proton precipitation, LLPP, [Gvozdevsky et

al., 1997]), however, during the active times, it can strongly intensify [Usanova et al., 2012] and provide almost isotropic distributions. In that case it can be difficult to distinguish IB and LLPP boundaries and the equatorial boundary of isotropic precipitation can be erroneously defined a few degrees equatorward from the true boundary of adiabatic/ nonadiabatic motion in the equatorial magnetosphere. Finally, the disagreement during geomagnetic active time may arise because other unknown mechanisms. To clarify which of the above-mentioned reasons give the major contribution to the discussed discrepancy, the additional investigations are required.

In the Future, we will modify the fitting function for the empirical pressure formula or reassigning weights for the different terms to steer the gradients toward realistic values. The new fit will be then used again to obtain a B-field configuration that will be compared with observations.

References

- Gvozdevsky B. B., Sergeev V. A., and Mursula K.: Long lasting energetic proton precipitation in the inner magnetosphere after substorms, *J. Geophys. Res.*, 102(A11), 24 333–24 338, 1997.
- Lvova, E. A., Sergeev, V. A., & Bagautdinova, G. R. (2005, June). Statistical study of the proton isotropy boundary. In *Annales Geophysicae* (Vol. 23, No. 4, pp. 1311-1316). Copernicus GmbH.
- Lyons, L. R., & Williams, D. J. (Eds.). (1984). *Quantitative aspects of magnetospheric physics* (Vol. 23). Springer.
- McFadden, J. P., C. W. Carlson, D. Larson, V. Angelopoulos, M. Ludlam, R. Abiad, B. Elliott, P. Turin, and M. Marckwordt (2008), The THEMIS ESA plasma instrument and in - flight calibration, *Space Sci. Rev.*, 141, 277 - 302, doi:10.1007/s11214-008-9440-2.
- Mukai, T., S. Machida, Y. Saito, M. Hiraehara, T. Terasawa, N. Kaya, T. Obara, M. Ejiri, and A. Nishida (1994), The low - energy particle (LEP) experiment onboard the Geotail satellite, *J. Geomagn. Geoelectr.*, 46, 669 - 692, doi:10.5636/jgg.46.669.
- Sergeev, V. A., Malkov, M., & Mursula, K. (1993). Testing the isotropic boundary algorithm method to evaluate the magnetic field configuration in the tail. *Journal of geophysical research*, 98(A5), 7609-7620.
- Sergeev V. A., Sazhina, E. M., Tsyganenko, N. A., Lunbland, J. A., and Soraas F.: Pitch angle scattering of energetic protons in the magnetotail current sheet as the dominant source of their isotropic presipitation into the nigtside ionosphere, *Planet Space Sci.*, 31, 1147–1158, 1983.
- Sergeev V. A. and Malkov M. V.: Diagnostic of the magnetic con- figuration of the plasma sheet from measurements of energetic electrons above the ionosphere, *Geomagn. Aeron.*, 28, 649–653, 1988.
- Sergeev V. A., Bikkuzina G. R., and Newell P. T.: Dayside isotropic precipitation of energetic protons, *Ann. Geophys.*, 15, 1233– 1245, 1997.
- Shelley, E. G., Johnson, R. G., & Sharp, R. D. (1972). Satellite observations of energetic heavy ions during a geomagnetic storm. *Journal of Geophysical Research*, 77(31), 6104-6110.
- Usanova, M. E., I. R. Mann, J. Bortnik, L. Shao, and V. Angelopoulos (2012), THEMIS observations of electromagnetic ion cyclotron wave occurrence: Dependence on AE, SYMH, and solar wind dynamic pressure, *J. Geophys. Res.*, 117, A10218, doi:10.1029/2012JA018049.
- Wang, C.-P., Chao Yue, S. Zaharia, X. Xing, L. Lyons, V. Angelopoulos, T. Nagai, and T. Lui (2013), Empirical modeling of plasma sheet pressure and three-dimensional force-balanced magnetospheric magnetic field structure: 1. Observation, *J. Geophys. Res. Space Physics*, 118, doi:10.1002/jgra.50585.
- Williams, D. J., R. W. McEntire, C. Schlemm II, A. T. Y. Lui, G. Gloeckler, S. P. Christon, and F. Gliem (1994), Geotail energetic particles and ion composition instrument, *J. Geomagn. Geoelectr.*, 46, 39–57, doi:10.5636/jgg.46.39.
- Yue, Chao, C.-P. Wang, S. G. Zaharia, X. Xing, and L. Lyons (2013), Empirical modeling of plasma sheet pressure and three-dimensional force-balanced magnetospheric magnetic field structure: 2. Modeling, *J. Geophys. Res. Space Physics*, 118, doi:10.1002/2013JA018943.
- Zaharia, S., (2008). Improved Euler potential method for three-dimensional magnetospheric equilibrium. *Journal of Geophysical Research* (Space Physics) 113, A08221.

Figures

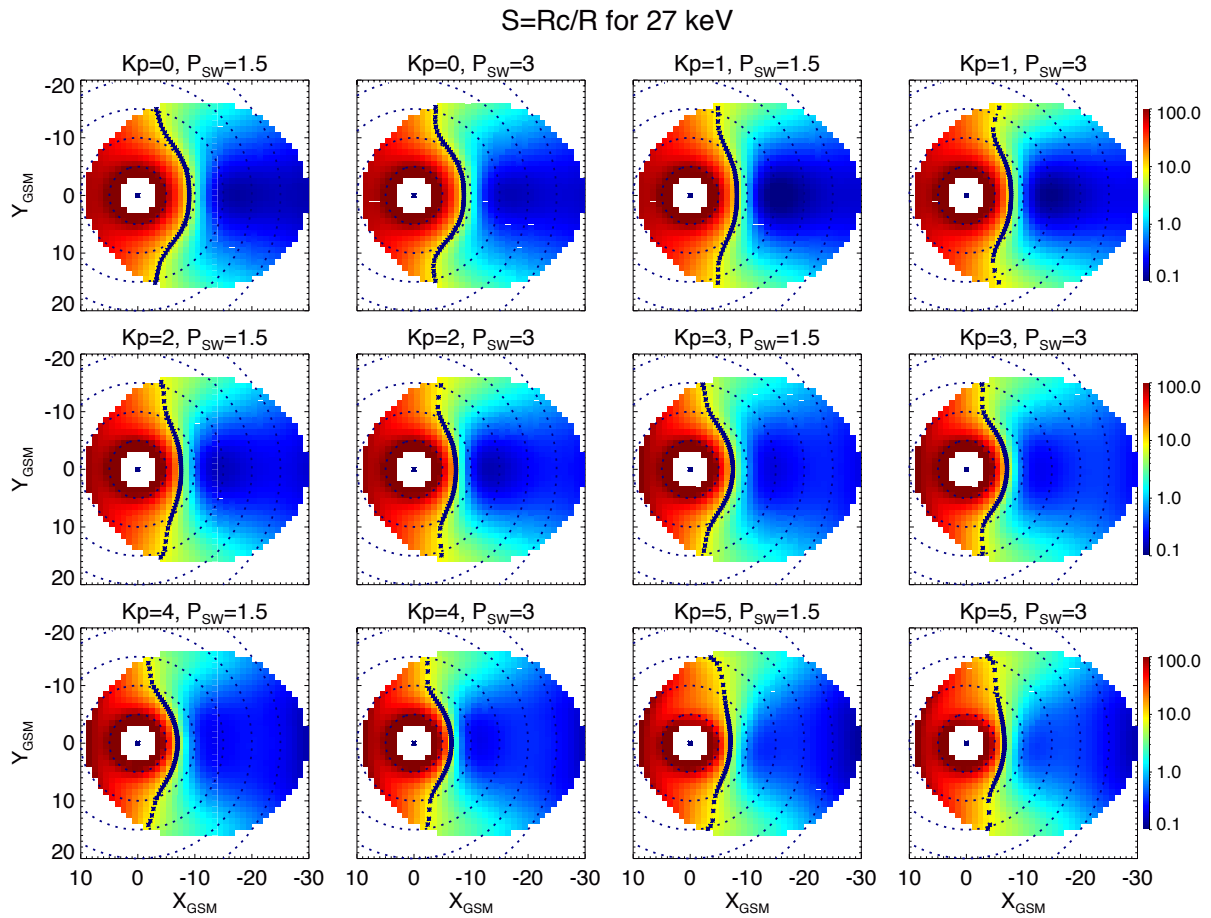


Figure 1: The ratio of curvature radius to gyro-radius for 27 keV proton on the equatorial plane for different Kp and solar wind dynamic pressure cases. The Black dots mark $S=8$

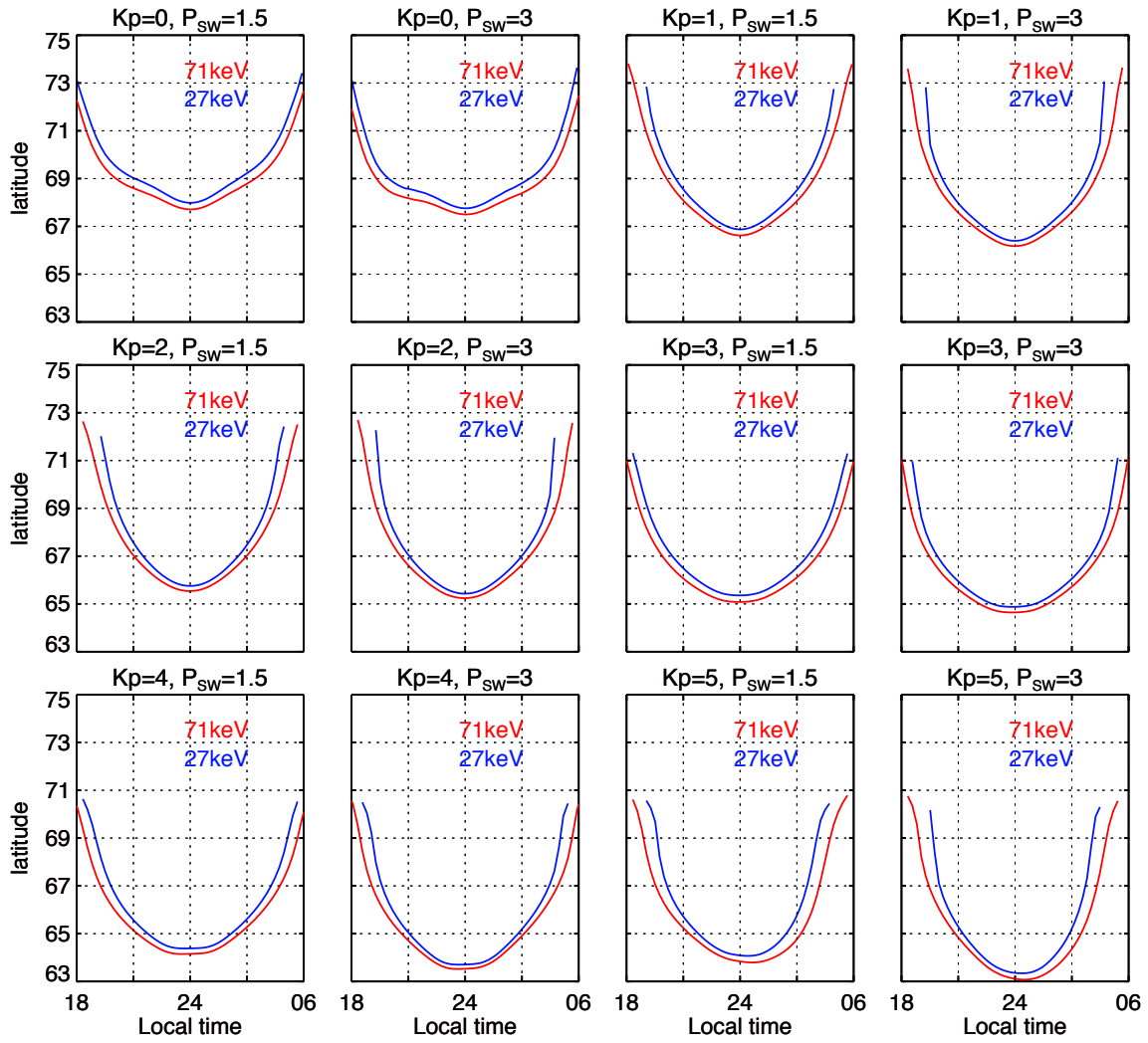


Figure 2: The IB distribution of 27 (blue line) and 71 (red line) keV proton on the ionosphere for different Kp and solar wind dynamic pressure cases

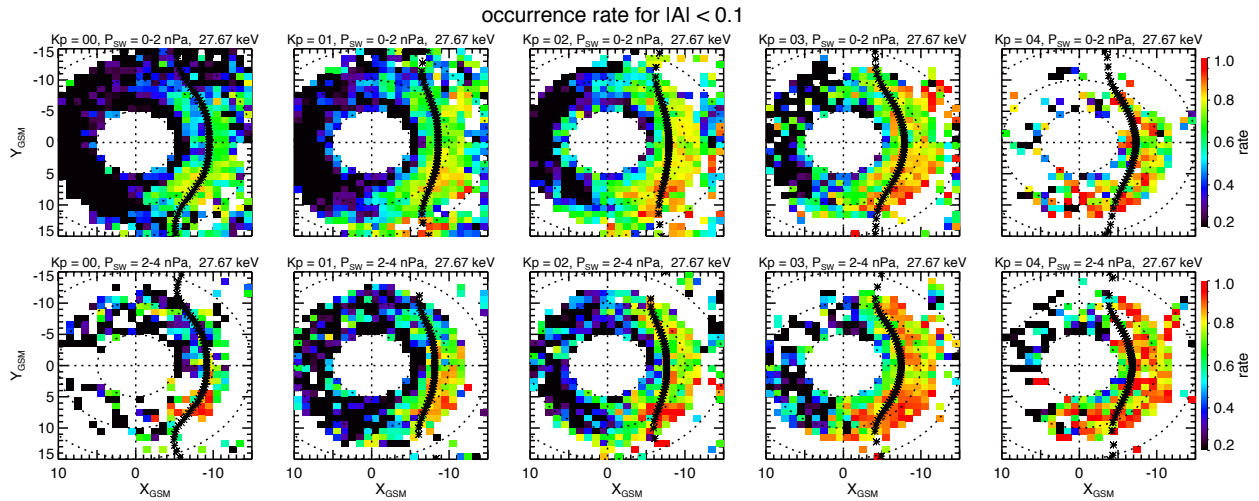


Figure 3: The 27.67 keV proton equatorial isotropic distribution based on THEMIS observation for different Kp and solar wind dynamic pressure cases. The Black dots mark S=8 for 27 keV proton

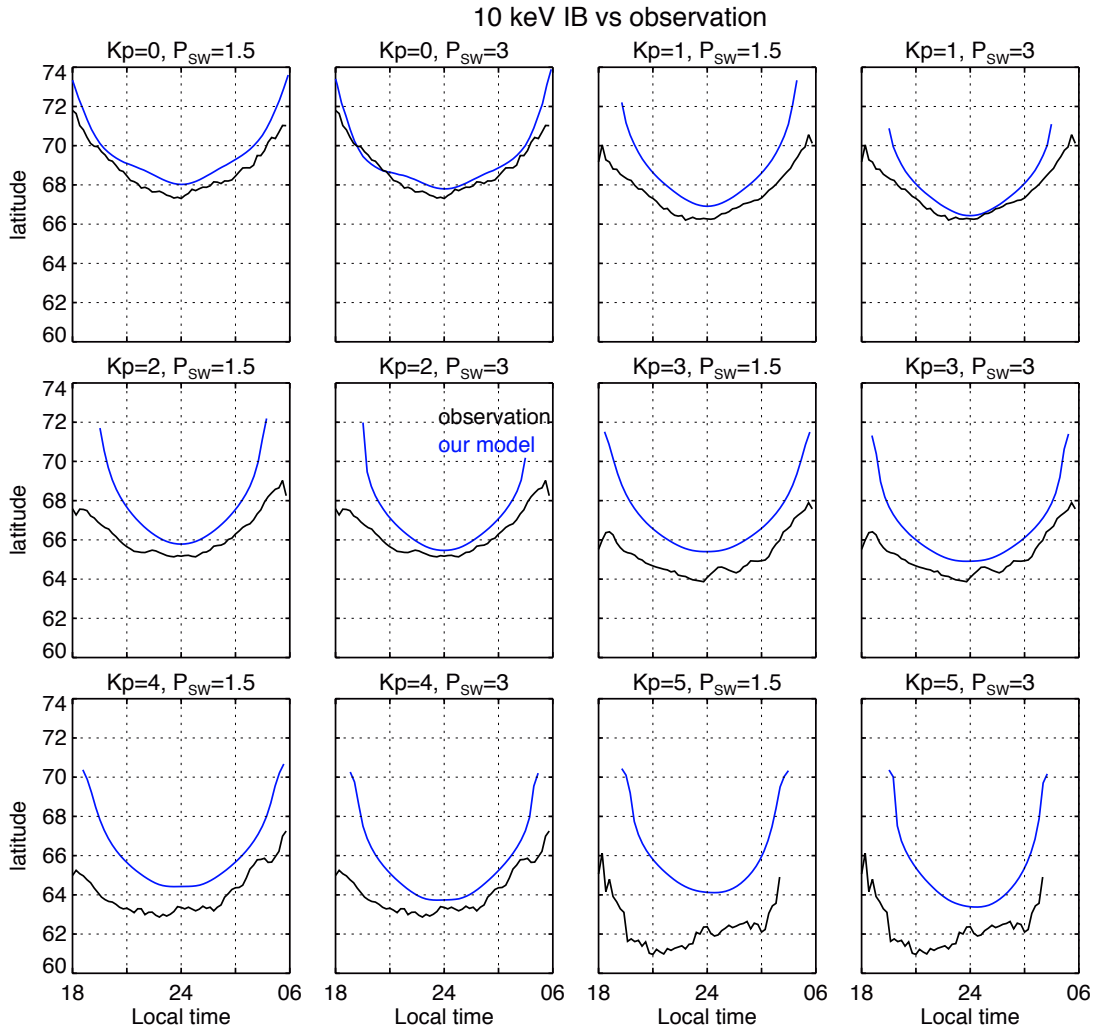


Figure 4: The IB distribution of 10 keV proton (blue line) on the ionosphere for different Kp and solar wind dynamic pressure cases. The Black lines represent the Fast satellite observation for different Kp (same Kp, the two black lines are the same)

Ionospheric precipitation flux (ergs s⁻¹ cm⁻²)

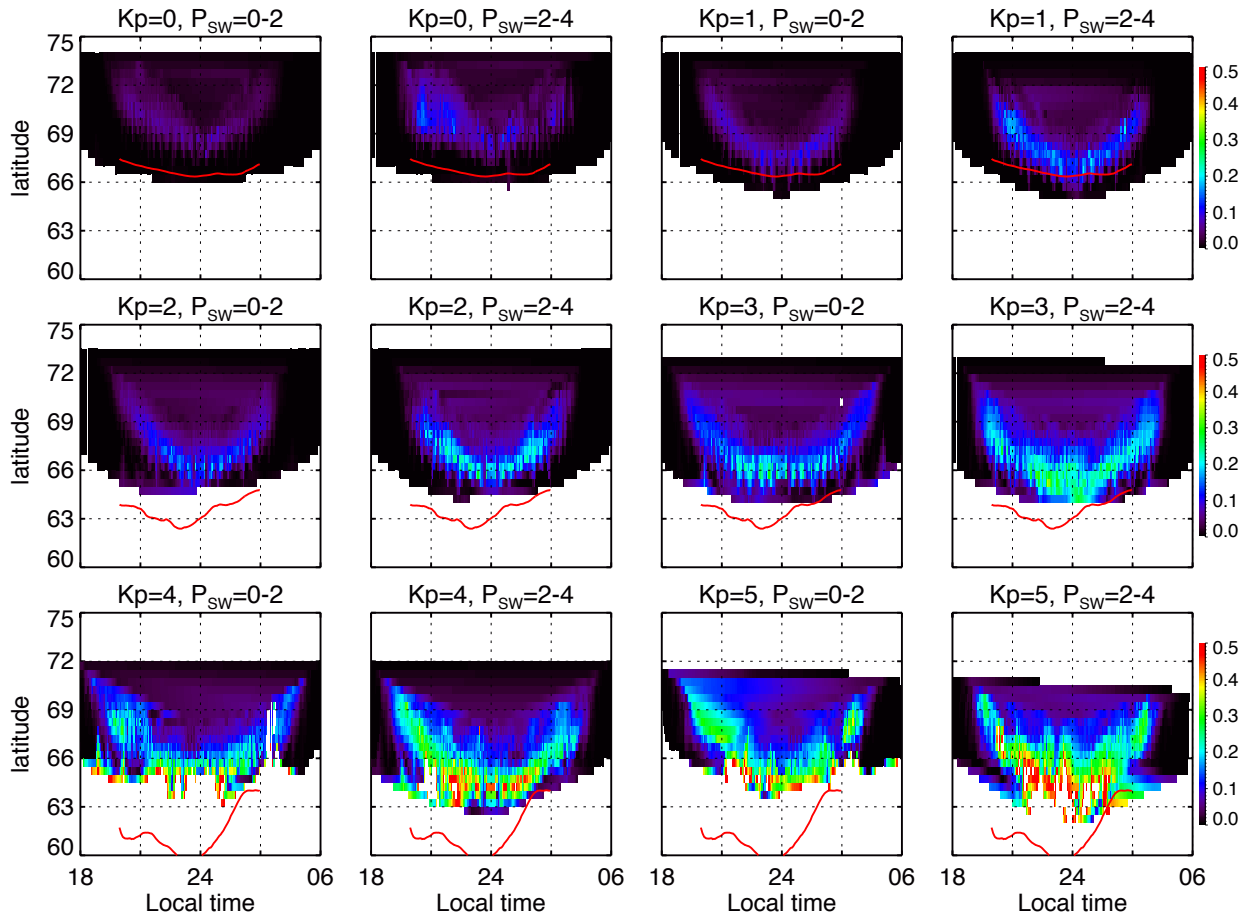


Figure 4: The maximum ion precipitating flux on the ionosphere for different Kp and solar wind dynamic pressure cases. The red lines are the equatorward boundaries of proton aurora derived from ground NORSTAR MSP for $Kp \leq 1$, $2 \leq Kp < 4$, $4 \leq Kp \leq 5$ (the four red lines on each row are the same).

Mysterious Southward Interplanetary Magnetic Field

X.-Y. Zhang

University of Michigan, Ann Arbor, MI 48109

John T. Steinberg

Los Alamos National Laboratory, Los Alamos, NM 87545

Abstract

The southward component of the interplanetary magnetic field (IMF) is a strong driver of geomagnetic activity. Well-defined solar wind structures such as interplanetary coronal mass ejections (ICMEs), corotating interaction regions (CIRs) and small-scale magnetic flux ropes (SMFRs) are the source of most long-duration, large-amplitude IMF Bs. We analyze IMF Bs-events unrelated with any well-defined solar wind structures at 1 AU using ACE spacecraft observations from 1998 to 2004. We find that ~ 10% of the strong Bs-events ($t > 1$ hour, $B_z < -5$ nT) are related with Alfvén waves, more than half of which show low-frequency, slow solar wind ($V_{sw} < 400$ km/s) properties. We also learn that one third of the Alfvén wave-type Bs-events triggered geomagnetic storms, and half triggered substorms. It is also presented that the contribution of Bs-events from ICMEs decreases significantly with the radial distance due to the over-expansion. However, there are still ~ 14% of the strong Bs-events show complex signatures in the plasma parameters, which need be studied in more details.

Keywords: IMF southward component, Alfvén waves in slow solar wind, geoeffectiveness

1. Introduction

The relationship between the interplanetary magnetic field (IMF) and the Earth's magnetospheric activities has been studied extensively since [Fairfield, 1966] found that the southward component of IMF (IMF Bs) is associated with ground magnetic disturbances on Earth while the northward component corresponds to quiet geomagnetic conditions. The observation of non-zero IMF Bs is also evidence for solar coronal activity and provides a tool to study it [Lindsay, 1999; Hochedez, 2005]. Thus IMF Bs is a key parameter to understand the Sun-Earth interaction, furthermore to extend our knowledge of space physics.

The interplanetary magnetic field (IMF) is the magnetic field that originates from the Sun and propagates outward by the solar wind. Based on the following assumptions: 1. magnetic field is radial at the solar corona; 2. the solar wind is flowing outward with a constant radial velocity; 3. the plasma in space is a perfect conductor; 4. the Sun is self-rotating, we can get an ideal model of the distribution of the IMF as shown in the schematic figure on the right (Figure 1), which is called the Parker spiral [Parker, 1958].

However, based on the classic Parker theory of the IMF, there is no significant, long lasting magnetic field component perpendicular to the ecliptic plane except for transients propagating outward from the Sun observed in the interplanetary medium as interplanetary coronal mass ejections (ICMEs) [Klein, 1982; Lindsay, 1995], interplanetary small-scale magnetic flux ropes (ISMFRs) [Moldwin, 2000; Feng, 2010; Zhang, 2012], and stream interaction regions (SIRs) [Smith, 1976; Rosenberg, 1980]. Borovsky [2008] presented a flux tube solar wind model in which the large

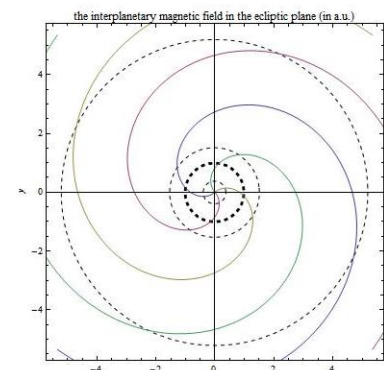


Figure 1

spread in magnetic field orientations at 1 AU is due to a braiding of magnetic flux tubes about the Parker spiral direction. In addition, *Borovsky* [2008] pointed out that small deviations from the spiral close to the source lead to large deviations from spiral at 1 AU. (Figure 2) He suggested that the Alfvén-like discontinuities at the boundaries of the flux tube are due to reconnection at the foot of the flux tubes. In contrast, turbulence in the solar wind [*Ragot*, 2006] or undamped Alfvén waves [e.g., *Burlaga*, 1982] have also been proposed to be the source of angular variations of the solar wind magnetic field about the Parker spiral direction.

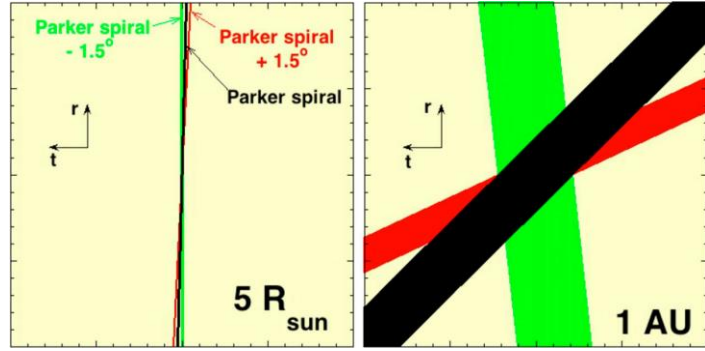


Figure 2

The properties and geoeffectiveness of these solar wind structures have been widely studied. [*Webb*, 1991; *Yashiro*, 2004] have found that the occurrence rate of CMEs peaks strongly during solar maximum, while CIR peaks during the late declining phase of the solar cycle [*Mursula*, 1996]. The interaction regions produced by nonrecurrent HSS occur throughout the solar cycle [*Bobrov*, 1983; *Jian*, 2011]. *Jian* [2006b] defined Interplanetary CME (ICME) mainly based on perpendicular pressure, and suggested that at one AU a Magnetic Cloud (MC) is observed during spacecraft crossings for only one third of ICMEs. *Gosling* [1993], *Xu* [2009], and *Richardson* [2012] showed that CIRs were more important for inducing moderate and small storms while MCs triggered intense storms more frequently. *Echer* [2008a] found that Dst has the highest dependence on the integrated B_s or E_y (product of B_s and V_x) than other interplanetary components. Besides the well-defined solar wind structures, there are discontinuities (tangential and rotational discontinuities, and slow shocks) related with B_s -events. *Burlaga* [1968] showed directional discontinuities in the interplanetary medium are always accompanied with a change of the direction normal to the ecliptic plane, which is IMF z-component most of the time.

Alfvén waves with wide period range (10^2 to $5 \cdot 10^4$ sec in the spacecraft frame) in the interplanetary medium were first observed by *Coleman* [1967] based on the comparison of an ideal, uniform model. It was found that if the fluctuations of the magnetic vectors and the flow velocity are (anti) correlated for ($B_x > 0$) $B_x < 0$, there are outward propagating Alfvén waves from the Sun, which is described in the schematic figure (Figure 3) [*Belcher*, 1971; *Denskat*, 1977; *Tu*, 1990a].

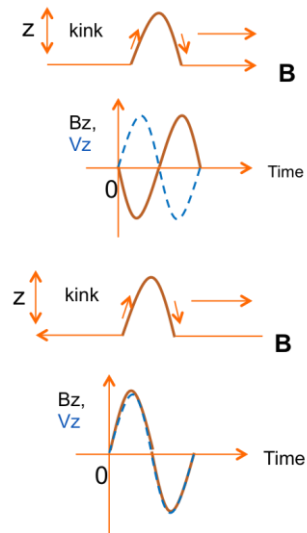


Figure 3

The cross helicity (Alfvén effect ratio) was first put forward by *Matthaeus* [1982] as one of the rugged invariants of 3-D ideal incompressible MHD turbulence theory. *Riley* [1996] used this quantity to describe the 'Alfvénicity', a measure of the correlation between variations of velocity and magnetic fields. If the cross helicity is close to unity, the fluctuations of the solar wind are purely Alfvénic, and if it is close to zero, the fluctuations are non-Alfvénic, that is the interplanetary medium is dominated by the convection of static structures [e.g., *Tu*, 1992]. Alfvén ratio was also introduced by *Matthaeus* [1982] to present the ratio between the kinetic and magnetic fluctuation energy. *Tu* [1993] showed that as the heliocentric distance increases, the normalized cross helicity and Alfvén ratio decrease, from near 1 at 0.3 AU in high-speed solar wind to substantially less than 0.5 at 1 AU.

To learn about the source of IMF B_s , we defined IMF B_s -events as continuous IMF B_s intervals with varying thresholds of B_s magnitude and duration, and categorized their association with different solar wind structures, including magnetic clouds (MCs), ISMFRs, ICMEs without MC signature (ejecta), stream interacting regions (SIRs), and shocks, as well as events unrelated with well-defined solar wind structures in previous work [*Zhang*, 2013]. We found that for strong B_s -events ($t > 1$ hours, $B_z < -5$ nT, observed by WIND at 1 AU), ~ 28% are not associated with any well-defined solar wind structure. The mystery about the source of these geoeffective, long-duration, large-amplitude B_s -events that are not related with any well-defined solar wind structure still remains and was the focus of work performed during the 2013 summer school. Through analysis of

these Bs-events using ACE magnetic field and plasma data, we found that Alfvén waves are a possible source of long-duration, large-amplitude IMF Bs intervals.

Because Alfvén waves in the solar wind may show southward IMF as one of the main features, [Lee, 2006; Tsurutani, 1987] their geoeffectiveness has also been studied extensively. Tsurutani [1987] showed that the high intensity ($AE > 1000$ nT), long duration ($T > 2$ days) continuous auroral activity (HILDCAA) events are induced by interplanetary Alfvén wave trains (IAWT) propagating outward from the Sun, which was suggested to be caused by magnetic reconnection between the southward components of the Alfvén wave magnetic fields and magnetospheric fields.

During the summer school, we analyze the magnetic field and plasma data with 64-second resolution from the ACE spacecraft from 1995 to 2004 to study the detailed features of the IMF Bs-events ($t > 1$ hour, $B_z < -5$ nT) that were considered to be unrelated with any well-defined solar wind structures [Zhang, 2013] based on previous published event lists.

2. Methodology

We used published event lists to identify IMF Bs-events associated with well-defined solar wind structures, [Zhang, 2013]. In this study, instead of relying on published event lists, we examine the 64-second averaged ACE magnetic field and plasma data at 1 AU from 1995 to 2004 in order to study the source of IMF Bs-events ($t > 1$ hour, $B_z < -5$ nT) unrelated with any well-defined solar wind structure.

Our methodology was:

(1). Compare the magnetic field data in GSE coordinates from the WIND and ACE satellites to determine the boundary of the Bs-event;

(2). Check the ion moments and superthermal electron (STEA) pitch angle data from ACE SWEPAM for features related to ICMEs, shocks or SIRs during the intervals from (1); if the measured proton temperature is significantly lower than the expected temperature based on the solar wind speed, and the STEA pitch angle in the energy channel of 272 eV shows a bi-directional distribution, this interval is categorized as an ICME; if there is a sharp increase of proton density, speed, temperature, and IMF magnitude, this event is considered shock associated; if there is a gradual increase of solar wind speed from the background average value ~ 400 km/s to over 500 km/s, and decrease of proton density, the event is labeled as a SIR.

(3). For the Bs-events showing no features of ICME, shock, or SIR from (2), perform linear regression between the magnetic field and velocity field for the x-, y-, z- components in GSE coordinates; if the slopes of all three components have the same order, this event is considered Alfvén wave related; if one or two components change only slightly in both magnetic and velocity fields, while the other two or one components show a good linear relationship, this event is also categorized as Alfvén wave-related.

(4). Examine the geomagnetic activity indices (SYM-H, AE/AU/AL, PC) starting from the same universal time of the Alfvén wave related Bs-event from (3) and ending 75 minutes later than the Bs-event, and compare with the results of our previous study [Zhang, 2013].

(5). To extend the study to observations at other radial distances, we also analyzed the magnetic field data from Ulysses, Helios, and Messenger at their ecliptic plane orbit. Based on the published ICME and SIR events list [Jian, 2006; 2008], we compared the distribution of ICME- and SIR- related Bs-events at 1 AU and 5.3 AU, and also compared the yearly occurrence of Bs-events at and within 1 AU. The threshold of the magnetic field southward component was scaled as following function: $B_{\text{ths}} = B_{\text{th}}/R$, where B_{th} is the threshold of B_z magnitude at 1 AU, R is the heliospheric distance of the spacecraft in unit of AU.

3. Results

Figure 4 gives an example of an Alfvén wave related Bs-event observed by the ACE satellite at 1 AU on November 19, 2002. The time period shown in the plot is 19:00 - 24:00 UT November 19, 2002, while the Bs-event is from 20:30 to 22:50 UT marked by the dashed lines. During this Bs-event, the magnitude of the magnetic field and B_x did not change significantly but averaged about 11 and 3 nT, respectively. IMF B_y showed an increase from -5 nT to 5 nT during the first half of the Bs-interval, and then decreased to ~ -10 nT until the end of this interval.

Between the dashed lines in the third panel, the solar wind speed fluctuates around 390 km/s, while the component in the Sun-Earth direction varied simultaneously with the magnitude. It is seen from the fourth panel that there were sign changes of the z- component of solar wind velocity in the same direction as the corresponding magnetic field component, which is also seen in the y- component of both the magnetic field and solar wind velocity. We also checked the solar wind condition over the solar rotation that covers this Bs-event, showing that the solar wind speed remained around 400 km/s for 3 days before this event and a SIR occurred 2 days later. The pitch-angle distribution of suprathermal electrons is peaked at 180 degrees that is anti-parallel to the magnetic field over the whole interval. The latitudinal angle of the IMF turned from 45 degrees to -90 degrees along with the southward turning and then turned back to ~ 0 degrees at the end of the Bs-event. The longitude angle of the IMF stayed at -45 degrees for most of the interval but there were some short perturbations to 0 degrees.

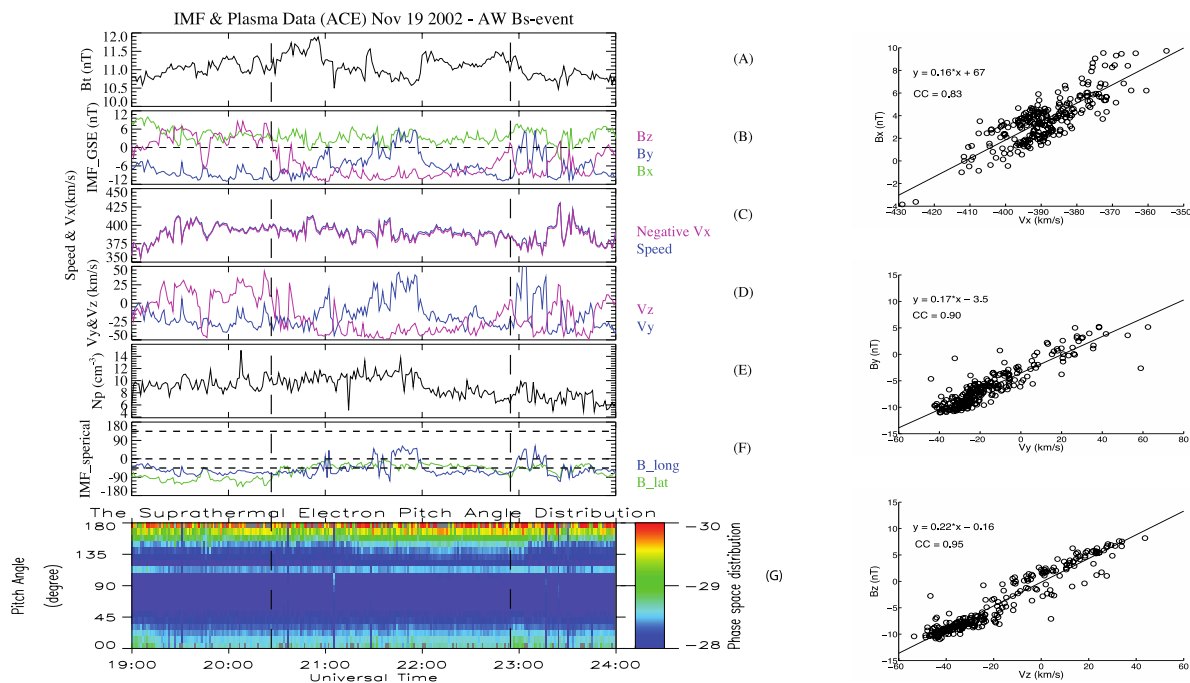


Figure 4 An example of an Alfvén wave related Bs-event observed by the ACE satellite at 1 AU. From top to bottom, panels show the (A) total interplanetary magnetic field (IMF) magnitude; (B) IMF x-, y-, z- components in GSE coordinates; (C) solar wind speed; (D) x-, y-, z- components of solar wind velocity in GSE coordinates; (E) solar wind proton density; (F) latitudinal (green) and longitudinal (blue) angles of IMF, black dotted lines at 135 degrees and -45 degrees in the longitudinal angles indicating IMF with Parker spiral direction; and (G) suprathermal electron pitch angle distribution at 272 eV.

Figure 5 The linear regression of x-, y-, z- components (from top to bottom) between magnetic field and velocity field for the event shown in Fig. 4. The scattered dots are observations from magnetometer on ACE, and the red line shows the linear regression result. The equation and correlation coefficient of the linear regression are shown in each panel.

Figure 5 shows the linear regression of the x-, y-, z- components (from top to bottom) between magnetic field and velocity for the event shown in Fig. 4. The scattered dots are magnetometer and velocity observations from ACE, and the straight line shows the linear regression result. The equation and correlation coefficient of the linear regression are shown in each panel. The correlation coefficients for x-, y-, z- component are 0.83, 0.90, and 0.95, while the slopes are 0.16, 0.17, and 0.22, respectively. Combined with the fact that the longitude angle of the IMF during this interval almost stayed at -45 degrees, the observations are consistent with Alfvén waves. We also calculated the cross helicity as 0.78 for this Bs-event (which is not shown in the plot).

We performed the above analysis on all of the unidentified events from the previous study. We found that there are 28 Bs-events newly identified as ejecta, 2 as SIRs, and 2 as shocks in this study that were not previously identified in published event lists, and that there are 57 Bs-events show Alfvén wave features. This study again finds

that most Bs-events are associated with ejecta, while about 10% of Bs-events are associated with Alfvén waves. About 14% of Bs-events are still not associated with any of these solar wind structures.

In order to understand the geo-effectiveness of Alfvén wave-related Bs-events, we examined the response of geomagnetic indices. Figure 6 shows the minimum SYM-H (nT), maximum AE (nT) and maximum PC from top to bottom for all the Alfvén wave related Bs-events (1998 April - 2004). The threshold of the duration and Bs magnitude of the Bs-events are 1 hour and 5 nT. The intervals of ground measurements start at the same universal time as the Alfvénic events but end 75 mins later than the Bs-events observed by ACE. From the top panel, it is seen that about one third of these events are followed by an interval of SYM-H less than -50 nT. Around half of the events induce substorms, indicated by maximum AE greater than 1000 nT. The last panel of Fig. 6 shows that more than half of these Bs-events are related with PC index intervals larger than 4. PC index was proposed by *Troshichev* [1986] to characterize the variability of the polar cap magnetic field. *Troshichev* [2011] and reference herein suggested that $PC \sim 2$ works as a threshold of a geomagnetic storm.

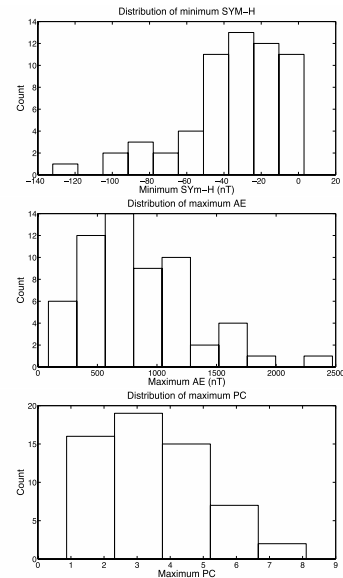


Figure 6 Histogram of minimum SYM-H (nT), maximum AE (nT) and maximum PC from top to bottom for all the Alfvén wave related Bs-events (1998 April - 2004). The threshold of the duration and Bs magnitude of the Bs-events are 1 hour and 5 nT. The intervals of ground measurements start at the same universal time as but end 75 mins later than the Bs-events observed by WIND.

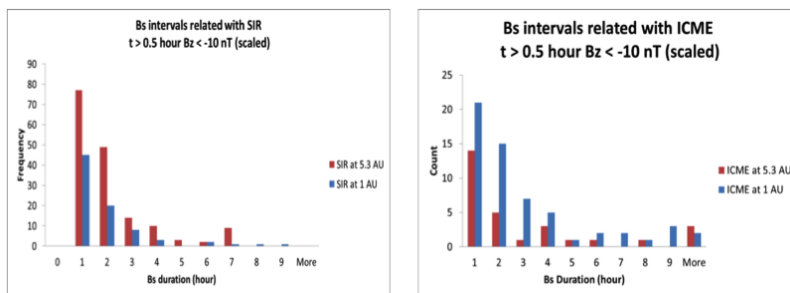


Figure 7 shows and occurrence rate of ICME- (left) and Sir- (right) related Bs-events ($t > 1$ hour, $B_{th} < -5$ nT) in terms of duration at 1 AU (in blue) and 5.3 AU (in red) respectively.

Because the occurrence and duration of Bs-events at different radial distances will depend on the causes of Bs, we extended our studies to include Ulysses beyond 1 AU and Helios within 1 AU. Figure 7 gives the distribution of Bs-events ($t > 0.5$ hour, $B_z < -10$ nT) related with ICMEs [Jian, 2006b, 2008] and SIRs [Jian, 2006a, 2008] in terms of duration observed by ACE at 1 AU and by Ulysses at 5.3 AU. It shows that the occurrence rate of SIR-related Bs-events increased at 5.3 AU compared to 1 AU, however ICME-type Bs-events decreased. The statistical analysis indicates that SIR-type Bs-events are the major portion of Bs-events ($t > 1$ hour, $B_z < -5$ nT) at 5.3 AU, rather than ICME-type Bs-events dominate at 1 AU. Comparing the frequency of Bs-events in different bins of duration at 1 AU and 5.3 AU, it presents that ICME-related Bs-events with longer duration occur more often at 5.3 AU than 1 AU, but oppositely for SIR-type Bs-events. The results suggest that the overexpansion of ICMEs is accompanied with a faster decrease of magnetic field magnitude within the structure than the ambient IMF.

Figure 8 shows that the occurrence rate of Bs-events during the recent solar minimum (in blue) is less than half of that during the similar phase in the previous solar cycle (in green). Comparing the results shown in red and green bars, it is indicated that the Bs-events within longer duration ($t > 3$ hours) observed by Helios within 1 AU occur more often than that measured by ACE at 1 AU.

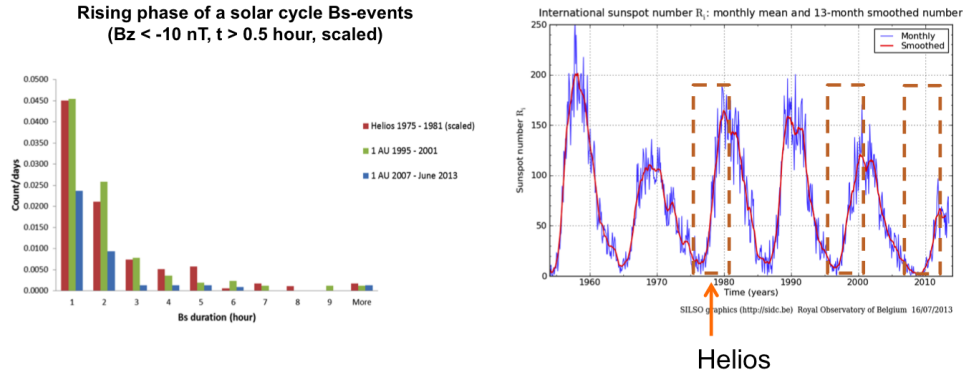


Figure 8 The distribution of Bs-events ($t > 0.5$ hour, $B_z < -10$ nT) occurrence rate in terms of duration observed by Helios (1975 – 1981) within 1 AU and by ACE at 1 AU during the similar phase of different solar cycles. The y-axis on the left shows the counts of events divided by the number of days for data available. The panel on the right shows the yearly averaged sunspot number for more than 5 solar cycles, with the dashed boxes presenting the periods analyzed shown in the panel on the left.

4. Conclusions

During this summer school, we analyzed the magnetic field and plasma data from ACE spacecraft from 1995 to 2004 to study the detailed features of the IMF Bs-events that were identified to be unrelated with any well-defined solar wind structure [Zhang, 2013]. In this study, Alfvén wave (AW) features Bs-events are defined mainly according to the linear correlation between the magnetic field and velocity components. We searched for the statistical properties of the solar wind conditions during the AW-type Bs intervals, and also the geomagnetic field response to those events. We found that:

- (1) Alfvén waves in slow solar wind carry long-duration, large-amplitude Bs intervals, and the perturbations on the Sun propagating outward are possibly the source of the low-frequency Alfvén waves;
- (2) These AW-type Bs-events are geoeffective, weaker than ICME and SIR related Bs-events, but impossible to predict the occurrence of Alfvén waves and either its geoeffectiveness from the coronagraph for several days in advance;
- (3) The contribution of ICME-related Bs-events decreases significantly with increasing radial distance, but they still occur more often in the category of long-duration at further distance than SIR-type Bs-events. It suggests that the overexpansion of the ICMEs makes the magnetic field within the structures drop much faster with increasing radial distance from the Sun than the ambient medium;
- (4) Although we have learned more about the source of IMF southward component, however, there are still long-duration, large-amplitude Bs-events with complex signatures in the magnetic field and plasma parameters, which could not be categorized into any of these solar wind structures and need further study in more details.

References

- Belcher, J. W., and L. Davis, Jr., Large-amplitude Alfvén waves in the Interplanetary medium, 2, *J. Geophys. Res.*, Vol. 16, P3534-3563, 1971.
- Bobrov, M. S., Non-recurrent geomagnetic disturbances from high-speed streams, *Planet. Space Sci.*, Vol. 31, P865-870, 1983.
- Borovsky, J. E., Flux tube texture of the solar wind: strands of the magnetic carpet at 1 au?, *J. Geophys. Res.*, Vol. 113, 2008.
- Burlaga, L. F., micro-scale structures in the interplanetary medium, *Sol. Phys.*, Vol. 4, P67-92, 1968.
- Burlaga, L. F., R. P. Lepping, and K. W. Behannon, Large-scale variations of the interplanetary magnetic field: voyager 1 and 2 observations between 1-5 au, *J. Geophys. Res.*, Vol. 87, P4345-4353, 1982.
- Denskat, K. U., and L. F. Burlaga, Multispacecraft Observations of Microscale Fluctuations in the Solar Wind, *J. Geophys. Res.*, Vol. 82, Issue 19, P2693-2704, 1977.
- Echer, E., W. D. Gonzalez, and B. T. Tsurutani, Interplanetary conditions leading to superintense geomagnetic storms ($dst \leq -250$ nt) during solar cycle 23, *Geophys. Res. Lett.*, Vol. 35, 2008a.
- Fairfield, D. H., and J. L. J. Cahill, Transition region magnetic field and polar magnetic disturbances, *J. Geophys. Res.*, Vol. 71 (1), P155-169, 1966.

Feng, H.-Q., J.-K. Chao, L. H. Lyu, and L. C. Lee, The relationship between small interplanetary magnetic flux rope and the substorm expansion phase, *J. Geophys. Res.*, Vol. 115, A09,108, 2010.

Gosling, J. T., The solar are myth, *J. Geophys. Res.*, Vol. 98, P18,937-18,949, 1993.

Hochedez, J.-F., A. Zhukov, E. Robbrecht, R. V. der Linden, D. Berghmans, P. Vanlommel, A. Theissen, and F. Clette, Solar weather monitoring, *Ann. Geophys.*, Vol. 23, P3149-3161, 2005.

Jian, L. K., C. Russell, J. G. Luhmann, and R. M. Skoug, PROPERTIES OF STREAM INTERACTIONS AT ONE AU DURING 1995 – 2004, *Sol. Phys.*, Vol. 239, P337-392, 2006a.

Jian, L. K., C. Russell, J. G. Luhmann, and R. M. Skoug, properties of interplanetary coronal mass ejections at one au during 1995-2004, *Sol. Phys.*, Vol. 239, P393-436, 2006b.

Jian, L. K., C. Russell, J. G. Luhmann, R. M. Skoug, and J. T. Steinberg, Stream Interactions and Interplanetary coronal Mass Ejections at 5.3 AU near the Solar Ecliptic Plane, *Sol. Phys.*, Vol. 250, P375-402, 2008.

Jian, L. K., C. Russell, J. G. Luhmann, P. J. MacNeice, D. Odstrcil, P. Riley, J. A. Linker, R. M. Skoug, and J. T. Steinberg, Comparison of Observations at ACE and Ulysses with Enlil Model Results: Stream Interaction Regions During Carrington Rotations 2016 - 2018, *Sol. Phys.*, Vol. 273, P179-203, 2011.

Klein, L. W., and L. F. Burlaga, Interplanetary magnetic clouds at 1 AU, *J. Geophys. Res.*, Vol. 87, P613-624, 1982.

Lee, D., et al., Repetitive substorms caused by alfvénic waves of the interplanetary magnetic field during high-speed solar wind streams, *J. Geophys. Res.*, Vol. 111, 2006.

Lindsay, G. M., C. T. Russell, and J. G. Luhmann, Coronal mass ejection and stream interaction region characteristic and their potential geomagnetic effectiveness, *J. Geophys. Res.*, Vol. 10, P16,999-17,013, 1995.

Lindsay, G. M., J. G. Luhmann, C. T. Russell, and J. T. Gosling, Relationships between coronal mass ejection speeds from coronagraph images and interplanetary characteristics of associated interplanetary coronal mass ejections, *J. Geophys. Res.*, Vol. 104, P12,515-12,523, 1999.

Matthaeus, W. H., and M. L. Goldstein, Measurement of the rugged invariants of magnetohydrodynamic turbulence in the solar wind, *J. Geophys. Res.*, Vol. 87, P6011-6028, 1982.

Moldwin, M. B., S. Ford, R. Lepping, J. Slavin, and A. Szabo, Small-scale magnetic flux ropes in the solar wind, *Geophys. Res. Lett.*, Vol. 27, P57-60, 2000.

Mursula, K., and B. Zieger, The 13.5-day periodicity in the sun, solar wind, and geo-magnetic activity: the last three solar cycles, *J. Geophys. Res.*, Vol. 101, P27,077-27,090, 1996.

Parker, E. N., Dynamics of the interplanetary gas and magnetic fields, *The Astrophys. J.*, Vol. 128, P664, 1958.

Ragot, B. R., DISTRIBUTION OF MAGNETIC FIELD ORIENTATIONS IN THE TURBULENT SOLAR WIND, *The Astrophys. J.*, Vol. 651, P1209-1218, 2006.

Richardson, I. G., and H. V. Cane, Near-earth interplanetary coronal mass ejections during solar cycle 23 (1996 - 2009): catalog and summary of properties, *Sol. Phys.*, Vol. 264, P189-237, 2012.

Riley, P., C. P. Sonett, B. T. Tsurutani, A. Balogh, R. J. Forsyth, and G. W. Hoogeveen, Properties of arc-polarized alfvén waves in the ecliptic plane: ulysses observations, *J. Geophys. Res.*, Vol. 101, P19,987-19,993, 1996.

Rosenberg, R. L., and J. P. J. Coleman, Solar cycle-dependent north-south field configurations observed in solar wind interaction regions, *J. Geophys. Res.*, Vol. 85, P3021-3032, 1980.

Smith, E. J., and J. H. Wolfe, Observations of interaction regions and corotating shocks between one and five AU: Pioneers 10 and 11, *Geophys. Res. Lett.*, Vol. 3, P137-140, 1976.

Tsurutani, B. T., and W. D. Gonzalez, The cause of high intensity long-duration continuous AE activity (hildcaas): interplanetary alfvén wave trains, *Planet. Space Sci.*, Vol. 35, P405-412, 1987.

Tu, C.-Y., and E. Marsch, Transfer equations for spectral densities of inhomogeneous MHD turbulence, *J. Plasma Physics*, Vol. 01, P103-122, 1990a.

Tu, C.-Y., and E. Marsch, The evolution of mhd turbulence in the solar wind, *Solar wind seven*, Vol. 00, P549-554, 1992.

Tu, C.-Y., and E. Marsch, A model of solar wind fluctuations with two components: alfvén waves and convective structures, *J. Geophys. Res.*, Vol. 98, P1257-1276, 1993.

Webb, D. F., The solar cycle variation of the rates of CMEs and related activity, *Adv. Space Res.*, Vol. 11, P37-40, 1991.

Xu, D., T. Chen, X.-X. Zhang, and Z. Liu, Statistical relationship between solar wind conditions and geomagnetic storms in 19982008, *Planet. Space Sci.*, Vol. 57, P1500-1513, 2009.

Yashiro, S., N. Gopalswamy, G. Michalek, O. C. S. Cyr, S. P. Plunkett, N. B. Rich, and R. A. Howard, A catalog of white light coronal mass ejections observed by the soho spacecraft, *J. Geophys. Res.*, Vol. 109, A07, 105, 2004.

Zhang, X.-Y., M. B. Moldwin, and M. Cartwright, The geo-effectiveness of interplanetary small-scale magnetic flux ropes, *Journal of Atmospheric and Solar-Terrestrial Physics.*, Vol. 95-96, P1-14, 2012.

Zhang, X.-Y., and M. B. Moldwin, The source, statistical properties and geoeffectiveness of long-duration southward interplanetary magnetic field intervals, *J. Geophys. Res.*, in press, 2013.



Los Alamos Space Weather Summer School
30 Bikini Atoll Rd, ISR-1, MS D466
Los Alamos, NM 87545

<http://SpaceWeatherSchool.org>

